A Study of EMAT (Electromagnetic Acoustic Transducer) Operation on Ferromagnetic Metals

Volume 1 of 1

Ian David Kiteley

Submitted in fulfilment for the degree of Doctor of Philosophy

University of Warwick

September 1999

Table of Contents

List of figures

Chapter 1

Chapter 2

Chapter 3

Chapter 4

Figure:

Table:

Chapter 5

Figure:

Chapter 6

Figure:

Acknowledgements

I would like firstly to thank Professor S. B. Palmer for taking me on as part of this project in the first place. His interest in the work was always a great motivator when my own enthusiasm was found wanting. Obvious thanks must also go to Dr. C. Edwards for useful discussions and suggestions of fruitful avenues of exploration along with Dr. S Dixon for similar reasons. Dr. C. Lim (Slim) must be thanked for his friendship, squash games, advice, discussion etc. with thanks to J. Reed for his technical support and advice, ie: how to solder properly. Thanks are also due to the members of the electronics workshop for building several pieces of equipment without which the project would never have continued. Dr. Anna Widdowson deserves my gratitude for convincing me on several occasions that I did actually want a PhD and it was in fact worth it, as does Dr. Kazali Zin. Similar thanks must also go to Dr. Gav Jackson, a better housemate and golf partner I couldn't have wished for. I would also like to thank Dr. G. Farrow, Dr. J. Burd and Dr. L. Morgan at the Britsh Gas technology centre, Loughborough, for their continued interest in the work and supply of numerous samples. Thanks are also due to Dr. Proykova at Portsmouth University for supplying the high temperature VSM and Mr. R Stokes for providing the PC on which this work was written. Finally, I would like to thank my parents and family for supporting me in whatever I have decided to do, without them I'd never have reached the point where these acknowledgements even needed writing.

Declaration

The work contained in this thesis is my own except where specifically stated otherwise and was carried out in the Department of Physics from October 1995 to September 1999. No part of this work has been previously submitted to this or any other academic institution for admission to a higher degree. Some of the work has appeared in the form of publications which are listed in the bibliography.

Bibliography

The text and diagrams included in this thesis were prepared using MS Word '97 and CorelDraw 7.0 throughout. Waveform and data analysis was performed using Wavemetrics IgorPro 4.0 for Windows and MS Excel '97.

Publications arising from this thesis:

As primary author;

1998: C. Edwards, I. D. Kiteley and S. B. Palmer; "Studies of the Ultrasound Generated by Electromagnetic Acoustic Transducers (EMATs) using a modified Michelson Interferometer."; QNDE 98 Snowbird, Vol 18A, pp 1064 – 1076.

Summary

Ultrasound is widely used as a tool for non destructive testing, being completely non invasive and much safer than some other methods, X ray techniques for example. Its low relative cost is also attractive purely from a business standpoint. Its use, however, is restricted more to applications where the ultrasonic transducer and test piece can be brought into close contact, thus allowing the use of couplant gels. In situations where a fully non contacting method is required the cost and complexity of an ultrasonic system is considerably higher. These usually take the form of laser based systems where a high powered laser pulse is focussed onto a sample surface and induces an ultrasonic pulse which is detected on the opposite sample face by some other type of transducer. Whilst giving high signal amplitudes etc. these systems are expensive, require regular maintenance and are very difficult to use on rough and dirty surfaces. A much cheaper alternative is to use EMATs (Electromagnetic Acoustic Transducers)

EMATs have enjoyed comparative success in generating both ultrasonic guided waves and bulk waves in oxides, invars, some steels and particularly aluminium. Their mode of operation means they can be used in the non contact regime and are also much cheaper than laser based systems. However, their low efficiency has precluded their use on many steels due to the lack of appreciable signal amplitude. This is especially true for the case of the spiral coil EMAT, most steels requiring significant signal averaging to discern the ultrasonic echoes induced by the transducer. The work presented in this thesis was aimed at determining which physical properties of the steels had the greatest influence on the electromagnetic transduction mechanism. The mechanism is known to be of purely Lorentz force origin in non magnetic metals whilst magnetostriction is thought to play an important role in ferromagnets.

This suggestion has been shown to be incorrect in the case of low tensile carbon and mild steels in that no direct correlation between magnetostriction and spiral coil EMAT performance was found, strongly suggesting a predominantly Lorentzian ultrasonic source. The same was not true for duplex stainless steels and invar that were found to exhibit significantly non linear dependencies of signal amplitude on applied magnetic field. Although it remains unclear whether this was due to a predominantly magnetostrictive source it is almost certainly linked to its two phase microstructure.

Measurements of high temperature EMAT efficiency have shown a correlation between the Curie point, T_c, and the disappearance of shear wave signals in all of the steels and alloys tested. The emergence of large longitudinal mode signals was also observed at temperatures just above T_c in several of the ferromagnetic samples, although the effect was absent in nickel. Its absence in this particular sample contradicts previously reported observations using the same EMAT geometry by other authors.

Use of a modified Michelson interferometer, as a detector, has shown the existence of a frequency doubling effect in all the samples tested, both ferromagnetic and non. The effect was found to be suppressed on application of a magnetic field, this behaviour being consistent with the action of either a 'rectified' magnetostrictive source or a self field Lorentz force. Definitive identification as to which of these is the dominant mechanism was found to be impossible given the small signal amplitudes although the effect itself has not previously been documented as far as the author is aware.

Chapter 1

Introduction to ultrasonic testing and Electromagnetic Acoustic Transducers (EMATs)

1.1: Introduction

Ultrasound is used extensively throughout the NDE industry in a range of ways [1, 2], defect detection being perhaps the most common although certainly not the only one. A great benefit of using ultrasound is that many different modes may propagate in a solid, allowing us to optimise detection of certain defect types by exciting and detecting the correct mode. Such uses include the propagation of surface and plate waves over large distances along otherwise inaccessible pipes etc. while they are still in service. This allows detection of cracks and other potentially disastrous defects that would be difficult to detect in any other way. Bulk modes are also used to detect defects within the interior of a sample and to make accurate thickness measurements rapidly. Ultrasound also has the advantage of being relatively non hazardous when compared to some other methods, such as X ray testing for example. Another great benefit of ultrasonic testing is that it can be used on a wide range of material types such as metals, alloys and composites, other types of NDE usually only being employable on specific types of material. It is not just in the field of practical NDE that ultrasound finds uses, for example single crystal elastic constants can be measured to high accuracy over a range of temperatures using ultrasonic velocity measurements [3]. These constants give important information on the state of the crystal, eg: ultrasound provides the quickest and simplest method for determining the magnetic phase transitions of rare earth elements and alloys [4].

Ultrasound is introduced into a sample by a number of different methods nowadays, the method used being dependent upon the particular application. We will briefly review those methods relevant to this thesis below.

1.2: Piezoelectric generation

The most widely used method of introducing ultrasound into a sample is by the use of piezoelectric transducers. These take the form of a piezoelectric crystal, cut in a particular orientation, that it is pulsed with a high voltage to generate strains at ultrasonic frequencies within it. These strains are coupled into the surface of a test sample via a viscous couplant gel or by immersing the whole system in a liquid bath, both of these methods having been used successfully in many applications. However, in both cases we are dealing with an essentially contacting technique which is useless in a situation where the test piece is hot or moving or both. For these applications a technique is required that is non contacting and therefore completely precludes the use of piezoelectric devices. It is also difficult to generate some wave modes using these transducers, such as radially polarised shear waves.

1.3: Pulsed laser generation

The use of pulsed lasers to generate ultrasound has received a good deal of attention in recent years [5]. The method usually employs a high powered pulsed laser, such as CO_2 or Nd:YAG, with the beam focussed onto the specimen surface. Depending on the energy of the beam, this induces either a thermoelastic or ablative source at the sample surface, the thermoelastic type being a good source of both longitudinal

and shear waves [6] whilst the ablative type produces predominantly longitudinal [7]. The use of lasers has the obvious advantage of being fully non contacting and also produces large ultrasonic amplitudes that are temporally sharp. The mechanism of ultrasound generation is also well understood, and modelled, allowing us to generate different ultrasonic modes by tailoring the laser pulse characteristics. A major disadvantage, however, is the high cost of the lasers, their physical size also leading to problems where space is at a premium. A much cheaper solution to the non contact problem is the use of electromagnetic acoustic transducers (EMATs).

1.4: EMATs

EMATs are comparatively cheap transducers that generate ultrasound in the surface of a metal without needing to be in contact with it. In non magnetic metals, they do this by virtue of the interaction between eddy currents, induced by an RF electromagnetic field, and a static magnetic field [8]. The case in ferromagnetic metals is considerably more complex and will be discussed later in chapter 2. The RF field is produced by a coil placed close to the metal surface and pulsed with a high, typically 20 Amps or more, current. The static field is produced either by an electromagnet or, for the handheld transducers of interest here, a strong permanent magnet, eg: NdFeB. A static field and a pulsed coil are the essential components of any EMAT, the geometry of each dictating the ultrasonic mode generated. The geometry of particular interest in the present work was that of a normal static field and a spiral RF coil and is discussed below. The major drawback of EMATs is in their low transduction efficiency, usually orders of magnitude lower than either piezo or laser systems. This has restricted their use to the role of detector in many

applications, such as hybrid laser-EMAT systems [9, 10] where a more efficient generation technique has to be used. This is certainly true in the case of most bare steel test pieces although the use of EMATs in send-receive mode has enjoyed some success on oxidised steels and at high temperatures [11, 12]. Due to their low efficiency it is clear that any send-receive EMAT system requires a great deal of optimisation in the design of both the transducer itself and the associated drive/receiver electronics.

1.5: Spiral coil-normal field EMAT

A schematic of the EMAT design studied here is shown in figure 1.1, it is the product of extensive development and has enjoyed success in use on epoxy bonded aerospace aluminium plates. As such, it already represents considerable optimisation of both coil design and drive/receiver circuitry to obtain broadband signals of a useful amplitude [13]. The transducer is of similar dimensions to piezoelectric types, is relatively simple to construct and is also fairly rugged. The spiral coil – normal field geometry was intended to generate radially polarised shear waves. These cannot easily be generated by piezoelectric transducers and therefore this particular EMAT design is of significant interest. However, the transduction mechanism on ferromagnetic steels is still not clearly defined for this geometry. As a great deal of ultrasonic inspection takes place on such steels there is a clear need for further investigations into this mechanism. From previous work, it was already known that most steels exhibited poor efficiency with this EMAT, compared to say aluminium, with a few notable exceptions. The aim of the work presented here was to identify the dominant transduction mechanism(s) acting in these steels and other

ferromagnetic metals and alloys. This, it was hoped, would enable both identification of the critical material parameters (eg: magnetic properties, electrical conductivity etc.) and subsequent optimisation of the EMAT design, eg: static field strength, for use on these materials.

1.6: Thesis outline

The thesis is divided into seven chapters, this introduction being the first. The second chapter covers the background theory of EMAT operation on both non magnetic and ferromagnetic metals. The experimental details of all the work discussed later will be described in chapter 3. Chapter 4 covers initial investigations into the magnetic field dependence of EMAT efficiency of several samples and any correlation between this and the samples magnetostriction. Chapter 5 describes the results of studies of EMAT efficiency just below and above the Curie point of the ferromagnetic samples. An investigation into the EMAT generation mechanism alone is described in chapter 6. This discusses the use of a modified Michelson interferometer to detect the epicentral displacement associated with ultrasound generated by the spiral coil and the magnetic field dependence of this displacement. Chapter 7 gives a final conclusion to the thesis, outlining the main achievements of the project, and discusses the most likely directions for further work to take.

Chapter 1 references

1: J. Blitz and G. Simpson; *Ultrasonic methods of non destructive testing*; published by Chapman and Hall - London; 1996.

2: J. Krautkramer; *Ultrasonic testing of materials*; published by Springer Verlag – Berlin; 1969.

3: E.A. Turov and V.G. Shavrov; *Usp. Fiz. Nauk* **140**, pp 429 - 462 (1983).

4: V. D. Buchel'nikov and A. N. Vasil'ev; *Usp. Fiz. Nauk* **162**, pp 89 - 128 (1992).

5: D. A. Hutchins, R.J. Dewhurst, S. B. Palmer and C. B. Scruby; *Appl. Phys. Lett.* **38**, pp 677 - 679 (1981).

6: L. R. F. Rose; *Journ. Acoust. Soc. America* **75**, pp 723 - 732 (1984).

7: L. Knopoff; *Journ. Appl. Phys.* **29**, pp 661 - 670 (1958).

8: K. Kawashima; *Journ. Acoust. Soc. America* **60**, pp 1089 - 1099.

9: R. J. Dewhurst, C. Edwards and S. B. Palmer; *Appl. Phys. Lett.* **49**, pp 374 - 376 (1986).

10: D. A. Hutchins, F. Hauser and Thomas Goetz; *IEEE Trans Ultrasonics* **UFFC-33**, pp 478 - 483 (1986).

11: D. R. Bilson, C. Edwards, M. S. Rohani and S. B. Palmer; Rev. Prog. in QNDE. 15, pp 2281 - 2287 (1995).

12: P. Crowther, C. Edwards, S. B. Palmer and S. D. Kenney; Insight 39, pp 618 - 622 (1997).

13: S. Dixon; PhD Thesis; Warwick University (1995).

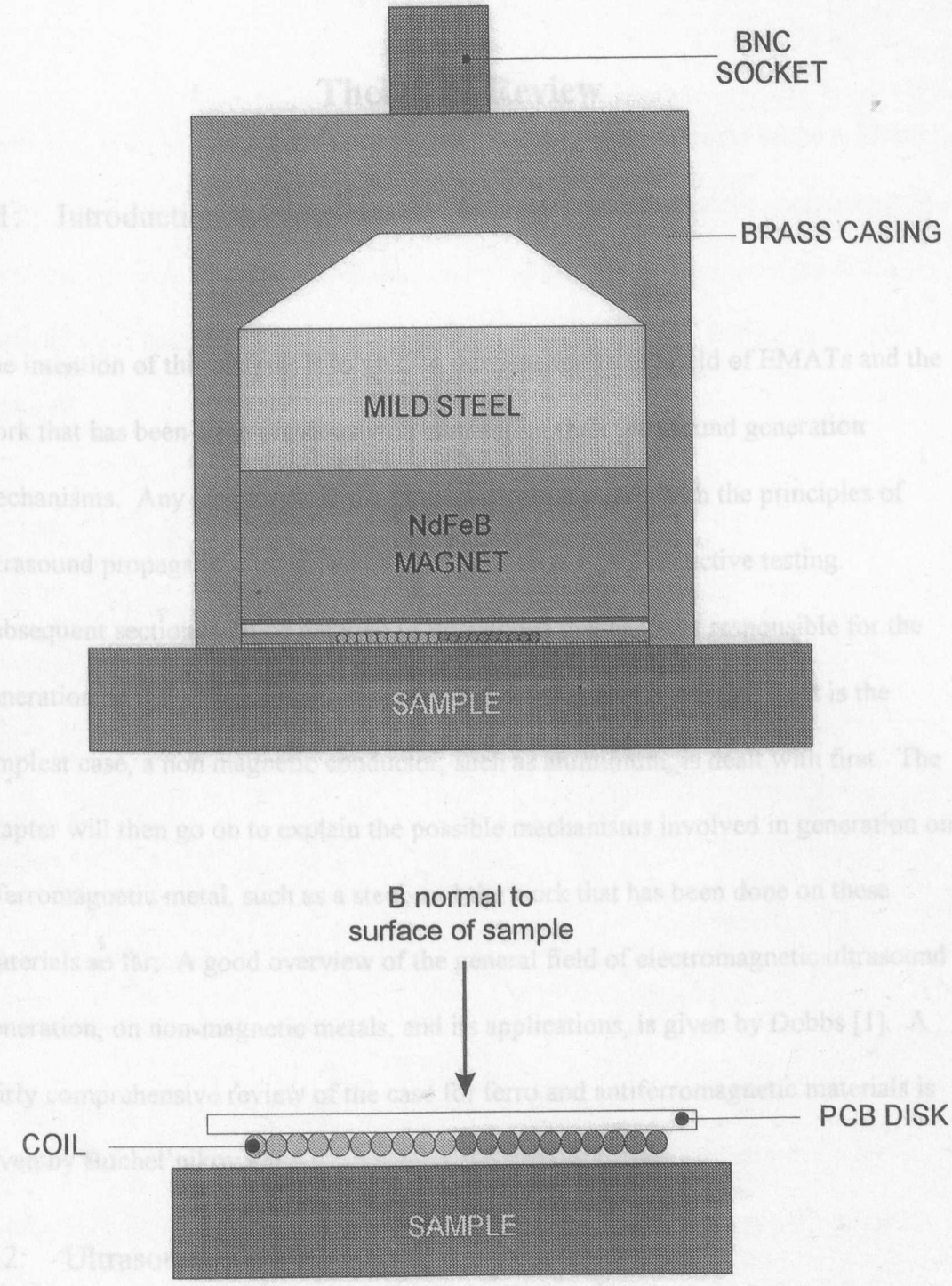

Figure 1.1: Construction of typical shear wave EMAT showing the relative orientations of the spiral coil and NdFeB magnet.

Chapter 2

Theory & Review

2.1: Introduction

The intention of this chapter is to give an introduction to the field of EMATs and the work that has been done previously on elucidating their ultrasound generation mechanisms. Any chapter on EMATs must obviously start with the principles of ultrasound propagation in solids and its relevance to non destructive testing. Subsequent sections will be devoted to the various mechanisms responsible for the generation of this ultrasound on magnetic and non magnetic metals. As it is the simplest case, a non magnetic conductor, such as aluminium, is dealt with first. The chapter will then go on to explain the possible mechanisms involved in generation on a ferromagnetic metal, such as a steel, and the work that has been done on these materials so far. A good overview of the general field of electromagnetic ultrasound generation, on non-magnetic metals, and its applications, is given by Dobbs [1]. A fairly comprehensive review of the case for ferro and antiferromagnetic materials is given by Buchel'nikov [2].

2.2: Ultrasound in solids

The propagation of sound in an elastic solid is described most conveniently in terms of the relationship between the stress, σ_{ij}, and strain, e_{kl}, within that solid [3], where σ_{ij} and e_{kl} are both 9 component tensors. This relationship is given by:

$$\sigma_{ij} = C_{ijkl}\, e_{kl} \tag{2.1}$$

where C_{ijkl} is an 81 component tensor describing the elastic stiffness of the medium. Simple considerations allow us to reduce the number of independent components of the stress tensor to 6 and therefore the number of independent components of C_{ijkl} down to 36. These components are usually expressed using the following simpler notation:

$$\begin{vmatrix} \sigma_1 \\ \sigma_2 \\ \sigma_3 \\ \sigma_4 \\ \sigma_5 \\ \sigma_6 \end{vmatrix} = \begin{Vmatrix} C_{11} & C_{12} & C_{13} & C_{14} & C_{15} & C_{16} \\ C_{21} & C_{22} & C_{23} & C_{24} & C_{25} & C_{26} \\ C_{31} & C_{32} & C_{33} & C_{34} & C_{35} & C_{36} \\ C_{41} & C_{42} & C_{43} & C_{44} & C_{45} & C_{46} \\ C_{51} & C_{52} & C_{53} & C_{54} & C_{55} & C_{56} \\ C_{61} & C_{62} & C_{63} & C_{64} & C_{65} & C_{66} \end{Vmatrix} \begin{vmatrix} e_1 \\ e_2 \\ e_3 \\ e_4 \\ e_5 \\ e_6 \end{vmatrix} \tag{2.2}$$

where i,j = 1,2,..,6

and 1 denotes 11, 2 denotes 22, 3 denotes 33, 4 denotes 23, 5 denotes 31 and 6 denotes 12

It is also true that $C_{ij} = C_{ji}$ in the most general case so we can further reduce the number of independent components down to 21. Accounting for crystal symmetry further reduces this number, obviously a perfectly isotropic medium requires only two independent constants, the longitudinal and shear. The fact that solids have these elastic constants allows us to propagate sound waves through them in a number of different modes, these waves being governed by the wave equation:

$$\frac{\partial^2 U}{\partial x^2} = \frac{1}{c^2}\frac{\partial^2 U}{\partial t^2} \qquad (2.3)$$

here U refers to the displacement whilst c is the velocity of the wave in the medium. The velocity c is equal to $\sqrt{C/\rho}$ where C is the elastic constant related to the oscillation direction of the medium and ρ is the density. Many wave modes may propagate in a solid, such as Rayleigh, Lamb and bulk waves [3]. For the purposes of this work we need only be concerned with the bulk wave type, that is waves propagating into the bulk of the solid, the two major types being shear, S, and longitudinal, L. The S type is mainly concerned with motion of the medium transverse to the propagation direction (for the plane wave solution at least) whilst L waves exhibit displacement in the same direction as they propagate. An important fact is that plane S waves have no volume change associated with them whereas L waves do, the importance of this will become clear when EMAT generation at and around the Curie point is discussed.

2.3: Impulse responses to point sources

The ultrasonic displacement within a body due to any applied force is given by convolution of the 'impulse response' of the system with the transient function of that driving force. The impulse response for different force distributions has been modelled by several authors for different force distributions and geometries. Work by Rose [4] focussed on the treatment of a laser induced thermoelastic point source, treating it as a surface centre of expansion (SCOE). Doyle [5] extended this work to account for thermal diffusion into the bulk to explain an anomalous positive spike in the waveform. The treatment of a normal point force acting at the surface was dealt

with as long ago as 1958 by Knopoff [6] and more recently extended to a finite sized transducer by Bresse [7], this dealing with a ring shaped thermoelastic source. The impulse responses given by the early models are shown in figures 2.1 and 2.2 and are explained below.

2.3.1: Thermoelastic SCOE

Rose's treatment of the thermoelastic laser source involved taking an expanding point source at some depth within the sample and allowing this to tend towards the surface. The governing equations for a Heaviside (H) time dependent laser pulse are:

$$U(t) = A\left[\dot{f}(t)H\left(t-\frac{z}{V_s}\right) - \dot{g}(t)H\left(t-\frac{z}{V_p}\right)\right] \qquad (2.4)$$

$$\text{where } f(t) = \frac{t\left(t^2 - S_s{}^2z^2\right)\left(2t^2 - S_s{}^2z^2\right)}{\left(2t^2 - S_s{}^2z^2\right)^2 - 4t\left(t^2 - S_s{}^2z^2\right)\left(t^2 + S_p{}^2z^2 - S_s{}^2z^2\right)^{1/2}}; \qquad (2.5)$$

$$\text{and } g(t) = \frac{t^2\left(t^2 - z^2S_p{}^2\right)\left(t^2 + S_s{}^2z^2 - S_p{}^2z^2\right)^{1/2}}{\left(2t^2 + S_s{}^2z^2 - 2S_p{}^2z^2\right)^2 - 4t\left(t^2 - S_p{}^2z^2\right)\left(t^2 + S_s{}^2z^2 - S_p{}^2z^2\right)^{1/2}} \qquad (2.6)$$

and S_s, V_s, S_p and V_p are the S arrival time, S velocity, L arrival time and L velocity respectively, the parameter A describes the laser pulse characteristics.

The epicentral ultrasonic waveform this produces at some point z inside the sample is shown in figure 2.1. The equation that determines the displacement of the opposite face is slightly modified from these, for our purposes though they are sufficient to

show the important features of the displacement due to a SCOE source. It consists of a negative step displacement due to the arrival of a longitudinal wave 1L. There then follows a gradual reduction in gradient until the positive step displacement due to the 1S shear wave arival. The L step is negative because the surface is a stress free boundary. The relative heights of the L and S steps being related to the Poissons ratio, ν, of the material, for aluminium it is 1:4 for $\nu = 1/3$. This waveform is of course only produced in the case of a purely surface force, taking into account thermal diffusion of the incident laser energy into the depth gives the waveform predicted by Doyle. The longitudinal step in that case has an initial positive spike, the amplitude of which depends on the thermal conductivity of the sample and the laser pulse rise time. This positive spike arises because the source is essentially buried (at depth δ) and therefore the stress free boundary condition for the SCOE is not fulfilled.

2.3.2: Point Normal Force

The action of a point normal force upon a surface was dealt with by Knopoff in 1958 [6]. Although his treatment was aimed at giving an accurate approximation to a seismic problem the same model can be applied to our case of a point normal force acting on the surface of a sample. Knopoff gave the solution for epicentral displacement assuming a step function input so the expressions he gives were differentiated to yield the response to a sharp delta function, ie: an impulse. The expressions he gives are:

$$U(t) = B\left[\dot{f}(w)H\left(t - \frac{z}{\alpha}\right) - \dot{g}(y)H\left(t - \frac{z}{\beta}\right)\right] \qquad (2.7)$$

$$f(w) = \frac{w^2(2w^2 - 2 + a^{-2})}{(2w^2 - 2 + a^{-2})^2 - 4(w^2 - 1)w(w^2 - 1 + a^{-2})^{1/2}} \qquad (2.8)$$

$$g(y) = \frac{2y(y^2 - 1)(y^2 - 1 + a^{-2})^{1/2}}{(2y^2 - 1)^2 - 4(y^2 - 1)y(y^2 - 1 + a^{-2})^{1/2}} \qquad (2.9)$$

where B is the parameter describing the force characteristics, $w = V_p t/z$, $y = V_s t/z$ and $a = V_s/V_p$.

As one would expect for a normal force the most prominent feature (figure 2.2) is the large positive spike associated with the L arrival, this is followed a short time later by a negative step for the S wave with a shallow positive gradient separating the two arrivals. As far as the author is aware no modelling has been done for the case of a buried purely normal force source, this distribution not really being very common in practice. Again the relative heights of the steps is related to the Poissons ratio of the material, in this case, however, the L step is very much larger than that of the S.

2.4: EMAT Generation on non magnetic metals

The discovery by Larsen & Saermark, in 1967 [8], of apparent helicon-phonon coupling in single crystal aluminium was one of the first observed examples of electromagnetic acoustic transduction. Their experiment was intended to study the generation of helicons at liquid helium temperatures but showed anomalous results that strongly suggested the generation of S waves with $\lambda = 2$ sample thicknesses. In 1967 it was discovered by Betjeman [9] that similar acoustic modes could be

generated in a commercially available aluminium rod at room temperature with a high (~1T) magnetic field applied. This result showed the existence of an effect that did not require helicons and was explained [10] in terms of a Lorentz force on the eddy currents induced in the metals surface. An outline of the classical treatment given by Dobbs is included here, the case of a singly polarised eddy current distribution is included here as it is the simplest case. The case of a spiral coil was dealt with in detail by Kawashima [11].

When an RF electromagnetic (e/m) wave is incident upon a metal surface a small fraction of its energy is absorbed within the skin depth δ, this generates eddy currents, j, in the surface which propagate as:

$$j = j_o e^{iwt} e^{-(1+i)z/\delta} \tag{2.10}$$

where the classical skin depth δ is given by:

$$\delta = \sqrt{1/\sigma\mu\omega} \tag{2.11}$$

with σ = electrical conductivity, μ = magnetic permeability and ω = angular frequency. In the presence of an applied field, $\mathbf{B}_o$, the electrons in the eddy current j experience a Lorentz force given by:

$$F = (jxB_o)/n \tag{2.12}$$

where n is the number of electrons per unit volume. If $\mathbf{B}_0$ is orientated along z, ie: B_z, the Lorentz force acts in the x or y direction. If we take the case of an RF magnetic field linearly polarised in the x direction (see figure 2.3b) we obtain RF eddy currents polarised in the y direction, J_y. These eddy currents experience a Lorentz force F_x that acts in the x direction. This force results in a change in the electronic charge distribution and therefore sets up an electric field $\mathbf{E}_x$. This is now the source of the force, $\mathbf{E}_x=\mathbf{F}_x/e$, that acts on the ions to produce a polarised S wave of amplitude ξ_x, this force can be written:

$$Z\mathbf{F} = [Z\mathbf{j}x\mathbf{B}_o] \tag{2.13}$$

where Z is the atomic number of the ions. The equation of motion for the ions can then be written as:

$$M\,\partial^2\xi/\partial t^2 - C\,\partial^2\xi/\partial z^2 = |Z\mathbf{j}x\mathbf{B}_o|/n \tag{2.14}$$

where M = ionic mass and C = elastic modulus (in this case shear). Introducing an expression for the eddy currents j calculated from Maxwells equations and putting in the density $\rho = nM/Z$ and S velocity $s = \sqrt{(C/M)}$ gives:

$$\frac{\partial^2\xi}{\partial t^2} - s^2\frac{\partial^2\xi}{\partial z^2} = \frac{(1+i)}{4\pi\rho\delta}\mathrm{B}_{\mathrm{dyn}}\mathrm{B}_o e^{-(1+i)z/\delta} \tag{2.15}$$

where B_{dyn} is the dynamic field generated by the coil at z = 0, ie: the surface. Solving this for the case where $\delta >> \lambda$ gives:

$$\xi(z) = \frac{B_{dyn}B_o(1-i)\delta}{8\pi\rho s^2(1-i\beta)}\left[\frac{(1-i)}{\delta q}e^{iqz} - e^{-(1+i)z/\delta}\right] \qquad (2.16)$$

This basically gives two components to the sound wave, the second of which is attenuated in the skin depth whilst the first propagates as the acoustic S wave. If we are concerned only with distances $z>>\delta$ the real part of the amplitude is given by:

$$|\xi| = \frac{B_{dyn}B_o}{4\pi\rho s\omega}\frac{1}{\sqrt{(1+\beta^2)}} \qquad (2.17)$$

where $\beta = q^2\delta^2/2$, called the skin depth parameter, and $q = \omega/s$, the wave number. Obviously then the EMAT generated amplitude depends inversely upon the metals density, skin depth and on the magnitudes of the static and dynamic fields B_o and B_{dyn}, aluminium being a relatively efficient EMAT generator due its low ρ and skin depth parameter, β. It should be added, however, that calculations presented later in this work suggest that the $\sqrt{(1+\beta^2)}$ term is relatively constant in all metals, whether non or ferromagnetic due to their high conductivity and correspondingly small δ. For now though let us continue with the case of a non ferromagnetic metal and go on to ultrasound detection by an EMAT, this being relevant for the send-receive system used in this work. The acoustic wave is incident upon and reflects from the metal surface beneath the coil, therefore the total particle amplitude is given by:

$$\xi(z) = \xi_o(e^{-jkz} + e^{jkz})e^{jwt} \qquad (2.18)$$

where ξ_o is some initial amplitude.

Eddy currents, J, are again induced due to the interaction between the electrons (coupled to the ionic lattice) and the static field B_o, these are given by:

$$J = \sigma \frac{\partial \xi(z)}{\partial t} B_o \qquad (2.19)$$

The induced eddy currents are proportional to the differential with respect to time of the particle amplitude. This means that the EMAT acts as a velocity sensor and not a detector of absolute particle amplitude. These eddy currents produce an RF electric field and an associated RFmagnetic field which radiates from the metal surface and is picked up by the coil. As for generation, the efficiency of detection is proportional to B_o, therefore for a non magnetic conductor the amplitude of the received voltage signal is proportional to B_o^2. It is also worth noting that the received voltage pulse is actually the double differential of the initial currrent pulse, the generating eddy currents also being proportional to dB_{dyn}/dt which is itself proportional to dI/dt through the coil.

2.5: Self field Lorentz generation

The Lorentz force due to application of a static magnetic field was discussed previously, however, no account was taken of the dynamic field of the coil and any effect this has on the eddy currents. This will be dealt with now for the case of a spiral coil on a non-magnetic conductor in the absence of any other magnetic fields. Due to the coils geometry, any field component with an orientation normal to the coils plane is effectively cancelled except at the very centre and circumference, see

figure 2.4. This is the case in free space and so is certainly true above a conducting metal where the skin depth also limits the fields spatial extent. Therefore, when the coil is pulsed, it produces an essentially radial magnetic field within the metals skin depth. For this example a sinusoidally varying tone burst is used as it is relevant to the experimental work presented later. The field resulting from this tone burst is given by:

$$\oint \mathbf{B}.\mathbf{dl} = \mu_o \mathbf{J} = \mu_o \mathbf{J}_o \sin(\omega t) \qquad (2.20)$$

Where **J** is the current density due to all the coil elements enclosed in the integral. For a tone burst $\mathbf{J} \propto \sin(\omega t)$ and therefore:

$$\mathbf{B}_{dyn} \propto \sin(\omega t) \qquad (2.21)$$

As stated earlier the eddy currents, $\mathbf{J}_{eddy}$, are proportional to $d\mathbf{B}_{dyn}/dt$ and therefore:

$$\mathbf{J}_{eddy} \propto \omega \cos(\omega t) \qquad (2.22)$$

The Lorentz force F due to B_{dyn} is now seen to be:

$$\mathbf{F} \propto \omega \cos(\omega t) \sin(\omega t) \qquad (2.23)$$

which can be reduced to:

$$\mathbf{F} \propto \omega \sin(2\omega t) \qquad (2.24)$$

This force acts normally to the surface at a frequency of 2ω and sets up an electric field $\mathbf{E}_z$ oscillating in the same direction, therefore driving a compressive wave that propagates into the bulk. It is also apparent that the eddy current density, $\mathbf{J}_{eddy}$, is proportional to ω, the driving frequency. This means that higher frequencies produce larger eddy currents, resulting in a higher Lorentz force **F** and subsequently larger ultrasonic amplitudes. This point is clear when dealing with a tone burst drive pulse but less obvious when dealing with the broadband spike used by the system of interest here. It should also be remembered that the generation again occurs over the whole skin depth, not just at the surface, and that the field at the coils edge and centre does have some small normal component.

2.6: EMAT generation on a ferromagnetic metal

The Lorentz mechanism outlined above will always be acting when an EMAT is used on a conducting sample, ie: a metal. This same mechanism acts on ferromagnetic metals but is altered due to the coupling between the magnetic and elastic subsystems of the metal. This coupling is termed magnetoelasticity which is normally taken to mean the interactions occuring in a single domain, ie: not including domain wall displacements. The term magnetostriction is used more generally to describe all of the effects involving a change in dimensions with a change in the magnetic state of a ferromagnet, including single and polycrystalline and multi domain specimens. For the purposes of this work, however, it is sufficient to consider magnetostriction and magnetoelasticity as equivalent, all of the theoretical work having been done using a single domain model. This is not unreasonable given that the static field employed in most EMATs is high enough to

reach this point on the magnetisation curve. A brief discussion of magnetostriction will now follow as it is thought to play an inportant role in EMAT generation, a review of the work done on EMATs on ferromagnets to date will follow later.

2.6.1: Magnetostriction

A fairly comprehensive account of the entire subject of magnetostriction has been given by Lee [12], the background presented here being but a short introduction to the effect. Magnetostriction is due, ultimately, to the same exchange interaction [13] that leads to all the other properties of ferromagnets. This exchange interaction is a purely quantum mechanical effect due to the spin alignment of two particles, in the case of Iron, Nickel and Cobalt these particles are electrons in the unfilled 3d 'shells'. At temperatures above its Curie transition the thermal energy of a ferromagnet is sufficient to overcome this interaction and it becomes paramagnetic. Below the Curie point the exchange interaction dominates thermal effects and leads to the effect known as spontaneous magnetostriction whereby a ferromagnets dimensions change spontaneously as it is cooled past its Curie temperature. The exchange interaction is characterised by the exchange energy constant, A. Magnetostriction is usually given the symbol λ and is equal to the strain $\delta l/l$ where δl is the change in length (or other dimension) and l is the original length. The deformation acts to minimise the total energy of the crystal which depends upon both the elastic and magnetocrystalline contributions. The magnetostriction in an isotropic ferromagnet such as nickel can be expressed by:

$$\frac{\delta l}{l} = \frac{3}{2}\lambda_s(\cos^2\theta - \frac{1}{3}) \qquad (2.25)$$

where cosθ is the angle between the magnetisation and the observation direction and λ_s is called the saturation magnetostriction. Quoted values of λ_s for nickel and iron are given as $-34x10^{-6}$ and $-7x10^{-6}$ respectively when magnetising the sample to saturation from the demagnetised state. An obvious consequence of equation 2.25 is that the induced strain is directionally dependent, observing parallel to the applied field gives $\cos\theta = 1$, and therefore a magnetostriction of λ_s, whereas orthogonally to this $\cos\theta = 0$ and therefore $\delta l/l = -\lambda_s/2$. This condition means that in applied fields in which increasing magnetisation is due to domain rotation there is no change in sample volume, this is commonly termed anisotropic magnetostriction. At fields above saturation there is a further increase in strain due to an increase in the magnetisation of the single domain of which the sample now consists. This is due to a tightening of the cones of precession of the individual moments on each atom, this precession being due to thermal energy, obviously this alters the interaction energy between neighbouring spins and thus the total free energy. Under these conditions there is a volume change associated with the strain and this is known as volume, or isotropic, magnetostriction, figure 2.5 illustrates this mechanism along with the ones responsible for the anisotropic magnetostriction discussed above.

2.6.2: Magnetostrictive ultrasound generation

Some of the earliest theoretical work on direct magnon - phonon (spinwave - sound wave) coupling was by Kittel in 1958 [14] on a ferromagnetic single crystal model. His work focussed on the frequency range over which both magnon and phonon wavelengths and frequencies were equal, ie: ferromagnetic resonance. However, this resonance occurs in the microwave region of the electromagnetic spectrum, ie: orders of magnitude higher than the MHz range over which most EMATs operate. The

earliest experimental work involving RF EMATs on ferromagnetic metals was performed by Thompson [15], Gitis [16] and Hanabusa [17] et al around 1972.

2.6.2.1: Surface acoustic wave (SAW) generation

Thompsons work was concerned with the generation of Rayleigh and Lamb waves, by meanderline coils, on aluminium and steel plates in the kHz frequency range, his work suggested that magnetostriction played an important role in the steel samples. Theoretical work by several authors has predicted that magnetostriction plays an important part when the static magnetic field is applied tangentially to the surface. An analysis by Il'in and Karitonov [18] predicts that the generation of rayleigh waves occurs predominantly by magnetostriction in a tangential polarising field, whereas in a normal field the waves are found to be produced mainly by the action of the Lorentz and magnetic mechanisms [19]. This agrees with the experimental evidence found by Thompson [20] in generating Lamb waves in Armco iron and subsequent work employing tangential field geometries [21,22]. Using a meanderline coil and tangential field (figure 2.6) he found that the dependence of the ultrasonic amplitude upon applied field showed a peak at the same point at which the magnetostriction curve had its maximum gradient. At induced fields above saturation the Lorentz mechanism was found to be dominant as magnetostriction is a much smaller effect at these fields and under these conditions the Lorentz mechanism is proportional to H as μ is unity. A small peak in efficiency in low applied field was attributed to the corresponding peak in Irons magnetostriction gradient $d\lambda/dH$. Thompson also observed a 135^{O} or -45^{O} phase shift between the Lorentz and magnetostrictively induced Lamb waves in the low and high field regimes respectively. This 45^{O} is due to the phase change undergone by the eddy

currents as we move deeper into the skin depth of the sample, the eddy current as a function of depth is given by equation 2.10 above. Integrating this over the skin depth δ gives [23]:

$$J = \frac{1}{\sqrt{2}}\delta J_o e^{i(wt-\pi/4)} \qquad (2.26)$$

We see, therefore, that the average eddy current density exhibits a $\pi/4$ phase shift from the eddy current density, J_o, at the very surface. This phase shift is always $\pi/4$, independent of the actual value for the skin depth, therefore the Lorentz force has a constant phase regardless of the static field. The magnetostrictive force, in contrast, undergoes a 180^O phase change as λ passes through the initial peak at ~ ??? T, this effect has been described more clearly by Komarov and is discussd below. Even though Thompsons work focussed on Lamb wave generation the same principles apply to all geometries, therefore the phase of the observed signal may also yield important information about bulk wave generation.

Theoretical work by Komarov [24] has predicted the waveform expected due purely to the magnetostriction of iron as the applied field is varied. This treatment was aimed at explaining the results of experiments on an iron rod magnetised along its length [25], the EMAT coil being a solenoid wound around the rod (figure 2.7). The theory predicts a rectifying, or frequency doubling, action due to the 180^O symmetry of the magnetostriction, the degree of rectification being field dependent. Figure 2.8 shows a simple illustration of the theory, it should be mentioned that this model takes no account of the change in H and therefore λ as we move down through the skin

depth, it also disregards any hysterisis in $d\lambda/dH$. We see that applying a sinusoidal magnetic field, at frequency f, to the sample produces elastic oscillations at 2f, when no external field is applied (point a). Application of a small static field moves us to the point b on the λ curve, pulsing the magnetic field as before now produces elastic oscillations as shown. At sufficiently high applied fields we move to the point c on the curve, here the oscillating magnetic field is too small to swing the strain down past the point a and we observe an elastic wave at frequency f. When the field is high enough to reach point d we again observe a frequency doubling effect although there is a 180^{O} phase shift between this and that observed at point a, just as seen by Thompson. Application of higher fields moves us to the region of the λ curve with negative gradient (point e) and now we again observe an elastic wave at frequency f, the phase shift between this and that seen at point c being 180^{O}.

2.6.2.2: Bulk wave generation

Gitis studied the temperature and field dependence of generation in nickel at ~ 5-10 MHz using pancake coils and a normal field applied to a single crystal rod orientated along the [110] direction. He found that both S and L waves were excited with equal efficiency and that the S wave signal fell by ~ 40dB at the Curie point in any applied field. He concluded that the mechanism responsible for S wave generation must be magnetoelastic in origin as the β parameter should change little with temperature when $B \sim B_s$, ie: μ is constant and small. He also observed a sharp peak in L generation around the Curie point, this was attributed to the interaction between two forces acting in ferromagnets. One of these is the normal 'ferromagnetic interaction', which aligns the spins parallel, whilst the other tends to align them antiparallel and is due to the overlap of the electron shells. The second of these

forces depends strongly on the volume therefore, at the Curie point, where more spins are aligned anti parallel, any applied field that acts to align them will strongly affect the volume. This results in enhanced L generation at this temperature, plane S waves being isovolumetric and therefore not experiencing any change in efficiency due to this effect.

Hanabusa et al conducted experiments on nickel, iron and cobalt polycrystals, again using a normal field but employing a solenoidal type coil to induce linearly polarised eddy currents in the sample (see figure 2.7). Their results showed an efficiency of generation in nickel that was around 100 times greater than that in iron or cobalt and 50 times greater than that in aluminium, the signal again dropping markedly at the Curie point. The relatively high efficiency observed in nickel was interpreted as being due to the large λ_s and small anisotropy K_1 of this metal. This conclusion was reached by expressing the periodic stress, T(t), induced in the surface in terms of a linear combination of the magnetoelastic tensor components, B. They obtained an expression:

$$T(t) = B\frac{hM_s\cos(\varphi_o - \varphi)\cos 2(\varphi_o - \varphi)}{H_i M_s\cos(\varphi_o - \varphi) + (d^2E_k/d\varphi^2)}\cos(wt) \qquad (2.27)$$

where h is the magnitude of the rf field (hcos(wt)), H_i is the static normal field, M_s is the saturation magnetisation, ϕ_o is the angle between the easy axis and the y axis in the yz plane and ϕ is the angle between the easy axis and the magnetisation. The size of B is of the order of λ_s times the elastic stiffness constants, therefore the stress is dependent upon the saturation magnetostriction. It is also notable that the term

$d^2E_k/d\phi^2$ in the denominator is always positive, therefore T(t) is reduced if this term is large, ie: there is high anisotropy. These two dependences combined predict that nickel should be significantly more efficient as an EMAT generator than either iron or cobalt, both of these metals having K_1 at least an order of magnitude higher than that in nickel whilst iron also has a λ_s 5 times smaller than that in nickel. Their analysis, however, did not go on to consider the detection process in any detail. It should also be mentioned that equation 2.27 is based on the assumption that the easy axis of magnetisation and its rotation occur only in the yz plane. This is possibly true at the centre of the solenoidal coil, neglecting end effects, but is certainly not the case when using a spiral coil, this type producing the radial field discussed earlier.

The review by Buchel'nikov and Vasil'ev gives possibly the clearest overall picture of the generation process in ferromagnets, particularly the hexagonal class into which many rare earth magnets fall. The cubic crystal class was treated by Povey, Meredith and Dobbs [26] who aimed to explain the results obtained from a single crystal nickel sample. Buchel'nikovs analysis, however, deals only with isotropic magnetostriction, and therefore is not really applicable at applied fields below saturation. It should also be noted that these treatments tend to focus on the case in single crystals and as such are not particularly relevant to the case of a polycrystalline steel. A recent study by Ogi [27] is perhaps the most relevant to the work in this thesis as it deals with generation of bulk waves in a steel plate. The experimental aspect of the study (figure 2.9) was concerned with electromagnetic acoustic resonance (EMAR) whereby, as a consequence of their frequency a much larger signal amplitude than would otherwise be possible was obtained. This was achieved by altering the drive pulse frequency until it equalled nc/2d where c is the

acoustic velocity and d is the plate thickness. For the plates used (10mm and 3mm thick) this correponds to the frequency range 3 - 6 MHz and so is close to the frequencies comprising the broadband drive pulse of interest in the present work.

As the theoretical analysis is somewhat lengthy it is not repeated here, the significant results being summarised instead. The most important result, as far as this work is concerned, is that for the case of a normal static field. His analysis showed that the combination of B_o and B_{dyn} gives rise to a tilted total field that leads to significant magnetostrictive S generation even when B_o approaches B_s. A second aspect is that both the S and L generation efficiencies are a maximum when B_o=0, although these are normalised to the Lorentzian L mode efficiency. We would therefore expect to at least generate S waves with no applied field. Further analysis predicted a peak in the total EMAT S efficiency at 0.15T with a continuous rise with increasing B_o when B_o>0.5T. The L efficiency was also predicted to undergo a very sharp peak at 0.45T with a rapid drop above this. It is worth noting that Ogis analysis only applies to the model of a linearly polarised current sheet, the case of a circular current sheet such as would be induced beneath a spiral coil may be somewhat different. In that case we have variations in the dynamic field along both axes which, due to the nature of anisotropic magnetostriction, cannot be treated independently. However, the case of a spiral coil on a polycrystalline ferromagnet has, as far as the author is aware, not been treated theoretically in any of the literature therefore the simplified model illustrated here must suffice for now.

2.6.2.3: EMAT generation around the Curie point

As mentioned by several authors EMAT ultrasound generation is seen to exhibit peaks in efficiency at and around magnetic phase transitions. These cases are well documented for the rare earth magnets such as Erbium and Thulium etc. [28] which exhibit several transitions over a wide range of temperature. A very obvious phase transition is the ferromagnetic-paramagnetic transition that occurs at the Curie point of all ferromagnetic metals. As stated previously, Gitis observed a peak in longitudinal wave generation in single crystal nickel around its Curie temperature, T_c, ($358^{O}C$). Work by Idris et al [29] has also shown an apparent increase in EMAT detection efficiency at temperatures ~ $10^{O}C$ above the estimated T_c on specialised steel types, this work involving laser ultrasound generation. Obviously, as temperature increases the skin depth also increases, due to reductions in both electrical conductivity and permeability. This effect alone could decrease ultrasonic transduction efficiency due to F_L becoming smeared out over δ. This effect also cannot account for the sharp increase in longitudinal efficiency observed at T_c. The review by Buchel'nikov et al mentions the peak in efficiency at T_c and ascribes it to an isotropic magnetostrictive effect. The fact that it is due to isotropic (volume) magnetostriction means that only the longitudinal wave suffers any effect, the shear wave being characterised by $\nabla.V = 0$. Buchel'nikov gives the efficiency of longitudinal generation due purely to magnetoelastic coupling (ie: with no applied field) as:

$$\eta \propto \frac{1}{S^3}\frac{(\gamma\chi M\rho\omega)^2\sqrt{(1-\xi)}}{4\pi\rho_M S^2(1+\beta^2)} x \begin{cases} \mu^{-2}(1-\xi)^{-3}, & \beta >> 1 \\ \mu(\mu-\xi)^{-3}, & \beta << 1 \end{cases} \qquad (2.28)$$

where ξ is a magnetoelastic interaction parameter, $\beta = (k_A/|k_E|)^2$, g is the magnetostriction tensor, M is the magnetisation, χ is the susceptibility, and S is the acoustic velocity. In this case $k_A=\omega/S$ and $k_E^2=2i/\delta^2$ so for the skin depths involved β is always $<<1$. The increase in η at T_c is due to the nonmonotonic variation in the product χM as the transition point is passed, once ferromagnetic ordering is established the liability of the spin subsystem decreases and the enhanced efficiency drops again.

Chapter 2 references

1: E. R. Dobbs; *Physical Acoustics*; Ed: W. P. Mason and R. N. Thurston; Academic Press, London; **10**, pp 127 - 189 (1973).

2: V. D. Buchel'nikov and A. N. Vasil'ev; *Usp. Fiz. Nauk*; **162**, pp 89 - 128 (1992).

3: J. D. Achenbach; *Wave Propagation in Elastic Solids*; published by North Holland (Amsterdam) (1973).

4: L. R. F. Rose; *Journ. Acoust. Soc. America* **75**, pp 723 - 732 (1984).

5: P. A. Doyle; *J. Phys D: Appl. Phys.* **19**, pp 1613 - 1623 (1986).

6: L. Knopoff; *Journ. Appl. Phys.* 29, pp 661 - 670 (1958).

7: L. F. Bresse and D. A. Hutchins; *J. Appl. Phys.* **65**, pp 1441-1446 (1989).

8: P. K. Larsen and K. Saermark; *Phys. Lett.* **24a**, pp 374 - 375 (1967).

9: A. G. Bejemann, H. V. Bohm, D. J. Meredith and E. R. Dobbs; *Phys. Lett.* **25a**, pp 753 - 754 (1967).

10: M. R. Gaerttner, W. D. Wallace and B. W. Maxfield; *Physical Review* **184**, pp 702 - 704 (1969).

11: K. Kawashima; *Journ. Acoust. Soc. America* **60**, pp 1089 - 1099 (1976).

12: E. W. Lee; *Reports on Progress in Physics* **18**, pp 184 (1955).

13: Eisberg and Resnick; *Quantum Physics of Atoms, Solids, Nuclei and Particles*; Wiley; p 498 (1985).

14: C. Kittel; *Phys. Rev.* **110**, pp 836 - 841 (1958).

15: R. B. Thompson; *Appl. Phys. Lett.* **28**, pp 483 - 485 (1976).

16: M. B. Gitis; *Soviet Physics - Solid State*; **14**, pp 2992 - 2995 (1973).

17: M. Hanabusa, T Kushida and J. C. Murphy; *Journ. Appl. Phys.* **44**, pp 5106 - 5110 (1973).

18: I. V. Il'in and A. V. Kharitinov; *Defektoskopiya*, pp 86 - 93 (1980).

19: A. Wilbrand; *New Proc. in Nondestr. Testing;* edited by P. Holler, (Springer, Berlin), p 71, 1983.

20: R. B. Thompson; *IEEE Trans Sonics and Ultrasonics.* **SU-20**, pp 340 - 346 (1973).

21: R. B. Thompson; *Journ. Appl. Phys.* **48**, pp 4942 - 4950 (1977).

22: R. B. Thompson; *IEEE Trans Sonics and Ultrasonics.* **SU-25**, pp 7 - 15 (1978).

23: Chikazumi; *Physics of magnetism.*

24: V. A. Komarov; *Defektoskopiya*, **no 4**, pp 40 - 45 (1981).

25: V. A. Komarov; *Defektoskopiya*, **no 5**, pp 20 - 27 (1978).

26: M. J. W. Povey, D. J. Meredith and E. R. Dobbs; *Journ. Phys. F: Metal Phys.* **10**, pp 2041 - 2053 and pp 2555 - 2572 (1980).

27: H. Ogi; *Journ. Appl. Phys.* **82**, pp 3940 - 3949 (1997).

28: C. M. Lim, S. Dixon, C. Edwards and S. B. Palmer; *J. Phys. D.* **31**, pp 1362 - 1367 (1998).

29: A. Idris; C. Edwards and S. B. Palmer; *Nondestr. Test. Eval.* **11**, pp 195 - 213 (1994).

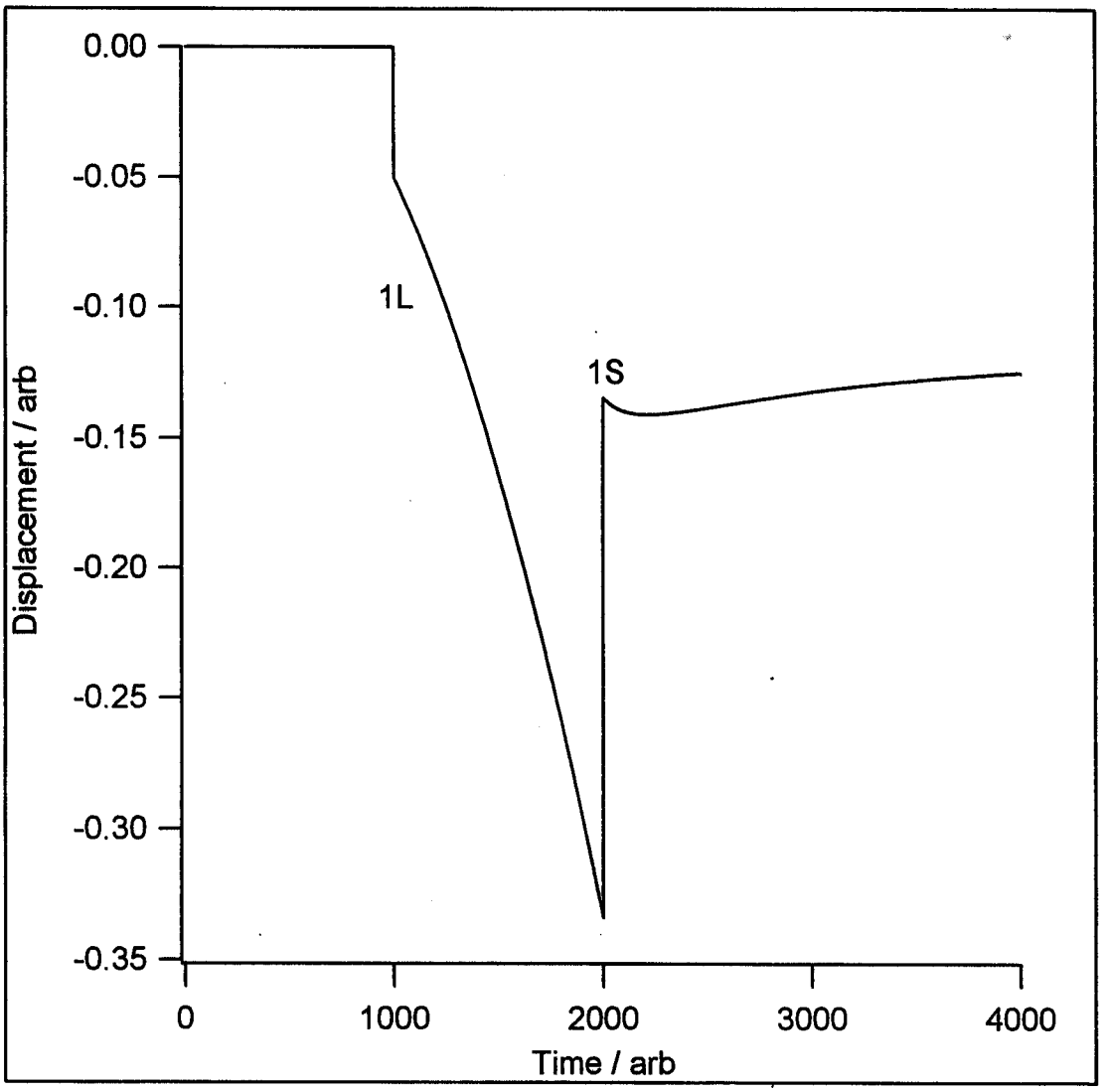

Figure 2.1: Epicentral displacement due to a thermoelastic point source of expansion (SCOE) as modelled by Rose.

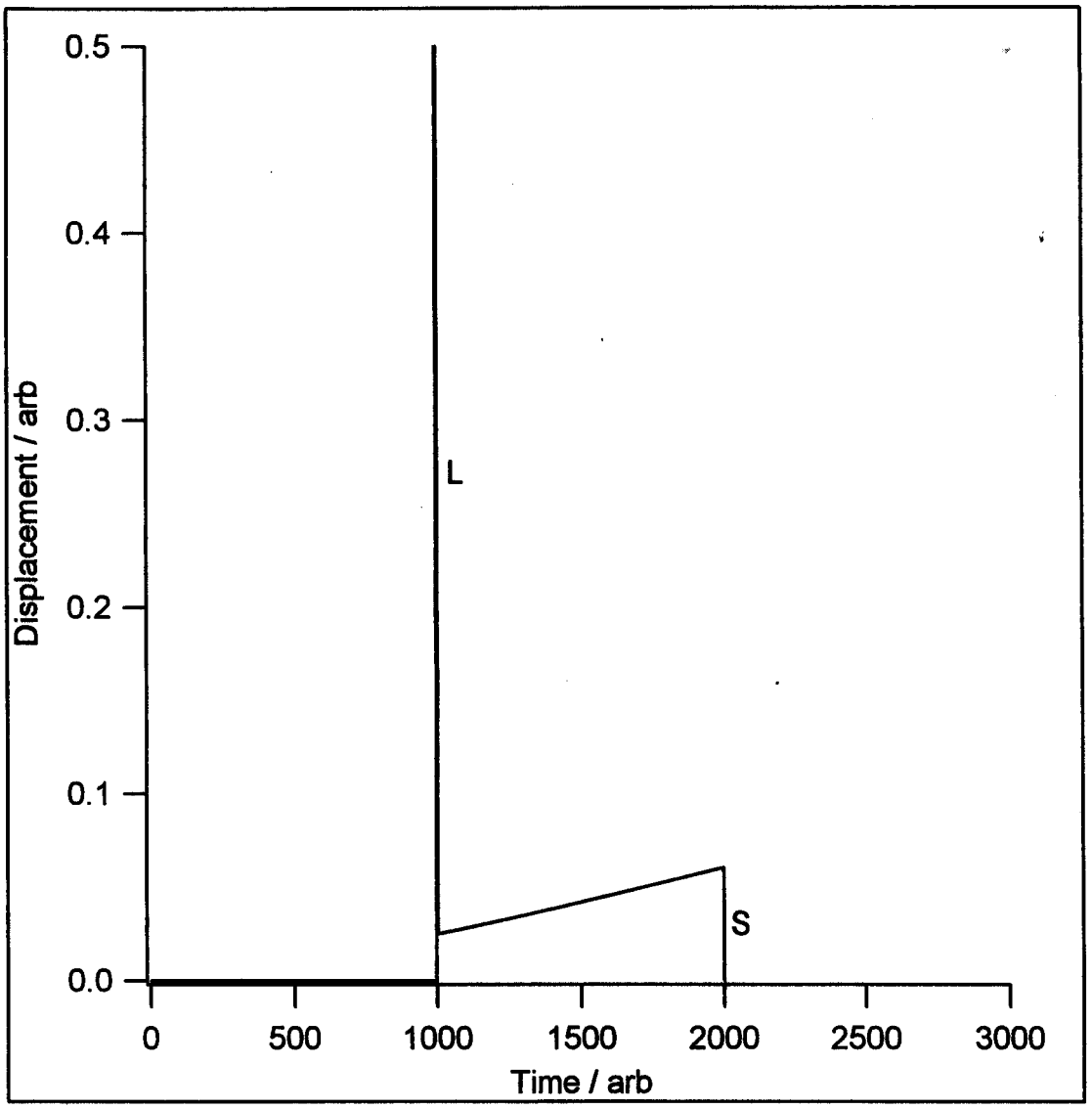

Figure 2.2: Epicentral displacement due to a point normal force as modelled by Knopoff.

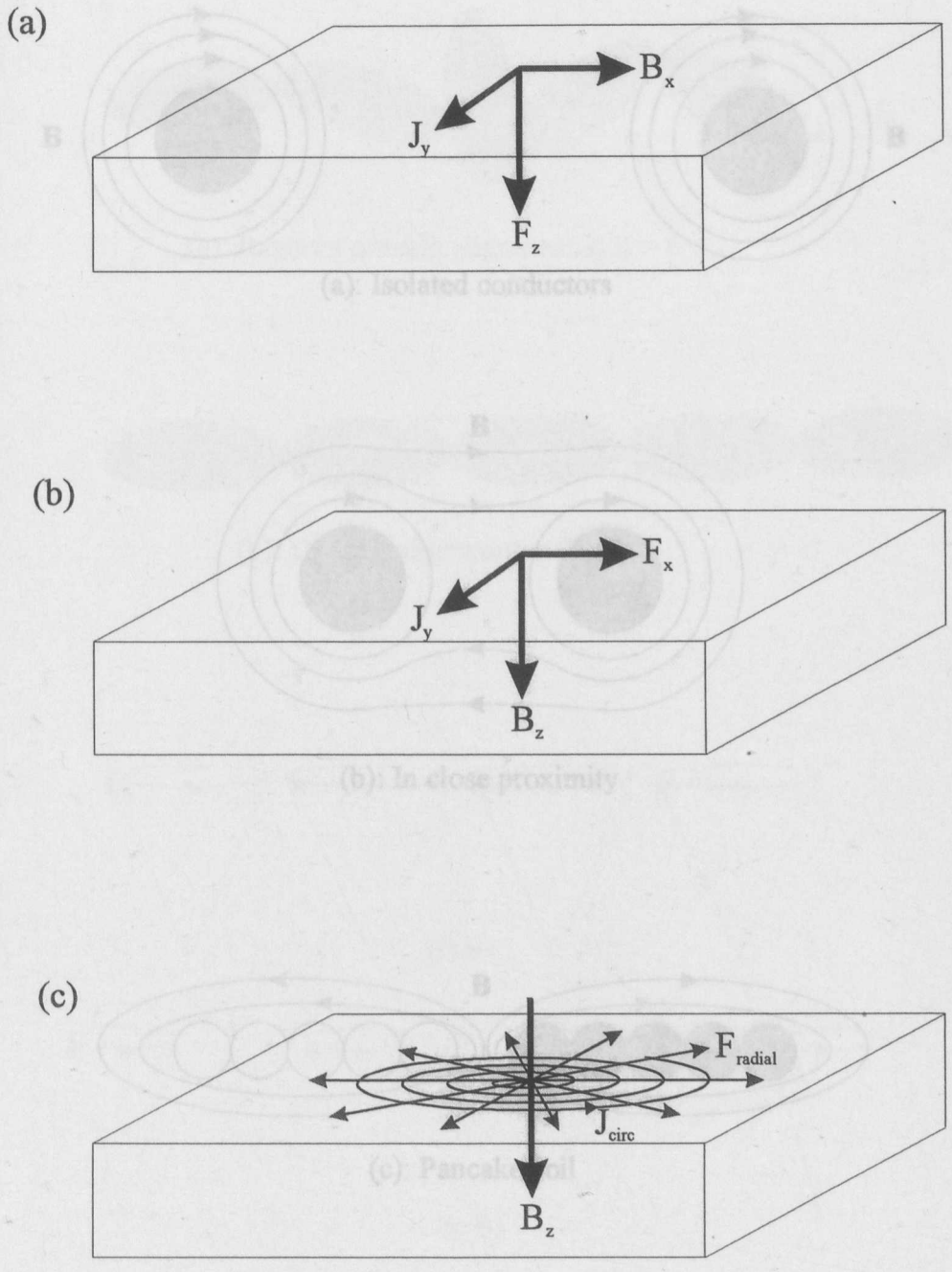

Figure 2.3: Lorentz force F due to:

(a): Linear current J_y and tangential applied field B_x
(b): Linear current J_y and normal applied field B_z
(c): Radial currents J_{circ} and normal applied field B_z.

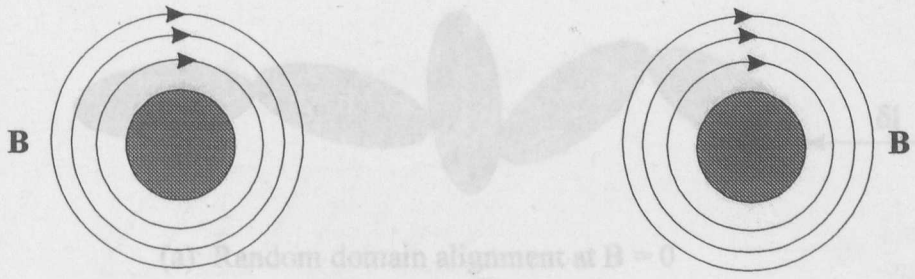

(a): Isolated conductors

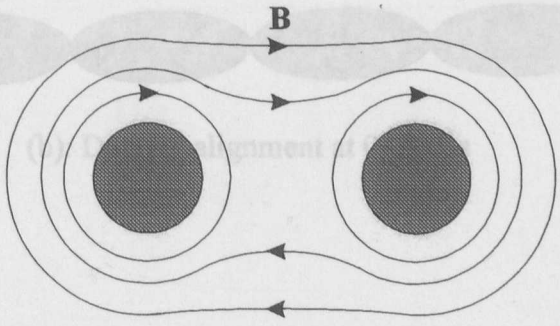

(b): In close proximity

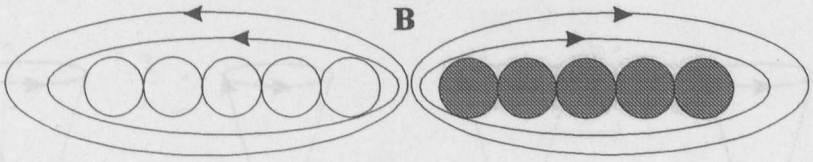

(c): Pancake coil

Figure 2.4: (a): Field pattern due to two effectively isolated current carrying wires.
(b): Field pattern due to the two wires in close proximity.
(c): Radial field pattern due to a current carrying pancake coil.

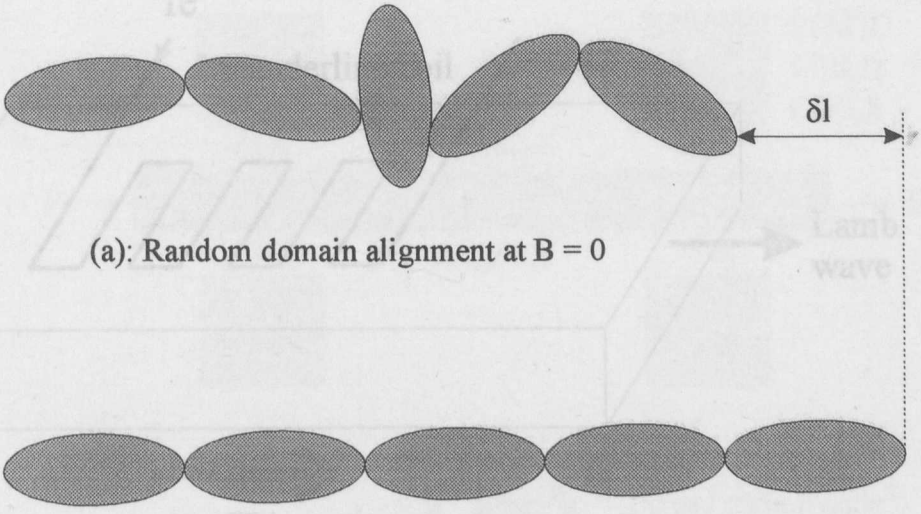

(a): Random domain alignment at B = 0

(b): Domain alignment at 0<B<Bs

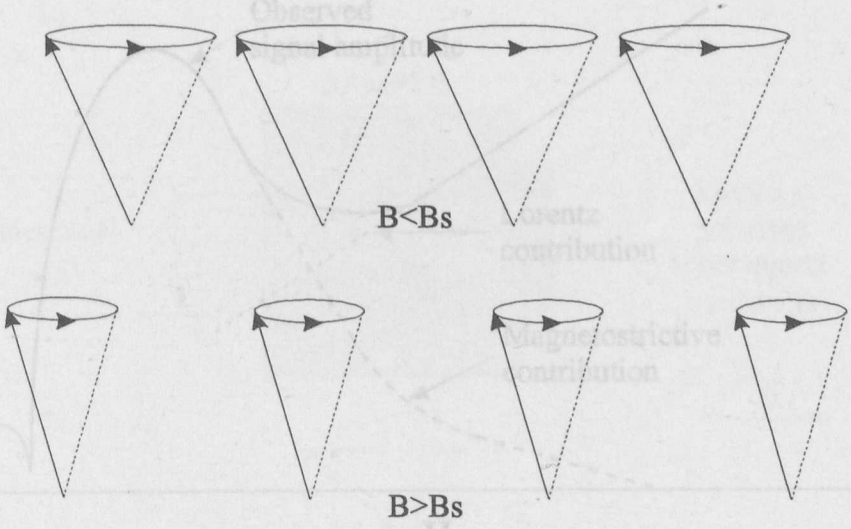

(c): Tightening of precessions of individual atomic moments leading to volume (isotropic) magnetostriction

Figure 2.5: Mechanisms of magnetostriction at (a): low (B=0), (b): intermediate and (c): high applied fields

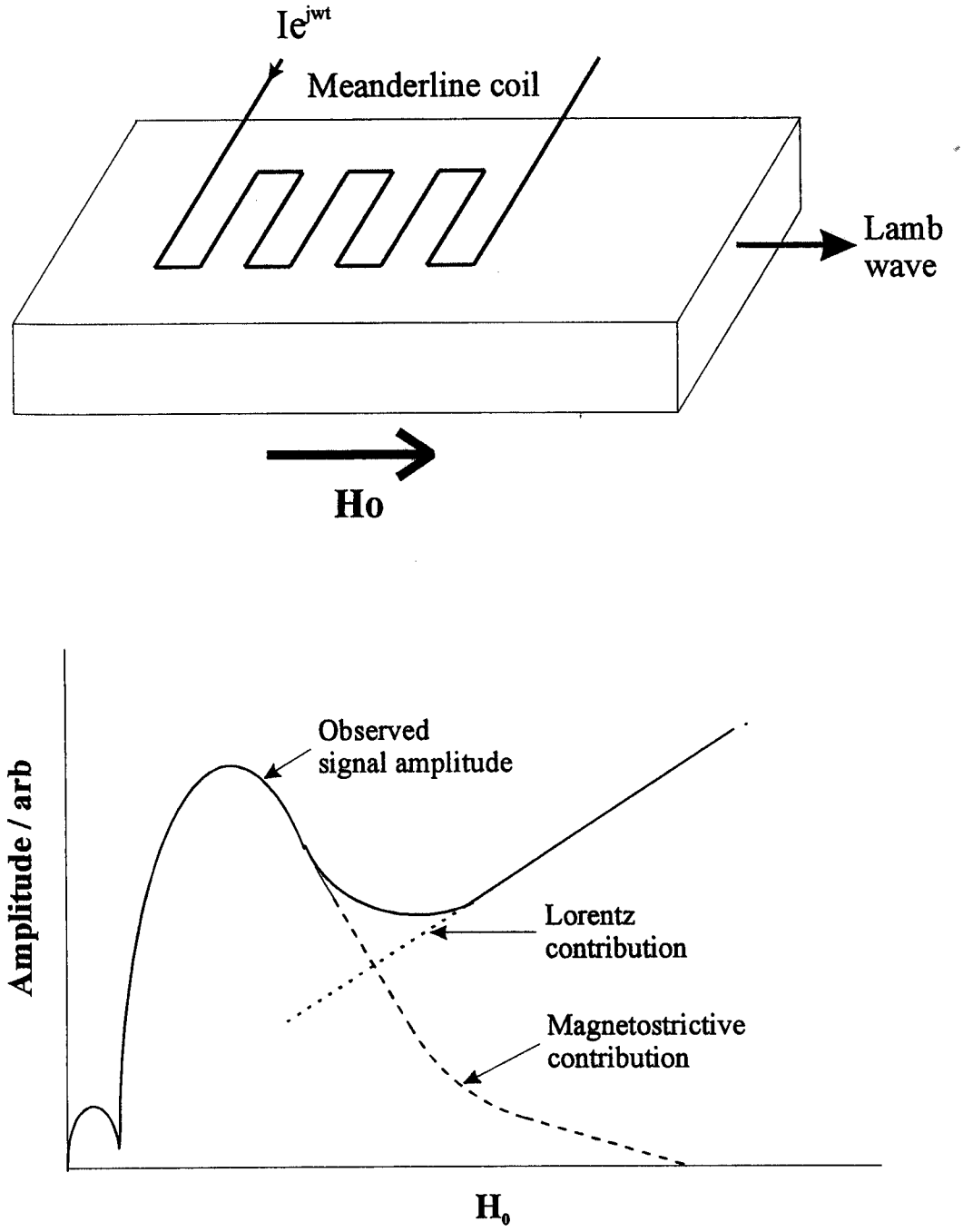

Figure 2.6: Top: Meanderline coil geometry used by Thompson to generate Lamb waves by magnetostrictive and Lorentz mechanisms

Bottom: Observed dependence of ultrasonic signal upon applied field Ho

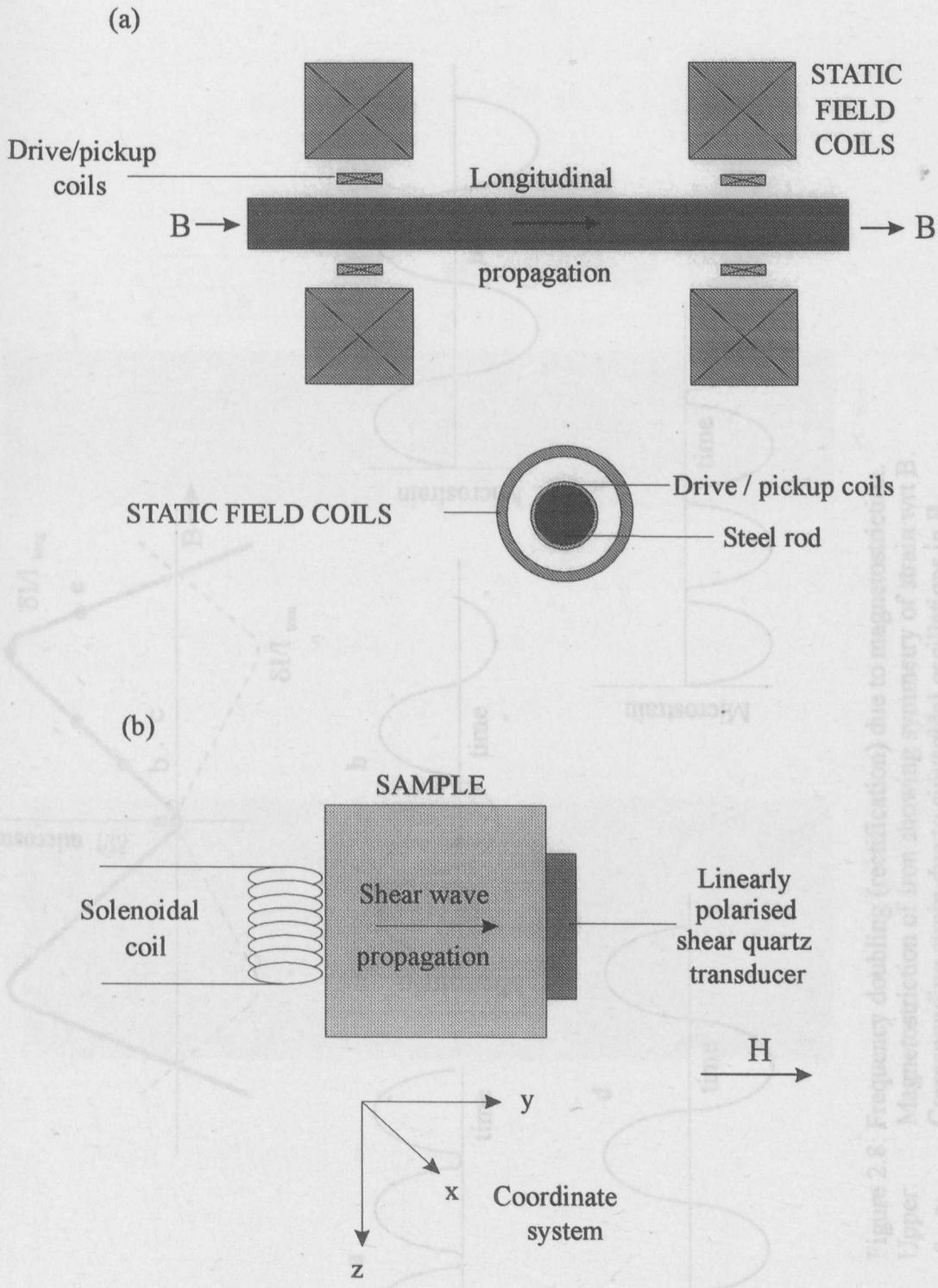

Figure 2.7: Experimental arrangements used by
(a) Komarov and (b) Hanabusa et al.

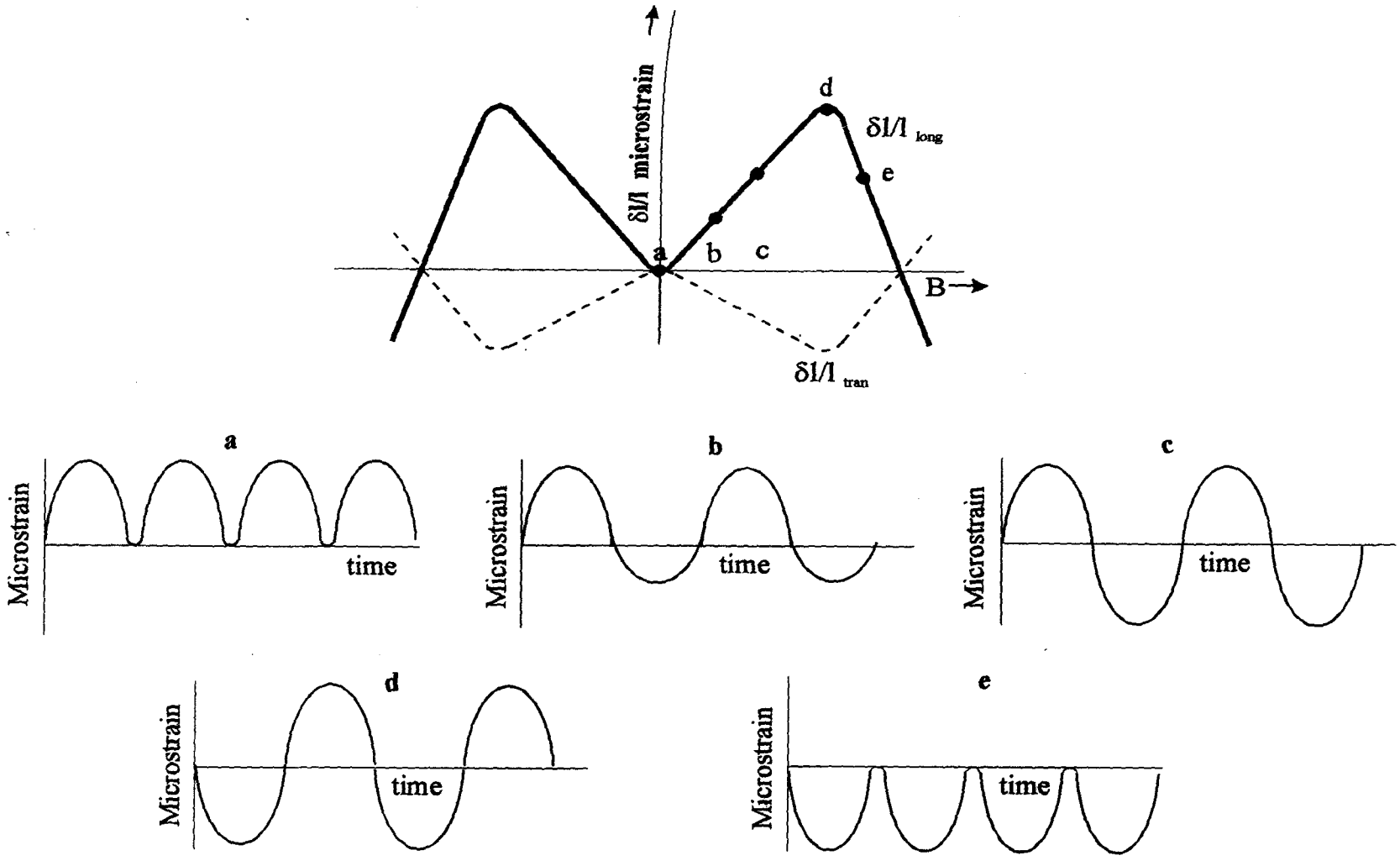

Figure 2.8: Frequency doubling (rectification) due to magnetostriction.
Upper: Magnetostriction of Iron showing symmetry of strain wrt B.
a - e: Corresponding strain due to sinusoidal oscillations in B.

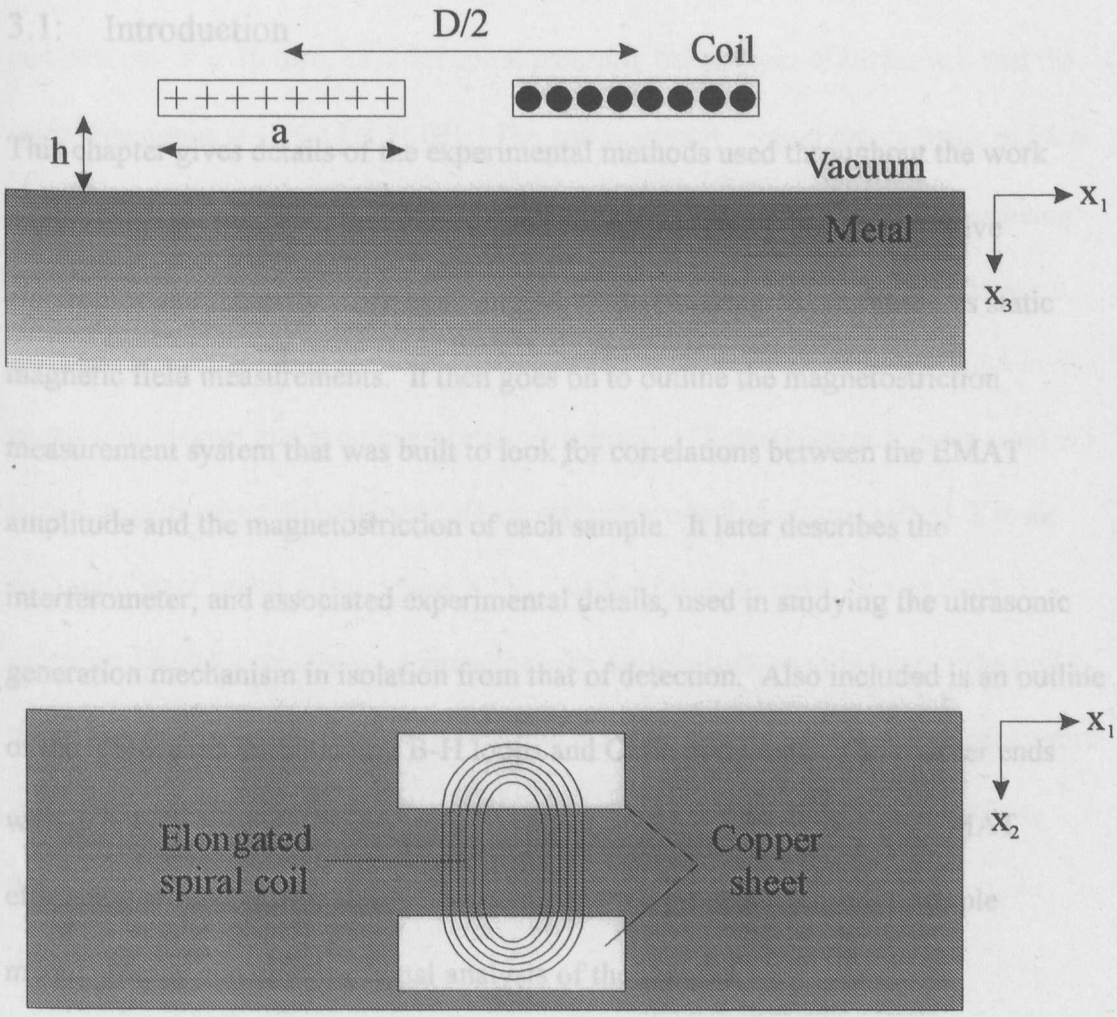

Figure 2.9: The experimental arrangement used by Ogi in investigating EMAT generation by an effectively linear coil.

Chapter 3

Experimental details and methods

3.1: Introduction

This chapter gives details of the experimental methods used throughout the work included in this thesis. It first describes the standard EMAT design and drive electronics and the early work done on EMAT detected signal amplitude vs static magnetic field measurements. It then goes on to outline the magnetostriction measurement system that was built to look for correlations between the EMAT amplitude and the magnetostriction of each sample. It later describes the interferometer, and associated experimental details, used in studying the ultrasonic generation mechanism in isolation from that of detection. Also included is an outline of the VSM used for obtaining B-H loops and Curie point data. The chapter ends with details of the high temperature EMAT arrangement, used to study EMAT efficiency around each metals Curie point, and the procedures used in simple metallography and compositional analysis of the samples.

3.2: EMAT design and electronics

3.2.1: EMAT construction

The EMAT design of interest throughout this work was that of a spiral pancake coil pulsed in the presence of a magnetic field B_o orientated normally to the sample surface. A schematic of a typical handheld EMAT is shown in figure 3.1 and

described here although a more detailed description is given by Dixon [1]. All components are housed in a brass or aluminium casing, typically around 25 mm in diameter, with a BNC connector on top for connection of the drive/receiver electronics to the coil. The coil itself is wound from 0.2mm diameter copper wire and consists of ~ 16 turns in a flat spiral pancake, the number of turns such that the coils impedance is ~ 50 Ω at 5MHz. The coil is usually wound onto a piece of PCB with the copper etched from the side onto which the coil is glued, the copper being left on the opposite face to act as screening. The copper shim shown has the same purpose, screening being required to prevent the coil from exciting ultrasound in the permanent magnet and producing 'magnet echoes'. The permanent magnet used is a high energy product disk shaped NdFeB magnet producing around ~ 0.35 T in air with mild steel backing (see figure 3.1). This field rises to typically ~ 0.6-0.7 T when the EMAT is placed on a ferromagnetic sample such as mild steel. The coil is protected from accidental damage by a thin araldite (or ceramic for high temperature work) layer glued over it. Obviously this protection is kept as thin as possible to reduce coil – sample separation, EMAT efficiency falling off exponentially with 'stand off' [1].

3.2.2: Drive/receiver electronics

The coil is pulsed by discharging a capactor rapidly across it, a peak current of a few tens of Amps typically being passed. A simple schematic of the drive circuit is shown in figure 3.2 with figure 3.3 showing the typical voltage pulse delivered to the EMAT coil, its double differential, and the observed ultrasonic echo waveform. The drive pulse was measured by placing a 1.1 Ω resistor in series with the EMAT and

monitoring the voltage across this as the coil was pulsed. Obviously, as it is a sharp pulse, the ultrasound it generates is broadband and therefore temporally sharp, this being a critical requirement for the original intention of adhesive bond testing. As stated in the previous chapter, for an EMAT send-receive system we expect the detected signal to be the double differential of the drive pulse. This is borne out by a comparison of b and c in figure 3.3 which appears very similar to the observed echo in the bottom trace. The frequency content of the drive pulse is centred around 5MHz but extends from ~0.5 to 10 MHz. As the drive/receive electronics are all designed for 50Ω impedances (standard coax impedance) maximum power transmission through the coil is obtained when its impedance is also 50Ω. This is the reason for winding the coil such that at 5MHz its impedance is 50Ω, this frequency being the dominant one in the drive pulse. It is possible to tune the coil by connecting a suitable capacitor across it, this gives higher signal amplitudes but leads to a more resonant drive pulse and therefore a loss in bandwidth. As these EMATs are designed with this bandwidth in mind the tuning capacitor is usually omitted. The ultrasonic echoes detected by the coil are amplified using a broadband (0.5 – 80 MHz) 2 stage preamplifier of ~ 50dB gain and are displayed on a digital storage oscilloscope.

3.3: EMAT amplitude vs applied field set up

The amplitude of the ultrasonic echoes generated by an EMAT and subsequently detected by the same coil was investigated as a function of applied static magnetic field using the set up shown in figure 3.4. It consisted of the sample in question being secured to one of the pole pieces of an electromagnet while on it's opposite

face was secured a small (21 turns, 0.08mm Cu wire) spiral coil. The magnet used was a Newport type F electromagnet powered by a 3 phase current supply, this supply enabling almost 2T to be produced in the 40 mm pole gap. The coil was taped to the sample surface and driven by the broadband system described previously. In this case the drive circuit was equipped with a variable power supply to enable the drive current pulse magnitude to be adjusted [2]. This was necessary when using very "efficient" samples as the signals when using maximum drive current caused the preamplifier of the receiver circuit to saturate, thus giving an amplitude measurement representative of the amplifier response and not the sample itself. Send - receive waveforms were collected and stored on a LeCroy digital storage oscilloscope over a range of magnetic fields, up to saturation. To obtain the best signal to noise ratio it was necessary to average the waveform over 1000 sweeps, this being especially true for particularly inefficient samples. The field was measured using a Bruker Hall probe which was mounted over the coil as close as possible to the sample surface, as the normal component of B is continuous across a boundary this gave a measure of the induced field essentially at the surface at which generation/detection was occurring.

3.4: Magnetostriction measurement

The bulk magnetostriction of all samples was measured using 120 Ω resistance strain gauges (supplied by micromeasurements UK) and was measured in two orthogonal directions simultaneously. To this end the gauges used consisted of three separate grids, two of which were aligned with the edges of the sample, figure 3.5, and connected to separate strain gauge amplifiers. The gauges were made of a non

magnetic grid encapsulated in a polyimide package with dimensions as shown in figure 3.5. Connection to the gauges was made with 0.08mm Cu wire soldered to PCB tags that were glued to the sample. A schematic of the rest of the equipment is shown in figure 3.6 and described below.

3.4.1: Sample holder

The sample holder consisted simply of an aluminium plate attached to the body of the magnet by an aluminium beam, the beam was machined such that the top of the plate lay in the centre of the pole gap. The sample was secured on top of this holder by two small aluminium clamps on either side, these ensured the sample did not move towards the pole pieces when the field was swept and also kept it aligned correctly. As the gauges were used in a Wheatstone bridge arrangement it was also necessary to glue six dummy gauges (3 for each measurement gauge) to the underside of the holder, these were also of 120 Ohm resistance but took the form of the more typical single foil variety. A "double wire" [3] connection was made to each of the measurement foils to try and eliminate any drift due to thermal EMFs.

3.4.2: Strain gauge amplifiers

The amplifiers used were simple low drift DC amplifiers available from RS with gain variable from 1 to 1000. The low drift character of the amplifiers was especially important given that a full measurement loop took typically an hour to complete and with high gain employed any drift would produce a noticeable effect on the data. The gain was usually set to 100 as this was found to give sufficient output for the PC

to read (tens of microvolts) whilst still keeping the noise/background drift satisfactorily low.

3.4.3: Magnet and field control

The Newport electromagnet was controlled by a system, courtesy of the electronics workshop, that set the current to the magnet coils proportional to the voltage it received from the PC (+/- 10 volts FSD), this enabled the field to be swept from ~ -2 to +2 T under computer control. The control unit could also be controlled manually to allow the field to be set by hand when necessary (see later Curie point measurement details). The current for the magnet was generated by a 3 phase Mawdsley DC generator, a schematic of which is shown in figure 3.7. The static field of the generator is produced by a coil (primary), fed by a portion of the current produced by the generator itself, ie: it is self energising. This current is controlled via the secondary winding shown that shares a common core with the primary. The power amplifier circuit is used to compare the DC voltage, across the secondary winding, with that produced across the shunt resistance in series with the magnet coils. Any difference between the two is used as an error signal, amplified, and fed back to the secondary winding to adjust the current through it. This adjustment will alter the static field to compensate for the error in current to the magnet and thus correct it. The system used provides a field stability of better than one part in 10^6.

3.4.4: Computer control

The whole system was controlled by a 286 PC equipped with a 12 bit combined A/D and D/A converter card (Talisman electronics), which was especially suited to the small signals produced by the strain gauge amplifiers. The card was used to both control the magnetic field and to read the output from the amplifiers. A program was written in Quickbasic that allowed the user to control the maximum field, number of loops, number of points and time between points for each measurement run, it also plotted the output from the amplifiers vs. the voltage being sent to the magnet control box. A typical measurement sequence is shown below:

a: set control voltage to required value.

b: wait for field to reach steady level and settle (~ 30 seconds).

c: read output from longitudinal strain gauge amplifier.

d: read output from transverse strain gauge amplifier.

e: write output voltage and both amplifier outputs to data file.

f: plot amplifier outputs vs. control voltage graphically on screen.

g: repeat sequence for next control voltage.

3.4.5: Field measurement

As several different sample sizes and shapes were used it was not possible to quote a sensible applied field in each case, sample geometry obviously determining the demagnetising factor (see later VSM details). To this end an Op-Amp integrator was

built, figure 3.8, that also produced an output that could be read by the PCs A/D card. This integrator was connected to a coil (25 turns of 0.1 mm Cu wire) wrapped around the sample in question and over the strain gauge, see figure 3.5. As the field was swept up and down this circuit integrated the voltage, V, induced in the coil according to:

$$\int V dt = NA \int dB \qquad (3.1)$$

where dB = change in samples internal induced field

N = number of turns on coil

A = cross sectional area of sample

and therefore provided a measure of the internal field in the sample. A second simple program was written that recorded the output of this integrator vs. the voltage sent to the magnet control box, thus producing a hysteresis loop in terms of internal field and applied voltage to the controller. Combining this with the data obtained previously from the strain gauges enabled a graph of microstrain against induced field (B) to be plotted. Clearly for this to be sensible it was necessary to start each loop from the same point on the hysteresis curve, this was done by saturating the sample first in 1.8 T and then reducing the field to zero before starting the experimental run.

3.5: Interferometric detection of EMAT generated ultrasound

The experimental layout is shown schematically in fig 3.9, it consisted basically of an EMAT coil generating on one side of a sample with an interferometer on the other

to detect the ultrasonic arrivals. The EMAT coil was mounted on the end of a 12.5 mm diameter mild steel rod which was further attached to two optical stalks. With no sample in place the optical bench was aligned such that the interferometers laser beam was co-linear with the centre of the coil (22 turns of 0.08 mm Cu wire), this ensured accurate alignment on epicentre to within 0.5 mm. The mild steel rod was wound with ~ 100 turns of 1mm Cu wire, as shown, to enable a static magnetic field to be applied. This was fed by a 30 Volt, 10 Amp supply allowing up to ~ 0.45T to be obtained when using magnetic samples. A 2.7 Ω rheostat was also placed in series with the field winding to limit the current through it to a maximum of 10 Amps, the voltage across this rheostat was recorded for each interferometer trace stored. Storage of the traces was carried out using an IEEE interface to transmit the data from the LeCroy 3400 digital oscilloscope to a PC. The ultrasound detected by the coil was also recorded at each field and stored in the same way. The EMAT coil was driven by a Matec pulse generator supplying a tone burst at ~ 5MHz, the exact frequency used being controllable between ~ 2 and 7 MHz.

3.5.1: Field measurement

In order to measure the field applied to the sample it was necessary to remove the coil from the end of the rod and replace it with a Hall probe of the same thickness. The field was then measured as a function of the voltage across the rheostat to enable a measure of the applied field for the voltages recorded above.

3.5.2: The Michelson Interferometer

The Michelson interferometer is an optical instrument designed to detect nm scale displacements of a mirror or, in this case, the mirror's surface. Two light beams are produced by passing a single beam through a beam splitter. The two beams are subject to slightly different optical path lengths due to differences in the distance between the two mirrors, one being the sample. This difference leads to a phase difference between the beams and thus to a modulation of the light intensity when they are recombined at the splitter.

3.5.3: Modified Michelson Interferometer

The design of the interferometer used in this work is essentially the same as that found in [4] and is shown schematically in fig 3.10. The light beam was supplied by a NdYAG laser, frequency doubled to operate at 532 nm. The fixed mirror was attached to a loudspeaker motor to allow cancellation of any low frequency (kHz) background vibrations. A portion (controllable) of any such signals were fed to the motor in a negative feedback loop to cancel their effect on the output of the photodetector. This allowed the MHz frequency ultrasound signals to be discerned "riding" on the back of these larger vibrations. Fig 3.11 shows the relative amplitudes of the ultrasound compared to this background "noise", the bandwidth of this particular instrument is around 80 MHz so any signals of higher frequency than the kHz background vibrations are detectable upto this limit.

The design of the interferometer is such that a change in measured intensity from one maximum to the next corresponds to a movement of the sample surface (out of

plane) of one quarter of the wavelength of the light used. This enabled calibration of the instrument in terms of absolute out of plane displacement by simply measuring the maximum unstabilised voltage from peak to peak and assuming the ultrasound signals were sitting on the linear region of the curve (fig 3.11). Averaging the signal over 500 sweeps allowed a resolution of ~ 10pm using this technique.

3.5.4: Sample preparation

To ensure maximum signal amplitude the samples were highly polished before mounting in the sample holder. The polishing was achieved using successively lighter grades of wet and dry emery paper, from 320 grit down to 1200 grit, followed by further finishing on 6 μm then 1 μm diamond wheels. This ensured that the samples had maximum reflectivity, important given the magnitude of some of the ultrasound signals observed.

3.6: High temperature Vibrating Sample Magnetometer (VSM)

The VSM was invented by Foner in 1956 [5] and is designed to measure the magnetisation of a material in an applied magnetic field. It works simply by vibrating the sample (sinusoidally) at right angles to a homogeneous magnetic field and measuring the voltage this moving magnetic moment induces in detection coils positioned close to the sample. Most modern instruments operate with a frequency of a few 10's of Hz and an amplitude of vibration of a few mm, all of them employ some form of phase sensitive detection to accurately measure the voltage induced in the coils.

3.6.1: General set up

The VSM used throughout this work was obtained from Portsmouth University [6] and was designed to investigate the high temperature magnetic properties of ferrites, this made it well suited for use in looking at magnetic properties around the Curie point of many metals and steels. Full details of the construction and design of the instrument can be found in [7] but a brief description and schematic (fig 3.12) of it is given below, along with any modifications made. Unlike most conventional VSMs it is mounted in the magnet horizontally to reduce any temperature variations due to convection currents in the furnace tube. It also features a large amplitude of sample oscillation (1 cm), operating at low frequency (4.166 Hz), this was originally aimed at reducing eddy currents in conducting ferrite samples. The whole instrument was mounted on an aluminium beam, which was further mounted on two rigid aluminium stands. These stands were bolted to the laboratory floor to ensure minimal noise due to vibration of the beam. The detection coil set was clamped rigidly to the pole pieces and consisted of 12 coils in all, wound from 48 SWG Cu wire. The four central coils (fig 3.12) comprised 27000 turns and were used to actually pick up the signal from the sample, the eight outer coils (24000 turns) originally having been used to cancel any magnetic image effects. The signals from the central coils were combined in a mixer box and then fed to an EG&G (model 5210) phase sensitive detector (PSD) where the magnitude of the signal was measured and displayed. The reference signal for the PSD was provided by an optical beam chopper mounted on the oscillatory drive motor of the VSM. It should be mentioned that for the work included in this thesis the compensation coils were not used, only the four main

sensing coils. As the hysterisis loops were measured in-plane in the present work the applied fields were all relatively low. Therefore the magnet pole pieces never approached saturation and the images were a constant extra signal dependent purely upon the magnetic moment of the sample. These image signals were assumed to be always proportional to the samples moment and could therefore simply be included in the calibration constant, found using a thin Nickel disk.

3.6.2: Furnace

The furnace consisted of an alumina tube wound, non inductively, with 1 mm non magnetic Nichrome wire along a double start screw thread such that any pick up from the furnace power supply was cancelled. The power supply used was a Eurocube thyristor stack the output from which was controlled by a Eurotherm 818 furnace controller. A non magnetic Pt/Rd (R type) thermocouple cemented to the inside of the tube provided the feedback for this controller. As the tube was intended to go up to ~ 800 °C it was also necessary to water cool the outer parts of the instrument, the coil set being particularly vulnerable to heat damage. The cooling was achieved by passing water through a 0.3mm gap between two stainless steel tubes. The inner one of these tubes housed the furnace tube and was polished inside to decrease radiative (α T^4) losses whilst the outer one was secured to the unit holding the coil set (fig 3.12).

3.6.3: Sample holder and thermocouple

The original sample holder was designed to hold spherical samples of ferrite material, this being the most convenient shape in terms of demagnetising factor correction, see below. The samples used here were cut from the surface of metal and steel blocks and it was decided therefore that disk shaped samples would be the most sensible to use. To this end the sample holder was modified slightly so that disks (~ 7mm diameter) could be clamped between two flat faces of ceramic, see fig 3.13. One flat was formed by the end of a ceramic cylinder secured inside the tube whilst the other was provided by the end of a hollow alumina tube down which a Pt/Rd thermocouple was cemented. This thermocouple was cemented such that the junction was flush with the end of the tube, ensuring good thermal contact with the sample disk. One end of the tube was mounted inside a spring loaded aluminium flange to facilitate clamping of the sample. The thermocouple output was recorded by a Comark digital thermometer to allow the sample temperature to be measured.

3.6.4: Automation

A 286 PC was used to control data acquisition from the VSM, for both room temperature B-H loops and high temperature Curie point measurements. A simple block diagram of the components of the system is shown in fig 3.14. In the case of B-H loops the program, as for the earlier magnetostriction work, used the D/A output to control the magnetic field. The PSD reading was measured by recording the analogue voltage output (FSD = ± 10V), from the instruments front panel, using the

A/D. The program allowed the user to define the maximum control voltage, number of points and time between points and also displayed the PSD output vs. control voltage graphically. Curie point measurements were somewhat simpler in that no field control was required. In this case it was necessary to simply program the furnace controller with the required ramp rates, maximum temperatures etc. and then record the sample temperature and PSD output over the time of the experimental run. A short program was written that recorded these two parameters every x seconds (x being user defined but usually ~ 10) and wrote them to a data file whilst displaying them graphically on screen. Sample temperature was recorded via the A/D by measuring the analogue voltage output (0-10V) from the Comark thermometer. The calibration range of this thermometer was over the range 200 – 1000°C, consequently only data within this range are assumed to be accurate and included in this work. Temperature measurements are quoted to an accuracy of 1°C based on the resolution of the A/D card (4096 points). The magnetic field used for high temperature experiments was set manually and left fixed throughout the run.

3.6.5: Demagnetising factors

The VSM is an instrument designed for making "open-circuit" magnetic measurements and as such any data obtained from it must be adjusted to account for demagnetising effects. These are due to the production of "magnetic poles" at each end of the sample which will act to reduce the effective internal field H_{eff} (fig 3.15). Therefore, any B-H loop obtained from a VSM must have the quoted H corrected to account for this effect. The demagnetising field is dependent upon the magnetisation of the sample and its geometry according to:

$$H_{eff} = H_o - N_d M \tag{3.2}$$

where N_d = demagnetising factor (purely geometry dependent).

M = magnetisation of sample.

H_o = applied field.

H_{eff} = effective internal magnetising field.

The demagnetising factor can only be calculated explicitly for the case of second order shapes such as ellipsoids, eg: the factor for a perfect sphere is exactly 1/3. This is due to these being the only shapes exhibiting uniform magnetisation and therefore demagnetising field. It should also be mentioned that the demagnetising factors for the three orthogonal directions of a sample always sum to 1. Several authors have calculated the factors for a range of ellipsoidal samples, Osborn [8] gives a more or less complete table of values for the whole range of aspect ratios whilst Stoner [9] gives a more detailed theoretical treatment of the problem. In terms of eccentricity Stoner gives N_d as:

$$N_d = \frac{1-e^2}{e^2}\left[\frac{1}{2e}\ln\frac{1+e}{1-e} - 1\right] \tag{3.3}$$

for an oblate spheroid magnetised along its short axis and:

$$N_d = \frac{1}{1-m^2}\left[1 - \frac{m}{\sqrt{(1-m^2)}}\cos^{-1} m\right] \tag{3.4}$$

for a prolate spheroid magnetised along its long axis (see fig 3.15 for definitions of e and m).

In our case we are concerned with a disk shaped sample magnetised parallel to its circular plane, N_d for this geometry can be approximated to [10]:

$$N_d = \left[\frac{k^2}{(k^2-1)^{3/2}} \sin^{-1} \frac{\sqrt{k^2-1}}{k} - \frac{1}{k^2-1} \right] \qquad (3.5)$$

where: k = ratio of diameter to thickness.

The relative permeability of a ferromagnet is defined as $\mu_r = B/\mu_o H_{eff}$, therefore an accurate measurement of μ_r requires corresponding accuracy in our measurement of both B and H_{eff}. B is defined as $\mu_o(M+H_{eff})$ and as M is usually much larger than H_{eff}, in ferromagnets, the uncertainty in our measured B is relatively insensitive to uncertainty in H_{eff}. However, as M is so large, H_{eff} depends critically upon N_d, therefore any error in this factor makes a significant difference to the H_{eff} we use in calculating μ_r. This effect can be seen quite clearly in figure 3.16, the B-H loop from a Nickel sphere used initially to ensure that the VSM was working correctly. The sphere had been spark planed from a pure Nickel rod and had dimensions of 3.8 x 4.1 mm, it was therefore slightly eccentric (e = 0.375). Placing the sphere in the original sample holder with its longer axis aligned with the field produced the initial hysterisis curve shown in figure 3.16a. Using a demagnetising factor of 1/3 resulted in the second curve shown (3.16b). Using equation 3.5 gives $N_d = 0.3124$ and results in the second corrected curve shown in figure 3.16c. The coercivity and saturation magnetisations are virtually identical for both curves. However, fitting a straight line to the linear region of each loop gives the gradient and therefore permeability of each

and here we see very marked differences. For the case of Nd = 1/3, μ_r = -114 whereas for N_d = 0.3124, μ_r = 62, a difference of 5% in N_d leading to 150% difference in μ_r with one value actually giving a negative result. As the quoted [11] μ_r for Ni is around 2000 it is also evident that neither value gives anything like the correct result. Clearly it is impossible here to obtain an accurate result for μ_r, small changes in N_d leading to huge errors in permeability. This example is included to highlight the problems inherent in permeability measurements on ferromagnets in an open circuit system. As all the samples of interest here were ferromagnetic it was decided that permeability measurements would be impossible and therefore any values of μ_r quoted are taken from the literature and not experimental results.

3.7: High temperature EMAT set up

3.7.1: General construction and furnace

The set up used for investigating high temperature EMAT response is shown in figure 3.17 and is the same as that detailed in [12]. It consisted of a split furnace (bore = 6cm) into which was clamped the sample under investigation, the furnace being powered by a Severn Furnaces controller. A K type thermocouple was run through a hole in one of the clamps to enable the sample temperature to be measured. This thermocouple was positioned such that the active junction sat just inside a small (1mm diameter) hole drilled into the sample surface ~ 5mm away from the outer edge of the EMAT. The EMAT itself was water cooled (described below) and was mounted on the end of a stainless steel tube which ran through a teflon bearing mounted on the outer frame of the furnace. The clamps were mounted on rods

running the length of the furnace tube and took the form of thick stainless steel washers (6 cm diameter) clamped together with 4 BA bolts top and bottom. Onto the stainless steel tube was also mounted a small microswitch, positioned so that it engaged against the head of a large screw secured on the outside of the furnace frame. This was used to trigger the oscilloscope to start data acquisition, the trigger from the EMAT drive box being routed through this switch. The position of the switch was adjusted so that it was closed just as the EMAT came into contact with the sample, this ensured that the EMAT contacted the hot sample for the minimum time necessary (see below).

3.7.2: Water cooled EMAT

Fig (3.18) shows the construction of the water cooled EMAT used in this work. Its design is essentially identical to that used for a standard room temperature EMAT but for the use of a ceramic face over the coil and high temperature araldite (400°C) to hold the components together. The water cooling was necessary to preserve the high remnant magnetic field of the NdFeB permanent magnet, this dropping off rapidly at temperatures over ~ 80°C. The cooling was achieved by passing water through a hollow cavity in the top of the brass EMAT case, the inlet and outlet tubes also contained within the stainless steel outer tube. The wires of the EMAT coil were connected to a BNC socket mounted on the end of the steel tube, the earth wire being connected to the case to ensure that the sample was earthed on contact with the EMAT. The coil was driven using the same drive box as used above for the EMAT amplitude vs. applied field work. Obviously as the EMAT was water cooled it constituted a very efficient heat sink and therefore could significantly alter the

temperature of the sample surface. For this reason it was only placed in contact with the sample for the absolute minimum amount of time required to obtain a satisfactory trace, usually around half a second. Work done previously [12] suggested that this would still lead to a temperature drop of ~3 ^{o}C at the surface so this is assumed throughout unless otherwise stated.

3.8: Metallurgical and compositional analysis

3.8.1: Metallography

Several metallographs of different samples are included in this thesis, these were obtained using the standard methods of polishing and etching in a suitable etch. In all cases the samples were polished using progressively lighter grades of wet and dry emery paper (similarly to the preparation of the interferometer samples) from 320 down to 1200. They were then polished using 6μm followed by 1μm diamond solutions to remove all traces of the coarse polishing by emery paper. A final polish was achieved using colloidal ¼ μm silica to remove even these light scratches. The samples were then etched, using nital in most cases, a solution of 2% nitric acid in ethanol, although for duplex stainless steel a more corrosive etch was required due to its higher resistance to acidic attack. In this case a solution of 3 parts glycerol, 3 parts hydrochloric and 1 part nitric acid, called glyceregia, was used [13] to show up the dual phase austenite/ferrite microstructure.

3.8.2: EDX (Energy Dispersive X-ray analysis)

Compositional analysis was carried out in a scanning electron microscope (SEM) using energy dispersive X-ray analysis. This basically involves scanning the electron beam across the sample and collecting the X-rays this beam induces. As X-ray energies are characteristic of a particular element, analysis of the emitted energy spectrum provides us with compositional information. Due to the nature of the technique it is virtually impossible to 'see' the very light elements such as hydrogen and carbon, the lowest Z element detectable being typically oxygen. This obviously makes the technique of no use for accurate analysis of carbon content in the steel samples so, unless given by the steels manufacturer, it is not quoted for the steels studied in this work.

Chapter 3 references

1: S. Dixon; PhD Thesis; Warwick University (1995).

2: P. Crowther, C. Edwards, S.B. Palmer and S. D. Kenney; *Insight* **39**, pp 618 - 622 (1997).

3: Micro measurements strain gauge technical note

4: A. C. Bushell, C. Edwards and S. B. Palmer; *Rev. Prog in QNDE.;* edited by D. O. Thompson and D. E. Chimenti, Plenum Press **11**, pp 1315 - 1322 (1992).

5: S. Foner; *Rev. Sci. Inst.* **30**, p 548 (1959).

6: R. D. Barlow et al; *Journ. Appl. Phys.* **61**, pp 3208 - 3210 (1987).

7: S. Price; PhD thesis; Portsmouth University 1985.

8: J. A. Osborn; *Phys. Rev.* **67**, pp 351 - 357 (1945).

9: E. C. Stoner; *Phil. Mag.* **7**, pp 803 - 821 (1945).

10: Chikazumi; *Physics of Magnetism.*

11: Kaye and Laby; *Tables of Physical and Chemical Constants*; published by Longman (1986).

12: A. Idris, C. Edwards and S. B. Palmer; *Nondestr. Test. Eval.* **11**, pp 195 - 213 (1994).

13: Communication with metallurgy dept. at British Gas Research Centre, Loughborough.

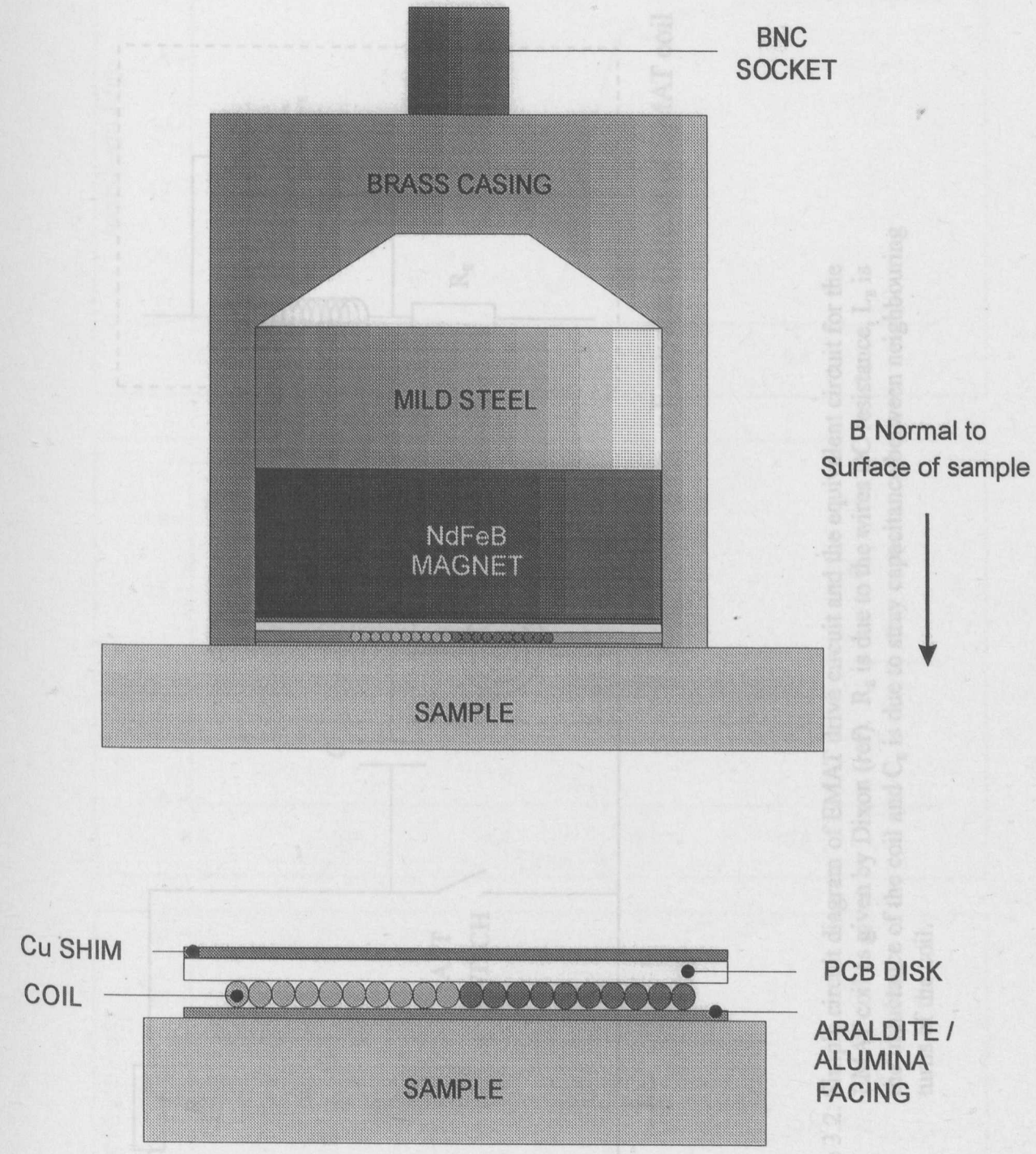

Figure 3.1: Construction of a typical spiral coil EMAT transducer. The transducer is similar in dimensions to those of the more common piezo-electric type. The Cu shim is included to provide screening between the coil and the conducting permanent magnet

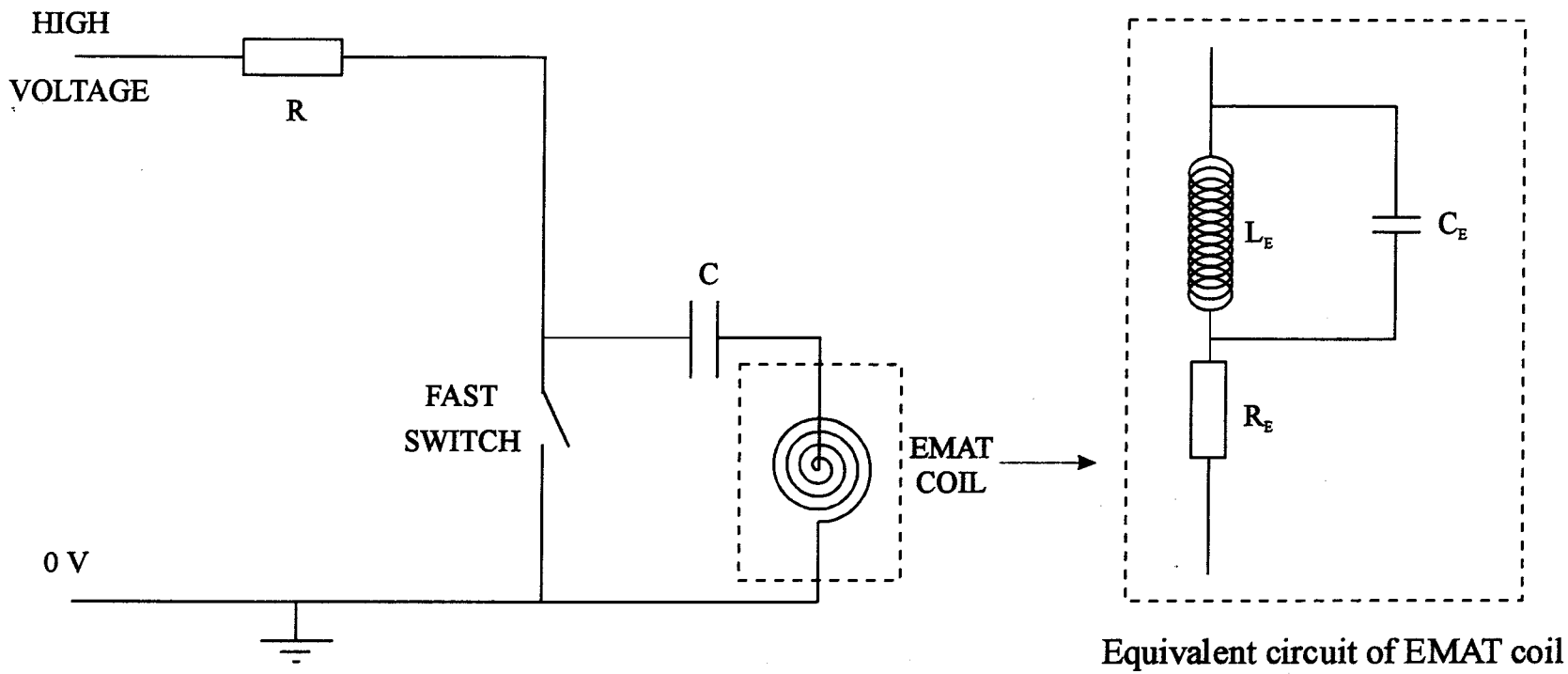

Figure 3.2: Simple circuit diagram of EMAT drive circuit and the equivalent circuit for the EMAT coil as given by Dixon (ref). R_E is due to the wires DC resistance, L_E is the inductance of the coil and C_E is due to stray capacitance between neighbouring turns of the coil.

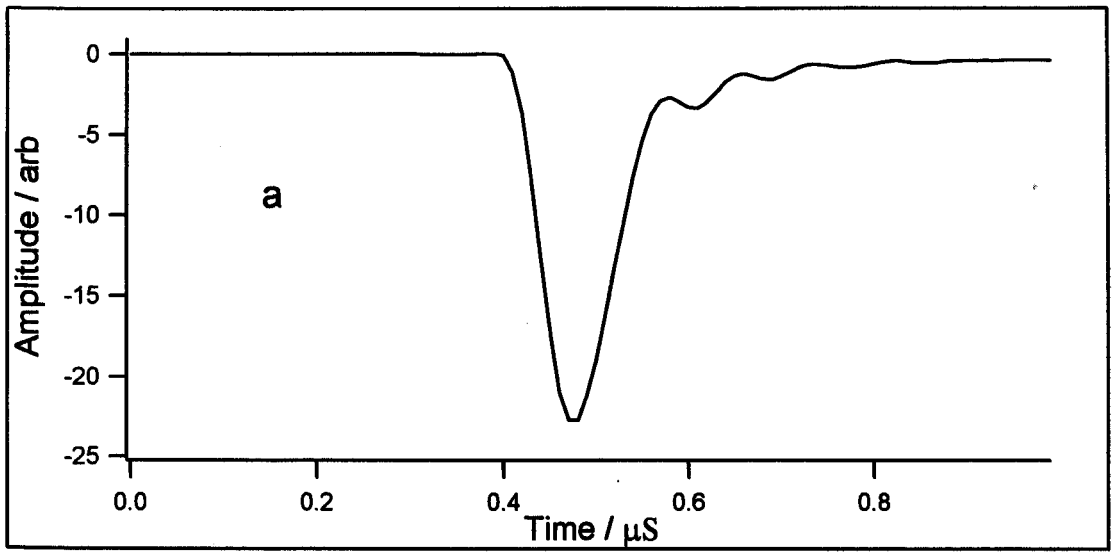

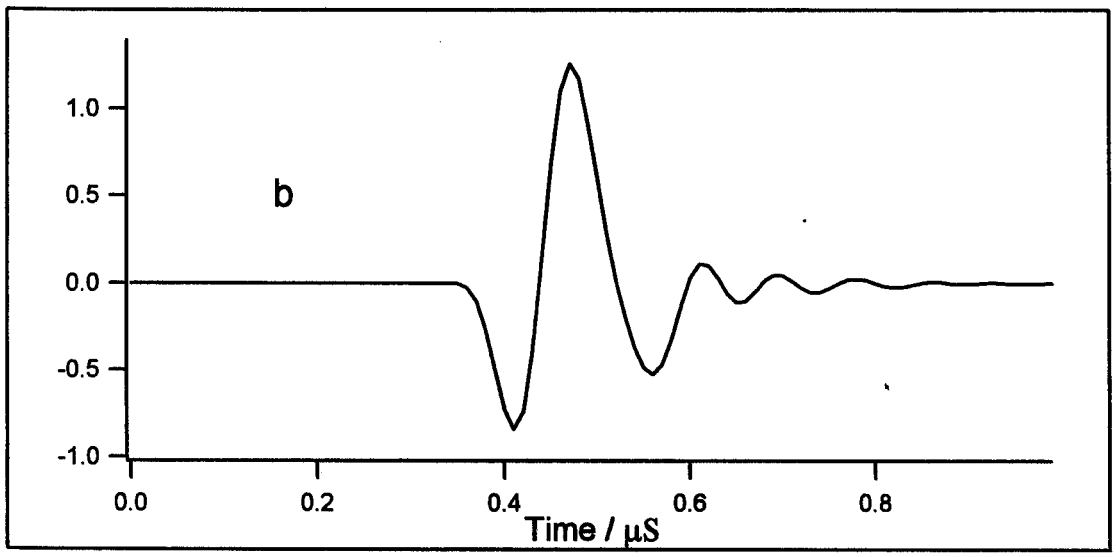

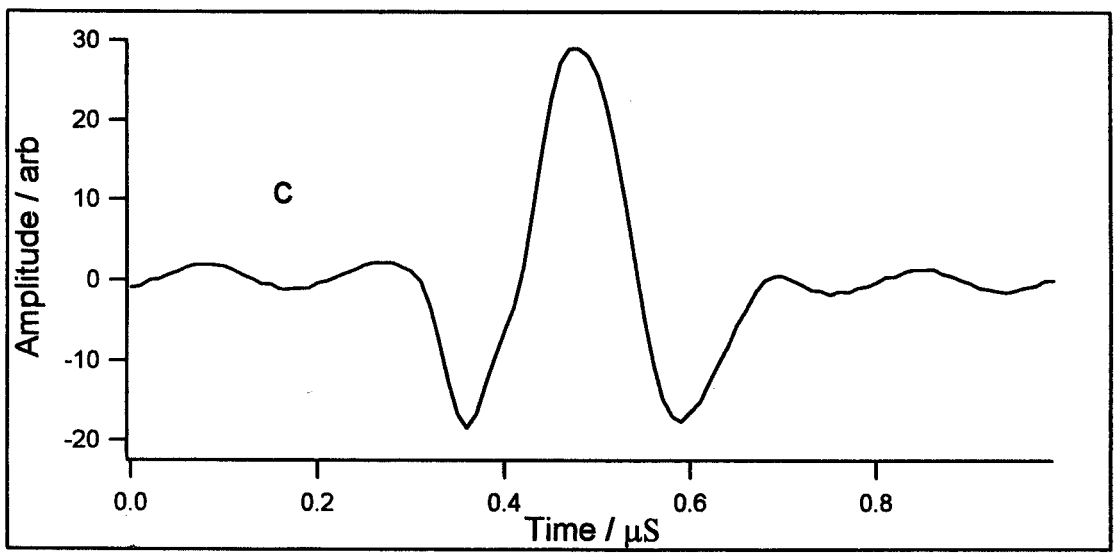

Figure 3.3: a: Drive pulse through EMAT on Aluminium
b : Double differentiated drive pulse
c: EMAT detected 2S echo from Aluminium.

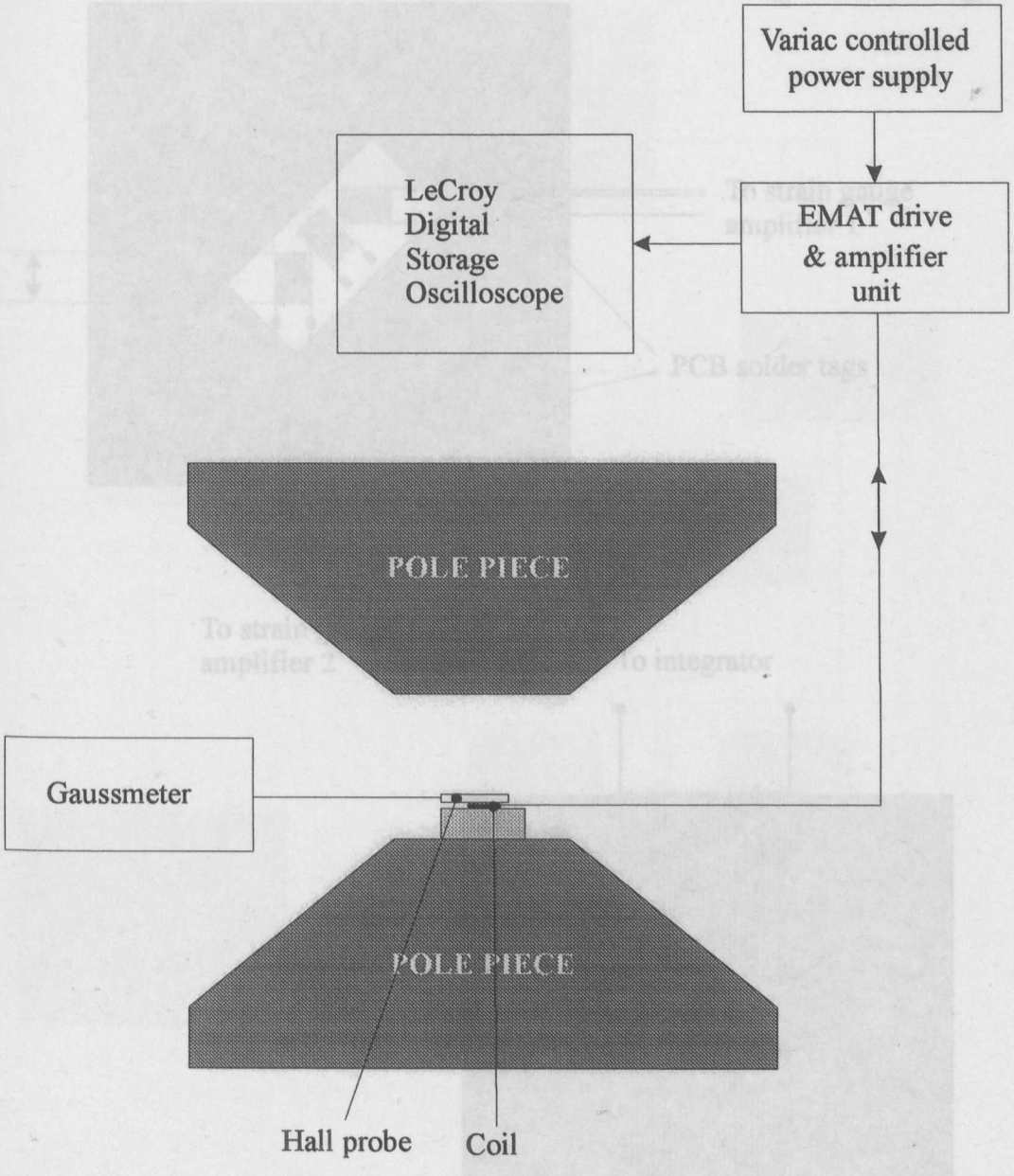

Figure 3.4: Schematic of set up used to measure dependence of send-receive EMAT efficiency on applied normal field. The Hall probe mounted directly over the coil gives a good measurement of B normal to the surface.

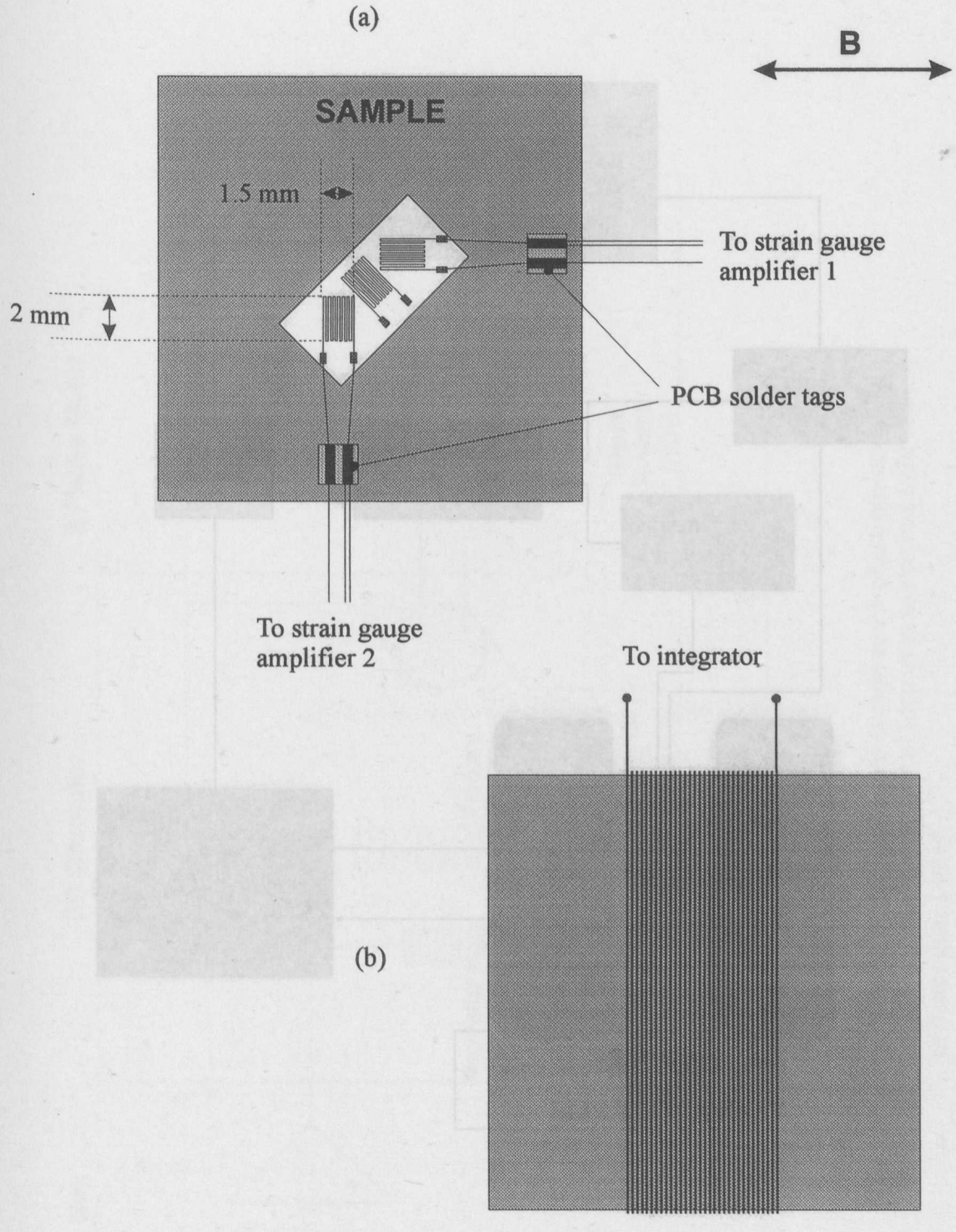

Figure 3.5: (a): 3-foil strain gauges used to measure longitudinal and transverse magnetostriction simultaneously.

(b): 0.1mm Cu coil wrapped round sample to allow field measurement by integrator.

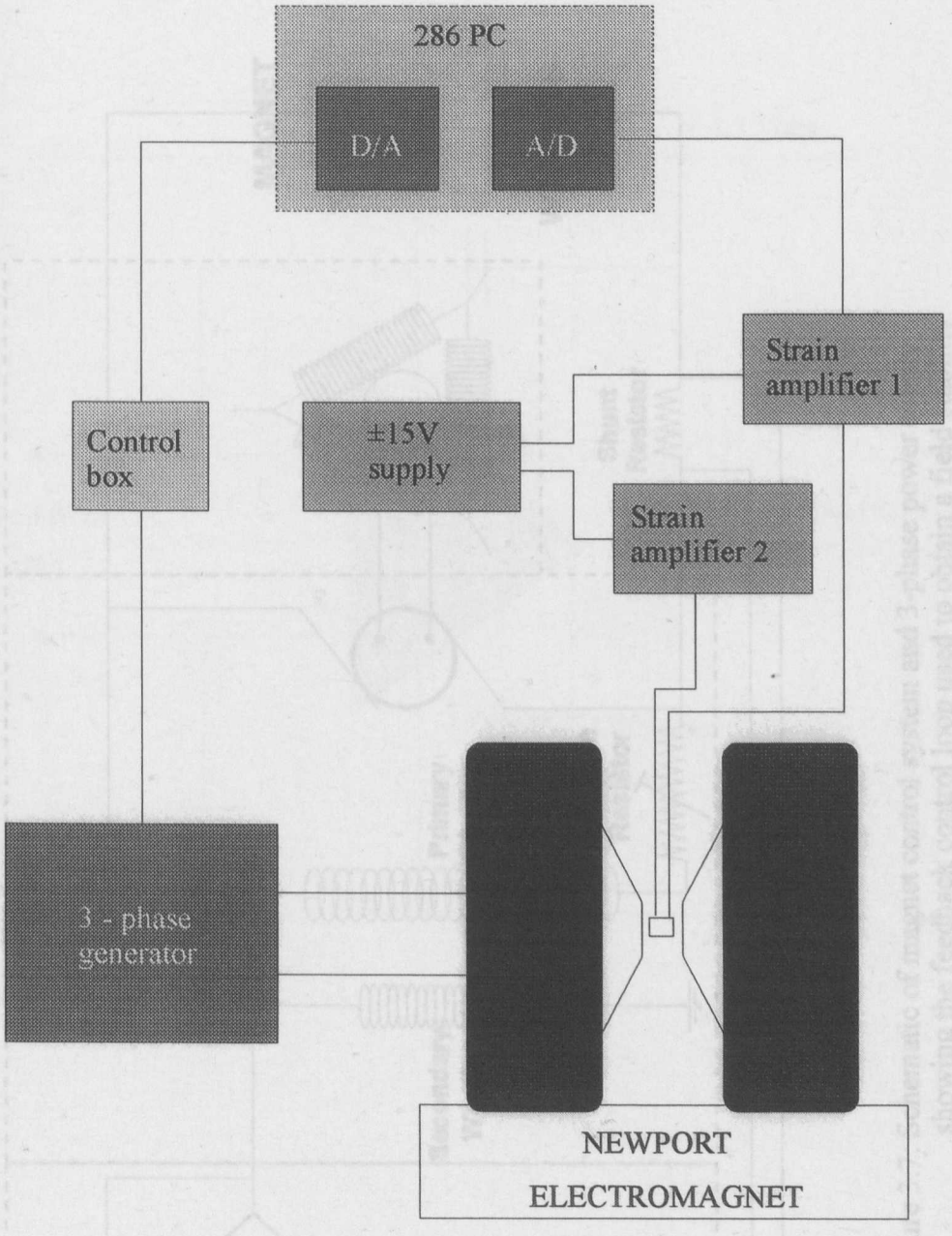

Figure 3.6: Schematic of magnetostriction measurement system. The system was fully automated with the program allowing the user to determine the magnet sweep rate, data point density and number of loops recorded.

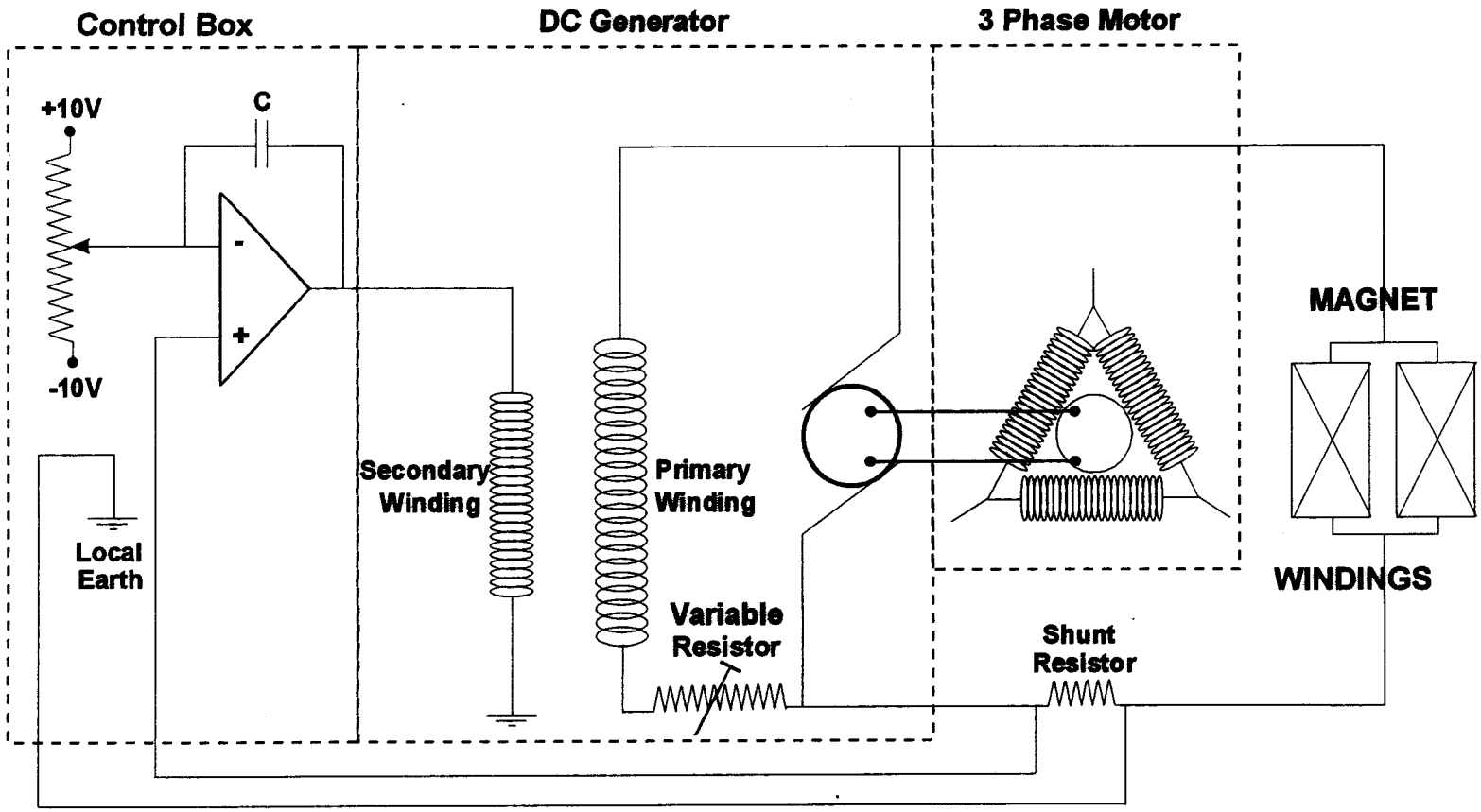

Figure 3.7: Schematic of magnet control system and 3-phase power supply showing the feedback control loop used to obtain a field stability of better than 1 in 10^6

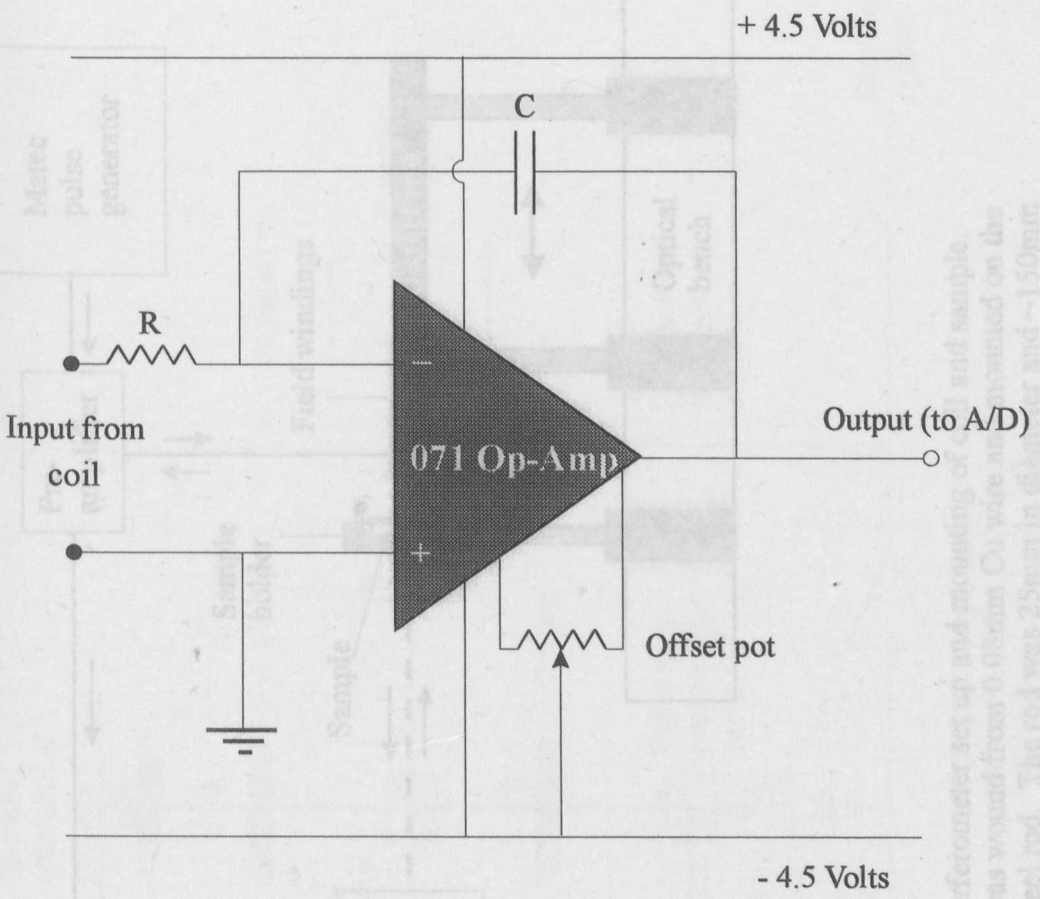

Figure 3.8: Integrator used to measure internal field of sample during magnetostriction measurements. The circuit comprised an 071 Op-Amp with C = 2.2 μF and R = 330kΩ to give an effective time constant of 0.7S. The offset pot was used to trim out any small initial differences in voltage between the two Op-amp inputs. This obviously would be integrated over the time of the experimental run and result in apparent drift in the field measurement.

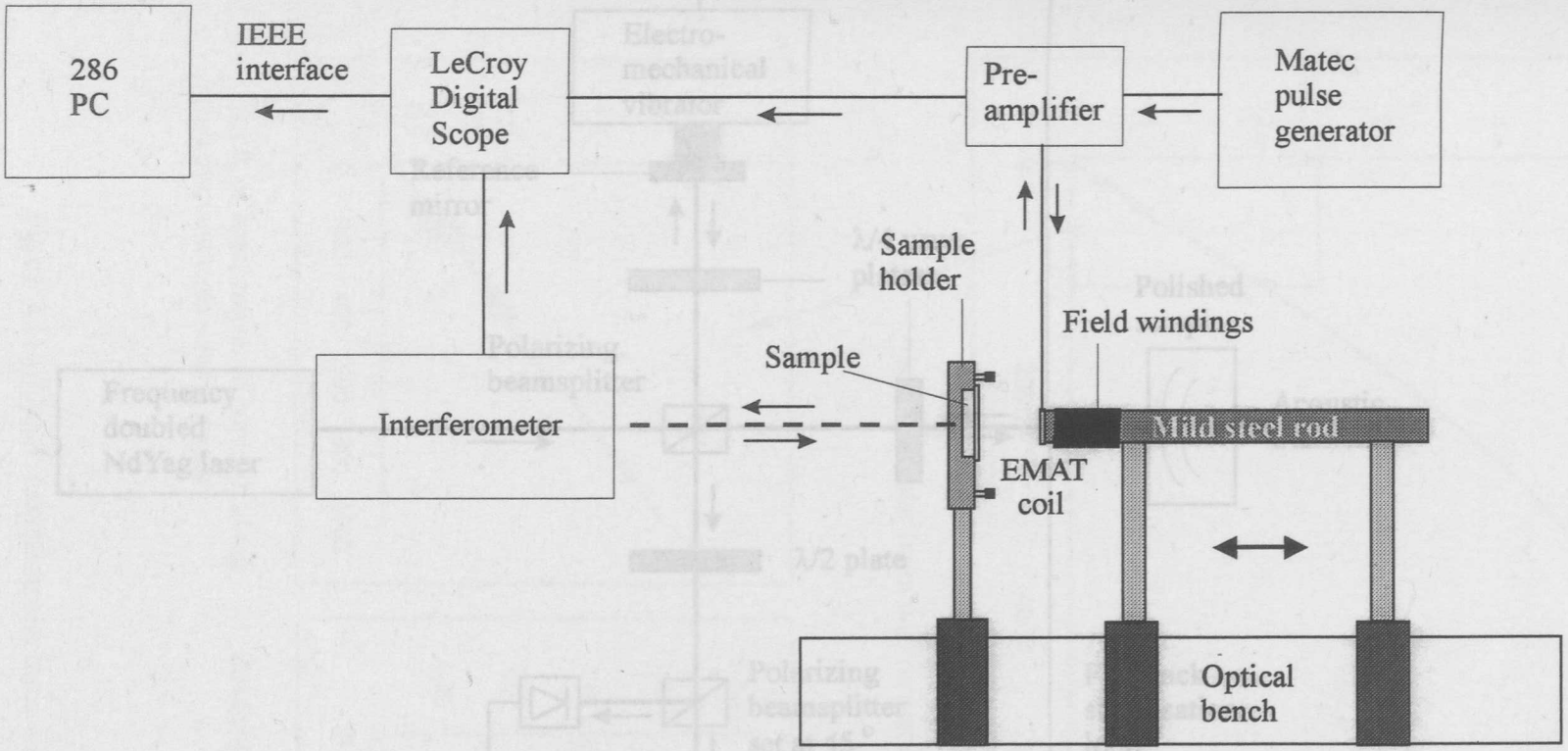

Figure 3.9: Schematic of interferometer set up and mounting of coil and sample. The EMAT coil was wound from 0.08mm Cu wire and mounted on the end of the mild steel rod. The rod was 25mm in diameter and ~150mm in length.

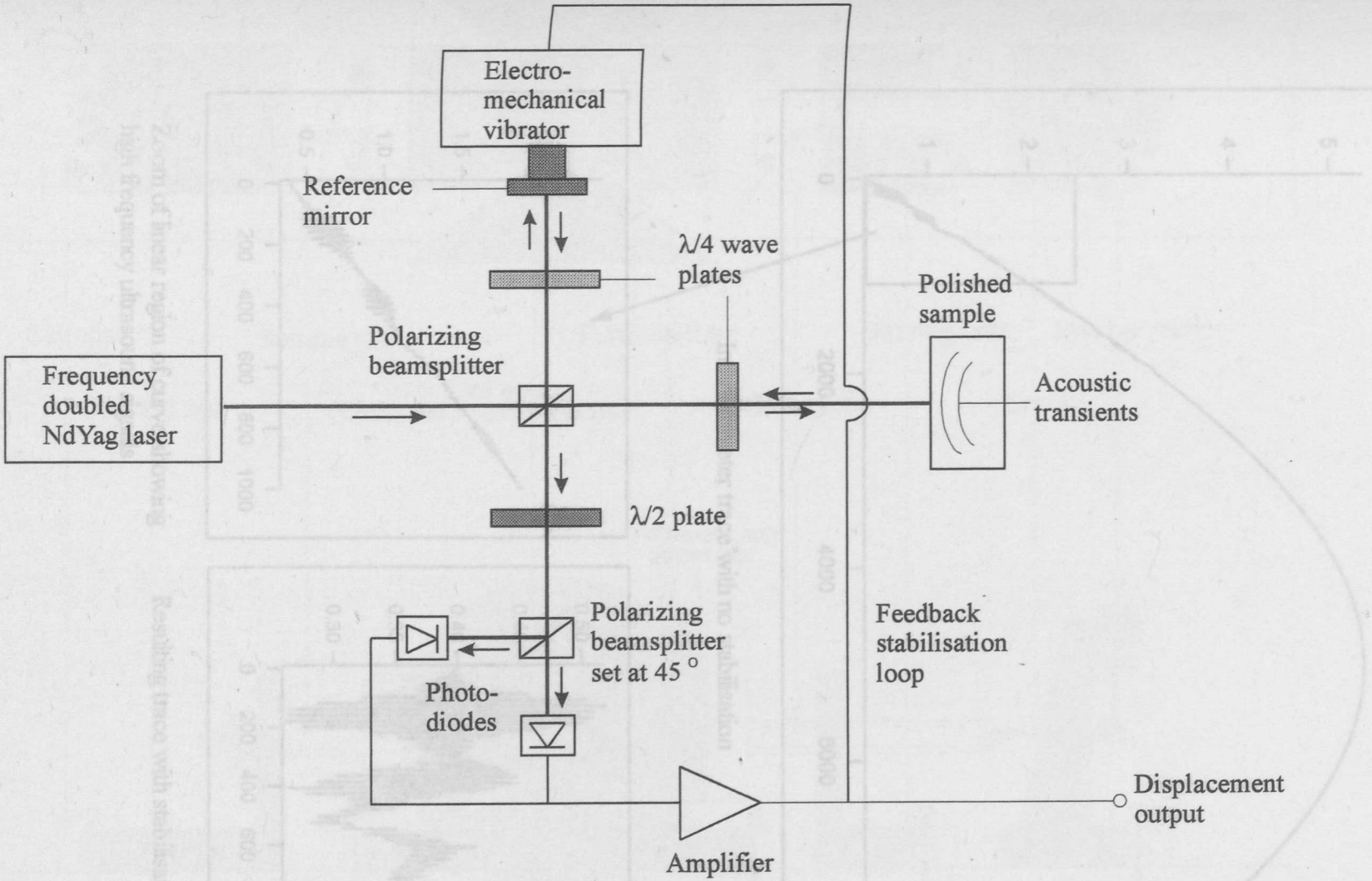

Figure 3.10: Michelson interferometer with feedback stabilisation. Laser used is a frequency doubled NdYag operating at 532 nm. The resolution of the instrument is ~ 0.01 nm.

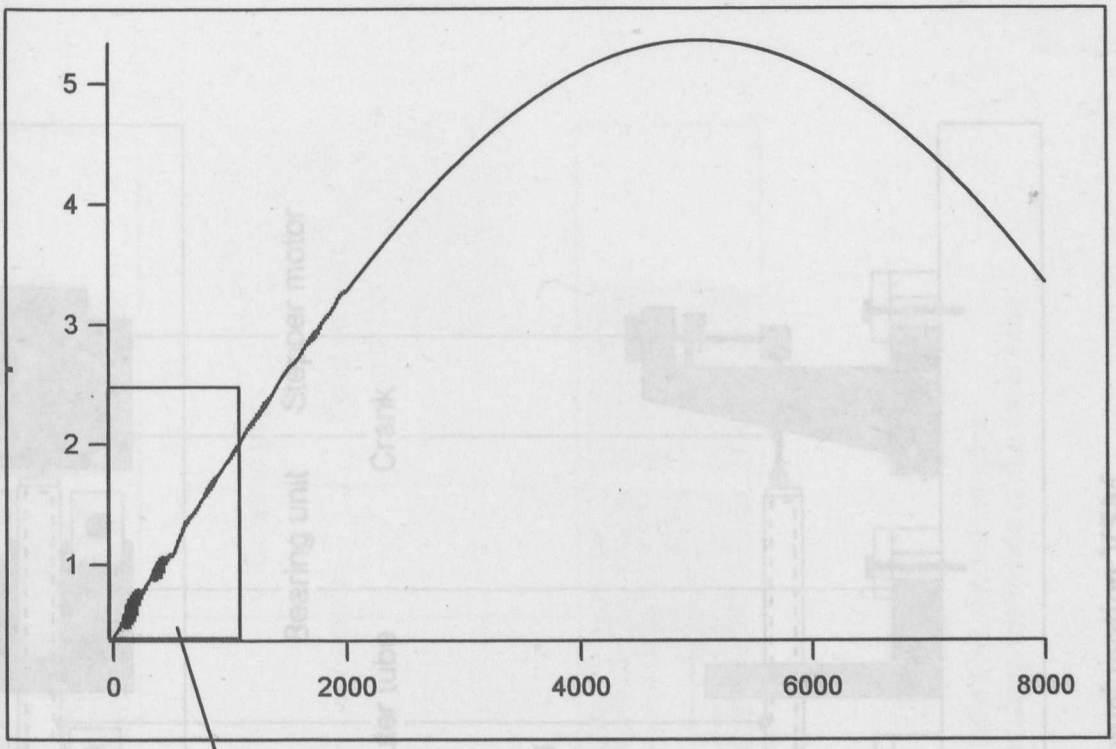

Interferometer trace with no stabilisation

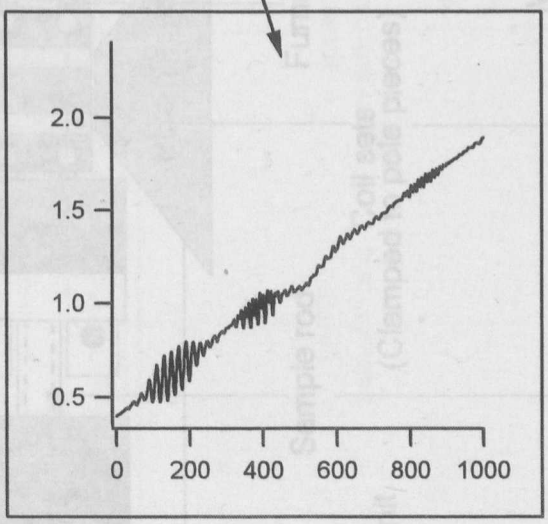

Zoom of linear region of curve showing high frequency ultrasound signals

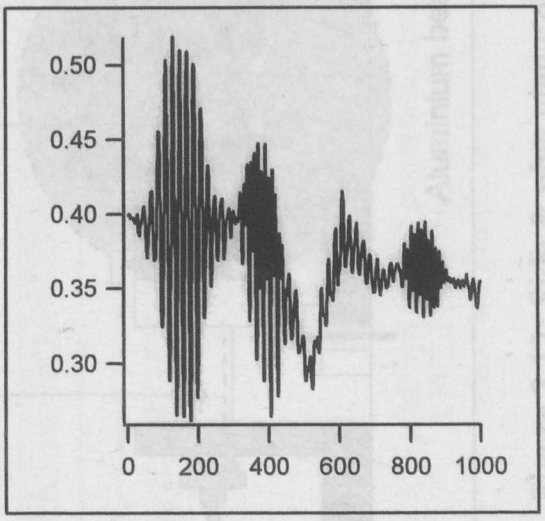

Resulting trace with stabilisation applied

Figure 3.11: Upper: Interferometer trace without stabilisation.

Lower: zoom of linear region of low frequency background and resulting trace with stabilisation.

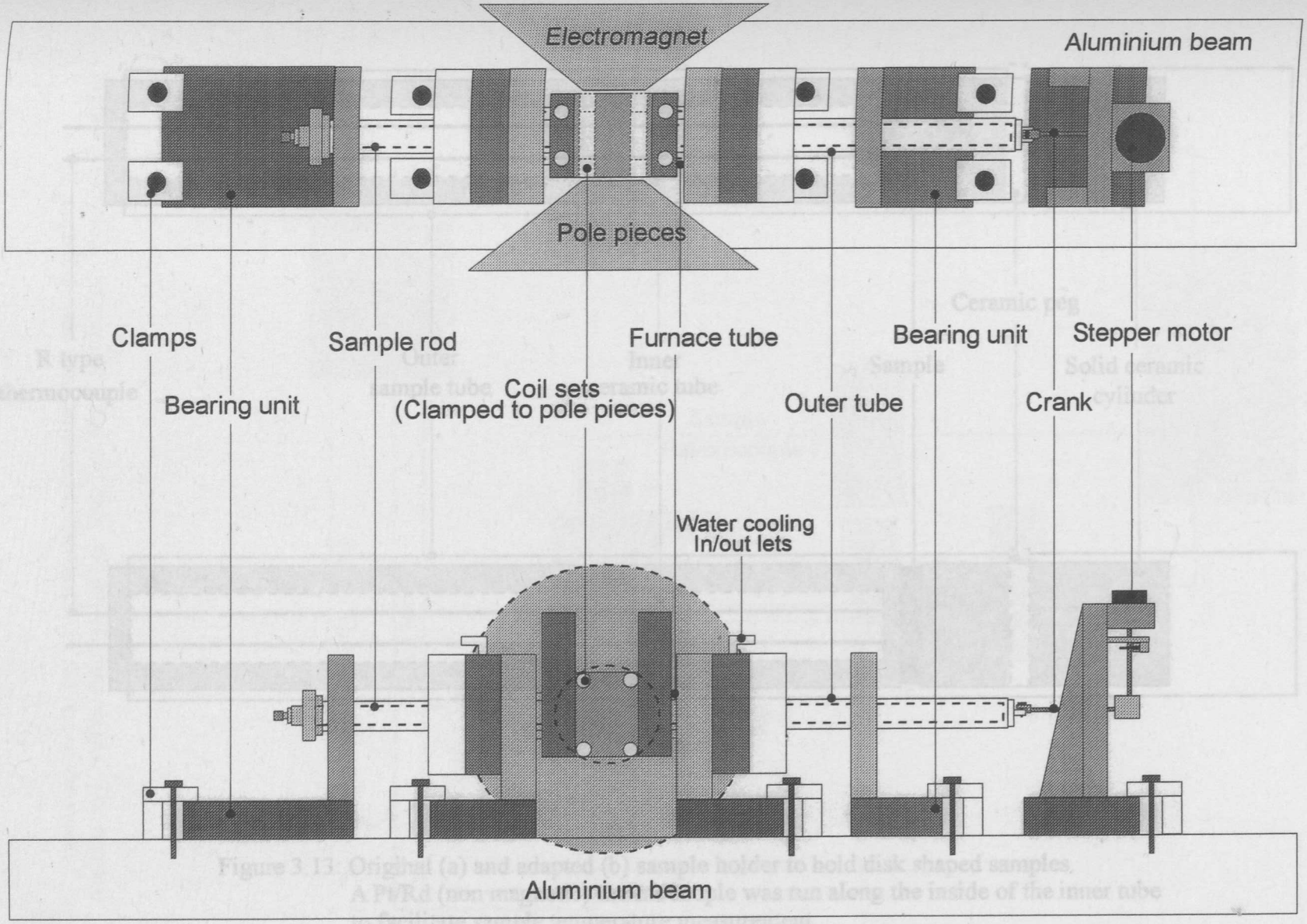

Figure 3.12: Side & plan views of the horizontal motion VSM.

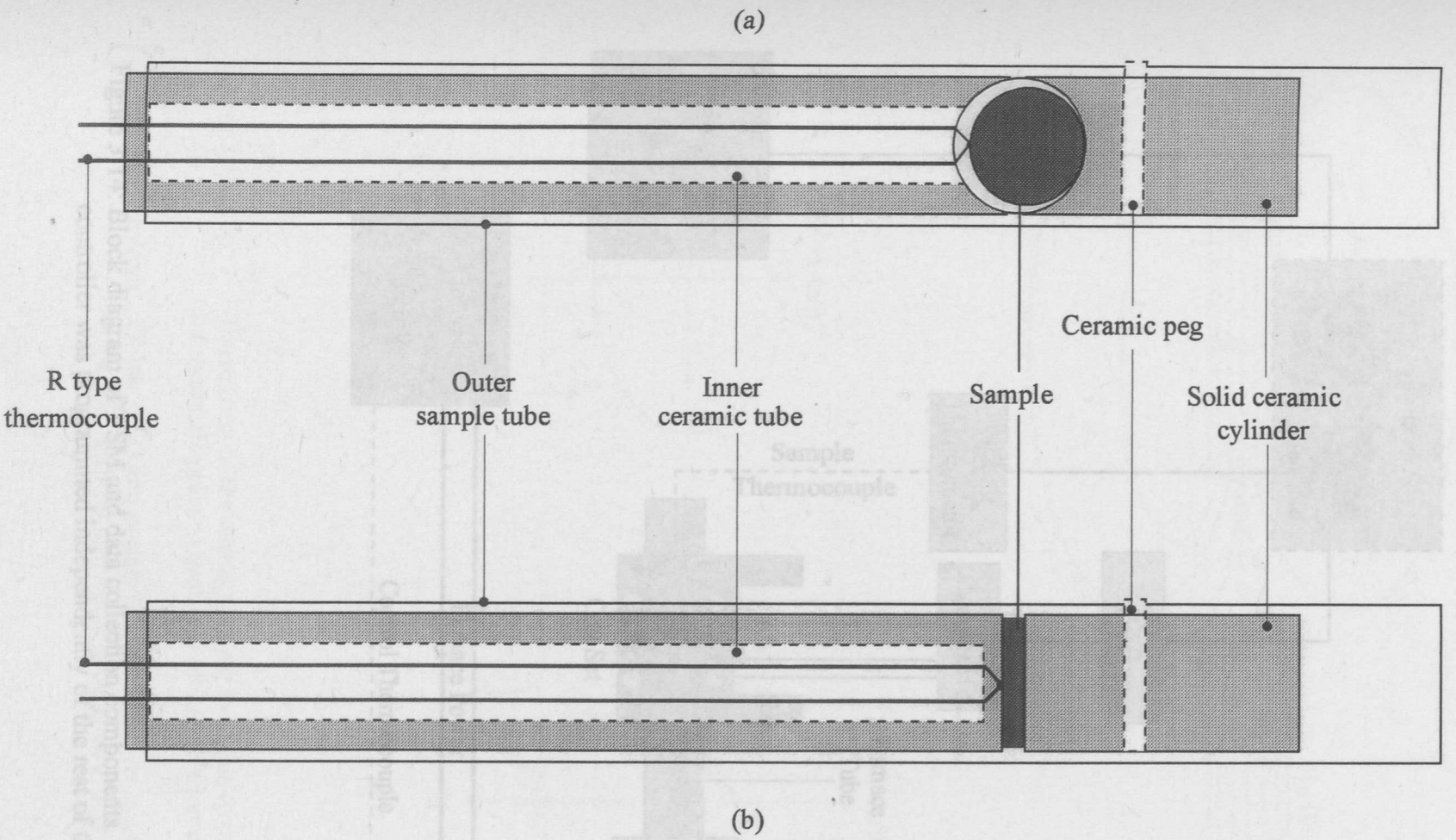

Figure 3.13: Original (a) and adapted (b) sample holder to hold disk shaped samples.
A Pt/Rd (non magnetic) thermocouple was run along the inside of the inner tube
to facilitate sample temperature measurement.

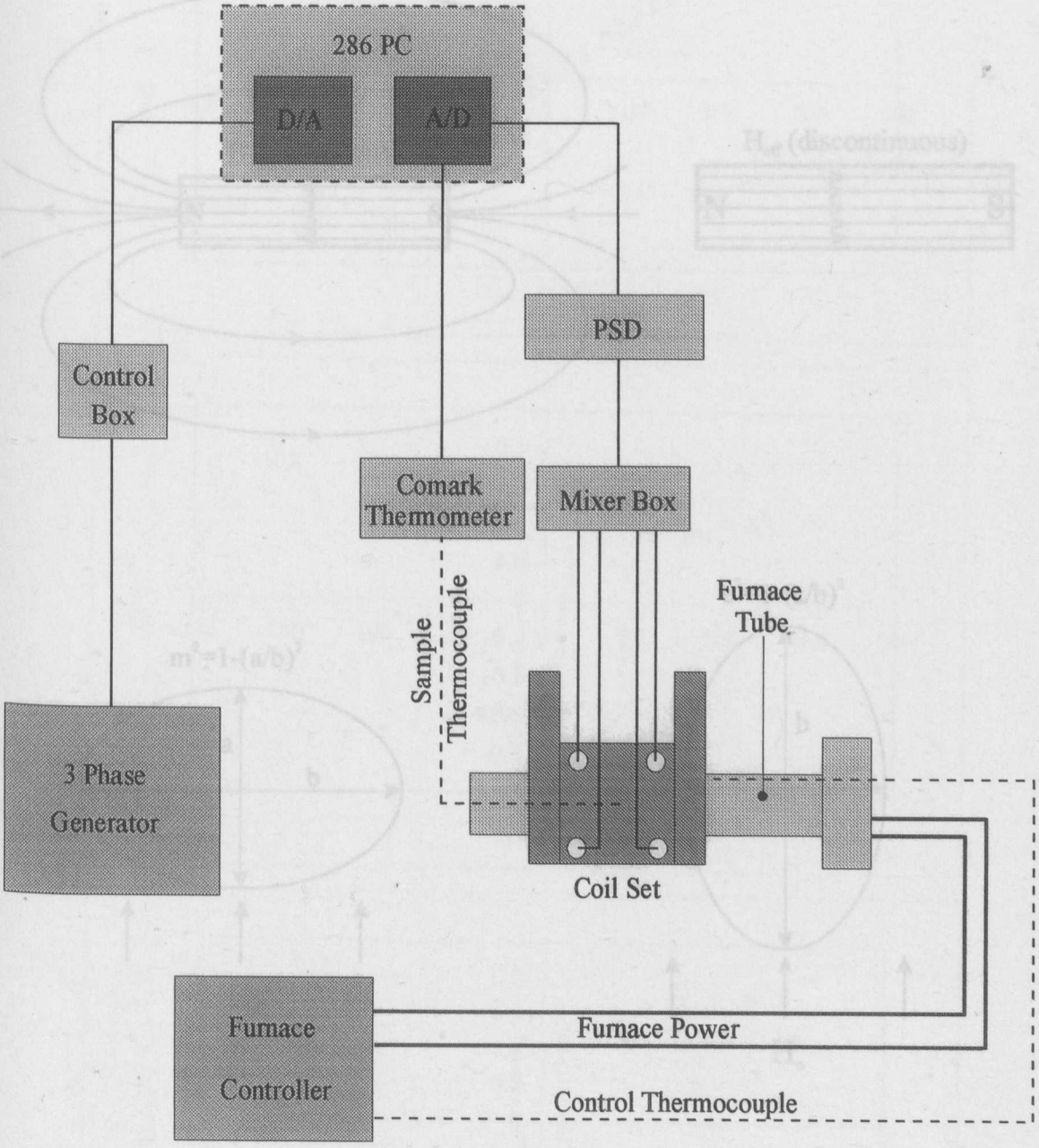

Figure 3.14: Block diagram of VSM and data collection components. The furnace controller was programmed independently of the rest of the system.

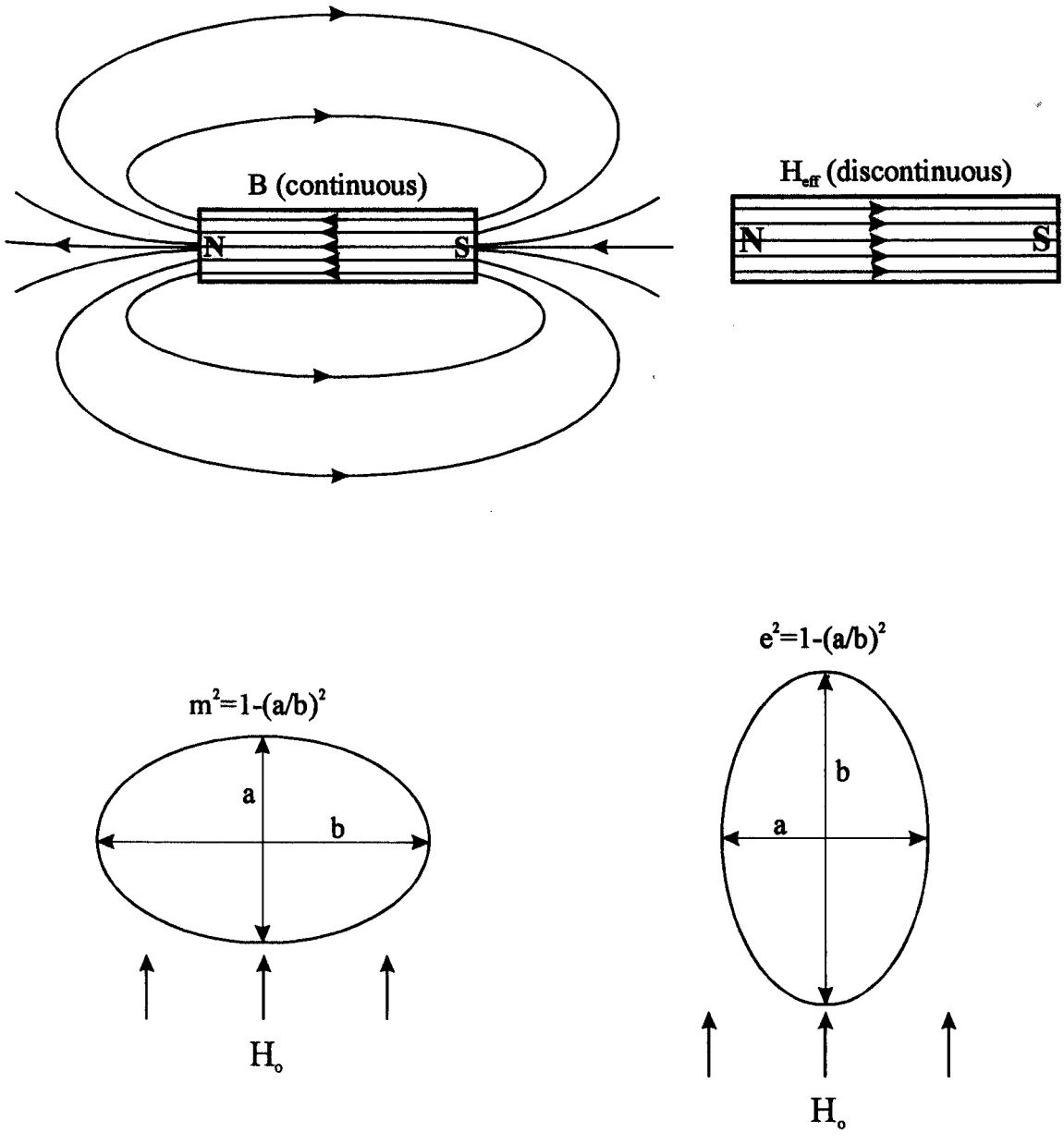

Figure 3.15: Top: Illustration of the demagnetising field due to the formation of magnetic poles at each end of a simple bar magnet.

Bottom: Oblate (left) and prolate (right) ellipsoids in a uniform field, Ho, with definitions of eccentricity as given by Stoner.

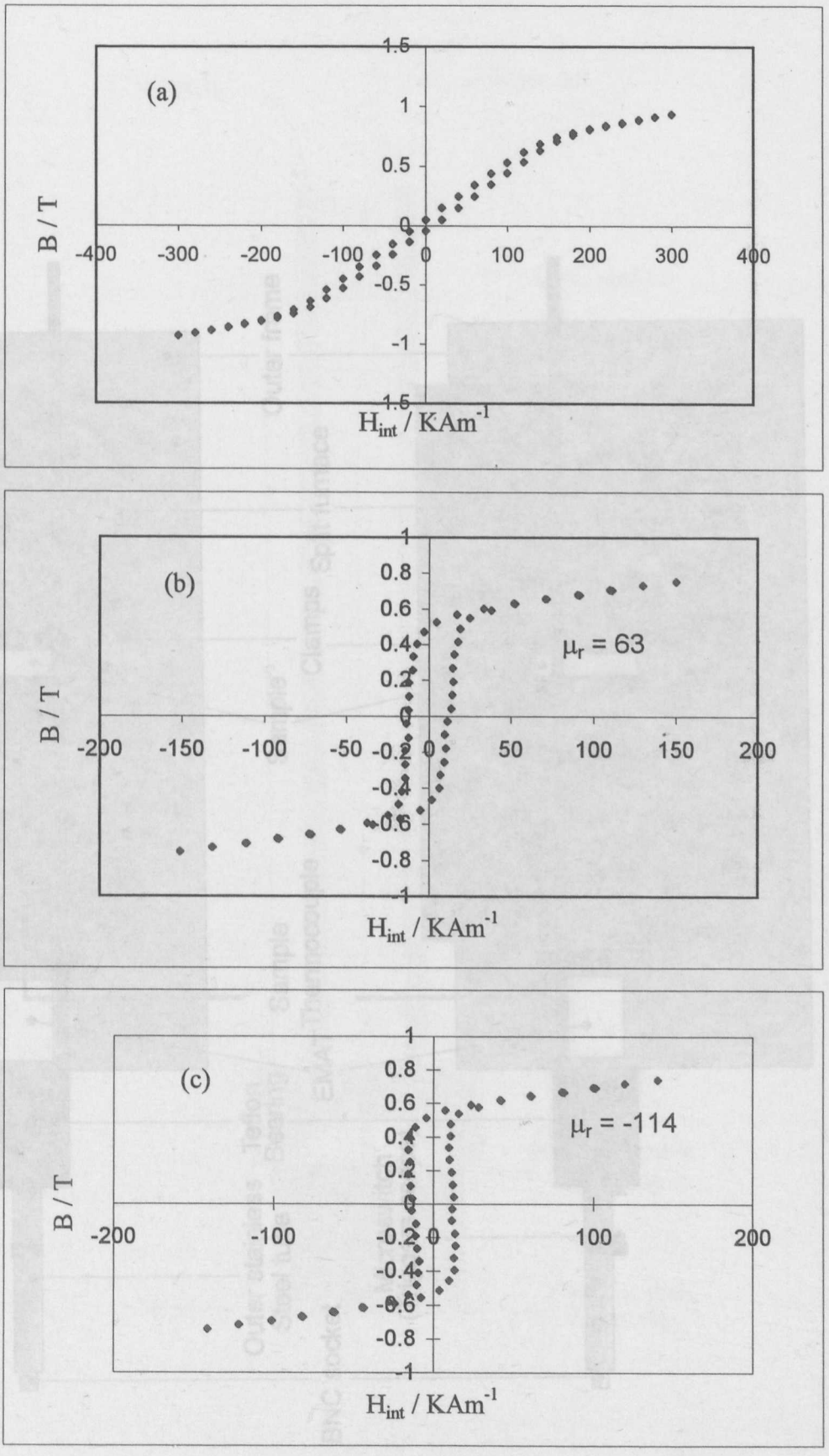

Figure 3.16: B - H loops for Ni sphere
(a): uncorrected, (b): $N_d = 1/3$
and (c): $N_d = 0.3124$

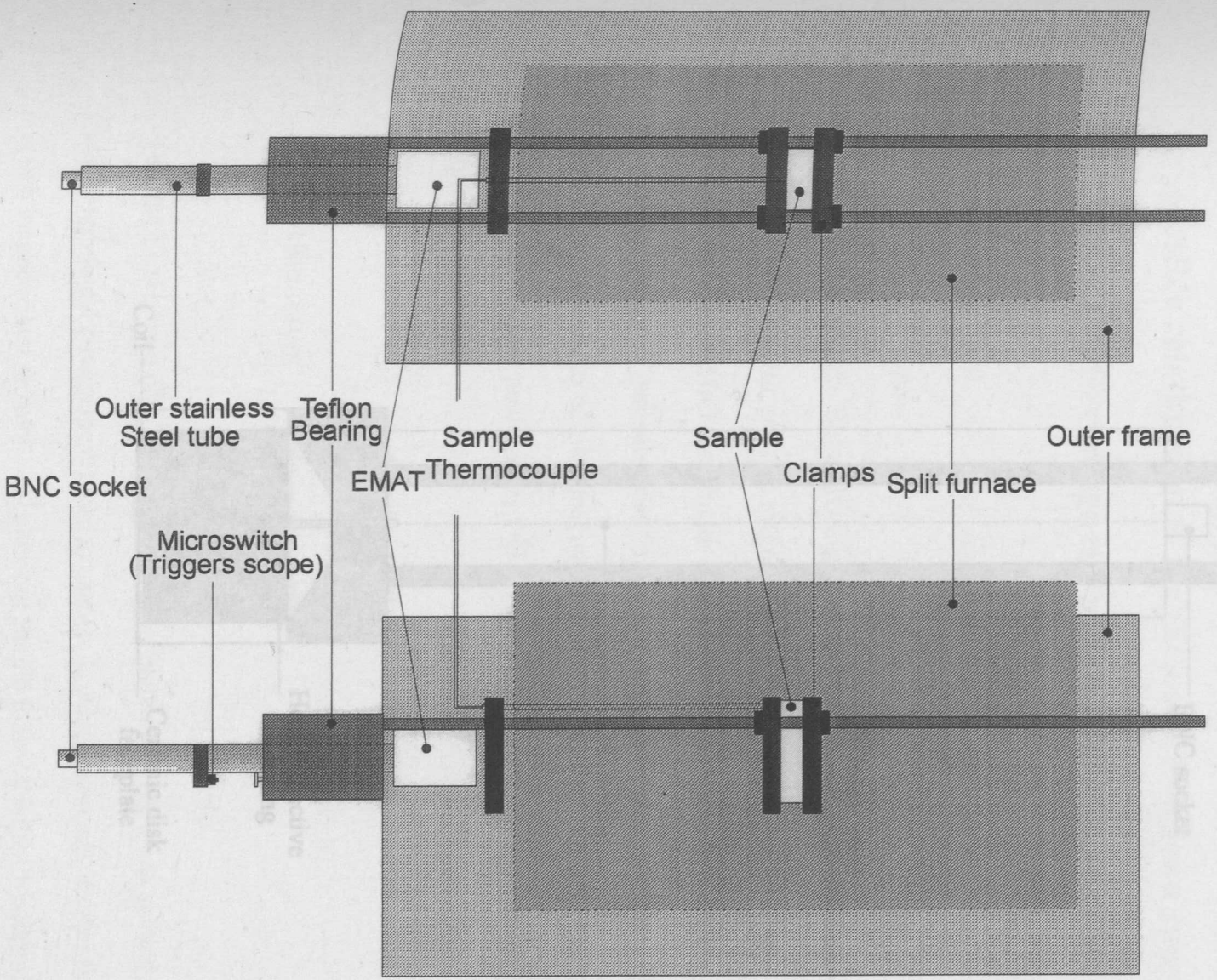

Figure 3.17: High temperature EMAT setup showing furnace and water cooled EMAT on stainless steel tube.

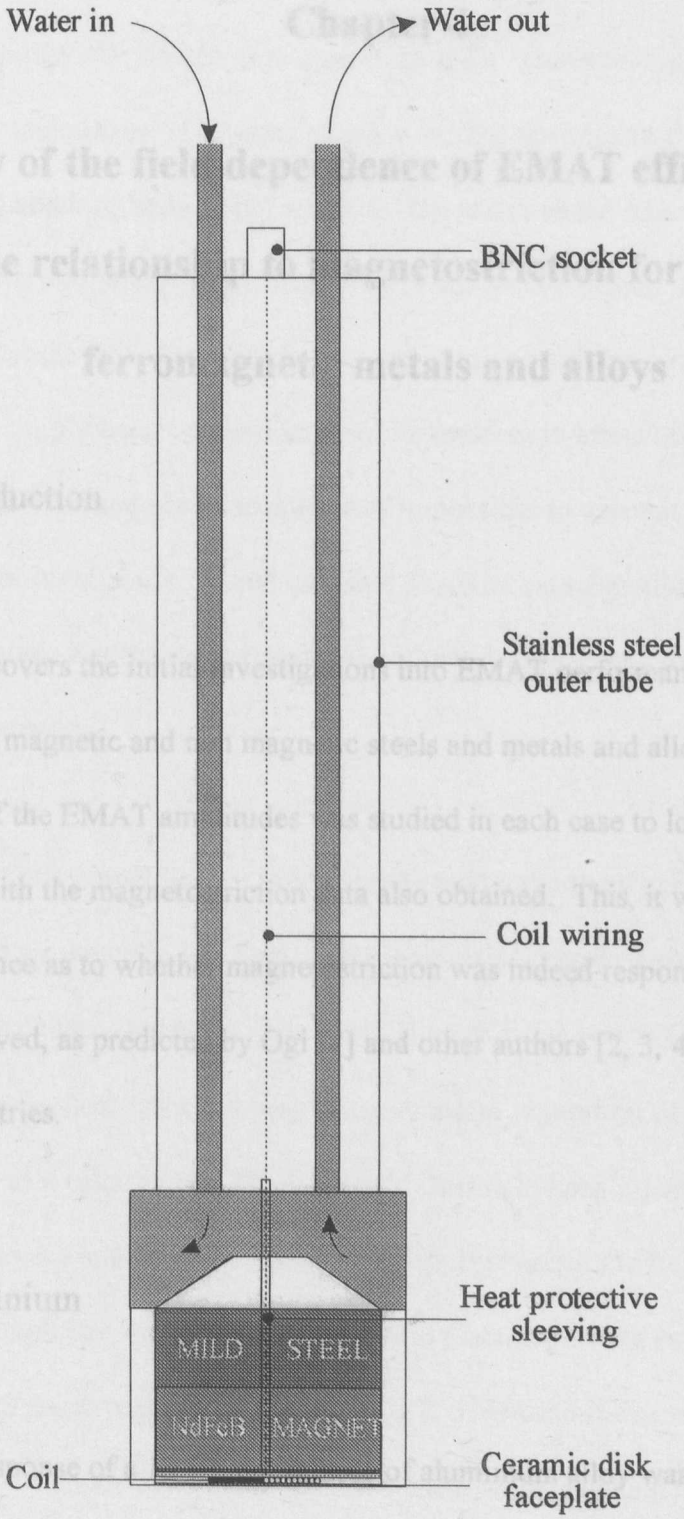

Figure 3.18: Construction of water cooled EMAT showing water cooled cavity in the top of the EMAT case and the stainless steel outer tube. The coil wiring was routed through a length o heatproof sleeving to reduce the risk of heat damage.

Chapter 4

A study of the field dependence of EMAT efficiency and possible relationship to magnetostriction for a range of ferromagnetic metals and alloys

4.1: Introduction

This chapter covers the initial investigations into EMAT performance on a range of samples, both magnetic and non magnetic steels and metals and alloys. The field dependence of the EMAT amplitudes was studied in each case to look for correlations with the magnetostriction data also obtained. This, it was hoped, would provide evidence as to whether magnetostriction was indeed responsible for the features observed, as predicted by Ogi [1] and other authors [2, 3, 4] for various EMAT geometries.

4.2: Aluminium

The EMAT response of a 12.72 mm sample of aluminium alloy was studied using the experimental arrangement given in chapter 3. Aluminium was studied first as it is non magnetic and therefore its behaviour should follow the theory outlined by Dobbs [5]. It was also used to ensure that all the drive electronics etc. were working correctly, aluminium being known to be relatively efficient in terms of EMAT performance. The drive pulse to the coil was set to its maximum output, producing a

peak current of 5.8A. Figure 4.1 shows the traces recorded over the field range 0 to 1T, the notation 2S, 4S, 6S etc. corresponds to shear echoes that have traversed 2, 4, 6 etc. sample thicknesses. The same notation is used throughout this work to denote both shear (S) and longitudinal (L) arrivals. The traces in the figure were the result of an average of 500 sweeps to reduce noise to acceptable levels. It is worth noting at this point that the signal amplitudes throughout this work are given in arbitrary units. This is simply because the combined differences in attenuation, thickness and coil impedance from sample to sample were impossible to account for quantitatively. It was therefore pointless to try and compare absolute signal amplitudes between different samples. For the same reasons the signal : noise levels are also not quoted throughout this work.

The absence of any signal in zero field is predicted by the theory for non magnetic metals, neglecting the coils self field, as B_o is zero and therefore so is the Lorentz force, F_L, on the eddy currents, j. The application of B_o as low as 0.1T allows us to discern ultrasonic shear wave echoes with a temporal separation of 7.88μs, this corresponding to a velocity of $3229 \pm 14 ms^{-1}$. This is in keeping with the accepted shear wave velocity in aluminium, $3200 ms^{-1}$ [6]. Increasing the field further to 0.4 T increases the amplitude of all echoes by the same factor with the emergence of an echo just before the first shear wave return (2S). This echo is due to a longitudinal wave produced by mode conversion from the shear wave, incident upon the opposite face. Obviously, as the L velocity, $6374 ms^{-1}$, is around twice that of the shear, this arrival occurs ~ ¾ of the way between t=0, when the coil is pulsed, and the 2S arrival. This mode conversion is denoted by SL, meaning one traverse of the sample at the shear velocity followed by the return trip at the longitudinal velocity. The

phenomenon of mode conversion is known to occur when a shear wave is incident at non normal incidence upon the metal-air interface. In this case, however, the effect is also observed for a shear wave at normal incidence, this is not predicted by classical wave theory for a linearly polarised shear wave and is due to the radial polarisation of the EMAT generated wave. Kawashima [7] gives an argument as to why this polarisation produces such mode conversions and the reader is referred to this for details. The fact that we observe any longitudinal arrival at all is due to EMAT detection of in plane motion associated with the out of plane motion of the longitudinal wave. The amplitude of the in plane motion is related to that of the out of plane by Poissons ratio.

The field dependence of the signal was determined by measuring the amplitude of the 2S echo, A_{2S}, in the train at each value of B_o. The square root of this is plotted as a function of B_o in figure 4.2, the square root is plotted simply for the sake of consistency with the results from later samples. As stated earlier, for a non magnetic conductor the signal amplitude in a send receive system should be proportional to B_o^2. This relationship is confirmed by the linear dependence of $\sqrt{A_{2S}}$ upon B_o shown in the plot. This agreement, of course, relies on the attenuation in the sample being independent of B_o, any change in this obviously also influencing the signal amplitude. Given the non magnetic nature of the sample this is a reasonable assumption since the predominant attenuation mechanism is grain boundary scattering which is not field dependent. In ferromagnetic metals other attenuation mechanisms act which are field dependent [8]. This said, however, they have only been studied in single crystals where any granular nature is absent. As grain scattering is the dominant source of attenuation in polycrystals it is unlikely that any

of the magnetic mechanisms will make a significant contribution to the attenuation in the present work.

In summary, the results from aluminium were as predicted by theory and showed that the EMAT system was working normally.

4.3: Nickel

The first ferromagnetic metal chosen for study was nickel, due both to its well documented magnetic properties and previous attention to its EMAT performance [9, 10]. The traces between 0 and 1.528T are shown in figure 4.3 for an 8.23mm thick sample of 99.98% pure nickel, using a pulse current of 1.8A. The large echoes with a separation of 4.96μs are due to shear waves, having a velocity of $3318 \pm 18 ms^{-1}$. It is apparent that these waves are present when B_o equals just 0.05T and therefore cannot be due to Lorentzian generation. This contrasts markedly with Hanabusa et als work that showed no such mode when B_o=0 although their work employed a linear solenoidal coil and a much longer drive pulse, 2μs. The field dependence of the S echoes ($\sqrt{A_{2S}}$) is plotted in figure 4.4a and shows a shallow peak at 0.69T ($\sim B_s$, the saturation induction) with a noticeable minimum at 0.3T. An expanded view of the 2S echo is shown in figure 4.5 for B_o applied in 'positive' and 'negative' directions respectively. With B_o just above or below zero the two signals are very similar in both phase and magnitude. However, application of $|B_o|$ between 0.25 and 0.3T leads to a marked difference in the relative phases and amplitudes of the echoes with field reversal. Application of still higher $|B_o|$ leads to increasing similarities in the pulse shapes perhaps indicating the re-emergence of a dominant mechanism. It is

also evident that detection of the SL mode conversions is enhanced when B_o is applied in the 'negative' direction. Figure 4.4b is a higher resolution plot of the $\sqrt{2}$S amplitude between –0.4 and 0.4T. It shows a small difference in the exact depth of the minima with a reversed field, perhaps indicative of a Lorentz contribution either adding to or subtracting from the amplitude depending on whether B_o is 'positive' or 'negative'. If this were the case we would expect to observe some minimum in $d\lambda/dB$ at 0.3T.

Magnetostriction data from the sample is shown in figure 4.6a and gives excellent agreement with the results of several authors (11, 12), λ_s being –35 microstrain with $\lambda_t = -\frac{1}{2}\lambda_l$. This data suggests $B_s = 0.65$T, in agreement with the value used for VSM calibration. Figure 4.6a also shows, however, that significant hysterisis exists between the ascending and descending portions of the λ curve. Every model so far derived that deals with magnetostrictive ultrasound generation has assumed negligable hysterisis in λ. Whilst this is reasonable in steels, see below, it is clearly not in nickel where differences of up to 8 μstrain exist between the same B on ascending and descending regions. More importantly, as figure 4.6b shows, this leads to marked differences in $d\lambda/dB$ and therefore ε_m, the magnetostrictive ultrasonic strain [1]. On the B descending arm of λ vs B the gradient undergoes a swing from 2 to 0 μstrain/T whilst it only swings between 1 and 2 μstrain/T on the ascending arm. More importantly, $d\lambda_t/dB$ reaches a minimum at ~ 0.3T on the B descending arm, just as expected from the EMAT results. Given the large hysterisis it is impossible to directly relate $d\lambda/dB$ to the EMAT amplitude, however, the explanation of a Lorentz source acting in conjunction with a predominantly magnetostrictive one seems feasible given the evidence.

4.4: Invar

Invar is an alloy of iron and nickel (36%Ni, 64%Fe) exhibiting the lowest known coefficient of thermal expansion, around room temperature, of any alloy [13]. This unusual property occurs as a result of the broad Curie transition it undergoes between ~ 0 and 250^{O}C, documented as far back as 1897 [14]. As such transitions are known to lead to greatly enhanced EMAT efficiency, particularly in rare earths [15], it was thought that this alloy may exhibit similar behaviour. Figure 4.7 shows the traces recorded between 0.067T and 1.728T on a 13.32mm thick sample using a pulse current of 1.72A. As for nickel the dominant features in these traces are the S mode echoes, having a velocity of 2654 ± 10ms^{-1}. The amplitude of these follows the dependence shown in figure 4.8a, $\sqrt{A_{SS}}$ being plotted vs B_o. This plot shows a non linear increase in signal with increasing B_o until a peak is reached at 1.25T, application of higher fields is seen to reduce the amplitude although it is still significant at the highest attained field of 2.1T.

The B-H loop of this sample, figure 4.8b, shows a B_s of 1.3T which is consistent with that published [6] and suggests a link between the EMAT efficiency and B_s. The magnetostriction data (figure 4.9a) also suggest a B_s of 1.25T, this being evident from the turning point in λ_t. The high scatter in λ_l below 0.8T could not be accounted for by experimental inadequacies, the integrity of the glue bond between strain gauge and sample is evident from the λ_t data. The fact that it is symmetric with field reversal also serves to confirm its validity as a genuine experimental result, although no mention of it could be found in the literature. It is noteworthy that the gradient of both λ_l and λ_t is very shallow below 0.8T, we would therefore expect to

generate only small magnetostrictive strains with the static field below this. This is borne out by the low EMAT amplitudes below 0.8T and the sharp rise following this to the peak at 1.25T. It should also be noted that the volume magnetostriction is high in this sample, evidenced from the field dependence of λ_l and λ_t above 1.25T. The fact that the S amplitude only becomes significant when $B_o > 0.8T$ suggests that ε_L in this sample is very small (given its δ (~2μm) and ρ this is unexpected), furthermore the Lorentz mechanism should act in all conductors, magnetic or not. It should be remembered though that the pulse current here was a factor of 3.3 lower than that used on aluminium. This was necessary to avoid amplifier saturation at higher B_o and can therefore account for the lack of Lorentz signal. The fact that the S amplitude rises so rapidly with $B_o > 0.8T$ cannot be accounted for by a sudden increase in F_L and is a very strong indication that shear wave generation on invar is due to a magnetostrictive source.

The question must be asked though; if magnetostriction is indeed the dominant ultrasonic source why is $d\lambda/dB$ (see figure 4.9b) not a maximum at the same point as the EMAT efficiency, B_s?. It should be remembered, however, that as B_s is reached μ changes by factors in the 100's, therefore δ increases by factors of 10 and the ultrasonic source becomes much thicker. As Buchel'nikov states [16]; a magnetostrictive source is most efficient when δ is large, this contrasts with the Lorentz mechanism that is only efficient when $\delta << \lambda$. Consequently as B_s is approached the magnetostrictive contribution should become higher and that from the Lorentz mechanism should drop. Above B_s ε_m becomes the volume magnetostriction whilst F_L increases only linearly with B_o as μ_r is now unity. This could account for the peak in EMAT efficiency at B_s and the lack of any apparent

Lorentz contribution when $B_o > B_s$. This argument does however contradict the results shown below for mild steel which indicate that the Lorentz mechanism is insensitive to even the large changes in μ in going from $B_o=0$ to B_s. It is also worth noting that although λ_t undergoes a turning point at B_s (figure 4.9) the same is not true of λ_l. What effect this could have on the ultrasonic generation is not clear and has not been modelled anywhere in the literature. To conclude, the model of a magnetostrictive source undergoing a peak near B_s due to an increase in δ fits the results to an extent. It is very difficult, however, to give a more quantitative argument as the situation is complex to say the least and has enjoyed relatively little theoretical treatment.

4.5: Mild steel, low carbon tensile steels and cast irons

The EMAT response and magnetostriction of a range of low carbon tensile steels, mild steel and cast irons was studied. The tensile steels and cast irons were kindly provided by British Gas and consisted of a range of bars of various thickness with compositions as shown in table 4.1 below. The mild steel was cut from a 12.56mm thick bar provided by the stores, no compositional information was provided. The aim of this work was to assess whether the composition of the steels, primarily the carbon content, had any significant effect on the EMAT efficiency. Given the much higher carbon content of cast irons (~ 3%) it was hoped that these samples might show measurably different behaviour to that of the steel specimens.

4.5.1: Mild steel

Figure 4.10 shows the EMAT traces recorded on the mild steel sample using a pulse current of 5.5A. The echoes that become apparent when $B_o > 0.15T$ have a velocity of $3223 \pm 10ms^{-1}$ and are therefore shear waves. The echoes are also several times smaller than those from either aluminium, nickel or invar. A plot of $\sqrt{A_{2S}}$ vs B_o exhibits the dependence shown in figure 4.11a. This shows small deviations from linear behaviour with a possible point of inflection at around 0.6T. Above 1.2T the plot appears linear although due to the H_{max} of the magnet it was not possible to go beyond B_s, this being measured from the B-H loop shown in figure 4.11b. This shows a B_s of ~ 2T which agrees with the magnetostriction results (figure 4.12) that show evidence of the onset of volume magnetostriction at the same point. The positive peak in λ_l, due to domain wall motion, occurs at 8.25 μstrain with a drop of 6.5 μstrain between this and the minimum at B_s due to domain rotation. The results also show a small deviation from anisotropic magnetostrictive behaviour, $\lambda_t \neq \frac{1}{2}\lambda_l$, due to the rolling process and its resultant grain orientation. Magnetostriction in iron single crystals is highly directionally dependent, due to the large magnetocrystalline anisotropy. Therefore, any process that produces a net grain orientation (usually <110>) in a steel affects the measured magnetostriction. Clearly then, if the bar exhibits some degree of orientation, it is quite likely that equation 2.25 for anisotropic magnetostriction will be invalid and $\lambda_t \neq \frac{1}{2}\lambda_l$ in either orthogonal direction, although it will still be isovolumetric. It is worth mentioning that the rolling process introduces residual stresses into the steel which also affect the magnetostriction. Kuruzar and Cullity [17] found that a 3% prestretched rod of iron behaves as if it is under compressive stress and as such exhibits a higher positive peak in λ_l. This fact is unmentioned by Ogi [1] who used plates 10mm or even only 1mm thick of low carbon steel. Whilst magnetostriction measurements were

certainly made by him, no measurement direction was stated, therefore his conclusion that magnetostriction is the dominant EMAT mechanism may be restricted to relatively thin, highly orientated steel plate samples. The fact that $\sqrt{A_{2S}}$ vs B_o is almost linear gives strong indications that magnetostrictive generation is relatively insignificant on 'thick' mild steel plate. This is further borne out by the 2S waveform which appears insensitive to changes in B_o and is also virtually identical to the 2S echo in aluminium.

4.5.2: Low carbon tensile steels

The compositions of the samples tested are tabulated below, including those of the cast irons described later, the specimens were chosen so as to give the broadest range of carbon contents possible.

Sample	C / wt %	Mn / wt %	Si / wt %	S / wt %	P / wt %	Ni / wt %	Cr / wt %
OLI-030	0.24	0.82	0.06	0.02	0.011	0.047	Not given
OLI-015	0.16	1.08	0.29	0.023	0.008	0.015	Not given
DLR	0.15	0.68	0.06	0.027	0.022	0.015	Not given
DHP	0.14	0.8	0.07	0.031	0.037	0.052	Not given
OLI-017	0.14	1.43	0.34	0.012	0.013	0.017	Not given
Spun cast iron	3.3-3.5	0.29-0.44	2.17-2.86	0.05-0.1	0.7-1.36	0.03-0.1	0.05-0.21
Pit cast iron	2.44-3.46	0.23-1.64	1.42-3.92	0.04-0.16	0.56-4.08	0.01-0.06	0.02-1.14
Ductile iron	3.7	0.2	2.9	0.01	0.05	0.1	0.05

Table 4.1: Compositions of the low carbon tensile steels and cast irons provided by British Gas

Figure 4.13a shows the $\sqrt{S}$ vs B_o for the OLI-0** range of steels, the actual traces are not shown here as they are virtually identical to those from mild steel. The pulse current in every case was set to its maximum of 5.5A. Due to thickness variations between samples the exact $\sqrt{S}$ echo amplitude plotted is different in each case to allow them to be shown on the same graph. It is clear that they are very similar to the results from mild steel with only small deviations from linear behaviour. An identical plot for the DLR and DHP samples, figure 4.13b, shows similar results. The magnetostriction of each sample is shown in figures 4.14 and 4.15 for the OLI-0** and D** samples respectively. The differences in the positive peak strains due to domain wall motion are quite pronounced with variations of up to 7 μstrain between samples. In contrast, the swing from this to the minimum is around 7μstrain in every sample, this being due to domain rotation. The fact that such a wide variation is observed in λ with so little variation in the EMAT response strongly suggests that, just as in mild steel, the Lorentz mechanism is dominant in generating and detecting shear waves in these steels.

4.5.3: Cast irons

Figure 4.16 shows the $\sqrt{S}$ vs B_o plots for the ductile, spun cast and pit cast irons, using a pulse current of 5.5A. Again, due to thickness variations, the exact echo measured was chosen so as to give similar amplitudes in the plot. The similarities in behaviour are quite evident between all three samples as well as with those from the mild and low carbon tensile steels. Given their much higher content it is therefore

safe to assume that the carbon constituent of all the steel and cast iron samples has no effect on the EMAT performance. Moreover, the magnetostriction data, figure 4.17, shows a marked difference between the cast irons and steels with the onset of domain rotation (1.4-1.6T). While the steels undergo a negative swing with an amplitude of 7μstrain in all cases, the cast irons do not. This difference has not been documented as far as the author is aware and has no immediately obvious explanation. It does, however, lead us to expect some effect on the EMAT signal, such as that observed in nickel above. Whilst there is some evidence of non linearity in the plots of figure 4.17 it is clear that this is comparatively weak and leads to only a small deviation from the behaviour of a non ferromagnet. It is therefore concluded that on the cast irons, mild and low carbon tensile steels the spiral coil EMAT generates and detects via a predominantly Lorentzian mechanism. The fact that μ changes by factors of several hundred between B_o=0 and B_s is also seen to have no effect on the shear amplitudes. This strongly supports the assumption that for good metallic conductors, at the frequencies used here, the actual value of δ is inconsequential to the Lorentz mechanism [18].

4.6: Duplex stainless steel

The EMAT response and magnetic properties of duplex stainless steel were studied just as for the steels and cast irons. In this case there were two samples available, one supplied by British Steel (BS) in the form of a 200mm diameter, 90mm thick, ingot, the other supplied as a 13.5mm thick bar by British Gas (BG). A sample was cut from the end of the BG supplied piece 60 mm square and 13.03 mm thick whilst a 60 mm square, 7.14mm thick, piece was cut from the centre of the BS ingot. It is

worth noting that duplex steel is unusually hard, compared to other stainless steels, and was therefore cut very slowly using abrasive elastic wheels.

4.6.1: EMAT response of British Gas duplex

Figure 4.18 shows the EMAT traces recorded on the BG sample between 0 and 2T using a pulse current of only 0.9A. A current this small was necessary to ensure that the amplifier did not reach saturation at even low B_o due to the highly efficient EMAT performance observed. With a field as low as 0.15T the signal amplitudes are several orders of magnitude larger than those observed on any of the other steel samples. A second important observation is the large degree of acoustic birefringence apparent in the shear echoes. By the 2nd echo the two polarisations are quite clearly separated in time, given the sample thickness this indicates a highly anisotropic microstructure. The velocities of these two shear modes are 3262 ± 12ms^{-1} and 3237 ± 13ms^{-1} respectively. A plot of $\sqrt{A_{6S}}$ (the 2nd of the birefringent pair) vs B_o is presented in figure 4.19 and shows a clear peak at 0.85T with a subsequent reduction in amplitude with further increases in B_o. Due to the necessarily low pulse current, a second unusual aspect of this samples behaviour is not visible in figure 4.18. This can be seen in figure 4.20a which shows the traces recorded in very low B_o using a pulse current of 5.5A. The sharp peaks with a temporal spacing of 4.6μs (V=5665ms^{-1}) are due to 2L, 4L, etc. echoes, ie: a longitudinal mode is generated in the absence of B_o. This echo cannot be due to a mode conversion from an S wave as (a): this would arrive at a later time, and (b): no S mode is apparent from which conversion could occur. The conclusion drawn from these results is that an L wave is actually generated by some mechanism. The detection of this wave must also occur via a mechanism that does not require B_o, ie:

it is not due to Lorentzian detection of the in plane motion associated with the L wave. Shown in figure 4.20b is a plot of the amplitude of this mode, the 2L echo, vs B_o, in both directions. This shows that the longitudinal generation/detection efficiency is a maximum when B_o is zero. It also shows that with B_o applied in one direction the L echo falls quickly to zero whilst it falls away much more slowly with B_o applied in the opposite sense. Also illustrated is the fact that reversing the coil wiring reverses the B_o dependence of the L amplitude. The zoom in figure 4.20a illustrates the form of the 2L echo and shows an initially sharp pulse with a broader peak occuring just after this, the possible origin of this mode and the very high S mode efficiency will be discussed later.

4.6.2: EMAT response of British Steel duplex

Figure 4.21 shows the EMAT traces recorded between 0 and 2T, using a pulse current of 5A, on the BS sample. The shear wave echoes have a temporal spacing of 4.43μs correponding to a velocity of $3227 \pm 20 ms^{-1}$. The amplitudes are large compared to those from other steels, although not nearly as large as those from the BG sample, with a plot of $\sqrt{A_{2S}}$ vs. B_o (figure 4.19b) showing a peak in efficiency at 0.7T. The S waveform also undergoes a change as B_s (see below) is passed, this being predicted by Buchel'nikov et al [16] as the generation mechanism shifts from magnetostrictive to Lorentzian. An obvious difference between this and the BG duplex is the lack of birefringence in the shear wave echoes, suggesting a far more isotropic microstructure. Also absent from the trace is any sign of a direct L mode, even though the maximum pulse current of 5A was used.

4.6.3: B – H curve and magnetostriction of duplex steels

A 0.25mm thick, 7mm diameter, disk was cut from the original BG bar and used in the VSM to obtain a B-H loop up to B_s, this loop is shown in figure 4.22a. The sample is seen to reach saturation at around 0.7T, just below the point at which the EMAT amplitude reached its peak. A similar disk cut from the BS sample, 0.45mm thick and 7mm diameter, yielded the B-H loop shown in figure 4.22b. This shows a saturation point also of ~ 0.7 T although, as the disk was thicker, B_s is more difficult to define than for the BG duplex.

The magnetostriction of both samples was measured and the results of this are given in figures 4.23a (BG) and b (BS). It is clear that both λ_l and λ_t are positive in the BG sample, ie: it does not obey the simple law governing anisotropic magnetostriction. It also does not undergo the peak in positive strain observed in all the other steel samples. The fact that both λ_l and λ_t are positive suggests the possibility of a volume expansion occuring in low B_o which could account for the anomalous L mode generation/detection. This effect may also be linked to anomalously high magnetostriction (see below) that could account for the very high S wave efficiency observed. In contrast to this, the BS sample exhibits a λ_t that is $\frac{1}{2}\lambda_l$ and opposite in direction, as expected for an isotropic sample.

4.6.4: Composition and microstructure

The term duplex is used to describe this particular steel type as it consists of a two phase microstructure made up of austenite and ferrite. This structure is obtained by a heat treatment whereby the mixed state is frozen in by rapid cooling from just above

the transition temperature. It is stabilised by virtue of a high Cr (~22%) and Ni (~0.2%) content, the austenitic structure being unstable below 1050^{O}C (ref). An important aspect of this structure is that the austenite is non magnetic whilst the ferrite is ferromagnetic, we therefore have, in effect, a dispersion of magnetic particles in a non magnetic matrix, or vice versa.

A metallograph of the BG sample was prepared, etched using glyceregia, and this is shown in figure 4.24a. It shows the two phase structure made up of austenite and ferrite (austenite etched darker), with a locally highly orientated columnar structure. This correlates well with the EMAT traces that suggested a high degree of birefringence due to microstructural anisotropy. The structure is also fairly coarse with grain sizes of the order of 50μm. The BS sample was etched in a similar manner, the metallograph is shown in figure 4.24b. This shows a far more isotropic microstructure with grains of austenite in a ferrite matrix, the austenite grains having an average size of around 10μm.

4.6.5: Discussion of duplex results

The EMAT response of both types of Duplex was significantly greater than that seen in any of the other steel types, the BG sample in particular giving signal amplitudes several orders of magnitude higher. There are several feasible explanations for this enhanced efficiency all of which rely on the two phase structure of the steel. The first of these is a concerted movement of the ferrite grains due to the non uniform pulsed field of the coil. The dynamic field is essentially radial, therefore any spatial gradient in this field could lead to a net radial force on the magnetic ferrite grains, see figure 4.25. This force would generate a radial stress and therefore the strain

required to produce a radially polarised shear wave. However, if this were the case then why should the BS sample have an efficiency so much lower than the BG sample?.

The second possibility is that of a phase change from the austenitic to the ferritic phase causing a volume change due to their different structures, figure 4.26. This volume change would be of the order of ~ 3% and be caused by the dynamic field transforming the metastable austenite to the stable ferrite structure. This volume change could also account for the anomalous longitudinal wave observed in the BG sample. The phase change could possibly be detected by some microscopic X-ray crystallographic technique although just setting up such an experiment would probably constitute a separate project in itself. A third possibility is that of microscopic focussing of the static magnetic field through the ferrite grains, figure 4.27, in preference to the austenite grains, these having a permeability several hundred times lower. This would lead to a locally higher B_o which in turn would generate a larger F_L on the eddy currents and thus a larger ε. This effect would be undetectable by the Hall probe, which measures an average B_o over a macroscopic area, and could also account for the reduction in efficiency when $B>B_s$ due to μ_r of both phases becoming unity.

The possibility obviously exists for magnetostriction to play a large part in the high EMAT efficiency. Although the results indicate little difference in the magnitudes of strain involved to those on say mild steel, we are again only measuring the average response over a comparatively large area, ie: the gauge area. Whilst this is reasonable for the relatively isotropic low carbon steels it does not take any account

of the two phase nature of duplex. Thus the local microscopic strains induced may be larger than those measured macroscopically. Again the use of an X-ray technique seems the most likely candidate for detecting this possible effect. The problem is further compounded in the case of the British Gas sample where we also have a locally highly orientated microstructure. Bakker [19] has measured the magnetostriction of several types of Duplex and determined that there is a marked difference between the saturation magnetostrictions of those samples with isotropic microstructures (λ_s = 5.7μstrain) and those with orientated (λ_s = 15.5μstrain) although again this was a macroscopic measurement (dilatometric). It is also worth remembering that δ for this steel is somewhat indeterminate, μ varying hugely over a microscopic scale. However, given that in mild steel no effect on EMAT amplitude was observed due to changes in δ, this seems to be unimportant, when considering the Lorentz mechanism at least.

4.7: Conclusion

To conclude, it has been shown that aluminium behaves as expected and obeys the predictions of the simple Lorentz theory. The results from the mild, low carbon tensile steels and cast irons have indicated that a predominantly Lorentzian mechanism is also responsible for S wave generation in these alloys. We have also shown that the large changes in μ occuring throughout magnetisation from B_o=0 to B_s have no significant effect on the Lorentz generation process. This supports the assumption that, when $\delta << \lambda$, ε is independent of both σ and μ for the Lorentz process. One of the original aims of this work was to assess which electrical and magnetic properties significantly affect EMAT generation on steels. It can be seen

then that in the case of the 'ordinary' steels tested the spiral coil EMAT performance is more or less independent of μ and σ, the Lorentz mechanism being dominant, at the frequencies used here at least. In contrast, nickel and invar have exhibited highly non linear B_o dependencies that are almost certainly due to an essentially magnetostrictive mechanism. Given their high λ_s this is reasonable and fits the experimental results. The duplex, however, does not exhibit such large magnetostrictive strains, macroscopically at least, and is therefore somewhat enigmatic. Its two phase nature is certain to be linked to its high EMAT performance although this link, as outlined above, could be via a number of possible mechanisms. The fact, however, that the S efficiency has a maximum at B_s, in nickel, invar and duplex, suggests a common magnetostrictive generation mechanism that peaks at B_s due to the increase in δ and thus thicker ultrasonic source. Above B_s λ is much smaller and therefore, even though δ is much larger than when $B_o<B_s$, ε falls. Whilst this explanation is consistent with the results the detection mechanism itself must not be forgotten. Given the EMAT amplitudes obtained and the fact that the pulse current was a factor of 3-4 lower than on aluminium Lorentzian generation is ruled out on nickel and invar. It obviously cannot be ruled out for duplex due to the possibility of B_o focussing through the ferrite grains. Lorentzian detection of the reflected ultrasound, however, may still give a significant contribution to the EMAT signal as it is linearly dependent on B_o. It is therefore possible that on these samples the EMAT generates via magnetostriction but detects via the Lorentz mechanism. This may go some way to explaining the observed peak at B_s whereby the overall EMAT efficiency is a compromise between the increasing Lorentzian detection with the decreasing magnetostrictive strains as B_s is approached.

Chapter 4 references

1: H. Ogi; *Journ. Appl. Phys.* **82**, pp 3940 - 3949 (1997).

2: R. B. Thompson; *Journ. Appl. Phys.* **48**, pp 4942 - 4950 (1977).

3: I. V. Il'in and A. V. Kharitinov; *Defektoskopiya*, pp 86 - 93 (1980).

4: V. A. Komarov; *Defektoskopiya*, **no 4**, pp 40 - 45 (1981).

5: E. R. Dobbs; *Physical Acoustics*; Ed: W. P. Mason and R. N. Thurston; Academic Press, London **10**, pp 127 - 189 (1973).

6: Kaye and Laby; *Tables of Physical and Chemical Constants*; published by Longman (1986).

7: K. Kawashima; *Journ. Acoust. Soc. America* **60**, pp 365 - 373 (1976).

8: M. J. W. Povey, D. J. Meredith and E. R. Dobbs; *Journ. Phys. F: Metal Phys.* **10**, pp 2041 - 2053 and pp 2555 - 2572 (1980).

9: M. B. Gitis; *Soviet Physics - Solid State*; **14**, 2992 - 2995 (1973).

10: M. Hanabusa, T Kushida and J. C. Murphy; *Journ. Appl. Phys.* **44**, pp 5106 - 5110 (1973).

11: E. W. Lee; *Reports on Progress in Physics* **18**, p 184 (1955).

12: Bozorth; *Ferromagnetism*; Van Nostrand (New York) (1951).

13: A. Y. Romanov and V. P. Silin; *JETP* **86**, pp 120 - 127 (1998).

14: Ch. E. Guillaume; *Compt. Rendue Acad. Sci.*; Paris, **125**, p 235 (1897).

15: C. M. Lim; PhD Thesis; Warwick University (1998).

16: V. D. Buchel'nikov and A. N. Vasil'ev; *Usp. Fiz. Nauk*; **162**, pp 89 - 128 (1992).

17: M. E. Kuruzar and B. D. Cullity; *Internat. Journ. Magnetism* **1**, pp 323 - 325 (1971).

18: R. B. Thompson; *IEEE Trans Sonics and Ultrasonics* **SU-25**, pp 7 - 15 (1978).

19: H. L. M. Bakker; *Mat. Sci. and Tech.* **5**, pp 1135 - 1139 (1989).

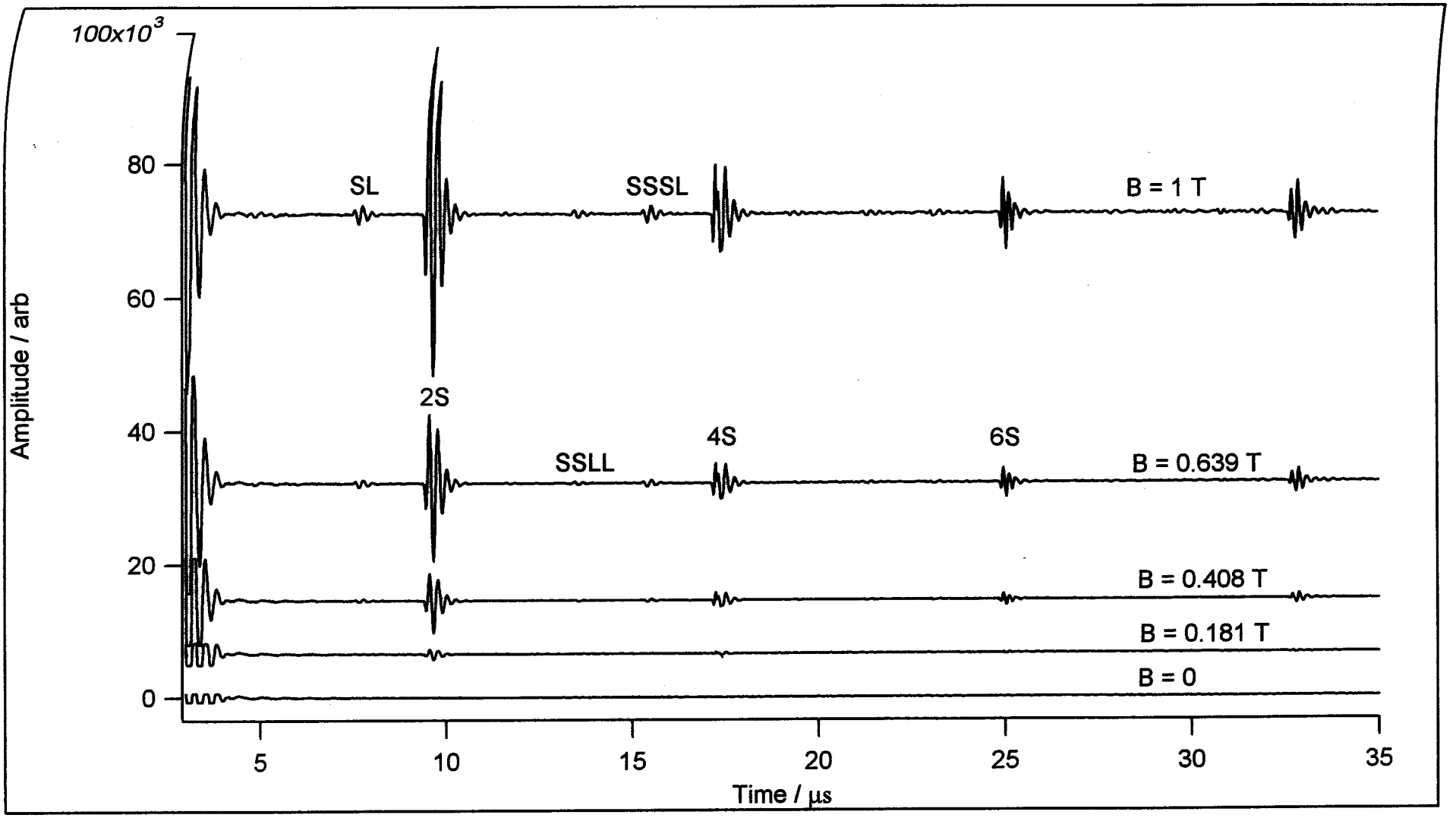

Figure 4.1: EMAT traces recorded on aluminium alloy between 0 and 1T

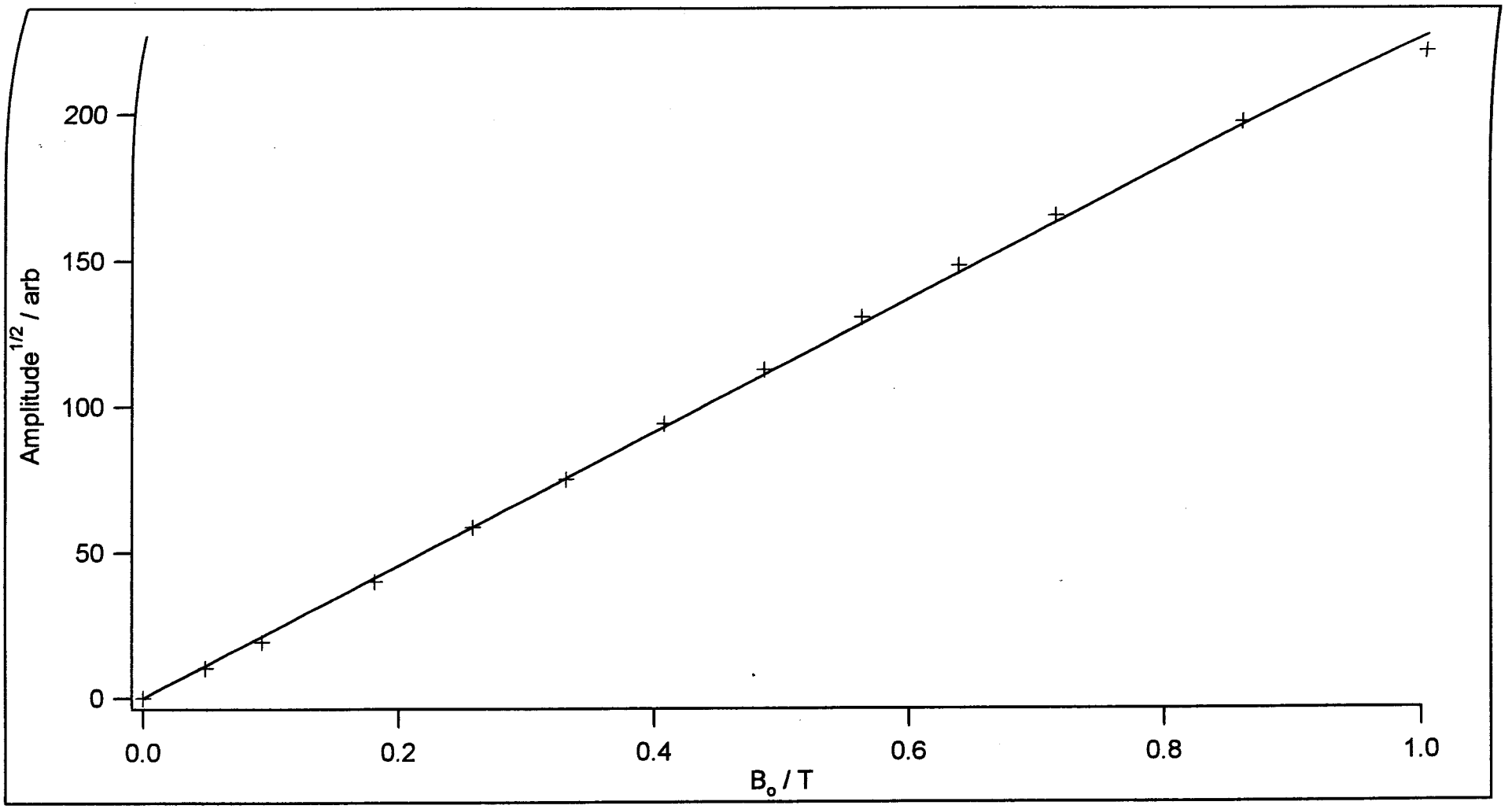

Figure 4.2: Amplitude$^{1/2}$ vs B_o for EMAT on aluminium alloy

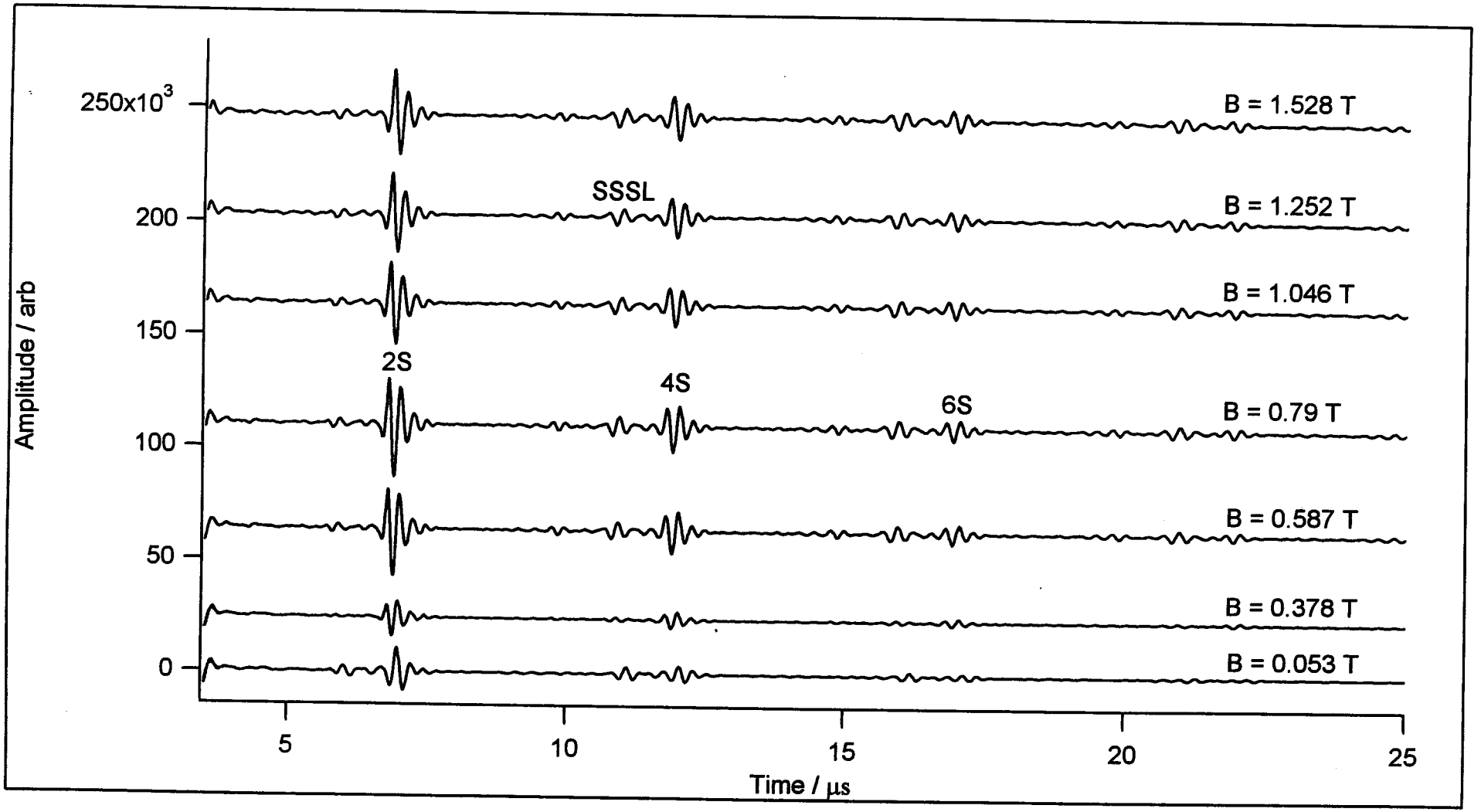

Figure 4.3: EMAT traces from pure nickel between 0.05 and 1.53T

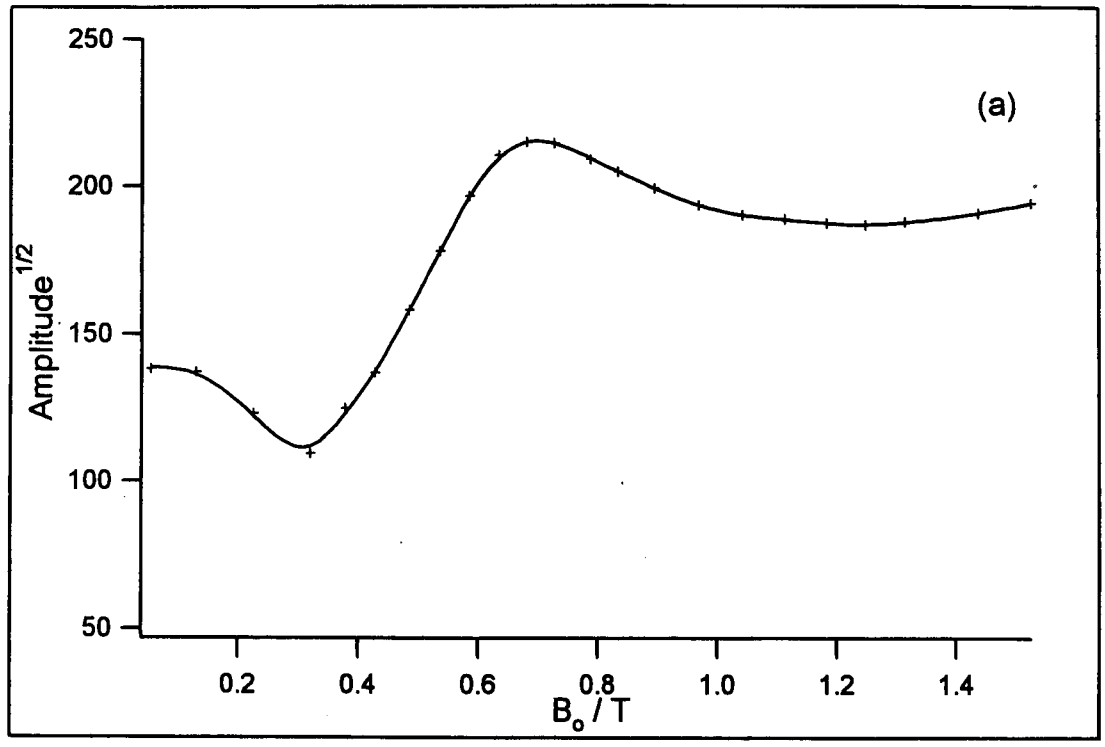

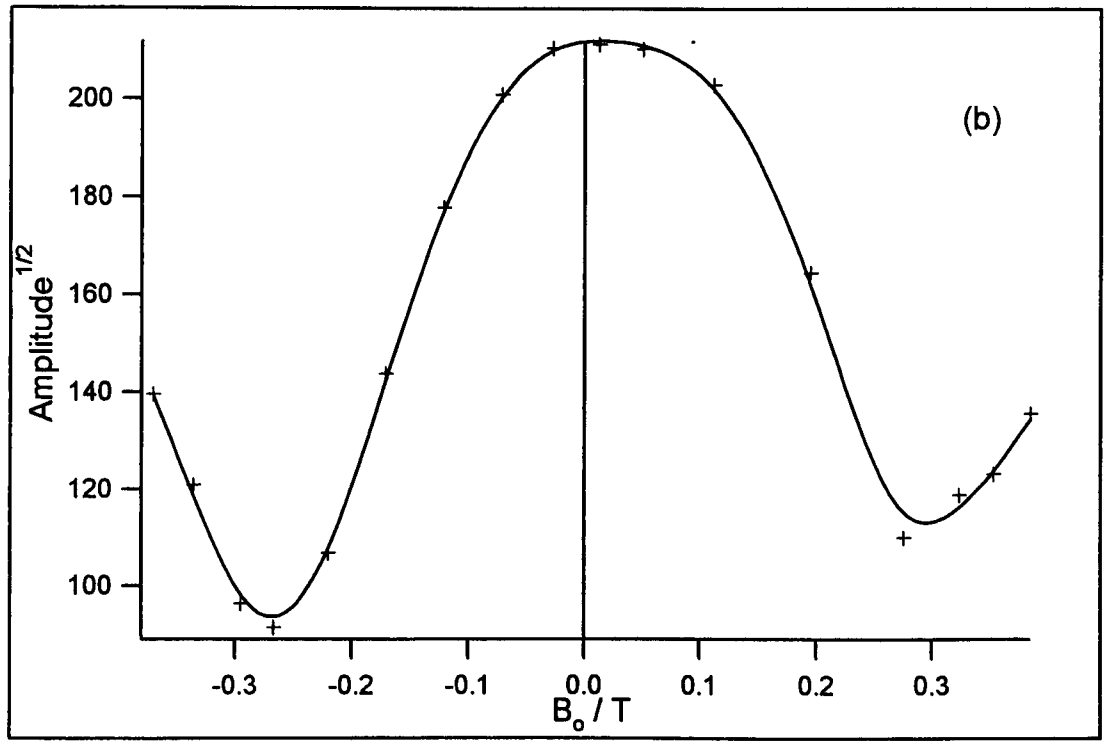

Figure 4.4: (a) 4S amplitude$^{1/2}$ vs B_o for EMAT on nickel
(b) Zoom of B_o dependence between -0.4 and 0.4T

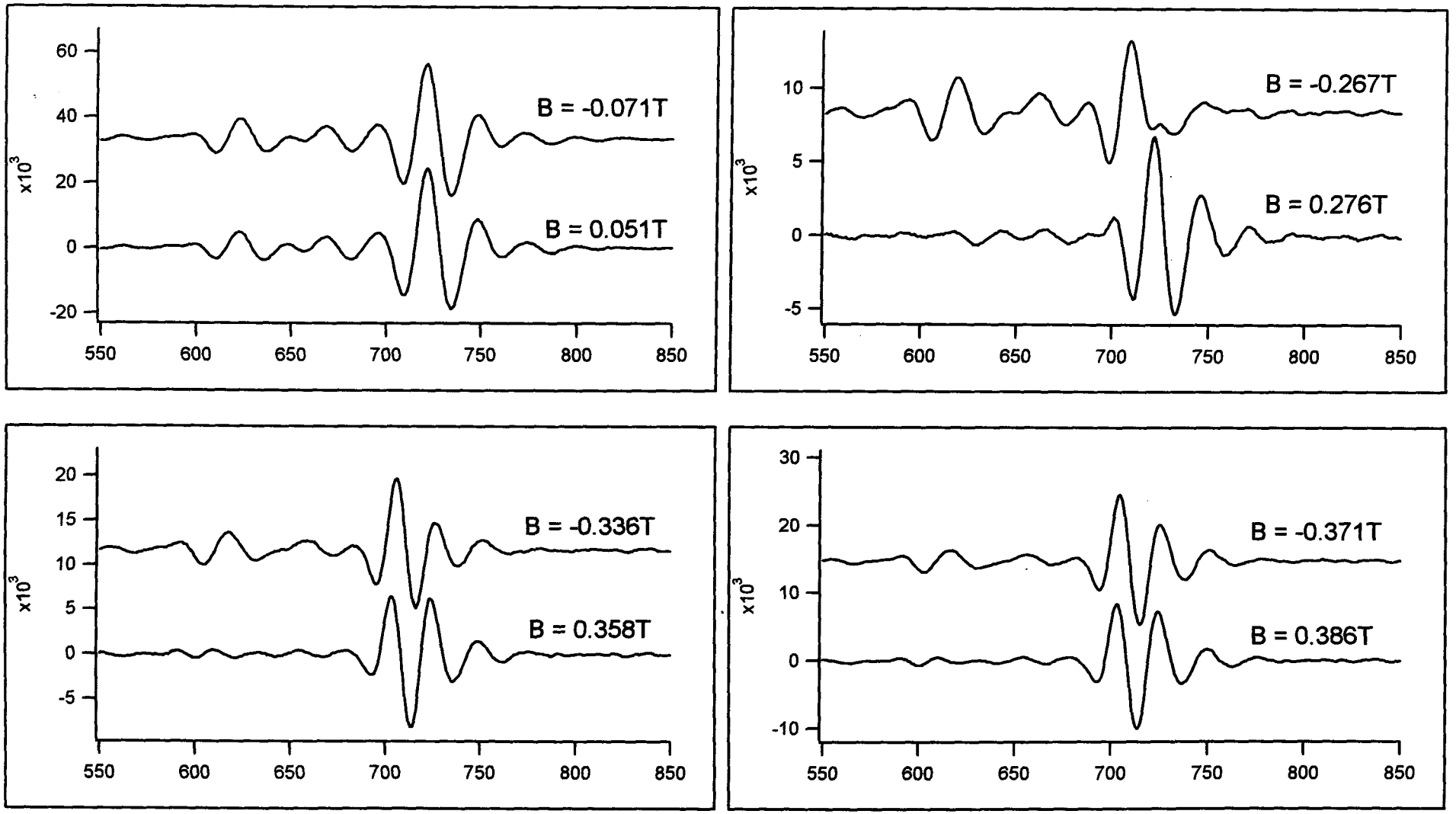

Figure 4.5: Zoom of the 2S echo with B_o in 'positive' and 'negative' directions

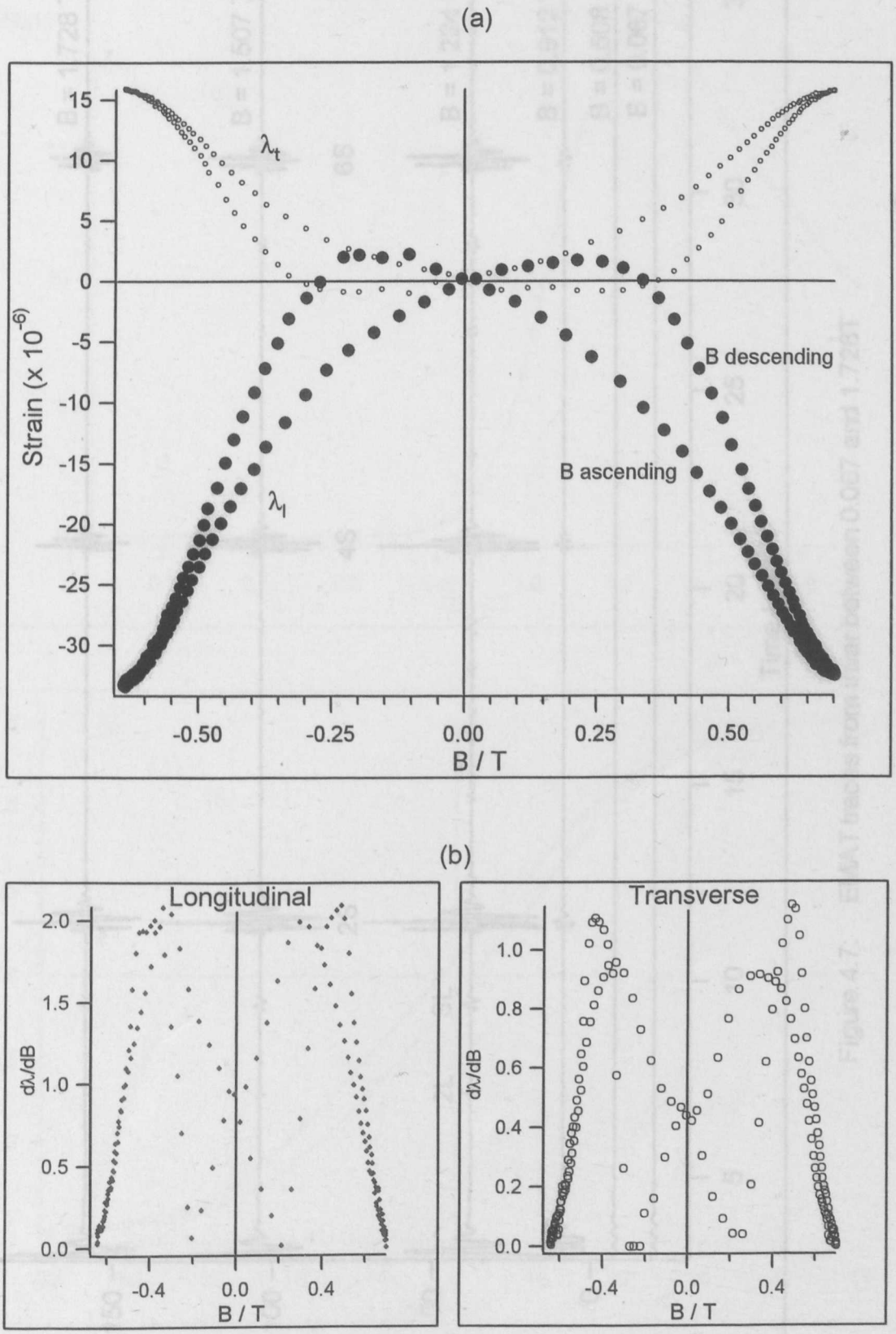

Figure 4.6: (a) Magnetostriction of pure nickel
(b) dλ/dB of pure nickel

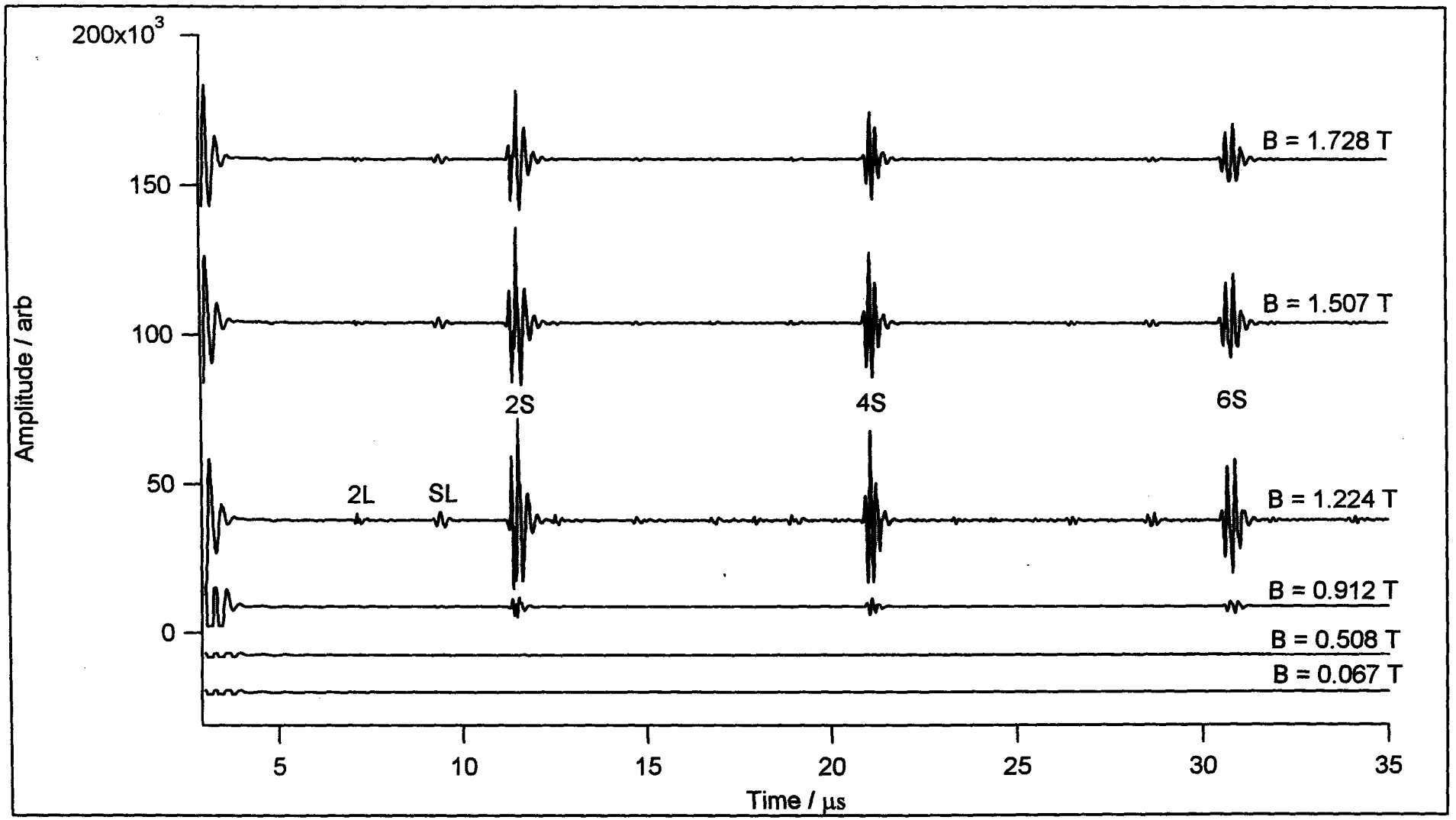

Figure 4.7: EMAT traces from invar between 0.067 and 1.728T

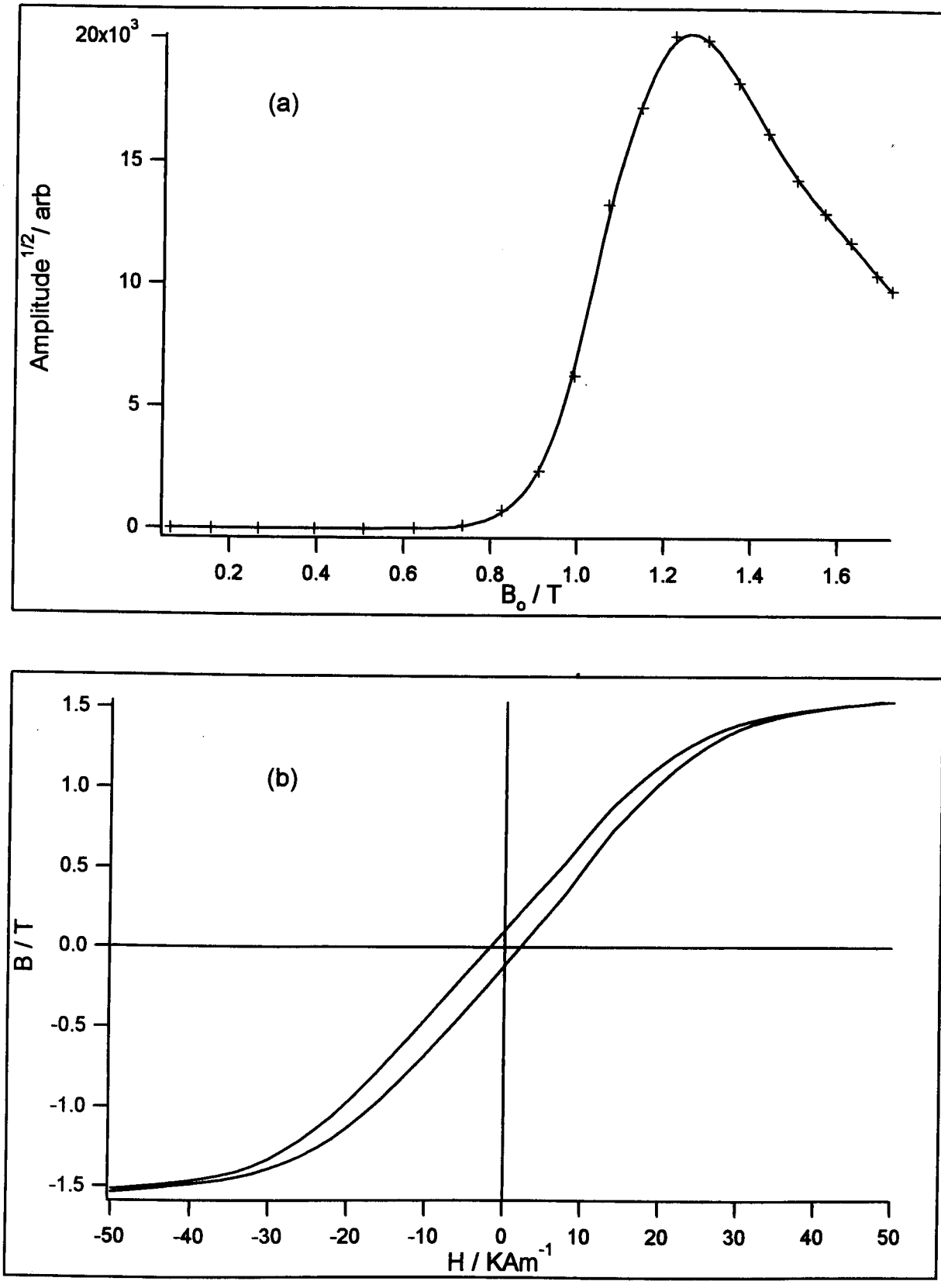

Figure 4.8: (a) Shear amplitude$^{1/2}$ vs B_o for EMAT on invar
(b) B - H loop of invar

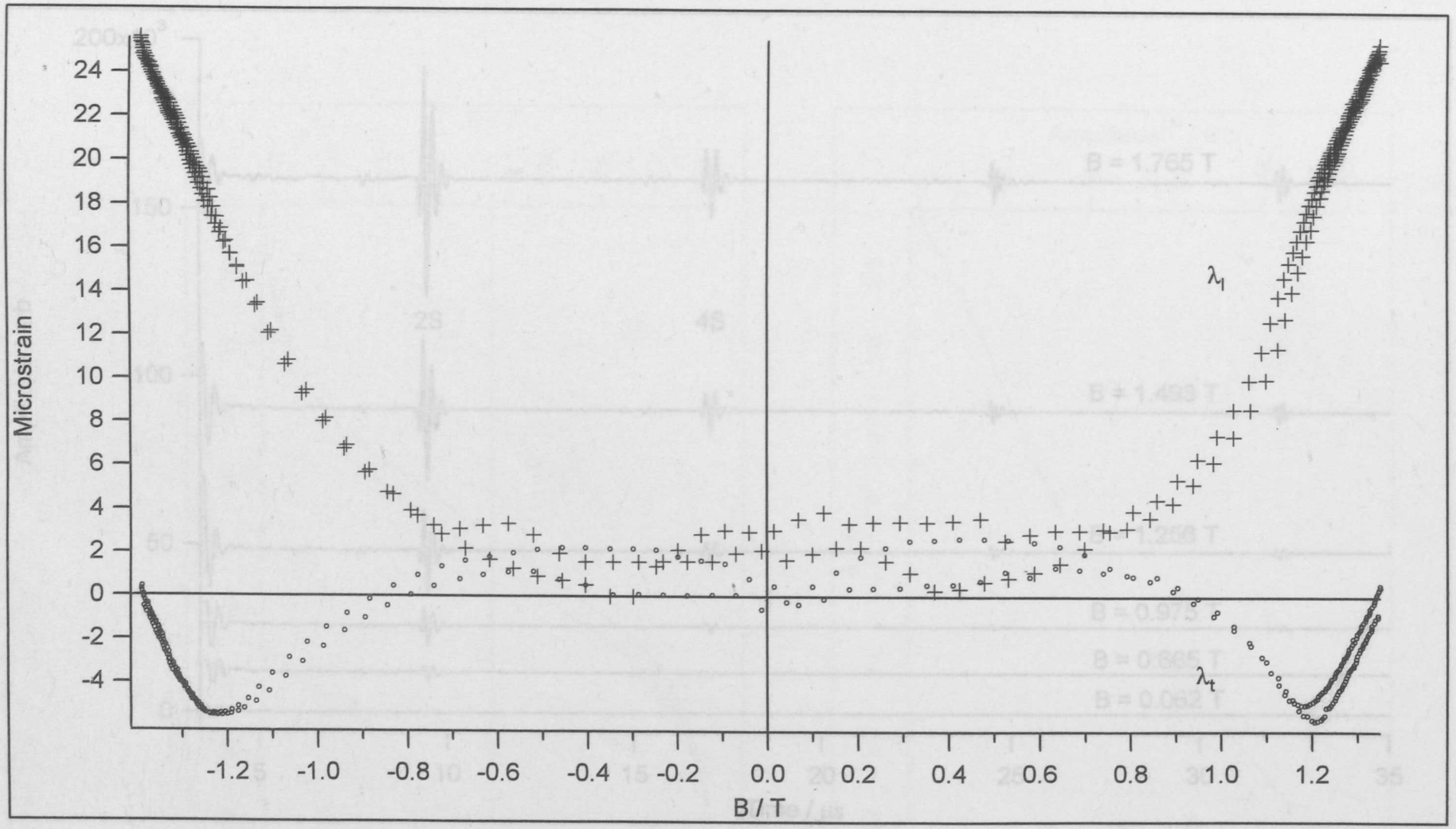

Figure 4.9: The magnetostriction of invar

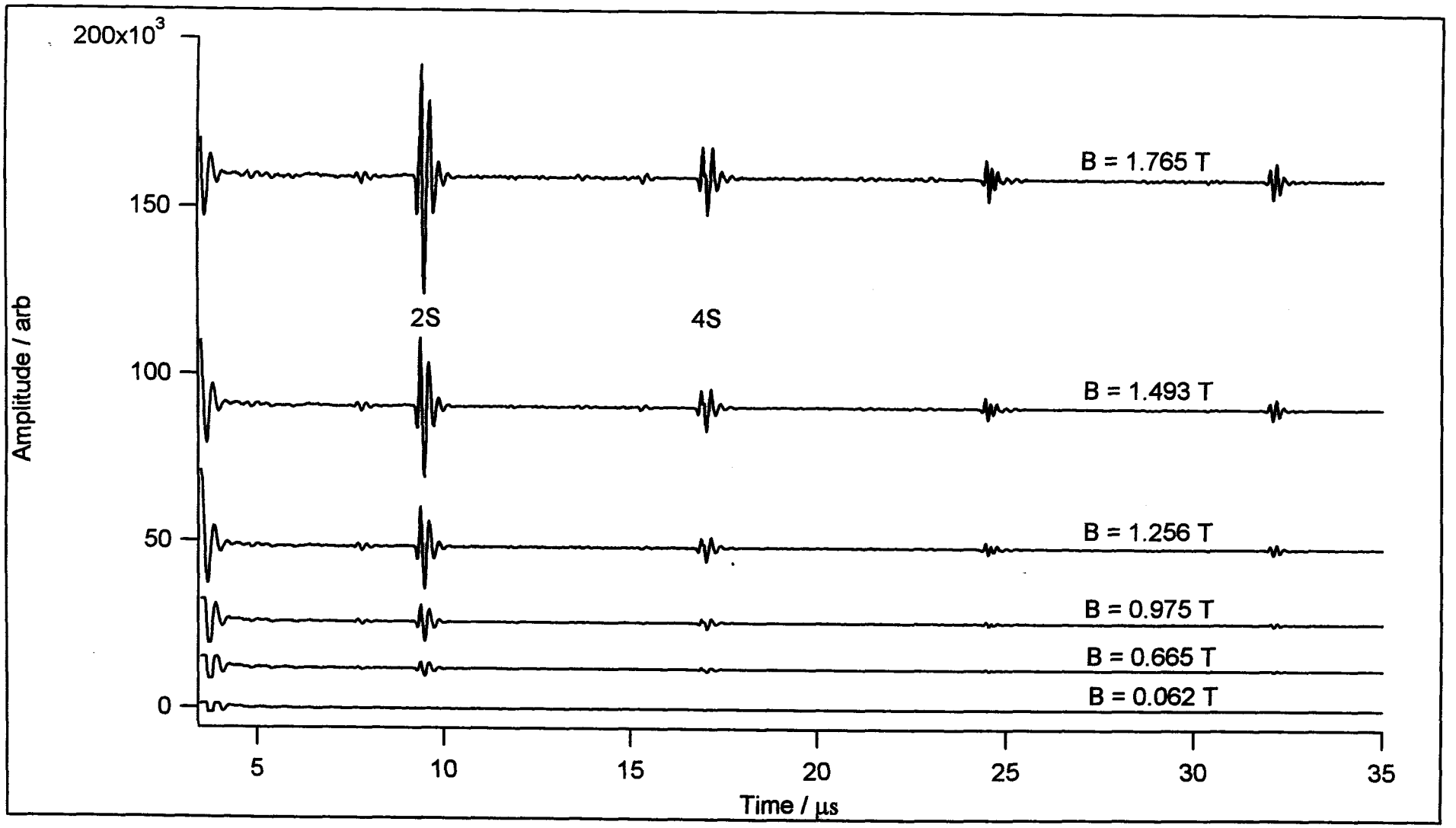

Figure 4.10: EMAT traces on mild steel between 0.062 and 1.785T

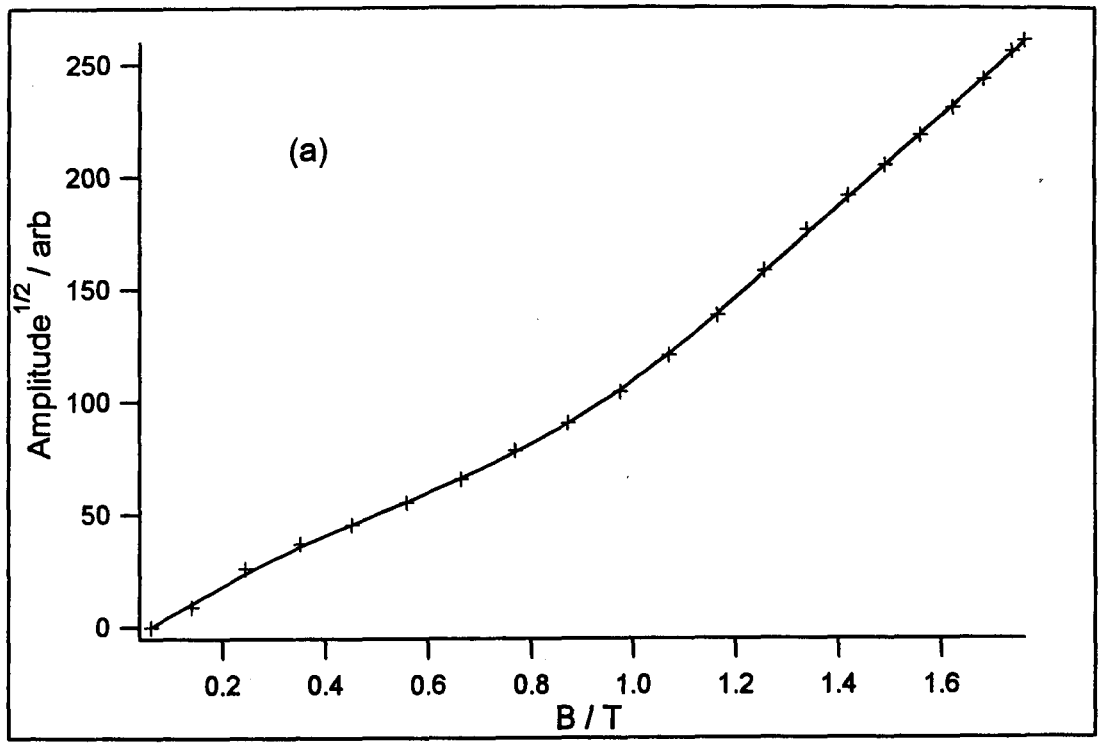

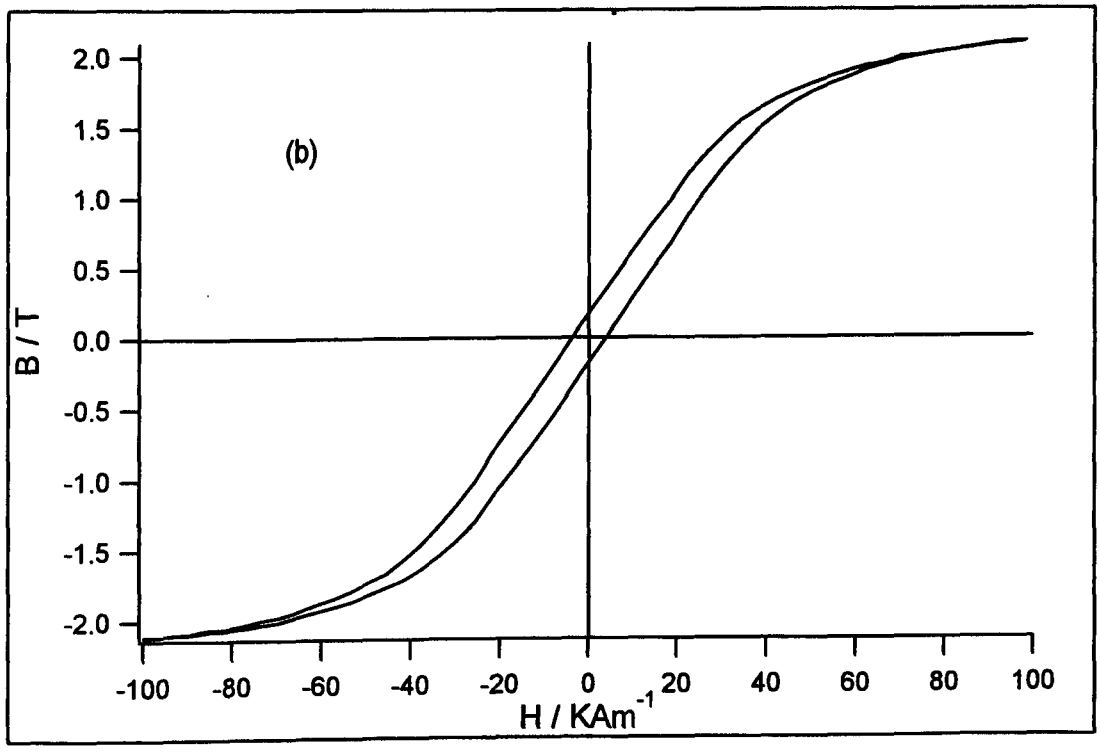

Figure 4.11: (a) Amplitude$^{1/2}$ vs B_o for EMAT on mild steel
(b) B - H loop of mild steel

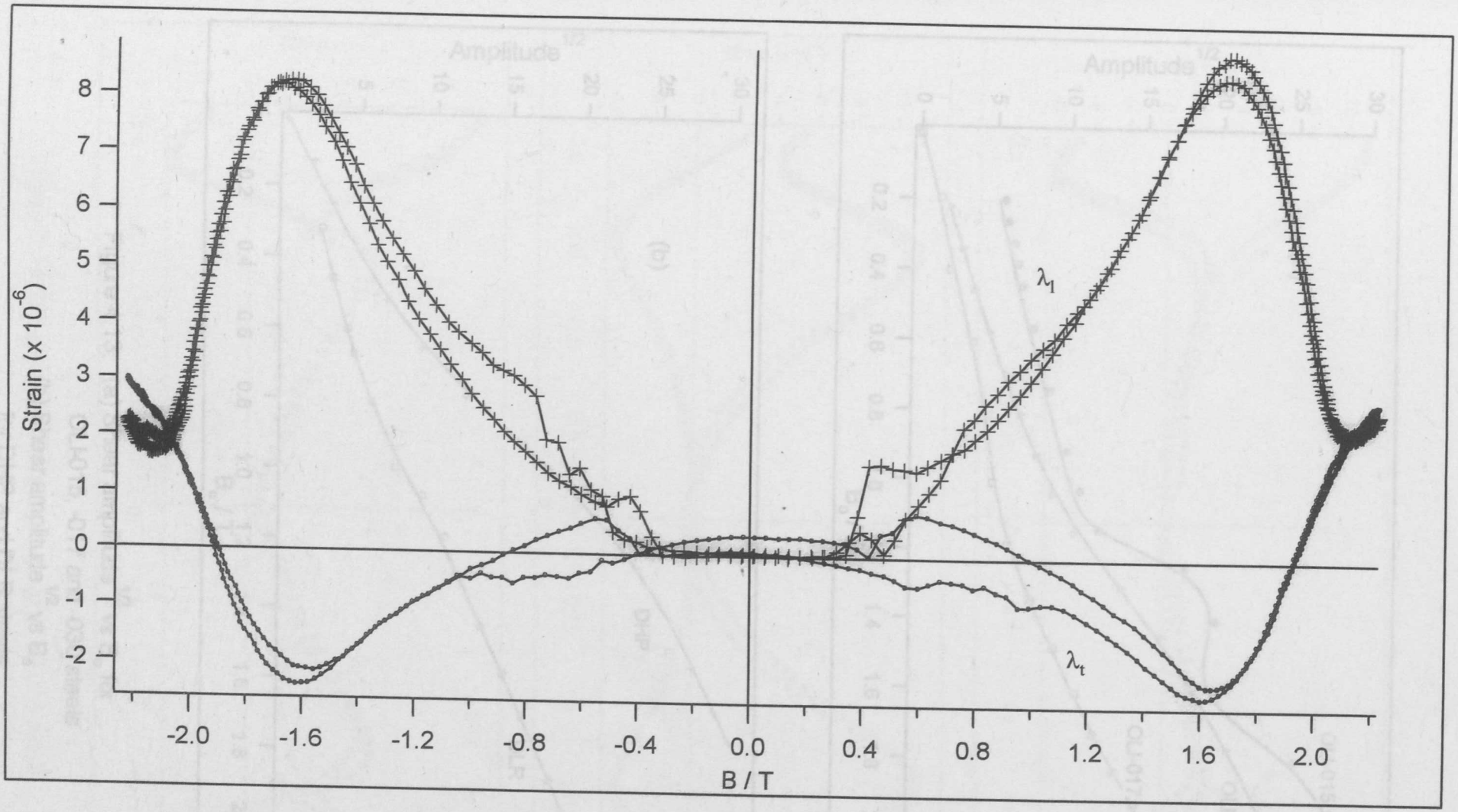

Figure 4.12: The magnetostriction of mild steel

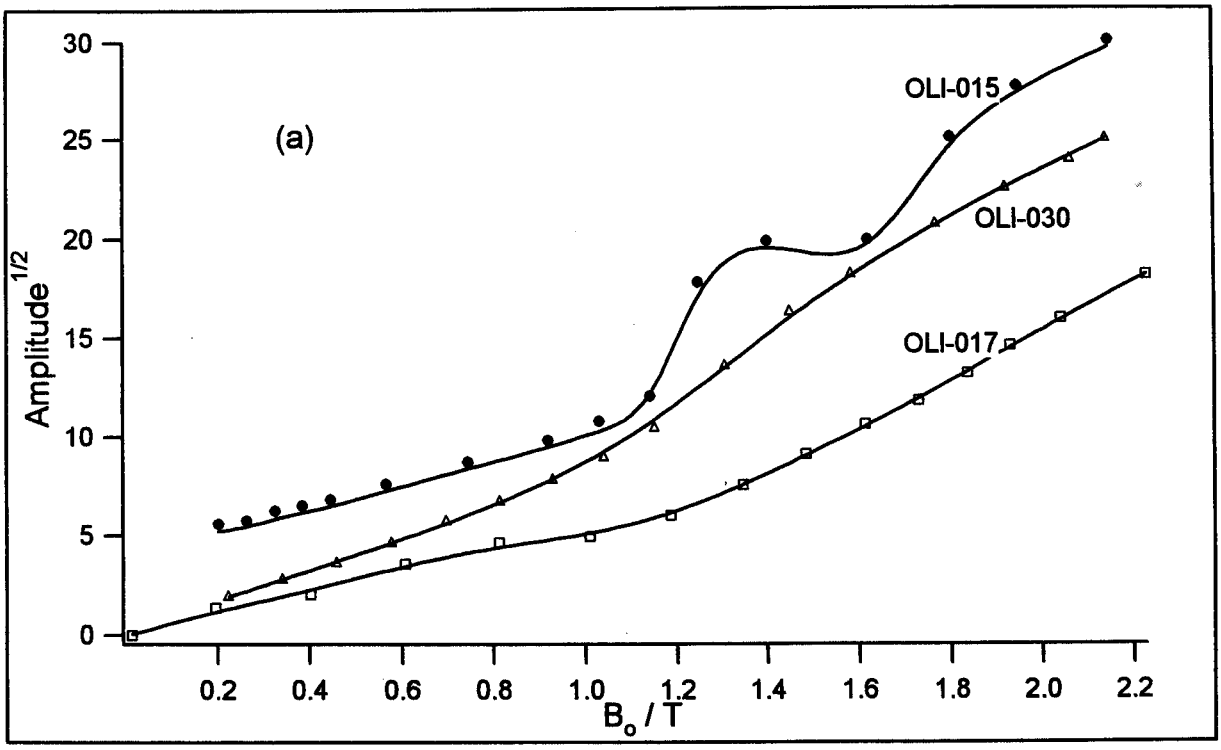

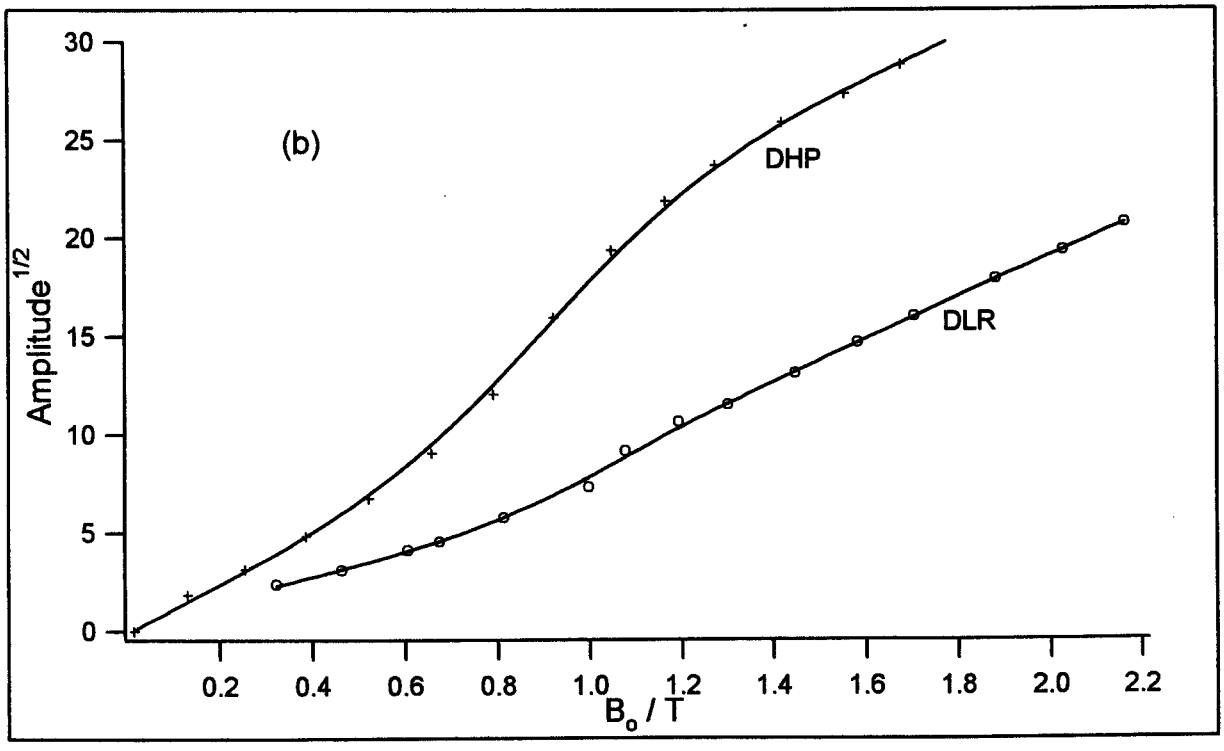

Figure 4.13: (a) Shear amplitude$^{1/2}$ vs B_o for OLI-015, -017 and -030 steels
(b) Shear amplitude$^{1/2}$ vs B_o for DHP and DLR steels

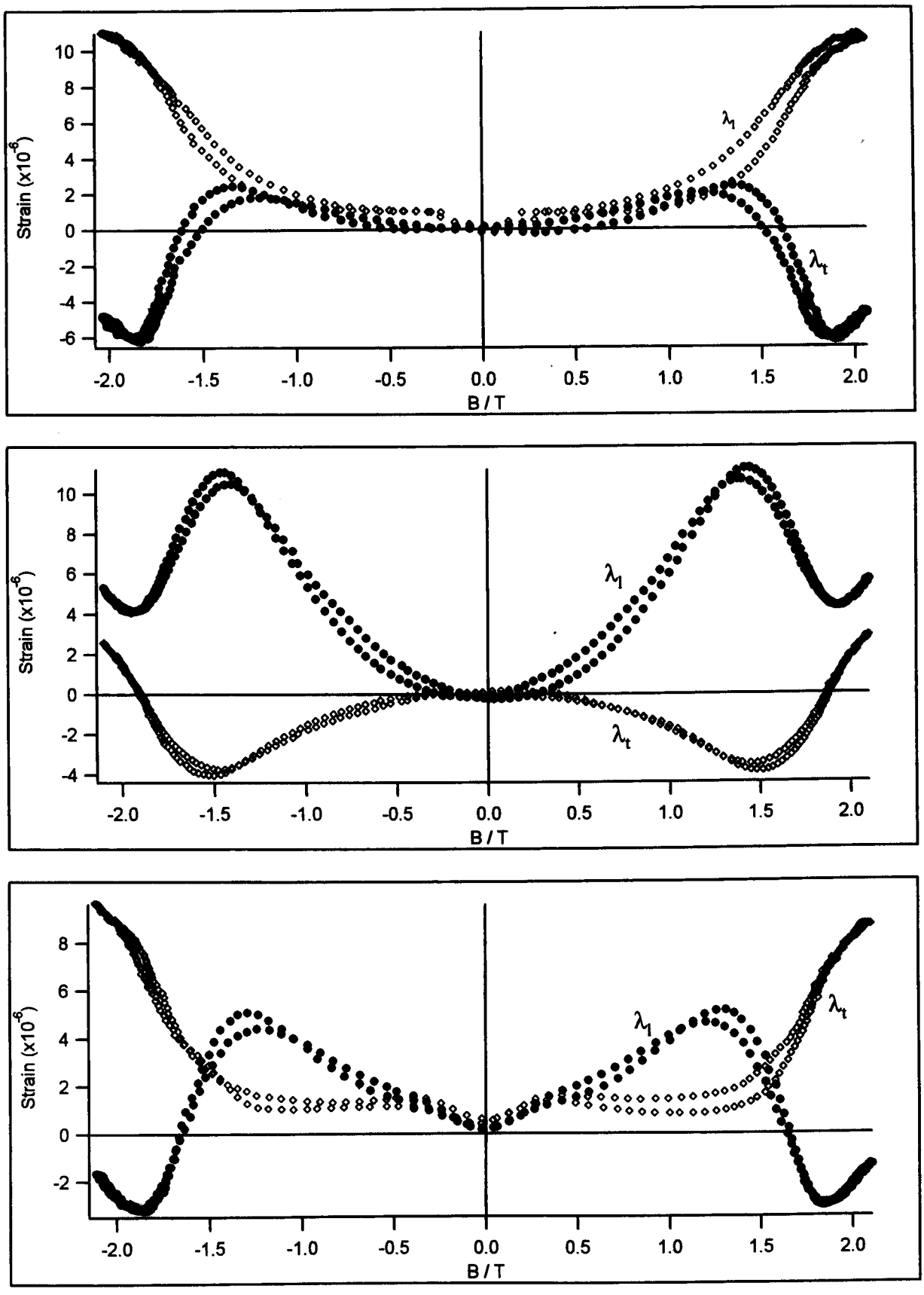

Figure 4.14: Magnetostriction curves for (a): OLI-015 steel
(b): OLI-017 steel
(c): OLI-030 steel

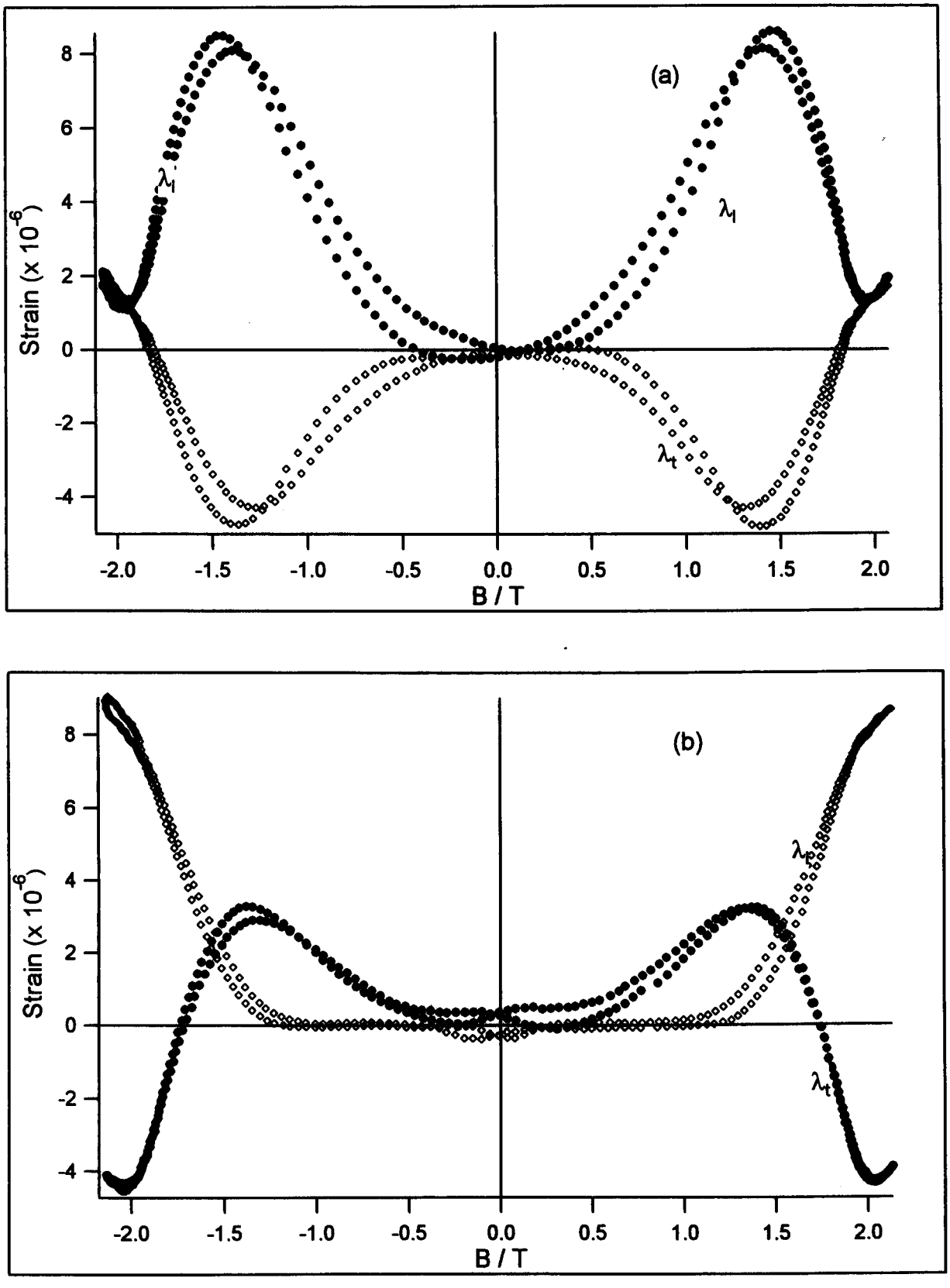

Figure 4.15: Magnetostriction of (a) DHP and (b) DLR steels

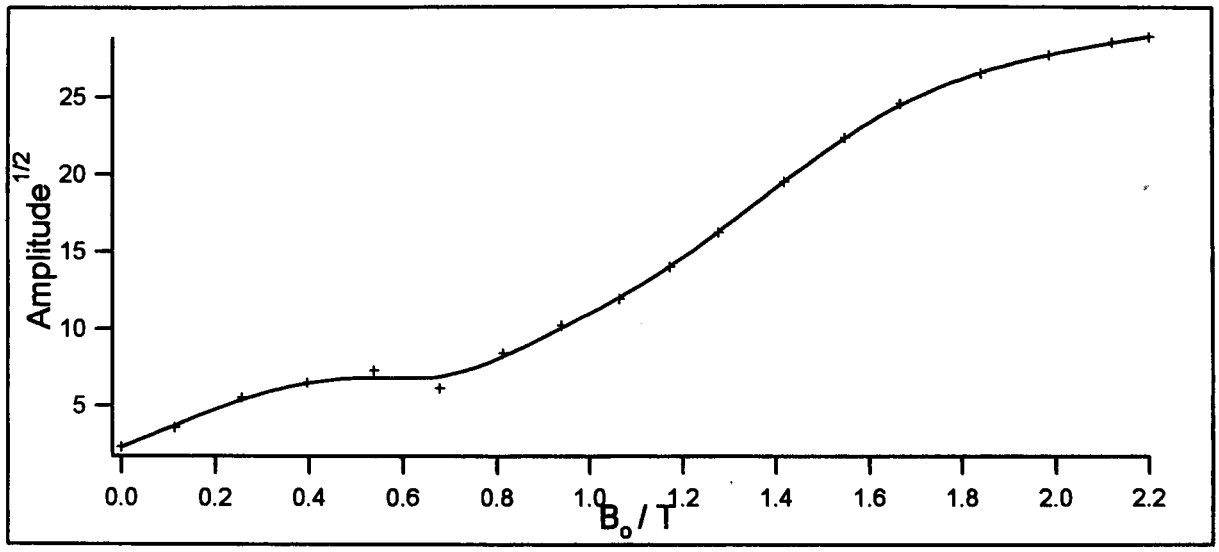

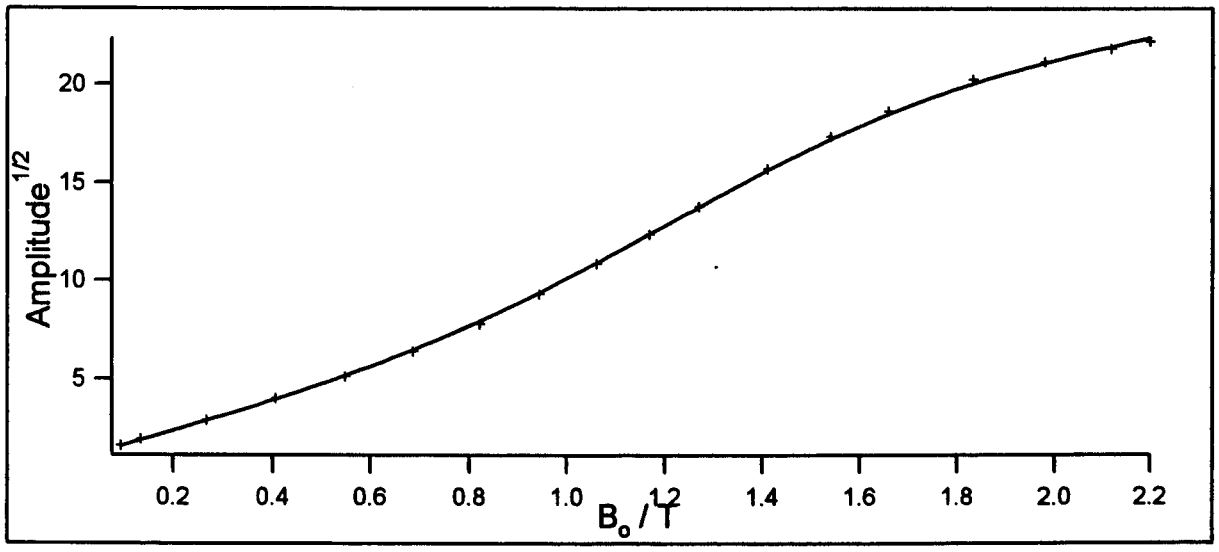

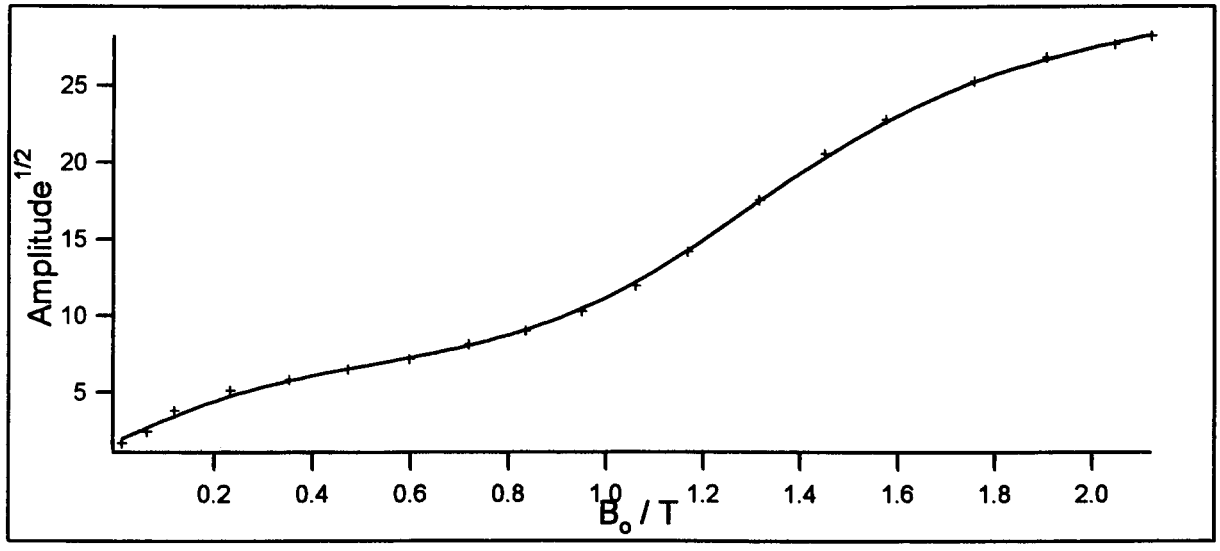

Figure 4.16: Shear amplitude$^{1/2}$ vs B_o for (a): Ductile iron
(b): Pit cast iron
(c): Spun cast iron

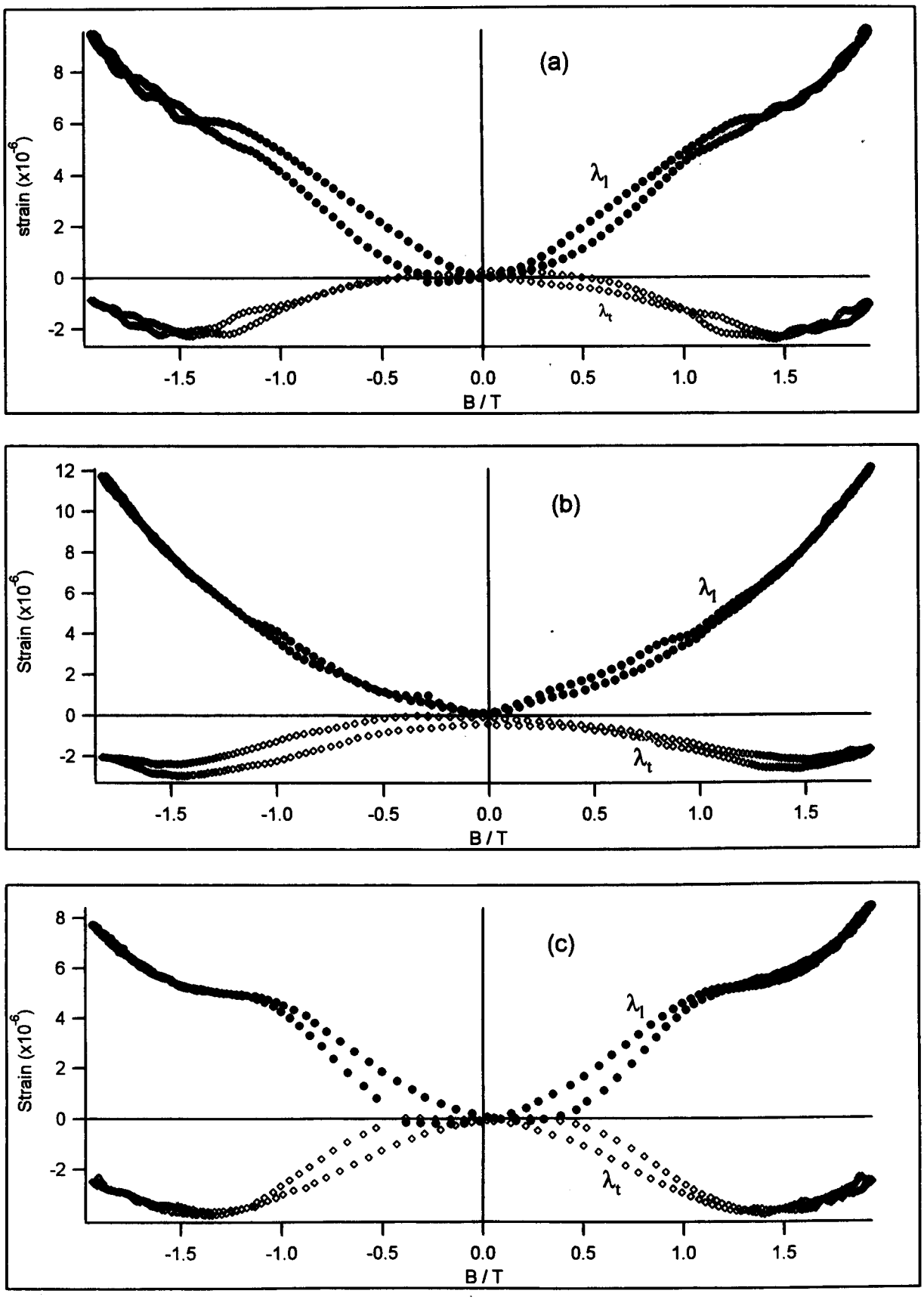

Figure 4.17: Magnetostriction curves for (a): Ductile iron
(b): Pit cast iron
(c): Spun cast iron

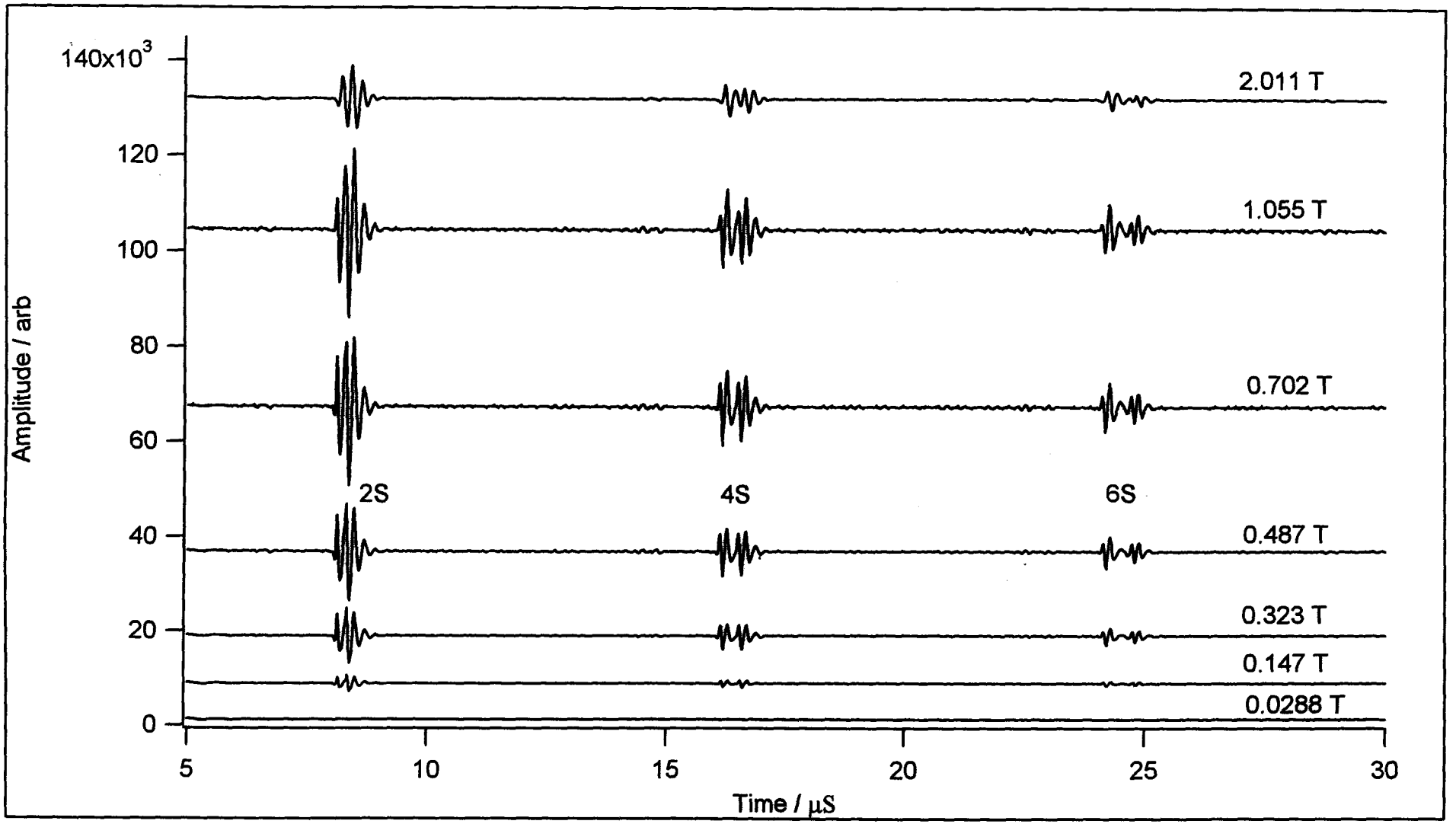

Figure 4.18: EMAT traces from British Gas supplied duplex between 0.028 and 2.011T

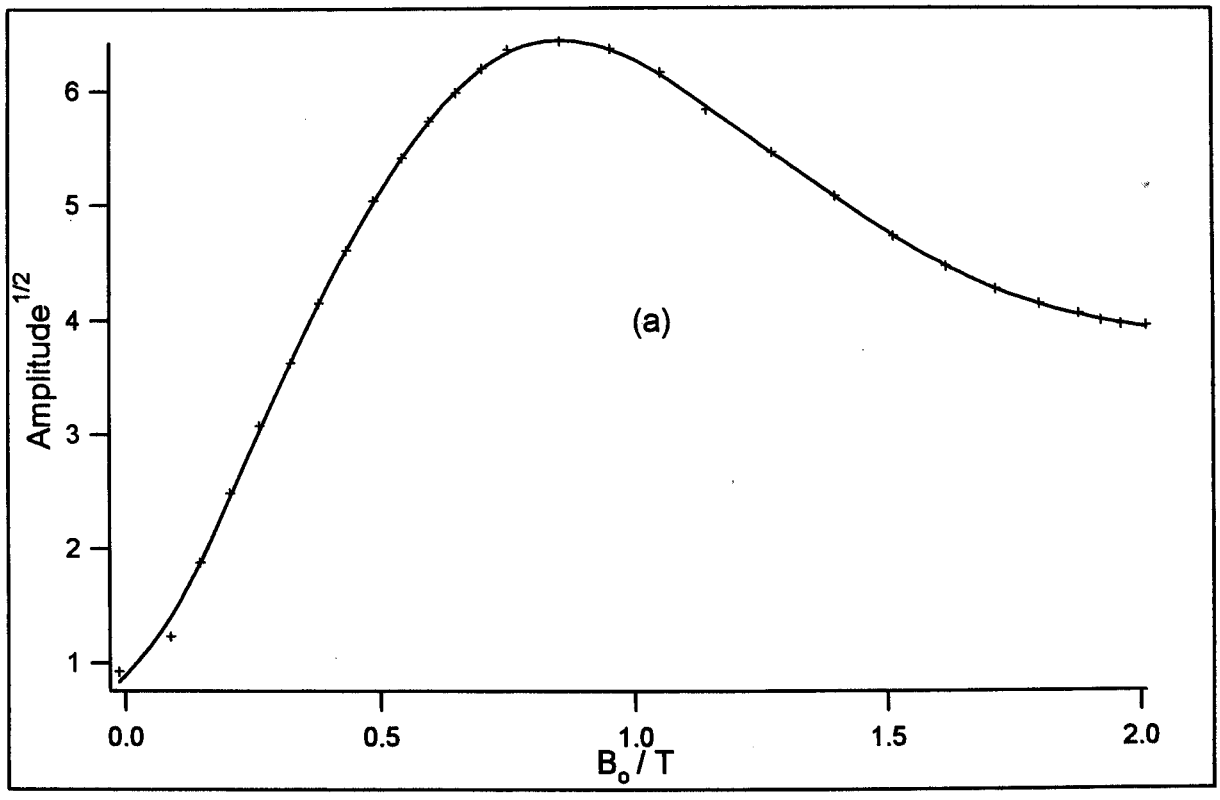

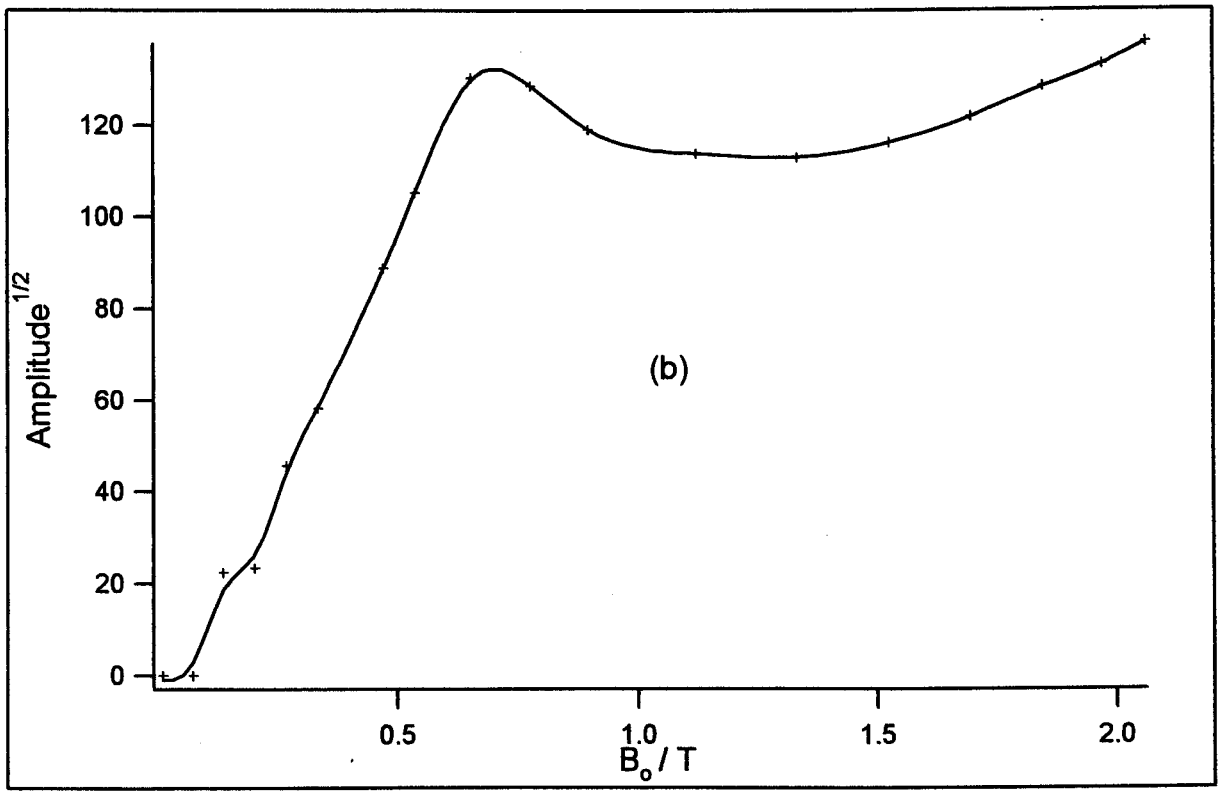

Figure 19: Shear amplitude$^{1/2}$ vs B_o for EMAT on
(a) British Gas supplied duplex
(b) British Steel supplied duplex

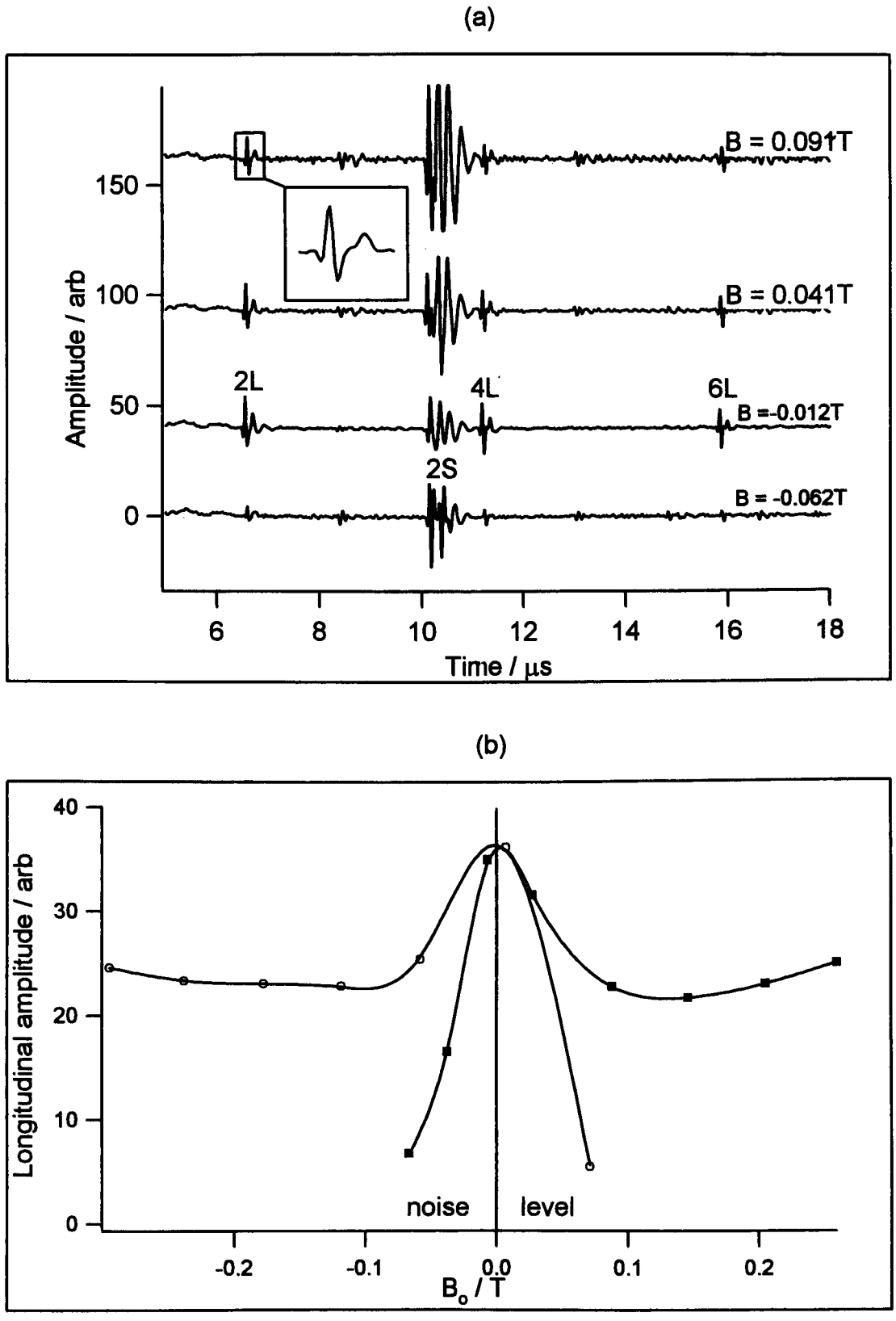

Figure 4.20: (a) EMAT traces from British Gas supplied duplex in low B_o showing anomalous L mode generation
(b) B_o dependence of L amplitude with coil pulsed in alternate senses

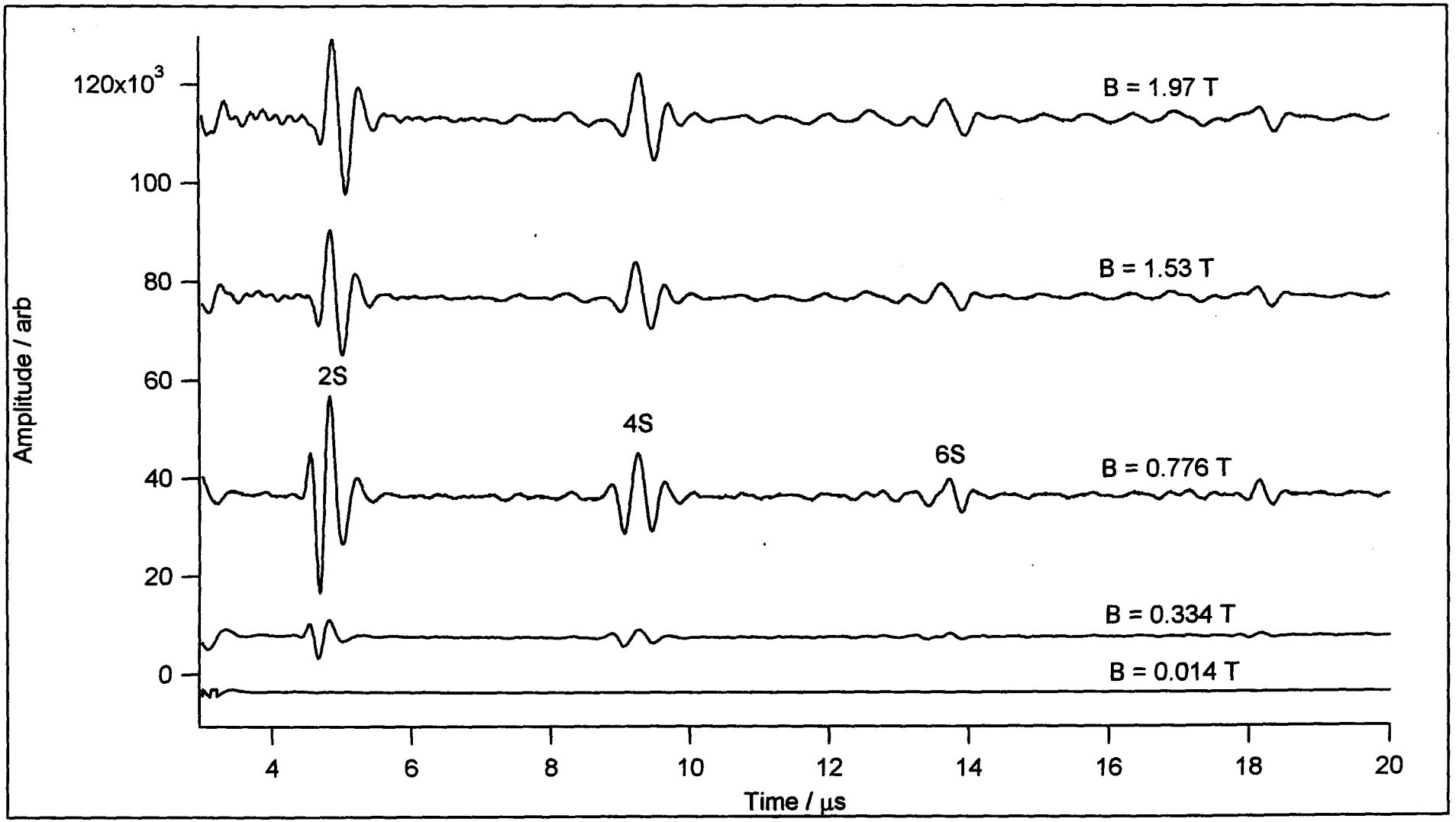

Figure 4.21: EMAT traces from British Steel supplied duplex

(a)

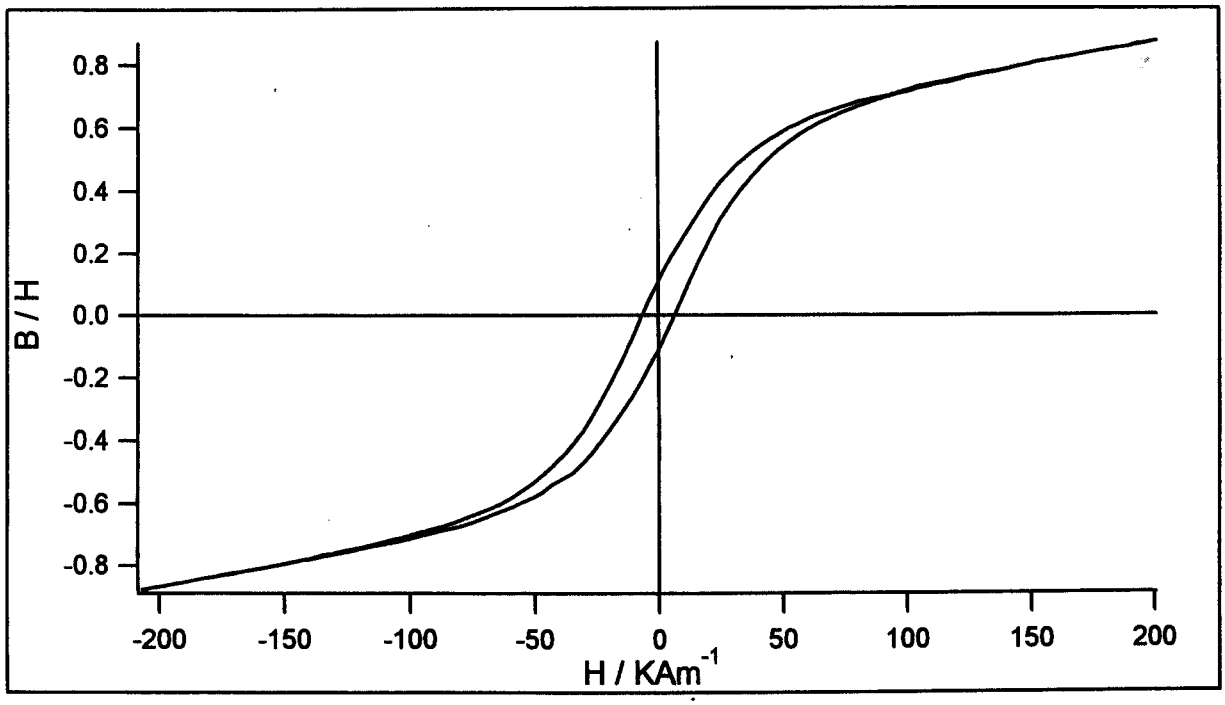

(b)

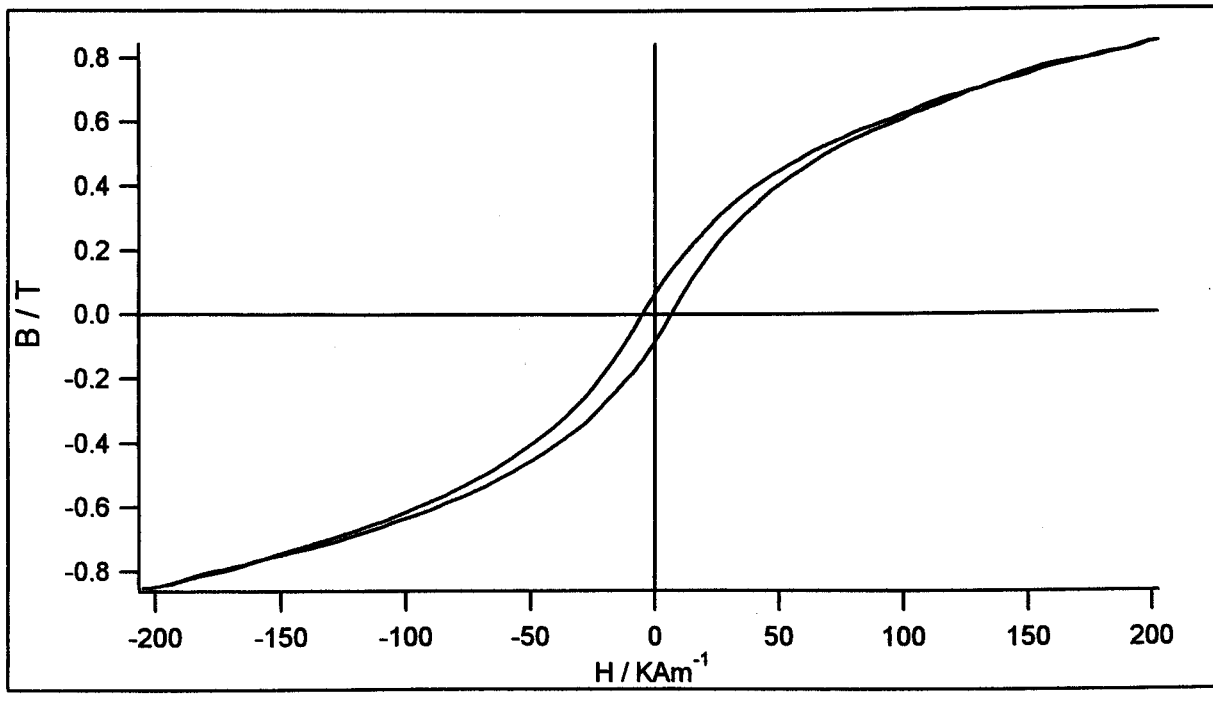

Figure 4.22: B-H loops for duplex steels; (a) British Gas supplied
(b) British Steel supplied

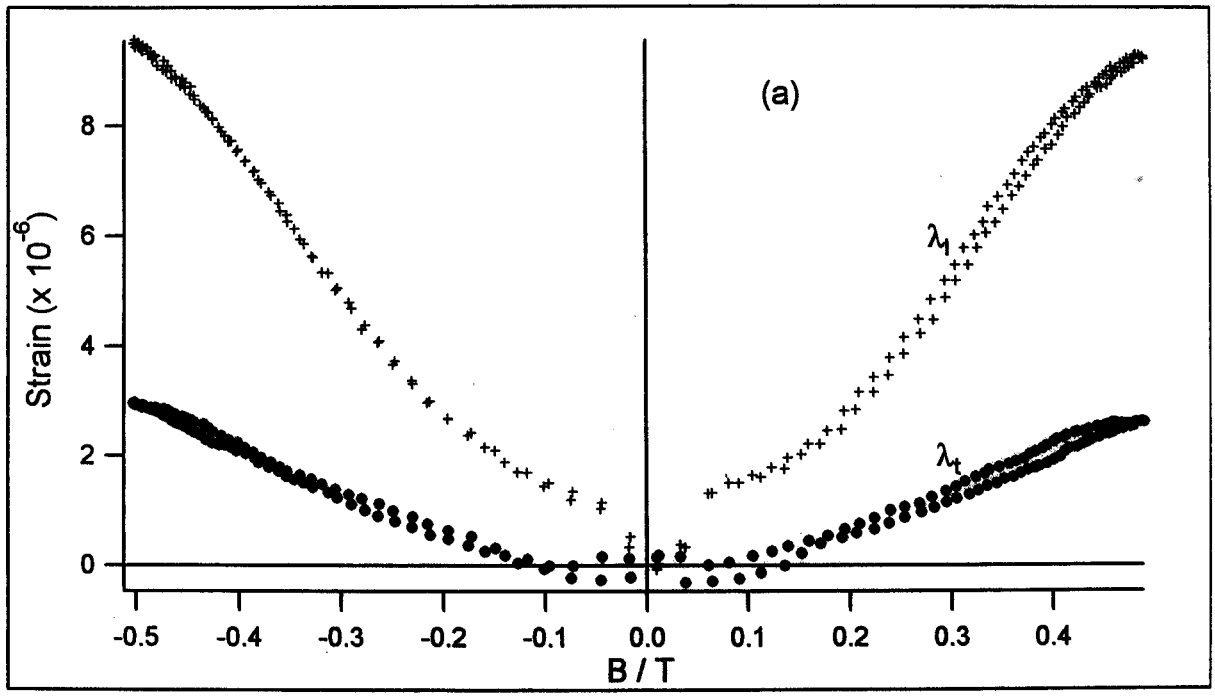

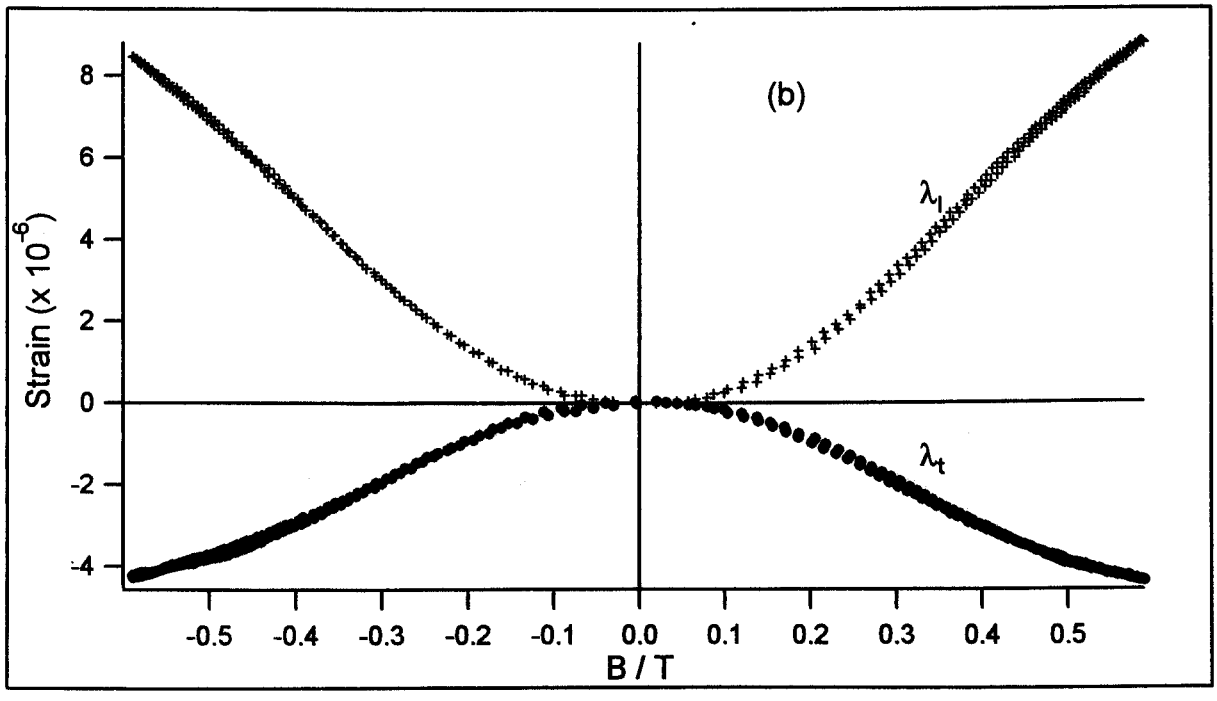

Figure 4.23: Magnetostriction of duplexes; (a) British Gas supplied
(b) British Steel supplied

(a) x 200

(b) x 400

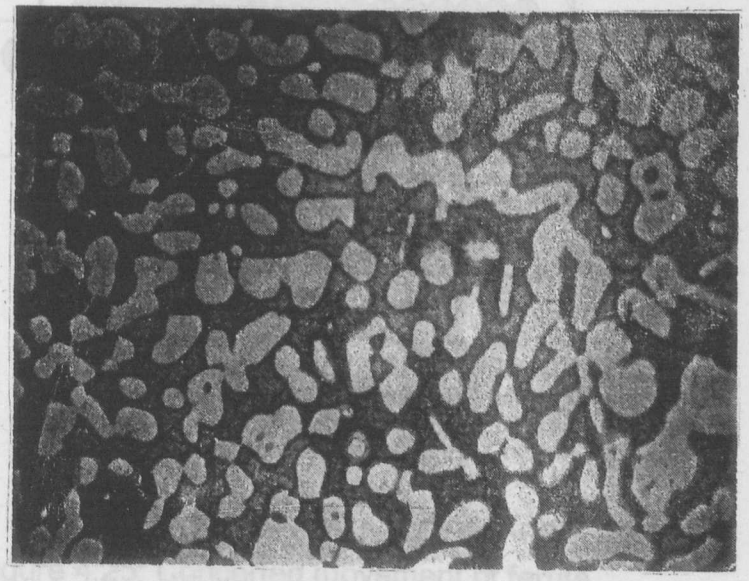

Figure 4.24: Metallographs of (a) British Gas supplied duplex and (b) British Steel supplied duplex.

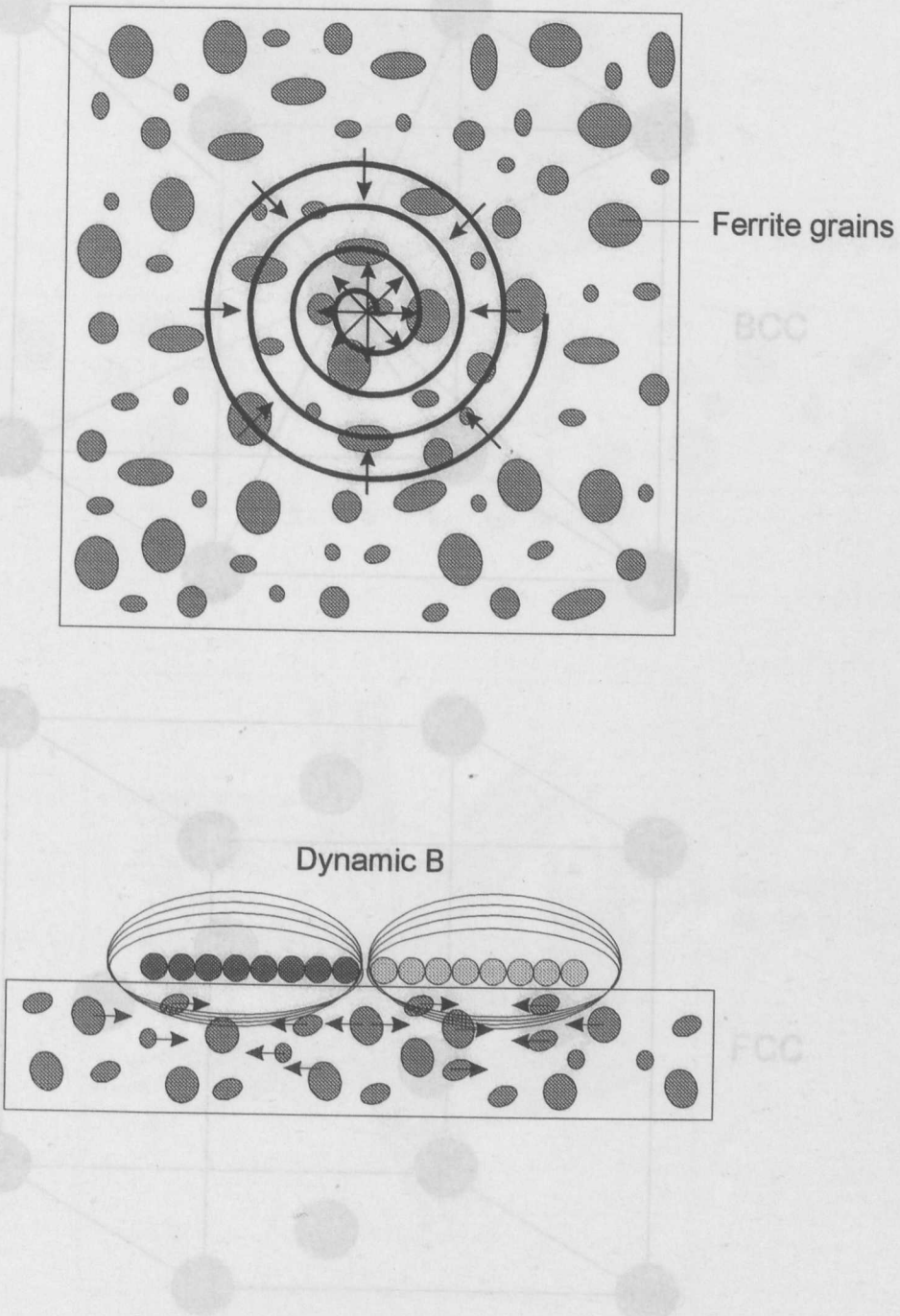

Figure 4.25: Concerted movement of ferrite grains due to radial dynamic field

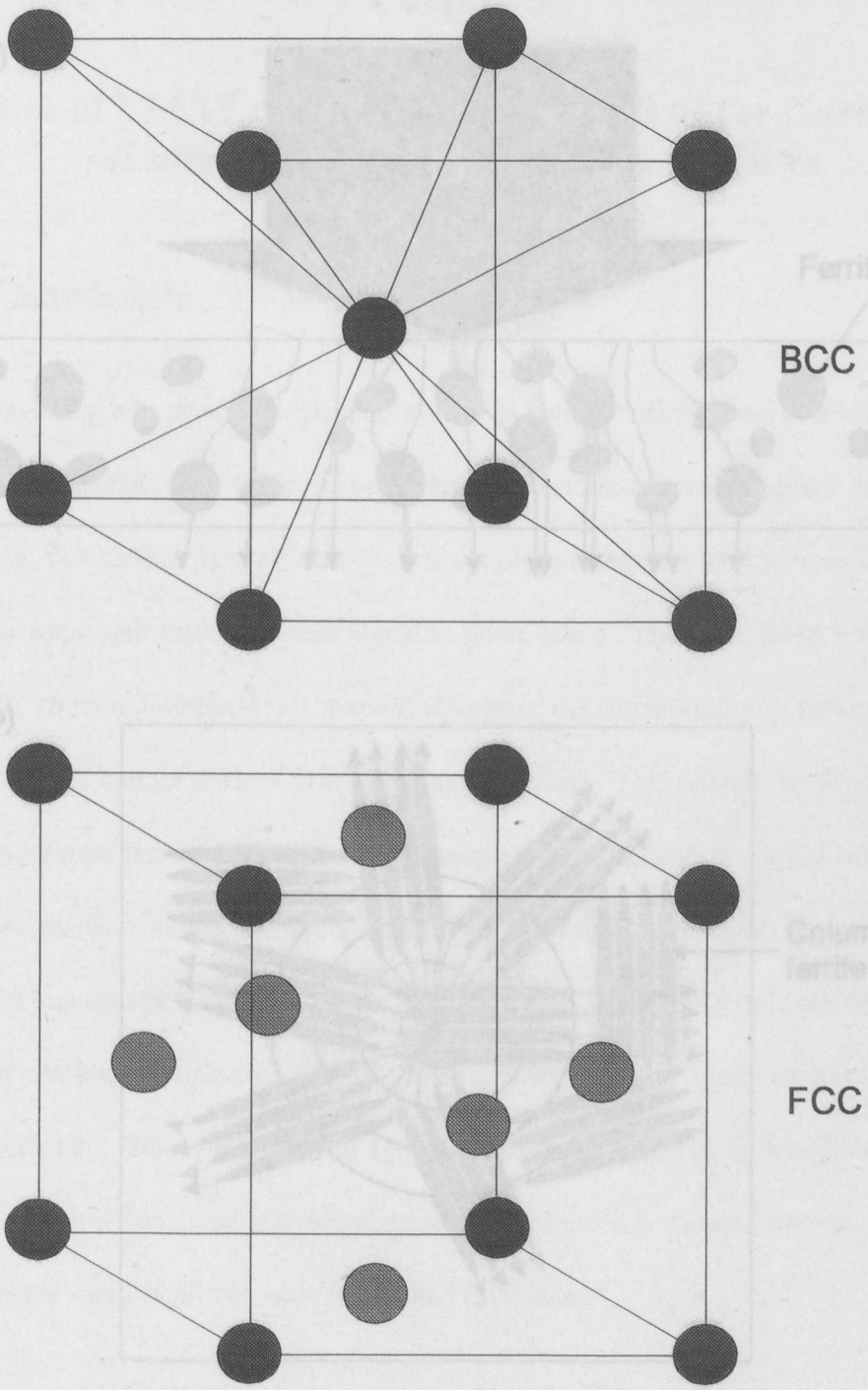

Figure 4.26: Ferrite (BCC) and austenite (FCC) structures of iron. Volume change from BCC to FCC is ~ 3% and proposed to be a possible mechanism for ultrasound generation via a field induced phase change.

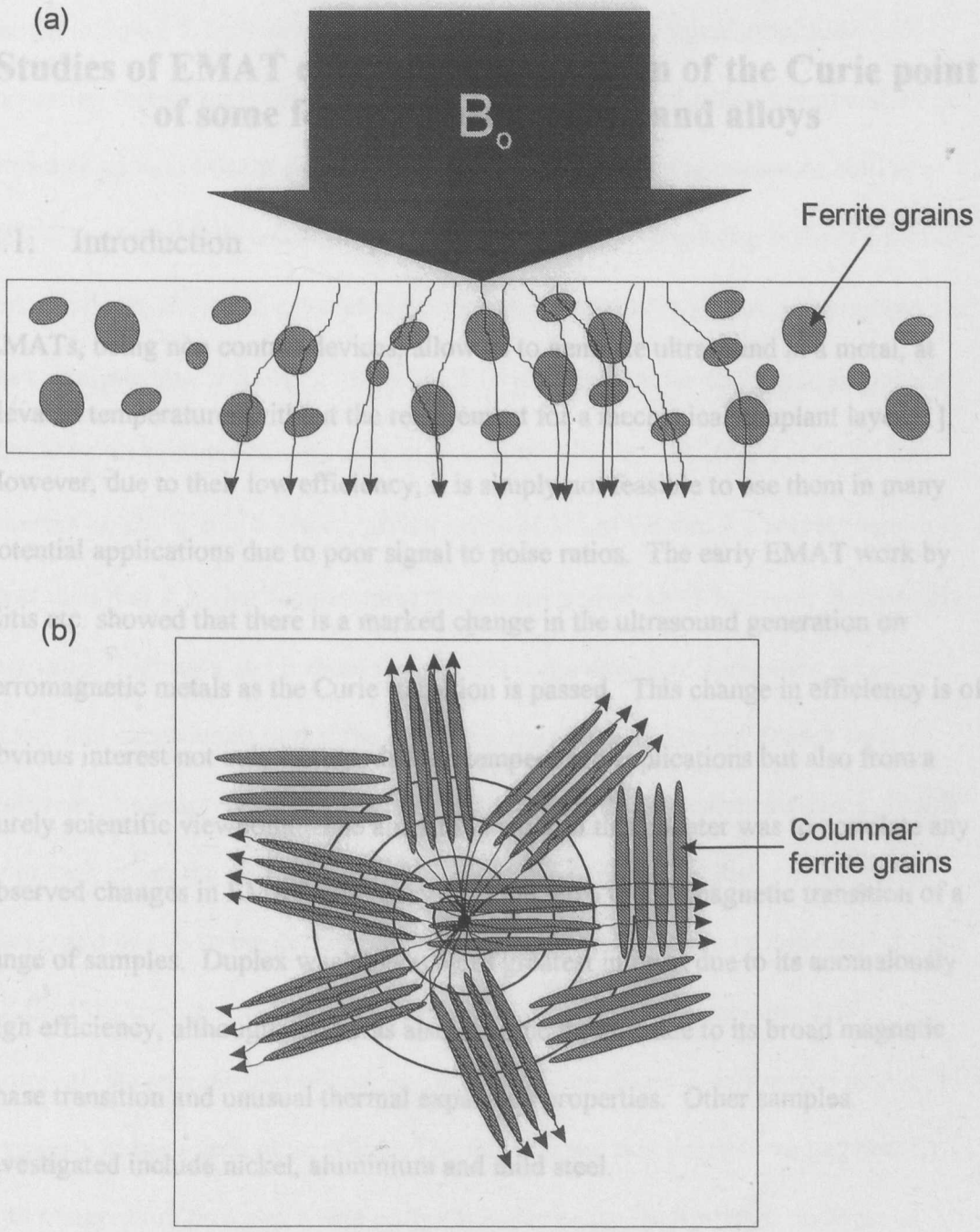

Figure 4.27: Potential for the focussing of both (a) the static B_o in duplex two phase structure and (b) the radial dynamic field in the locally orientated British Gas supplied duplex.

Chapter 5

Studies of EMAT efficiency in the region of the Curie point of some ferromagnetic metals and alloys

5.1: Introduction

EMATs, being non contact devices, allow us to generate ultrasound in a metal, at elevated temperatures without the requirement for a mechanical couplant layer [1]. However, due to their low efficiency, it is simply not feasible to use them in many potential applications due to poor signal to noise ratios. The early EMAT work by Gitis etc. showed that there is a marked change in the ultrasound generation on ferromagnetic metals as the Curie transition is passed. This change in efficiency is of obvious interest not only as regards high temperature applications but also from a purely scientific viewpoint. The aim of the work in this chapter was to correlate any observed changes in EMAT efficiency with the ferro to paramagnetic transition of a range of samples. Duplex was obviously of greatest interest due to its anomalously high efficiency, although invar was also of some interest due to its broad magnetic phase transition and unusual thermal expansion properties. Other samples investigated include nickel, aluminium and mild steel.

5.2: Aluminium

The temperature dependence of the signal from aluminium was studied using the high temperature EMAT system described in chapter 3. The sample was 12.76 mm thick and produced the room temperature EMAT trace shown at the bottom of figure 5.1. The echoes are similar in form to those shown in chapter 4, the only difference

being due to the different EMAT used. EMAT traces at higher temperatures are also shown in figure 5.1, these exhibit a consistent decrease in signal amplitude with increasing temperature. Figure 5.2a is a plot of the 2S amplitude vs temperature, it shows an apparent linear decrease in signal with increasing temperature until at ~ 420^{O}C the signal falls below the noise level. The lower graph (fig 5.2b) is a plot of the skin depth at 5MHz, calculated from quoted values of σ [2], vs. temperature, and the corresponding $1/\sqrt{(1+\beta^2)}$. Equation 2.17 predicts that the ultrasonic amplitude should be proportional to this term in β, assuming $\lambda >> \delta$. At 20^{O}C δ is 0.066mm whereas at 420^{O}C it is 0.11mm, giving ratios of λ/δ of 9.8 and 5.1 respectively, it is clear then that at higher temperatures the assumption of $\lambda >> \delta$ becomes increasingly less valid. Figures a and b show that there is some degree of agreement between theory and experiment, in that the amplitude decreases and doesn't reach zero. However, the exact forms of the amplitude temperature dependence differ noticably from each other, the experimental data showing an apparently linear relationship. This could be due to the dependence of the detection efficiency on conductivity, the RF field the coil detects being proportional to σ according to equation 2.19. However, the introduction of conductivity simply produces a similar plot to 5.2b, ie: it appears to have little or no effect. The fact that the skin depth increases linearly with temperature provides a clue as to a possible cause for the linear decrease in signal amplitude. As mentioned by Buschelnikov, when dealing with a purely Lorentzian generator it is preferable to have as small a skin depth as possible. This leads to a larger eddy current density j and a correspondingly higher Lorentz force and therefore ultrasonic amplitude. It is clear that as a consequence a linear increase in skin depth should give rise to a linear decrease in Lorentz force, and amplitude, and therefore a linear decrease in the received signal, just as observed. It may appear

that this argument is in direct contradiction to that given earlier where it was suggested that efficiency is independent of σ when it is sufficiently high. However, that argument was for the case of $\lambda >> \delta$ which becomes increasingly invalid as the temperature increases. It is also important to remember that no account has been taken of the increasing similarity in the magnitudes of δ and λ_{us}, this being known to be an important factor in EMAT generation [3]. However, as this has not been theoretically modelled for a paramagnetic metal, as far as the author is aware, it is not known whether this could also be responsible for the observed linear signal decrease.

5.3: Nickel

Figure 5.3 shows the EMAT traces recorded on a 12.57mm thick sample of nickel between room temperature and 400^{O}C. They exhibit clear shear wave signals with smaller echoes, due to mode conversion, between 2S and 4S. The quoted Curie point of nickel is 358^{O}C, therefore, based on the observations of Gitis, a longitudinal mode was expected to emerge around this temperature. It is clear from the figure that no such echo emerged at any point during the experiment. Given that Gitis used essentially the same geometry as that used here this absence must be due to the single crystal nature of his sample. This said, however, the proposed mechanism responsible for the longitudinal generation is a volume magnetostrictive effect which is isotropic in nature. Given this fact we would still expect to observe some longitudinal mode excitation, even in a polycrystalline block.

Figure 5.4a is a plot of the 2S amplitude vs. temperature, this shows quite different behaviour to that of aluminium with a rise in signal below 100^{O}C followed by a

levelling off between 100 and ~280^{O}C. This levelling off can be attributed to amplifier saturation recognisable from the echo pulse shape at 219^{O}C in figure 5.3. Above 280^{O}C the amplitude drops off until, at 365^{O}C, it is no longer discernible from the noise. Given the ~ 7^{O}C difference between this and the quoted 358^{O}C it was decided that this samples Curie point merited experimental measurement. The same disk as used earlier was clamped in the VSM and it's magnetic moment measured over the temperature range 250 – 400^{O}C. The curve labelled (a) in figure 5.5 shows the disks remnant moment after it was initially saturated, the Curie point on this curve is 359^{O}C, in good agreement with the literature [4]. It should be mentioned that the Curie point throughout this work has been taken as the point at which the ascending and descending temperature curves diverge. Curve (b) is the disks moment with a field of 40KAm^{-1} applied, as one would expect, the Curie point for this curve is somewhat higher at 364^{O}C. Given that the field from the EMATs permanent magnet is ~ 40KAm^{-1}, due to the thickness of the ceramic facing, 365^{O}C is a reasonable value for the Curie point in the EMATs field. The observed shear wave behaviour agrees with Gitis's results in that the efficiency dropped to zero at T_c and experienced a gradual rise at lower temperatures than this. He surmised that shear waves were generated by the magnetoelastic mechanism, this conclusion being based on the rapid disappearance of the signal at the Curie point. This was further supported by the rise in signal at lower temperatures that cannot be explained by the Lorentz mechanism outlined earlier. The rise was attributed by Hanabusa et al to a reduction in magnetocrystalline anisotropy, K, with increasing temperature, this leading to larger rotations of the domain magnetisation vector, for a given applied field, and thus to larger strains.

The results strongly suggest that the magnetoelastic mechanism is responsible for shear wave generation in nickel using a spiral coil EMAT, good agreement being found with the data of Gitis. The absence of any longitudinal mode, however, is surprising given the results published previously. This suggests that the isotropic magnetostriction, that should be the same for both single and polycrystals, is different in the two cases. It is possible that simply not enough electromagnetic energy was delivered to the surface to generate a longitudinal mode although this seems unlikely given the large shear wave amplitudes. It is also possible that the L mode was generated but simply not detected by the EMAT, this always being a possibility when using a send-receive system. However, to confirm this would require the use of a through transmission set up with a different detecting transducer. This would be relatively simple at room temperature, eg: the interferometric work described later, but difficult at higher temperatures due to the need for either cooling the detector (eg: a capacitance device) or surface oxidation (eg: laser detection).

5.4: Invar

Figure 5.6 shows the EMAT traces recorded on invar between 22^{O}C and 192^{O}C. The only echoes apparent are the 2S, 4S etc. shear waves, exhibiting a small degree of birefringence which leads to the non exponential decay. It is also clear that the temporal separation between echoes actually decreases with increasing temperature. The plot of shear velocity vs temperature in figure 5.8a shows a smooth rise from 2648ms^{-1} at room temperature up to 2803ms^{-1} at 205^{O}C. This increase in shear velocity corresponds to an increase in the shear modulus, this increase having been observed previously by Manosa et al [5] in studies on single crystals of the Invar alloy $Fe_{72}Pt_{28}$. Invar is also known to exhibit an anomalous dependence of its elastic

properties on applied pressure although the reader is referred to the literature [6] for details of this.

The shear echo amplitude follows the dependence shown in figure 5.9 with a notable peak at 206^{o}C followed by a sharp drop to zero at temperatures above 240^{o}C. Above 200^{o}C it becomes difficult to measure the shear echo amplitude due to the effect illustrated in figure 5.7 which shows the EMAT traces recorded between 195^{o}C and 282^{o}C. The sudden emergence of huge longitudinal echoes effectively swamps the shear wave signals, these being several orders of magnitude smaller. The velocity of this mode, just as for the shear, also exhibits a smooth increase (figure 5.8b) with increasing temperature. The amplitude of the L mode exhibits the form shown in figure 5.9 (6L), with a smooth peak at 242^{o}C and a drop to zero above 280^{o}C. The fact that the shear efficiency drops to zero simultaneously with the peak in longitudinal efficiency suggests that the two sources are closely related, ie: magnetoelastic in origin.

The Curie point of this sample was studied in the VSM and produced the results given in figure 5.10, all data being obtained in zero applied field after initial saturation. As the PC compatible thermometer was only calibrated above 200^{o}C it was necessary to perform measurements below this temperature manually, hence the smaller number of data points below 200^{o}C. These results show the broad Curie transition, typical of this alloy [7], that occurs between ~180 and 280^{o}C. As the transition is so broad it is difficult to define an accurate Curie point, although a Tc of ~ 255^{o}C is suggested by the data, this makes comparison with the maxima in shear and longitudinal efficiency somewhat difficult too. However, Yamada et al [8]

investigated the volume magnetostriction ,$\delta\omega/\delta H$, of this particular invar composition and found a pronounced peak at 282^{O}C, somewhat higher than the experimental T_c. This was assumed to be the Curie point although other authors [9] have quoted somewhat different values using other methods of measurement, none as low as 255^{O}C however.

The fact that the longitudinal efficiency falls to zero 40^{O}C lower than the quoted peak in isotropic magnetostriction suggests two possibilities. Either the experimentally recorded temperature is too high, due to the EMATs cooling effect, or there is a genuine difference between the two maxima. Significant cooling of the surface by the EMAT is ruled out by the short contact time, around 1 second, so we must therefore conclude that the discrepancy is real. The fact that the measured T_c is also ~ 25^{O}C lower than that quoted in the literature strongly suggests that the difference is due to a genuine difference between the sample studied here and that used by Yamada. It is already known that the broadness of the Curie transition in invar is caused by inhomogeneity in composition throughout the alloy [10]. This leads to a distribution of ferromagnetic and paramagnetic regions within the sample, the ratio of one to the other being dependent on the applied field. It is feasible then that different samples of the same macroscopic composition exhibit different magnetic properties due to differing degrees of inhomogeneity. This is consistent with the VSM and EMAT data, both of which indicate a lower T_c than that given in the literature.

5.5: Duplex stainless steel

5.5.1: British Gas duplex

Figure 5.11 shows the EMAT traces recorded on Britsh Gas duplex between 20 and 543^{o}C. The anomalous longitudinal generation described earlier in the thesis is present up to 400^{o}C at which point it falls below the noise level. Shear wave signals, however, are still present upto 530^{o}C. The temperature dependence of the 6S amplitude is shown in figure 5.12 and shows a smooth decrease to zero at ~ 530^{o}C. Above this temperature there is a rapid increase in the L mode efficiency although the amplitudes of the L echoes are nothing like as large as those seen in invar. The temperature dependence of the L mode amplitude is also shown in figure 5.12 with a clear peak at 535^{o}C followed by a sharp decrease and a gradual tailing to zero at 555^{o}C. As mentioned earlier, the fact that the low field magnetostriction showed anomalous behaviour, ie: λ_l and λ_t being positive, suggested that some volume magnetostrictive effect could be responsible for the longitudinal generation. This now seems unlikely given the small size of the longitudinal mode at high temperatures where we would expect the volume magnetostriction to become dominant. The velocities of both the S and L modes are seen to decrease with increasing temperature (see figure 5.13). The shear wave velocities between 92 and 503^{o}C reduce linearly from 3217ms^{-1} to 2915ms^{-1} and 3132ms^{-1} to 2829ms^{-1} for the first and second echoes of the birefringent pair respectively. The longitudinal velocity drops from 5702ms^{-1} at 92^{o}C down to 5313ms^{-1} at 542^{o}C.

5.5.2: British Steel duplex

The EMAT traces from the BS sample between 21°C and 553°C are shown in figure 5.14a. The shear wave echoes are the only ones visible with an amplitude – temperature relationship as plotted in figure 5.14b (2S). This shows a similar form to that for the BG sample with a smooth reduction to zero over the range 270 – 530°C but little change at lower temperatures. In contrast, there is little evidence of a longitudinal mode at all, the trace at 510°C showing a very weak L mode echo that appears at this temperature. Neither the longitudinal or shear velocities have been included in the present work because the small signal amplitudes made accurate timing measurements impossible. The fact that no L mode emerges at T_c suggests that the volume magnetostriction is smaller than that of BG duplex. This is unexpected, given the similarities in their compositions, although it does correlate with the results from nickel that showed a marked difference between the L mode behaviour of Gitis' single (anisotropic) and polycrystal (isotropic) nickel samples as the Curie transition was passed.

5.5.3: Curie point of duplex stainless steels

The Curie points of both duplex samples were measured in the VSM, the samples being the same as those used to obtain the B-H curves. Figure 5.15 shows the data obtained from the BG sample, the curve labelled (a) being the disks remnant field after saturation whilst (b) and (c) are with applied fields of $50KAm^{-1}$ and $230KAm^{-1}$ respectively. Figure 5.16 shows Curie point data recorded on the BS sample using the same applied fields. The fact that (a) in both samples shows an increase in moment between 200°C and 400°C could be accounted for by the conversion of some austenite phase into ferrite, thus giving a higher PSD signal due to the remnant

field of the pole pieces. However, this transformation being irreversible, we would expect a repeat of the experiment to give a slightly different result if this was indeed the case. In fact repeating the experiment yielded an identical result, thus discounting this possibility. A more likely explanation is that thermal energy allowed easier movement of domain walls within the ferrite grains, this coupled with a small remnant field from the pole pieces would lead to an increase in the size of favourably orientated domains and therefore a larger magnetic moment. The fields applied for (b) and (c) were high enough to complete all domain wall motion so in these cases we are dealing purely with the decrease in net magnetic moment due to thermal precession. It is also apparent that T_c increases with applied field in both samples, just as expected. T_c for the BG sample is estimated as $540^{O}C$ in zero field whilst for the BS sample it is estimated at $530^{O}C$. In $50KAm^{-1}$ this changes to $544^{O}C$ and $536^{O}C$ for the BG and BS samples respectively.

As for the previous ferromagnetic samples there is a definite correlation between the shear wave efficiency and T_c, the signal disappearing completely as T_c is reached. This supports the conclusion reached earlier that shear waves are generated in duplex predominantly by a magnetostrictive mechanism. The anomalous longitudinal generation in BG duplex is also seen to decrease with temperature although it passes through zero at $\sim 400^{O}C$ as opposed to T_c. The fact that the longitudinal efficiency, in both samples, experiences such a small increase around T_c was surprising given the previous similarities between the results from duplex and invar. It suggests significant differences in their spontaneous magnetostrictive properties that would benefit from accurate measurement.

5.6: Mild steel

A 6mm thick mild steel sample cut from a 6.25 thick bar was clamped in the furnace and EMAT traces collected between 590^{o}C and 790 ^{o}C (figure 5.17). A thinner sample than that used previously was necessary as the furnace clamps could not accommodate the thickness of the original piece. The range from room temperature upto 590^{o}C was omitted as it was desirous to heat the block for the minimum possible time, therefore the sample was heated rapidly to 590^{o}C and subsequent heating done over a slow ramp to ensure a stable homogeneous sample temperature. The reason for minimising the experimental time was to minimise the degree of sample oxidation occuring over the course of the experiment. It was already known that some ferrous oxides lead to enhanced EMAT efficiency [11] and therefore this effect could significantly influence the results. Even given this effort to avoid the effects of oxidation, there was still a noticeable 'skin' of black oxide on the block after the experiment. As the block is mildly birefringent, measurements of the 2S amplitude were found to be unreliable, the 4S amplitude vs. temperature is plotted in figure 5.18a, this showing a far more consistent waveform over the temperature range. Just as for the previous ferromagnetic samples the amplitude shows an increase with temperature until a point somewhat short (660^{o}C) of the Curie point. Beyond this it falls rapidly, reaching zero at the assumed T_c (ref) of 760^{o}C. The longitudinal efficiency (figure 5.18b) also displays similar behaviour to that in invar and duplex although the peak is sharp at 773^{o}C with the amplitude reaching zero at 790^{o}C. It should be mentioned that the trace at 770^{o}C is not shown in figure 5.17 as the large size of the L echoes would obscure the details of the lower temperature traces. Given that the results of the previous chapter suggested mild steel generated and detected via a Lorentzian mechanism the similarity between these results and

those from the ferrous samples above is surprising. They suggest that this particular sample may exhibit a higher magnetoelastic contribution to the ultrasonic generation. Given the samples lower thickness this is feasible, the higher rolling stresses potentially leading to increased magnetostriction [12]. However, the presence of the black oxide, probably Fe_3O_4, alters the surface conditions to such an extent, even given its minute thickness, that this is the more likely source of differences between the two sets of results.

The temperature dependence of the remnance of the mild steel disk was measured and produced the data shown in figure 5.19. These suggest a T_c of 780^{o}C, the moment increasing with decreasing temperature below this. The small feature at ~ 560^{o}C was found to be repeatable with both increasing and decreasing temperature and was therefore assumed to be a genuine change in the remnant moment at this temperature. This said, no mention of any such feature could be found in the literature. The fact that the T_c of 780^{o}C is in disagreement with the EMAT amplitude dependence that reaches zero at ~ 760^{o}C contrasts with the shear wave behaviour in the previous samples, except invar, where the shear wave amplitude reached zero at or within a few degrees of T_c. However, no account was taken of oxidation of the sample in the VSM. On removal, the mild steel disk was found to be heavily oxidised on both surfaces, given its small thickness this constitutes a non trivial change in the samples composition throughout the experiment. The T_c data obtained in the VSM is therefore unreliable and would benefit from further measurements in a controlled atmosphere. This would have involved significant alterations to the VSM that were simply not feasible given the time available. In summary, the S mode temperature dependence shows similar features to the previous

ferromagnetic samples, except invar, in falling rapidly to zero around T_c with a measurable increase with increasing temperature below this. The L mode experiences a huge increase in efficiency just above T_c, this also agrees with the behaviour observed in the other ferrous ferromagnetic samples, the only difference being in the extent of the increase. The fact that the shear efficiency results seem to contradict those of chapter 4 can be attributed to the presence of the oxide skin which may exhibit vastly different magnetoelastic character to that of the underlying steel. This oxide and its effect on EMAT performance would benefit from detailed study that it is beyond the scope of the present work.

5.7: Conclusions and further work

5.7.1: Shear wave generation

The shear wave efficiency for all of the ferromagnetic samples showed very similar behaviour with a rapid drop to zero at, or very close to T_c. This is certainly consistent with earlier work on nickel and suggests that it is due to a similar cause, ie: an anisotropic magnetostrictive mechanism. We should not, however, discount the Lorentz mechanism simply because of the rapid drop in shear signal amplitude. As seen in aluminium, even the drop in σ with temperature causes a noticeable reduction in shear efficiency, although it does not fall to zero. This is, however, for a permanently paramagnetic metal and so takes no account of any change in μ and its corresponding effect on δ and B_o. We know already that B_o should fall by a factor of ~ 2 when the sample becomes paramagnetic, this being due to the loss of the effective 'image magnet' [13] within the sample. Therefore the Lorentzian send-receive efficiency should drop by a factor of 4, as it is dependent upon B_o^2. The

sudden drop in μ also has the obvious effect of drastically increasing δ, a drop from $\mu_r = 600$ say (eg: nickel) to $\mu_r = 1$ increasing δ by a factor of 25. Under these conditions we could expect the signal to fall very quickly until at T_c it was ~ 100 times less than when the sample was in the ferromagnetic state. This said, if the signals in duplex or nickel were of Lorentzian origin then we would still expect to observe them above T_c, given their large amplitude. This proves not to be the case and makes it very likely that magnetostriction is indeed responsible for the S mode generation. Again this agrees with the results of Gitis who found that the shear wave signal in nickel disappeared completely at T_c even when $M > M_s$. Under these circumstances μ_r is always equal to 1 and therefore the only change in the variables in equation 2.17 is B_o which does not suffer the large swing experienced by δ. A notable exception to the general trend is invar which exhibits a sharp increase in S efficiency just below T_c. This said, however, none of the other samples exhibit the unusual thermal and magnetic properties of invar so it would be naive to expect it to behave as they do. This is borne out quite clearly by the increase in both V_S and V_L with increasing temperature.

5.7.2: Longitudinal wave generation

As expected, the results for aluminium showed no L mode detection at any temperature in the range 20°C to 420°C. It will be shown in the proceeding chapter that an L mode is in fact generated in aluminium but is not detected due to the lack of any static radial field. The lack of an L mode in nickel suggests that the power into the coil may simply not have been sufficient to excite this mode around Tc. Given the large L amplitudes observed in invar and mild steel this suggests that the spontaneous volume magnetostriction is much smaller in pure polycrystalline nickel

than in either the 64%Fe:36%Ni alloy or mild steel. The fact that BG duplex displayed such a small peak in L efficiency at T_c suggests that the sample also exhibits a much smaller volume change on passing the ferro–paramagnetic transition. This is perhaps not unexpected given that half the alloy is paramagnetic in the first place. Thus, as T_c is passed, the ferrite grains undergo a volume change whilst the austenite grains do not. The lack of expansion in the austenite therefore 'absorbs', to some extent, the ferritic expansion and the overall effect is reduced. This, of course, is only a simple intuitive argument but could explain the observed behaviour. In contrast, the inhomogeneity in invar is field dependent [10], therefore in the EMATs field far more of the alloy is ferromagnetic and the 'damping effect' due to its paramagnetic phase is reduced, hence the large L amplitudes.

Chapter 5 references

1: C. Edwards and S. B. Palmer; *IEEE Trans. Mag.* **26**, p 2080 - 2084 (1990).

2: *C. R. C. Handbook of Chemistry and Physics*; Boca Raton, C.R.C. Press (1992).

3: V. A. Komarov, R. S. Il'yasov and N. I. Shakshin; *Defectoskopiya*, **no 4**, 83 - 92 (1983).

4: Bozorth; *Ferromagnetism*; Van Nostrand (New York) (1951).

5: Ll. Manosa et al; *Phys. Rev. B* **45**, pp 2224 - 2236 (1992).

6: V. P. Silin, D. Wagner and V. M. Zverev; *Physics Letters A* **185**, pp485 - 490 (1994)

7: E. F. Wasserman; *Ferromagnetic Materials* **6**, 240; edited by K. Buschov and E. Wohlfarth, Elsevier (Amsterdam) (1990)

8: O. Yamada and E. du Tremolet de Lacheisserie; *Journ. Phys. Soc. Japan* **53**, pp 729 - 734 (1984).

9: F. Ono; *Journ. Phys. Soc. Japan* **50**, pp 2231 - 2235 (1981).

10: A. Romanov and V. P. Silin; *JETP* **86**, pp 120 - 127 (1998).

11: P. Crowther, C. Edwards and S. B. Palmer; *Insight* **39**, pp 618 - 622 (1997).

12: M. E. Kuruzar and B. D. Cullity; *Internat. Journ. Magn.* **1**, pp 323 - 325 (1971).

13: J. Crangle; *The Magnetic Properties of Solids*; published by Arnold (London) (1977).

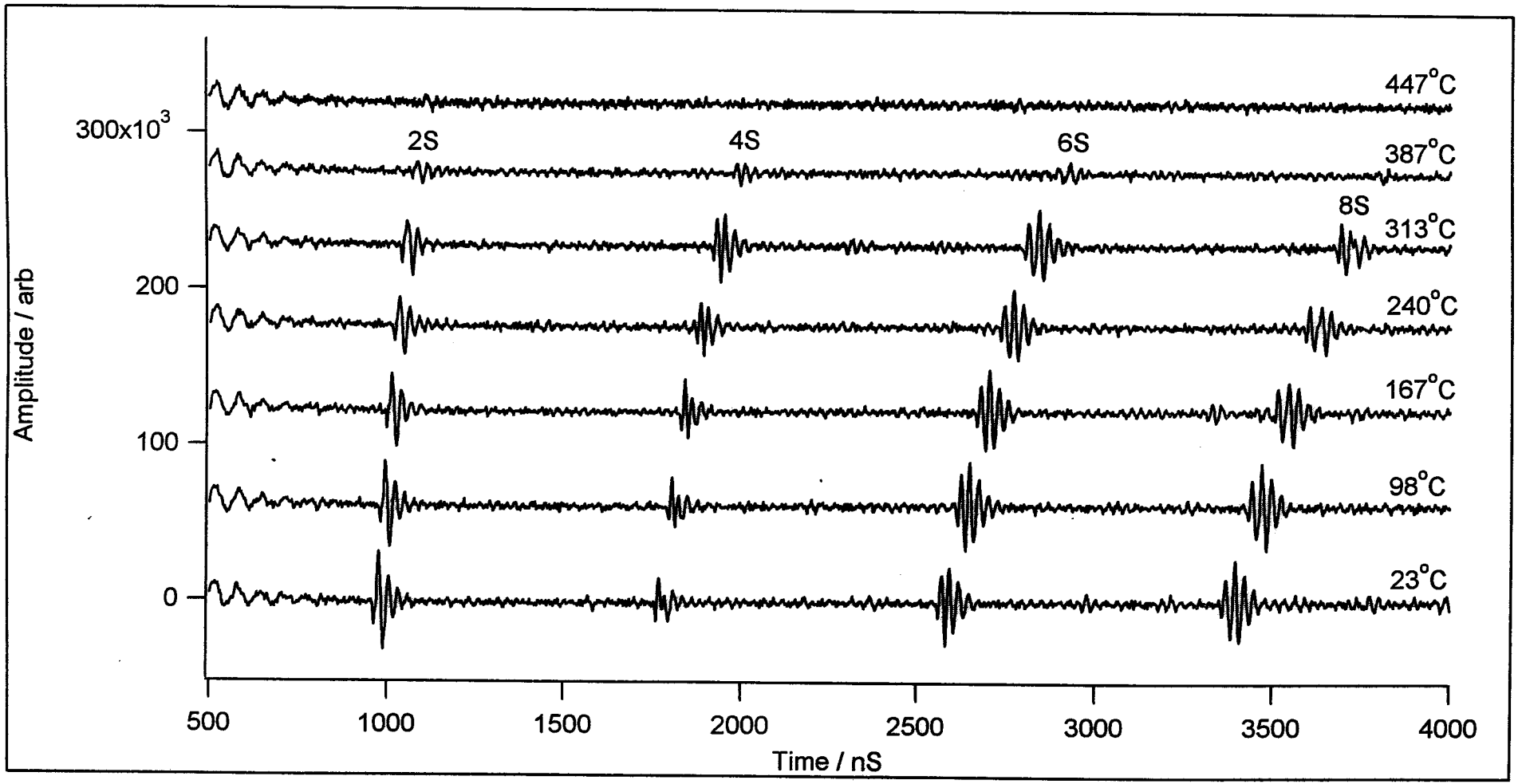

Figure 5.1: EMAT traces from aluminium between 23 and 447°C

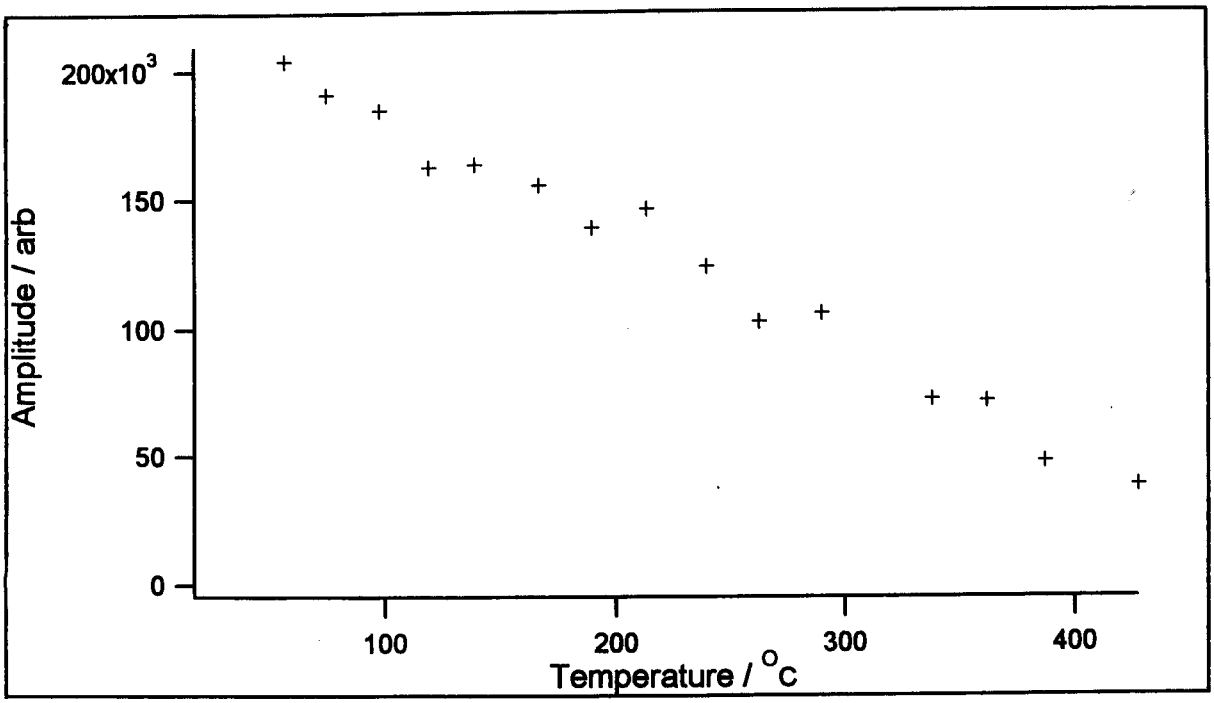

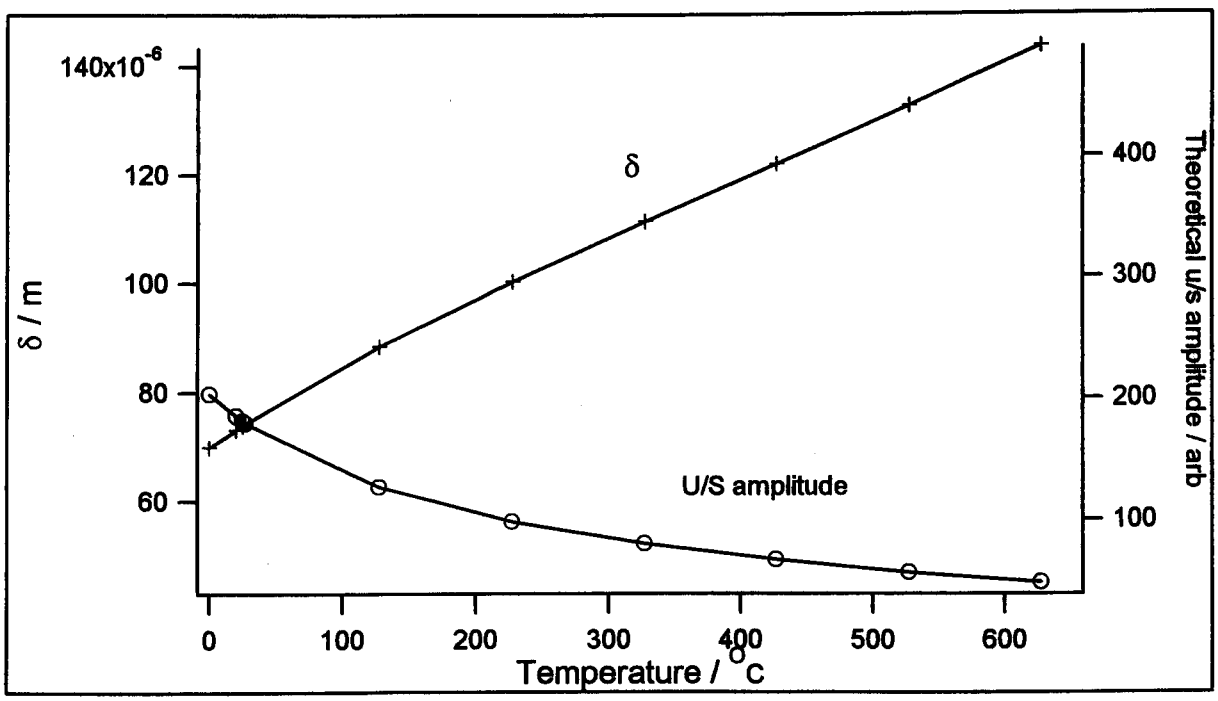

Figure 5.2: (a): 2S amplitude vs temperature for EMAT on aluminium

(b): δ and theoretical ultrasonic amplitude vs temperature

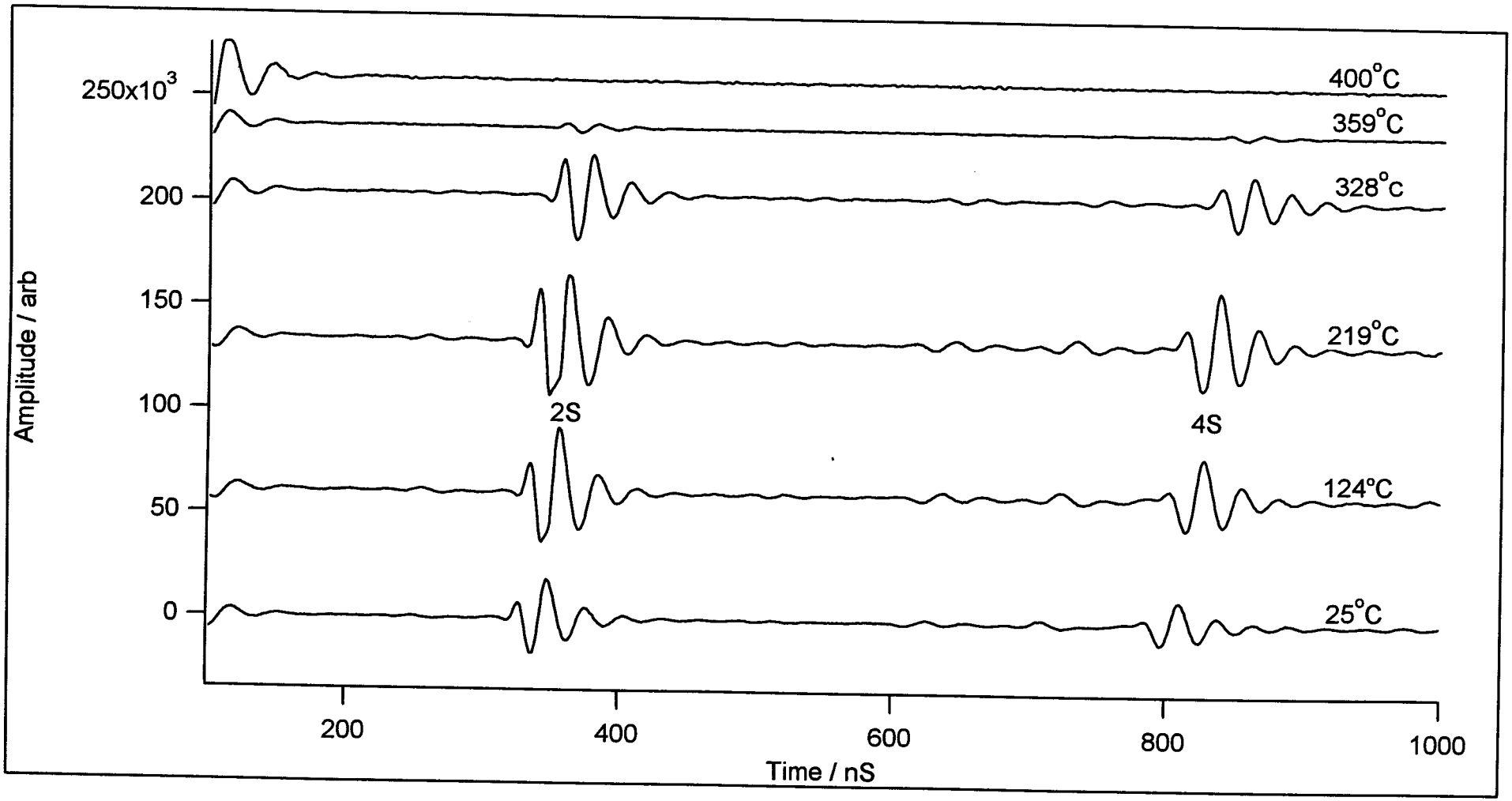

Figure 5.3: EMAT traces from nickel below and above T_c ($358^{\circ}C$)

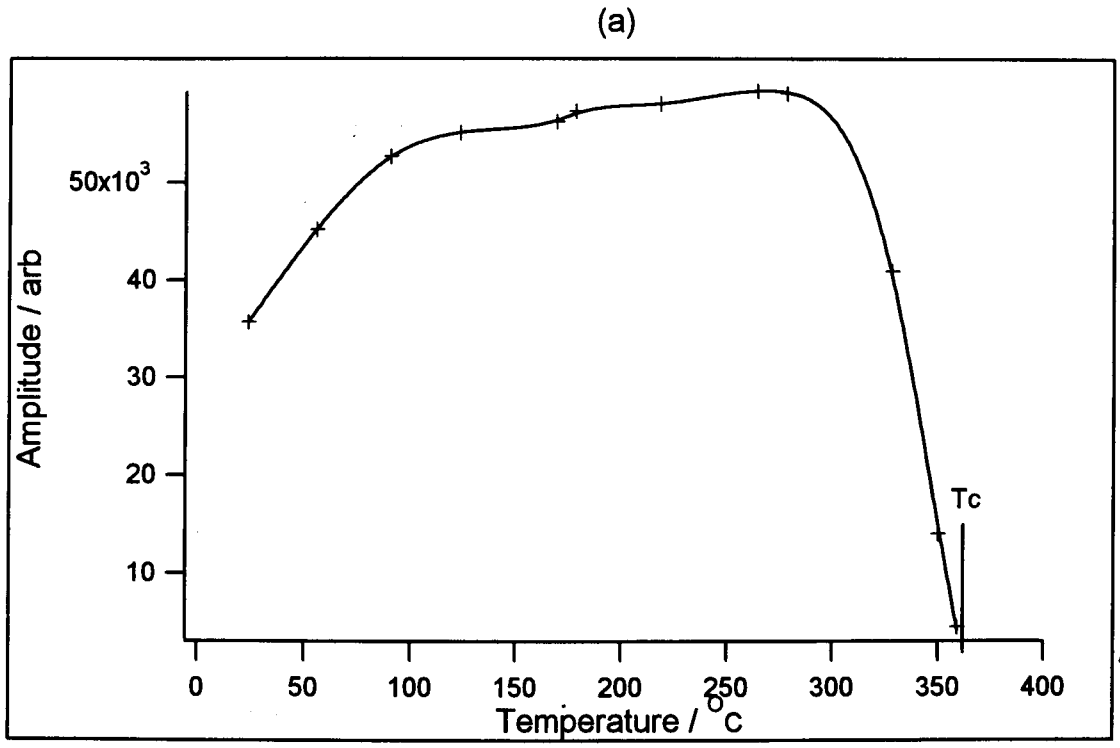

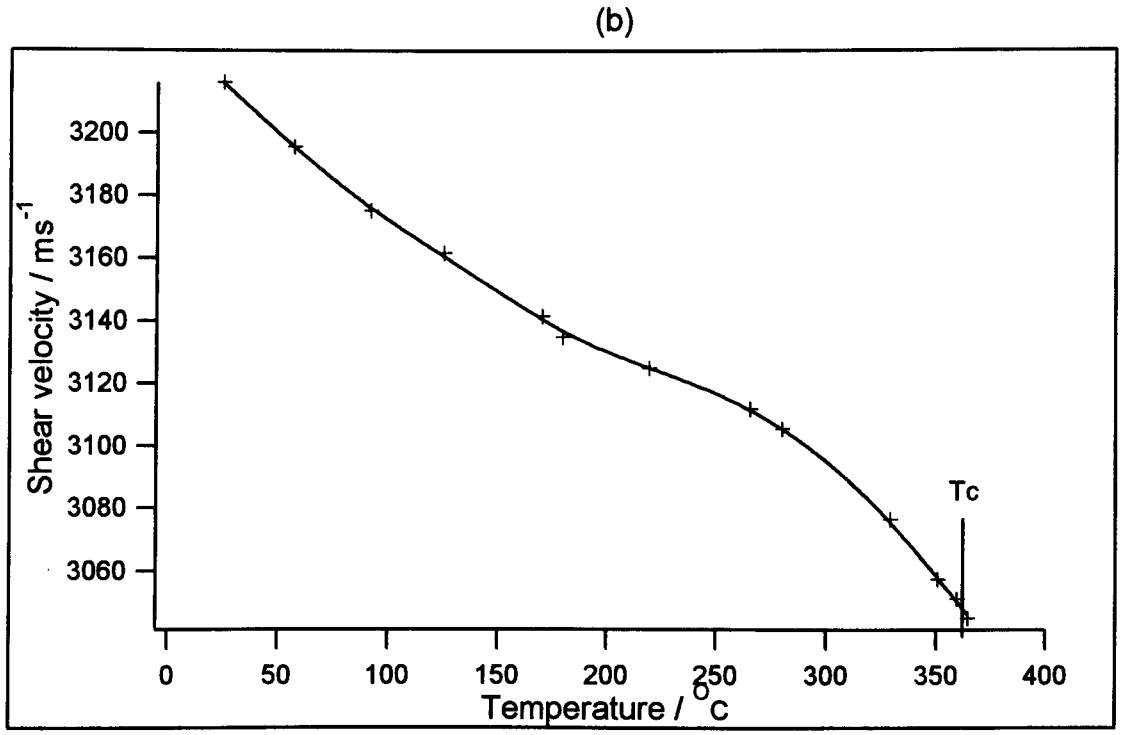

Figure 5.4: (a): 2S amplitude vs temperature for EMAT on nickel

(b): Shear velocity vs temperature in nickel

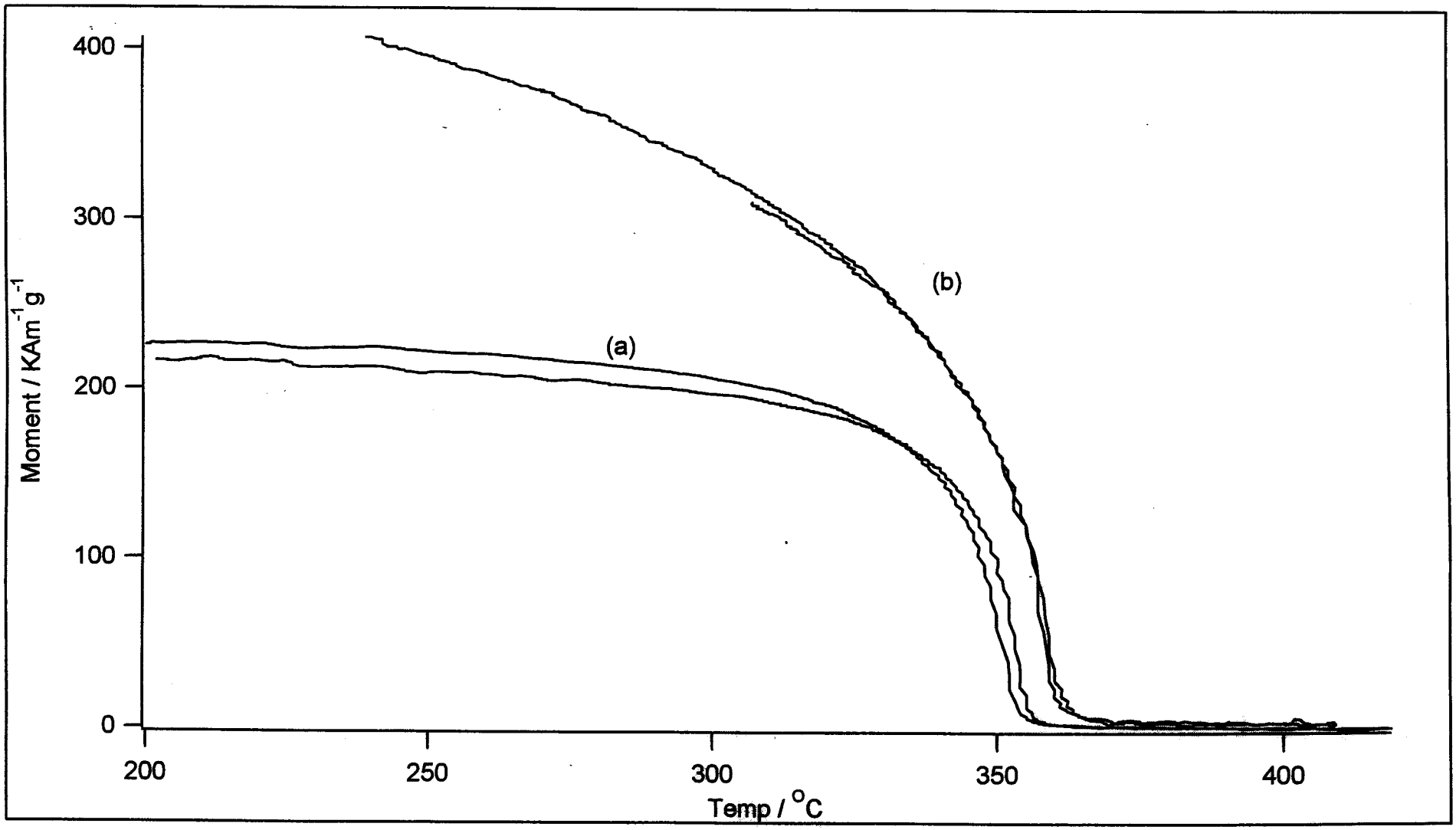

Figure 5.5: The magnetic moment of nickel vs temperature in applied fields of (a): 0 KAm^{-1} and (b): 40KAm^{-1}

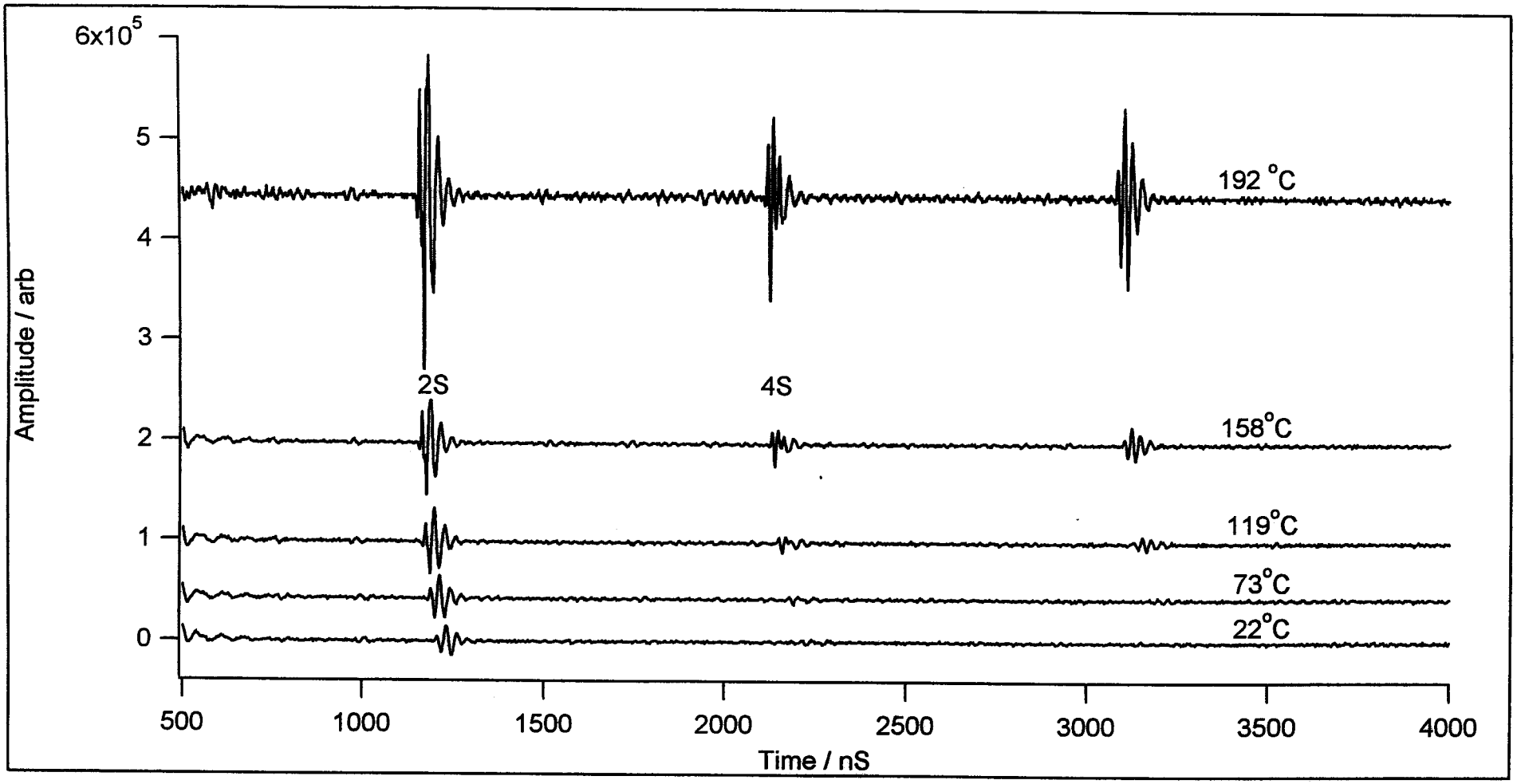

Figure 5.6: EMAT traces from invar below T_c

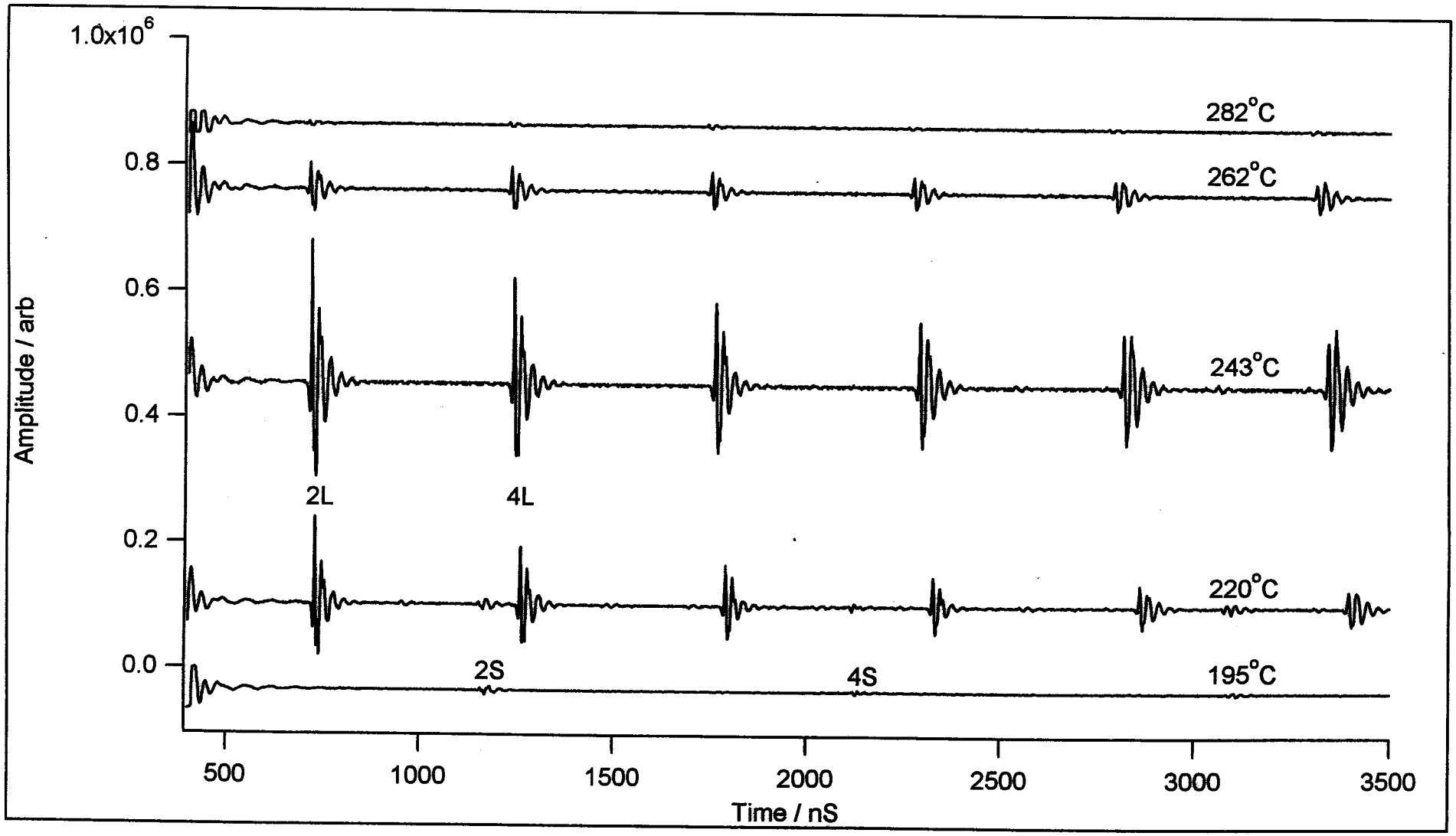

Figure 5.7: EMAT traces from invar above T_c

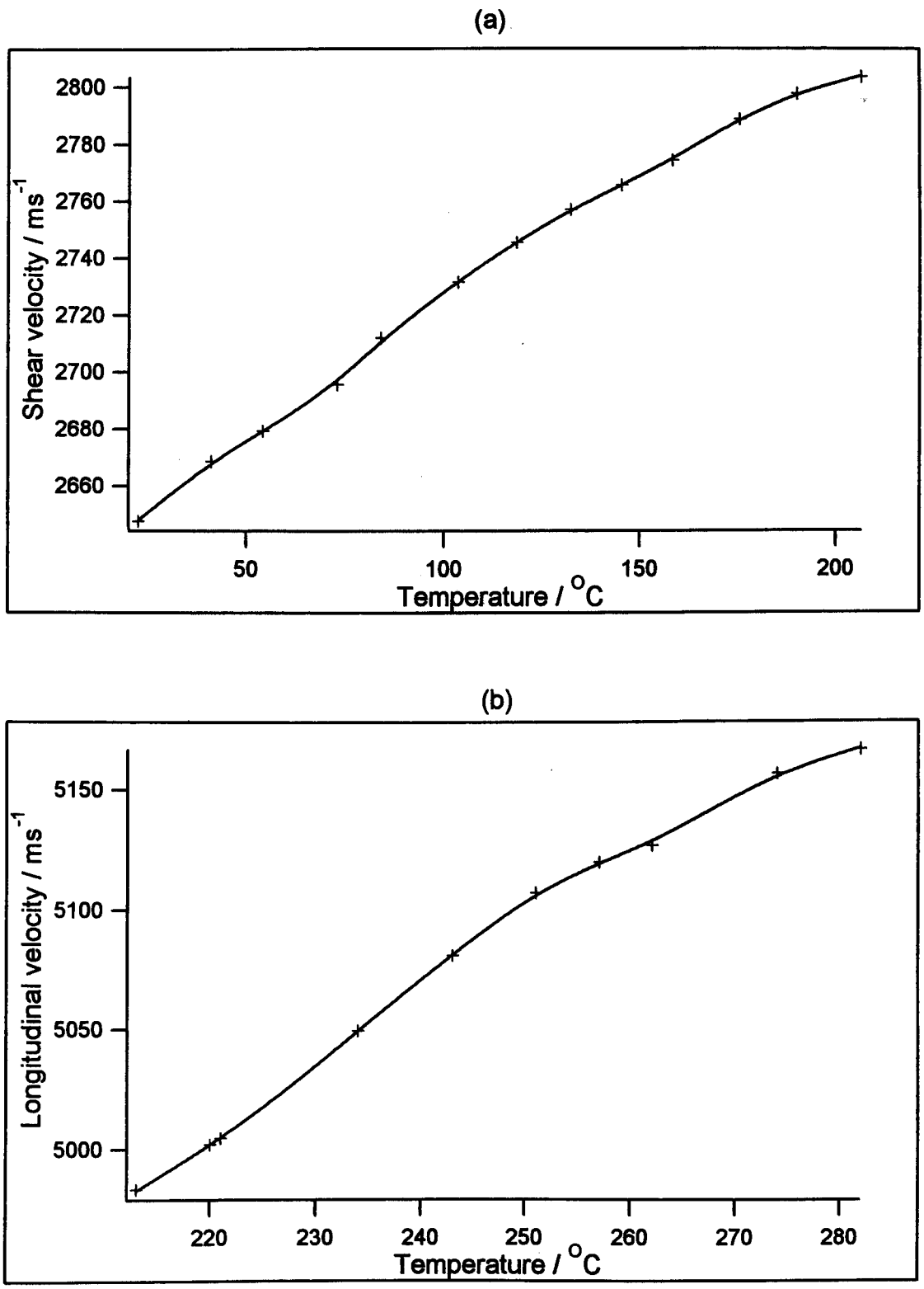

Figure 5.8: Temperature dependence of (a) shear and (b) longitudinal velocities in invar

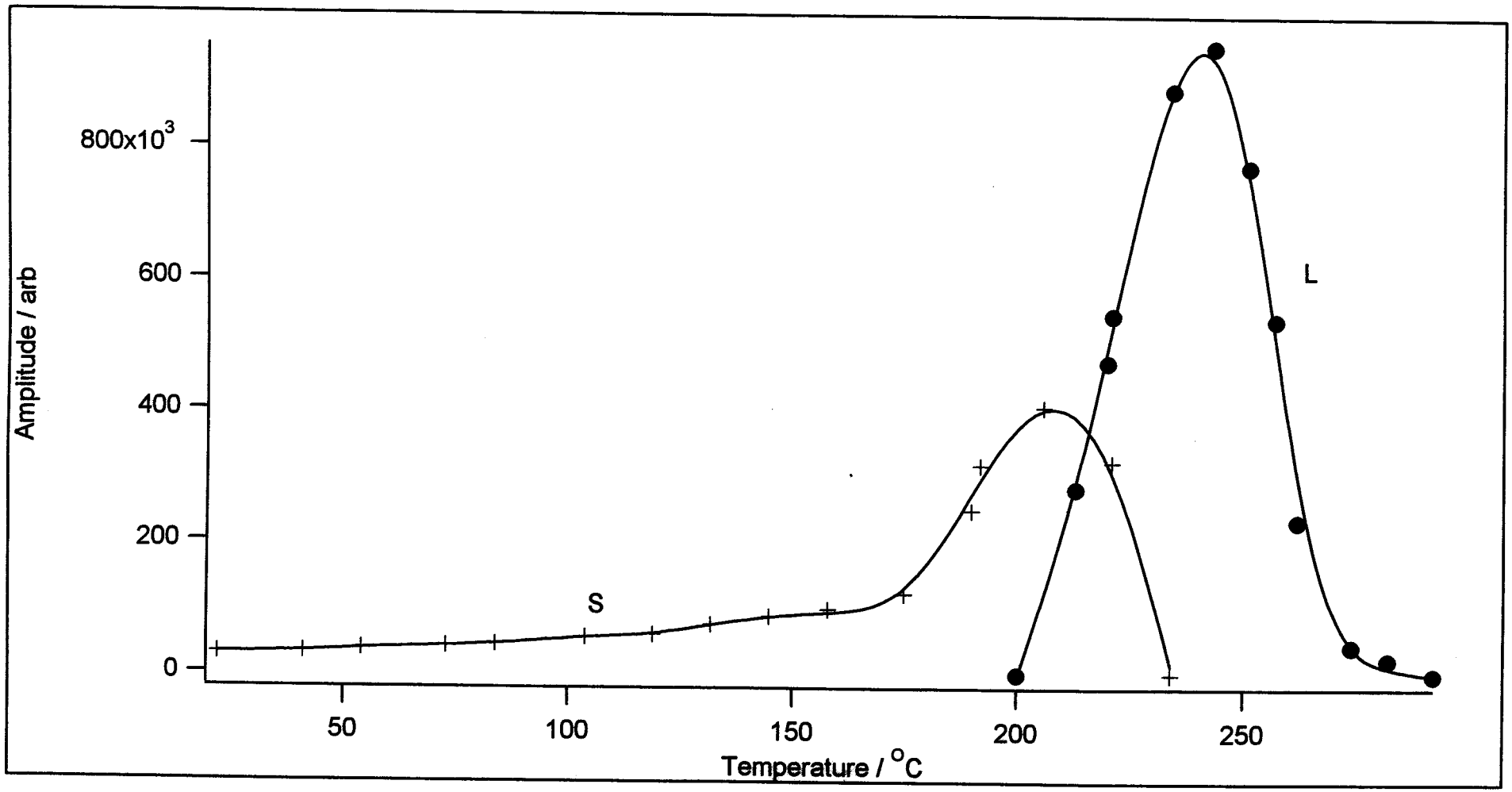

Figure 5.9: Temperature dependence of shear and longitudinal mode amplitudes on invar

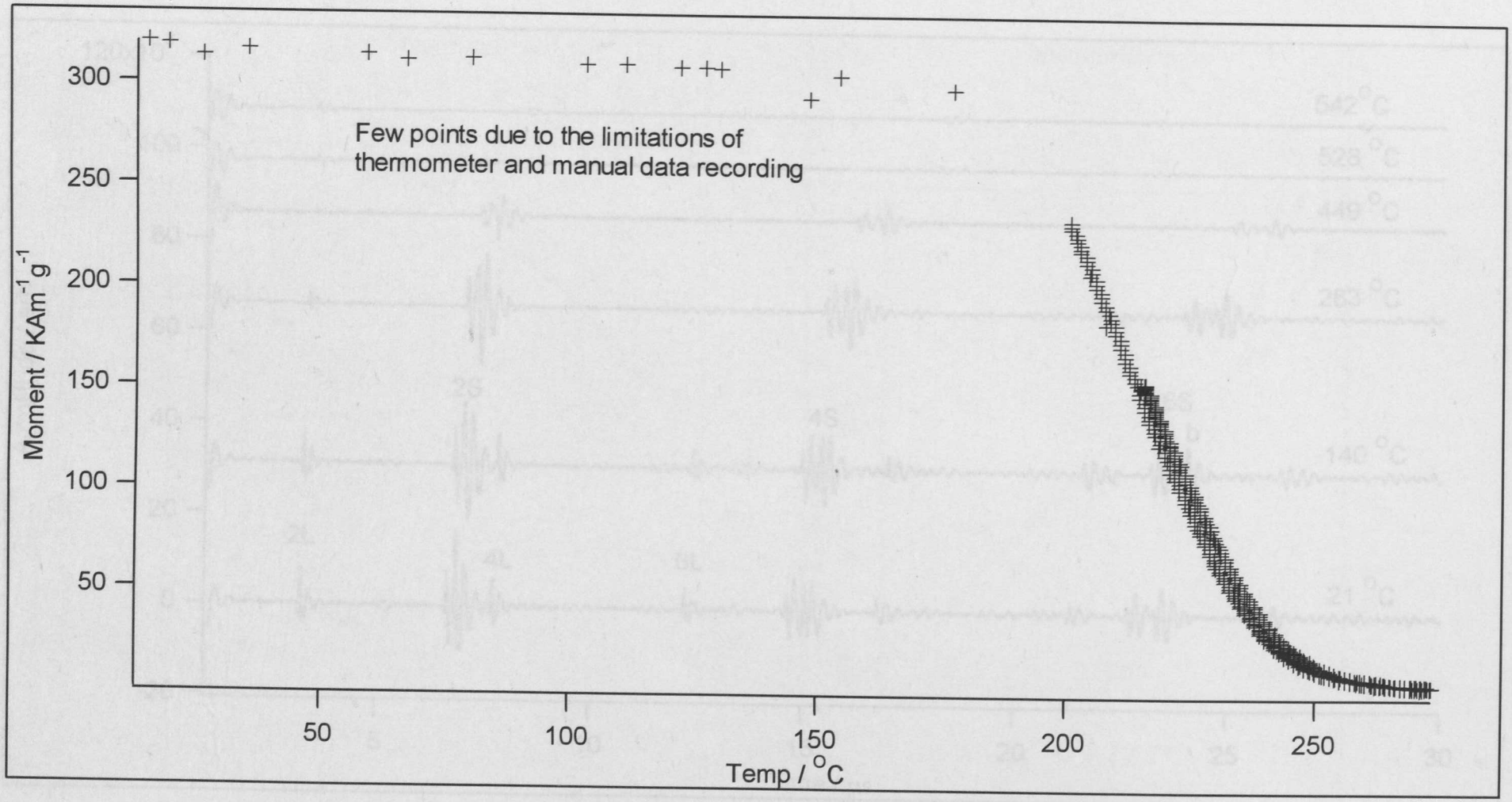

Figure 5.10: The remnant magnetic moment of invar vs temperature

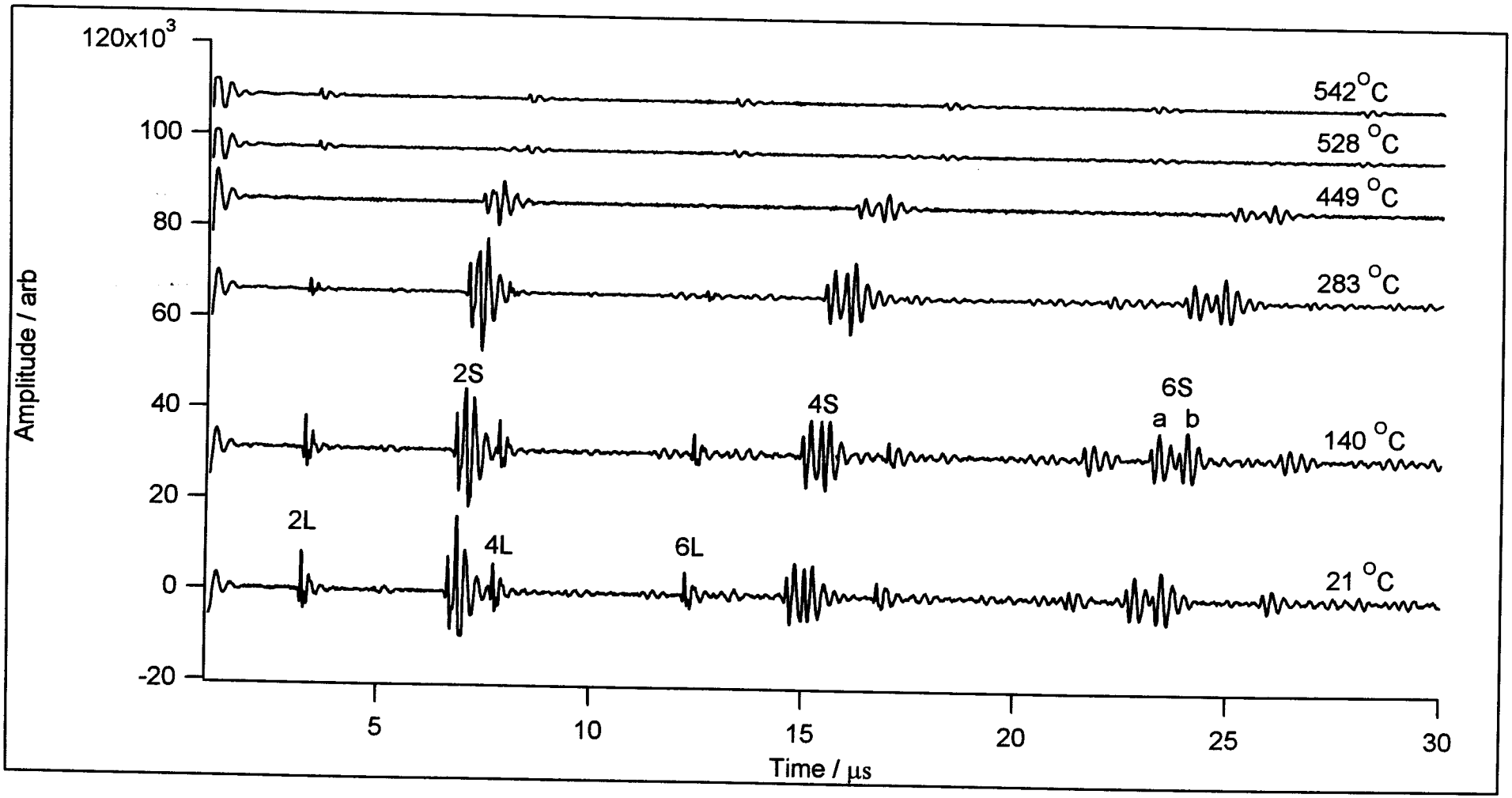

Figure 5.11: EMAT traces from British Gas duplex below and above T_c (544 °C)

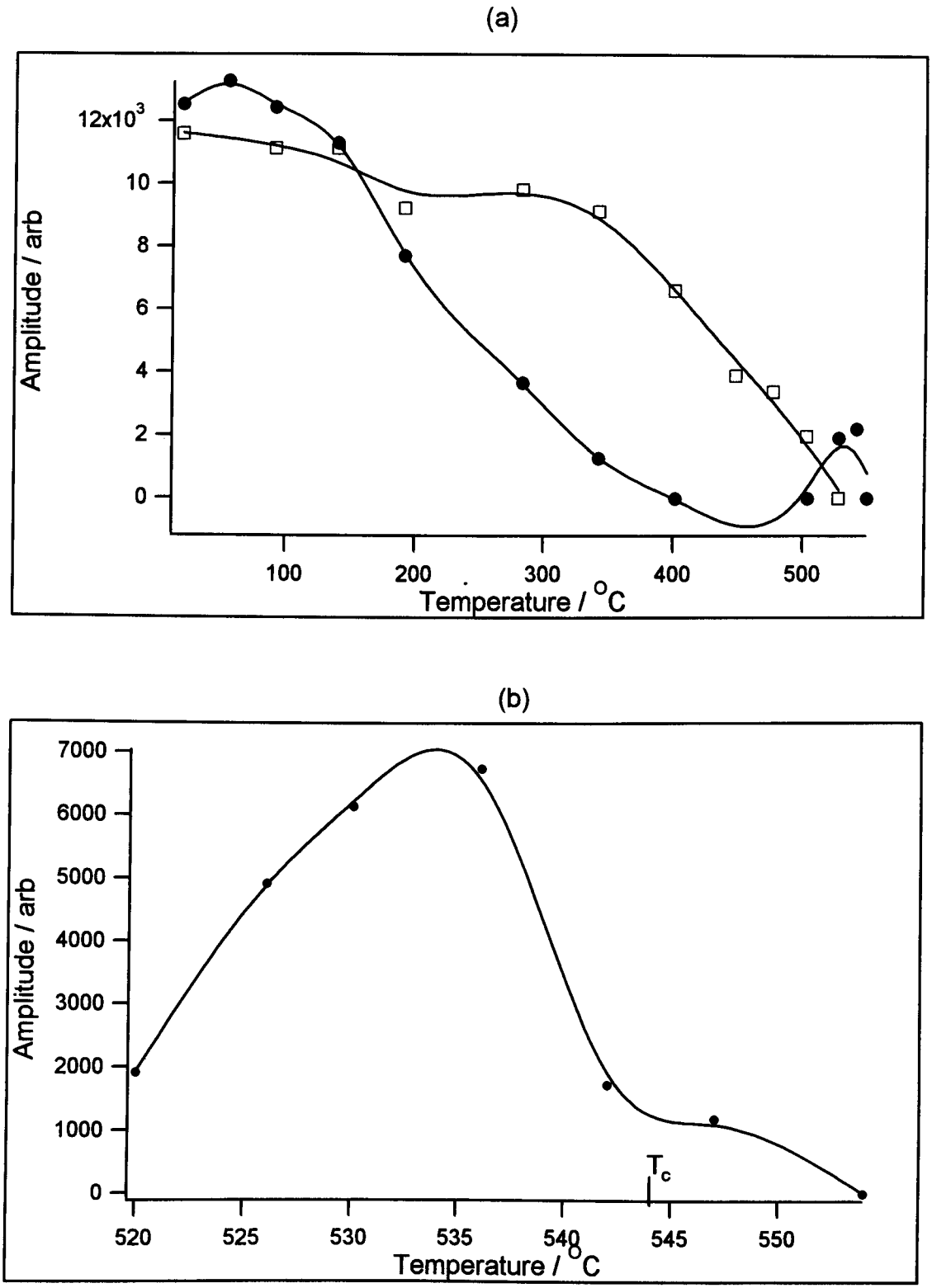

Figure 5.12: (a): Temperature dependence of shear and longitudinal amplitudes for EMAT on British Gas duplex

(b): Zoom of longitudinal dependence around T_c (544 ^{o}C)

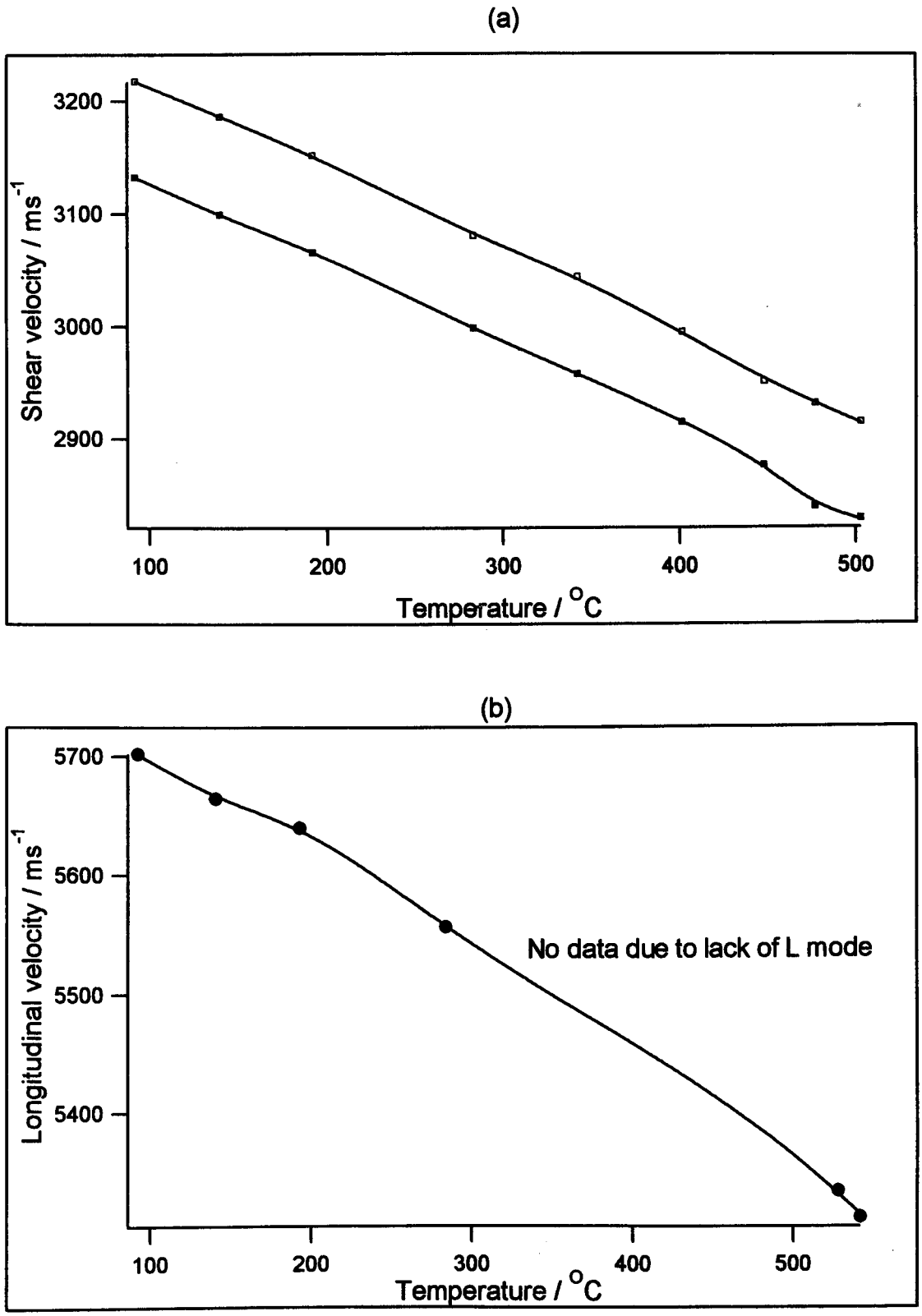

Figure 5.13: Temperature dependencies of (a) shear and (b)longitudinal velocities in British Gas duplex

(a)

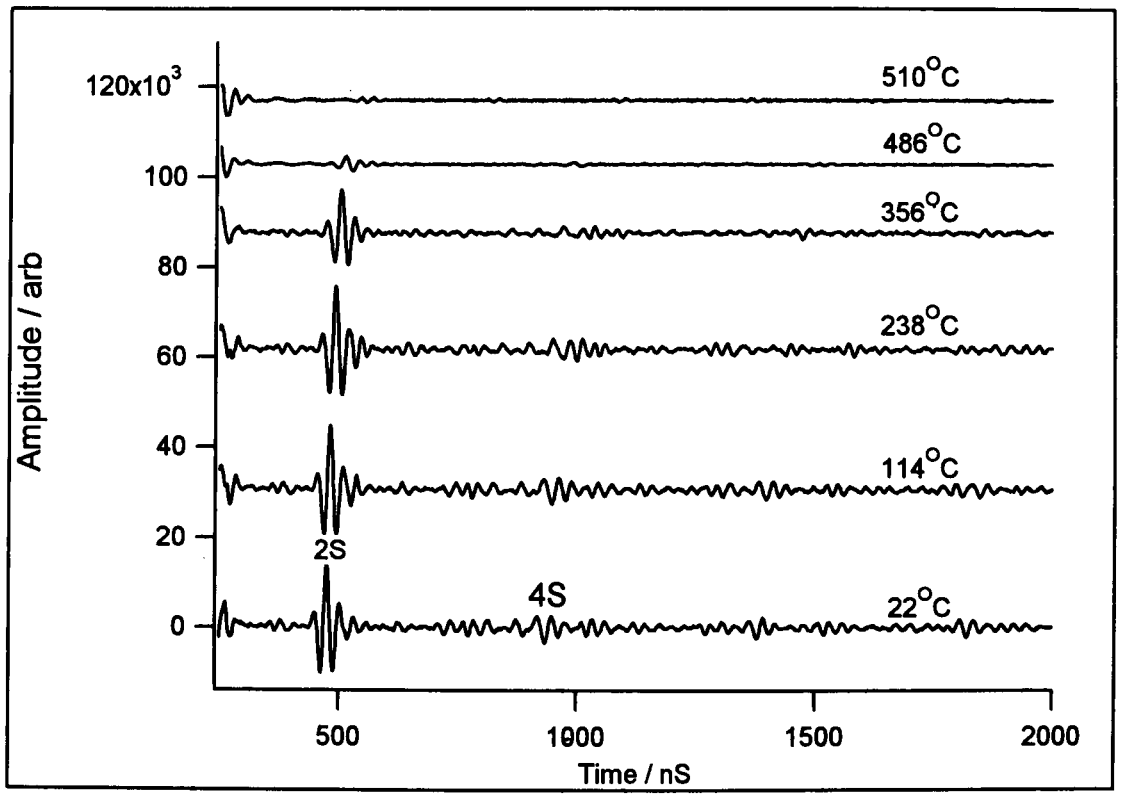

(b)

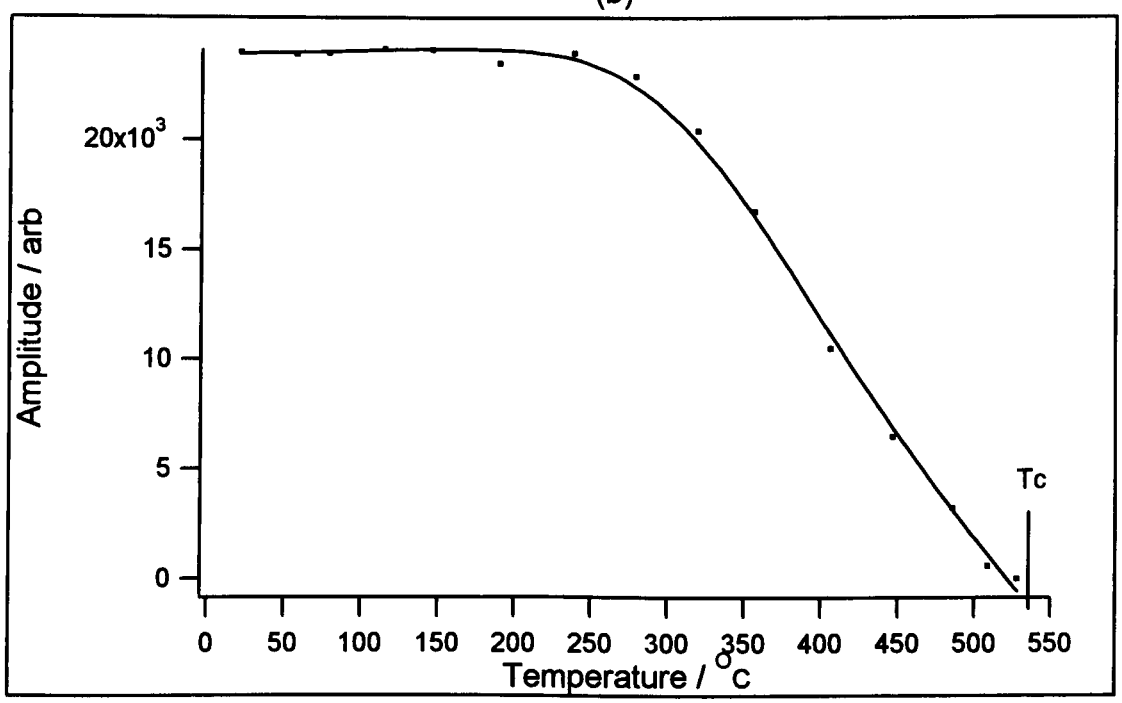

Figure 5.14: (a): EMAT traces from British Steel duplex below and above T_c (536°C)

(b): 2S amplitude vs temperature on British Steel duplex

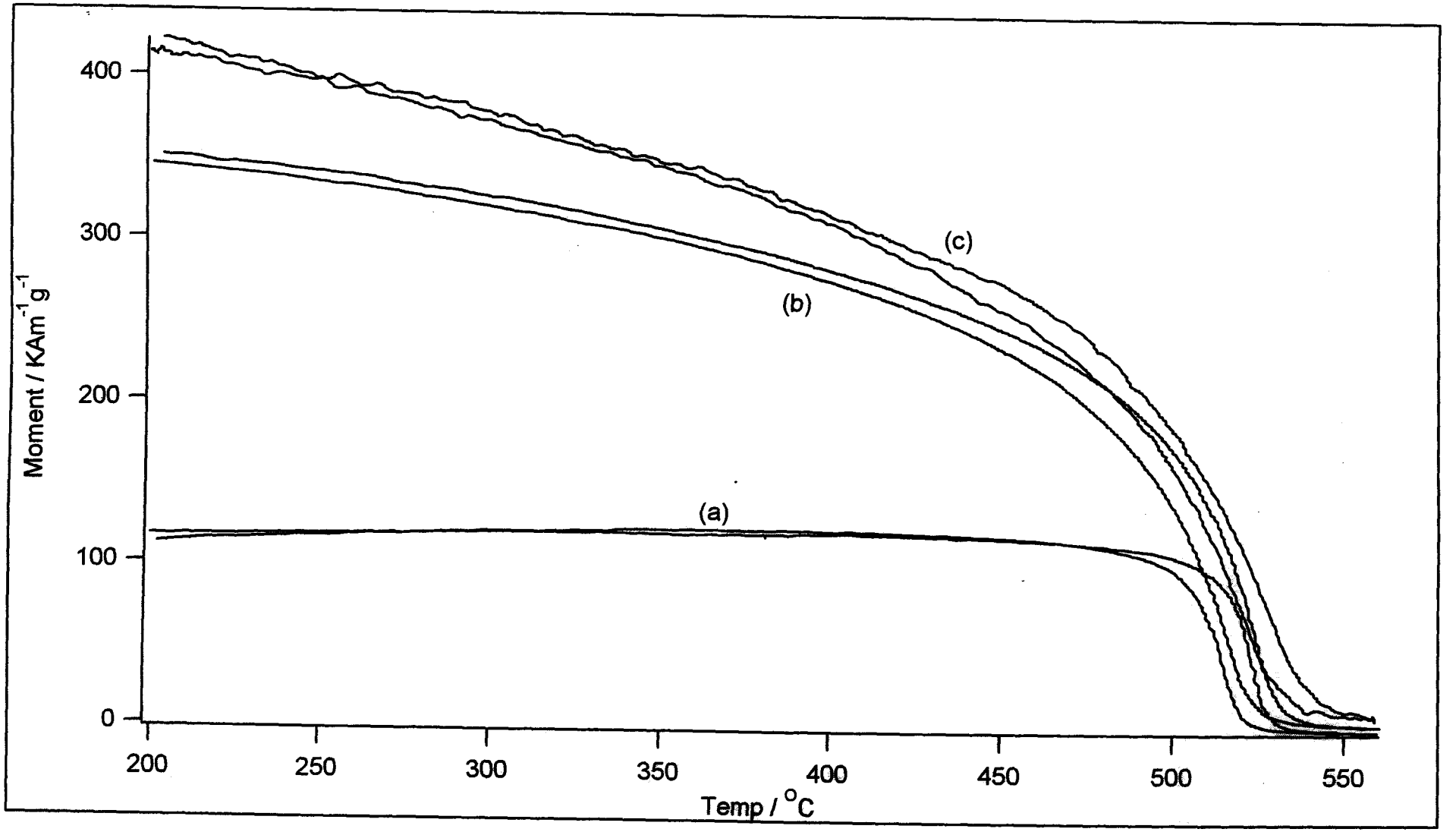

Figure 5.15: The magnetic moment of British Gas duplex in applied fields of:
(a): 0 KAm^{-1}, (b): 50 KAm^{-1} and (c): 230 KAm^{-1}

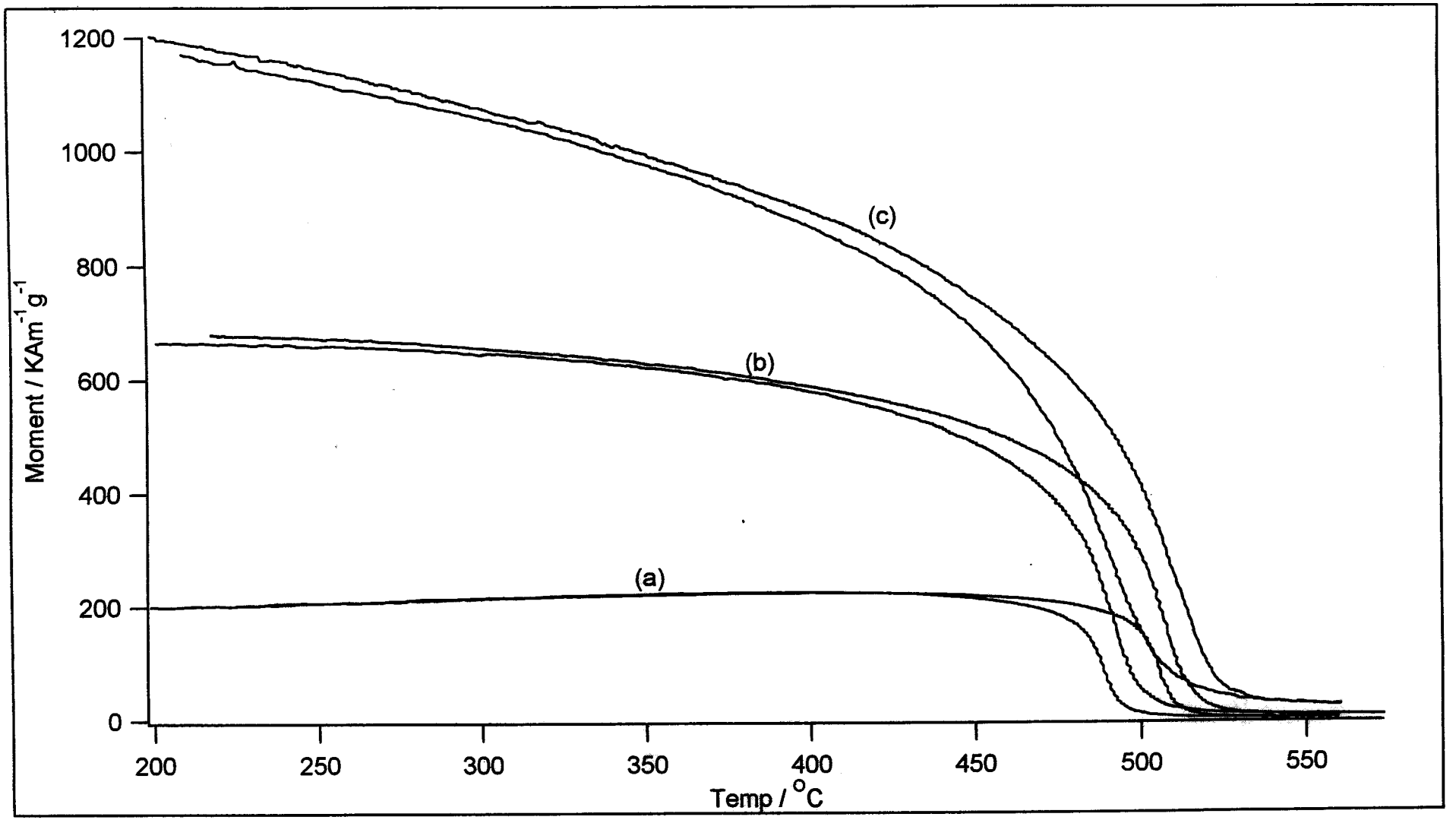

Figure 5.16: Magnetic moment of British Steel duplex in applied fields of:
(a): 0 KAm^{-1}, (b): 50 KAm^{-1} and (c): 230 KAm^{-1}

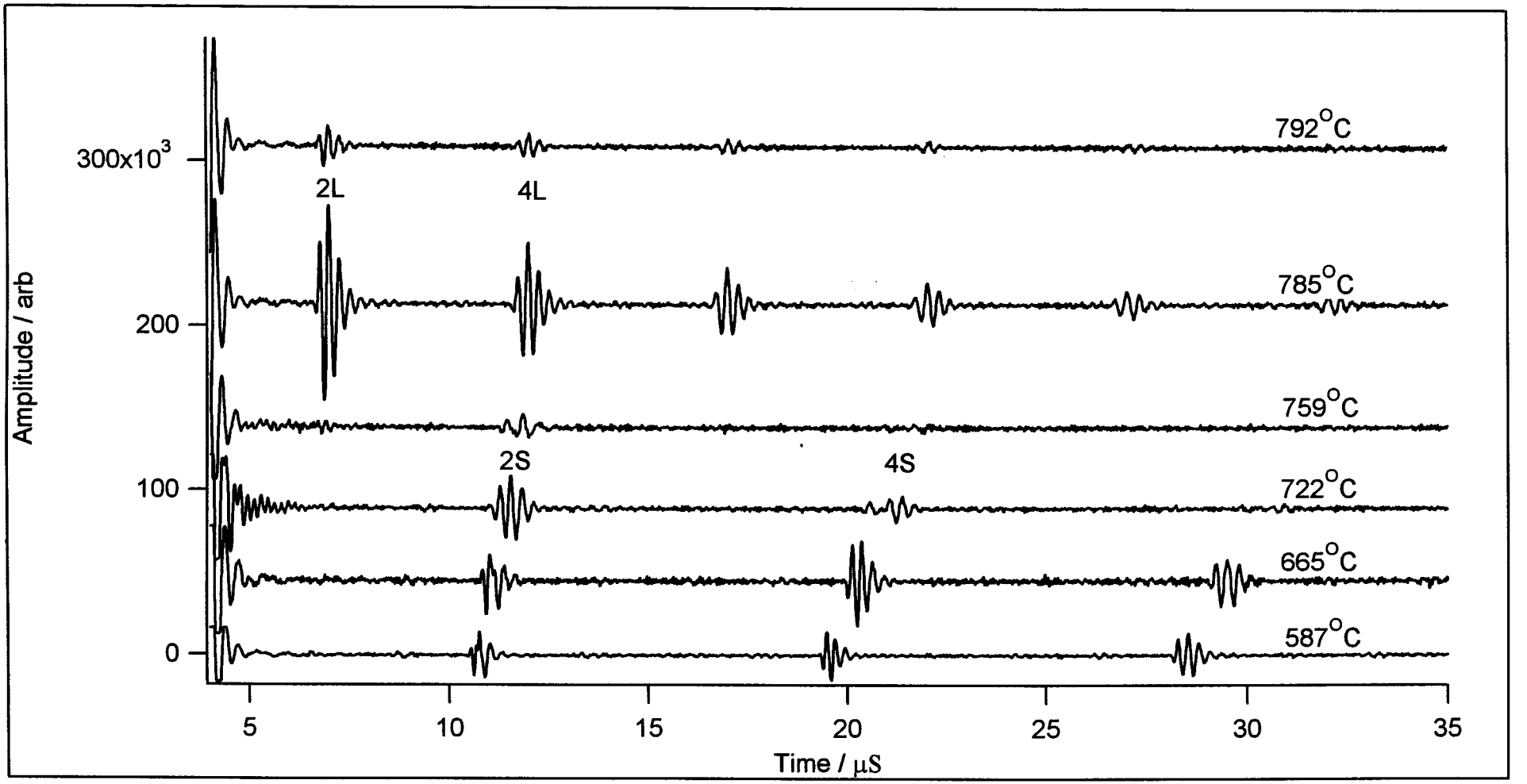

Figure 5.17: EMAT traces from mild steel below and above T_c (780°C)

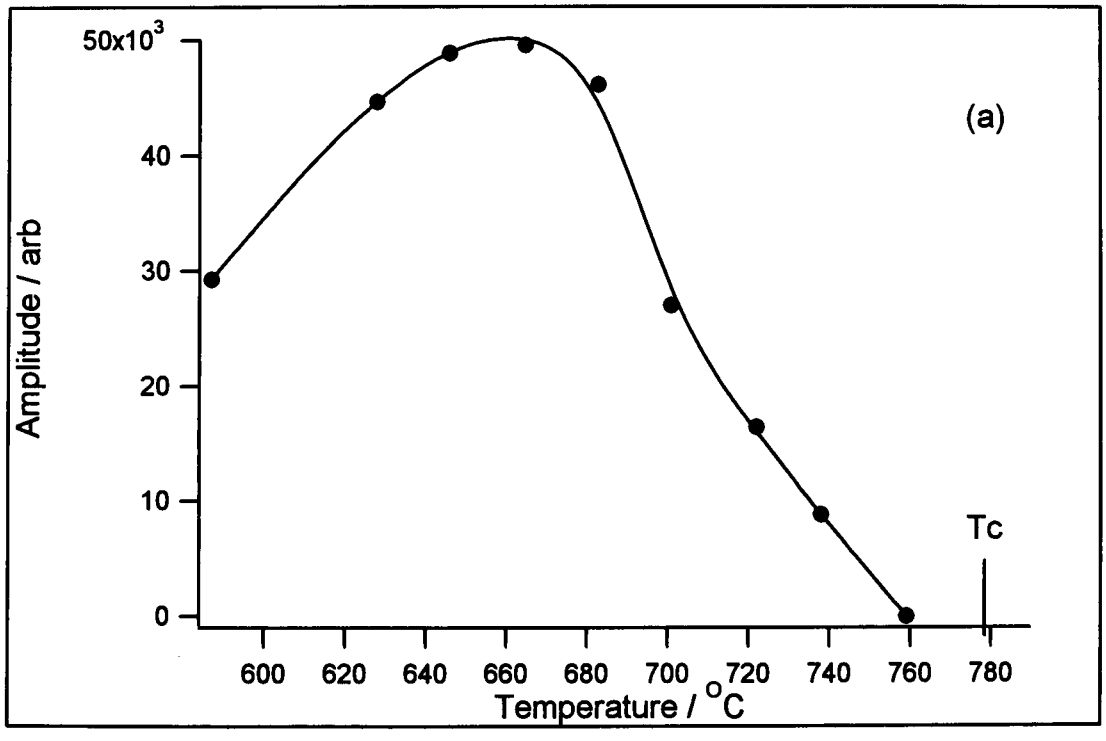

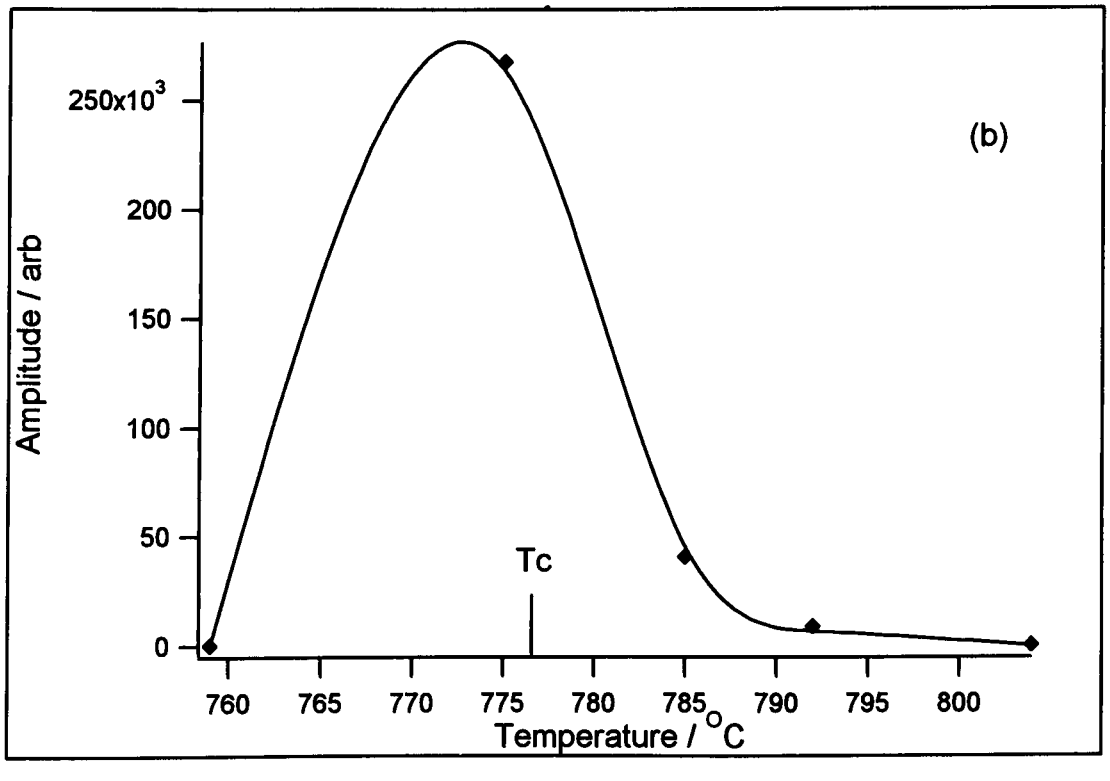

Figure 5.18: Temperature dependencies of (a) shear and (b) longitudinal amplitudes in mild steel

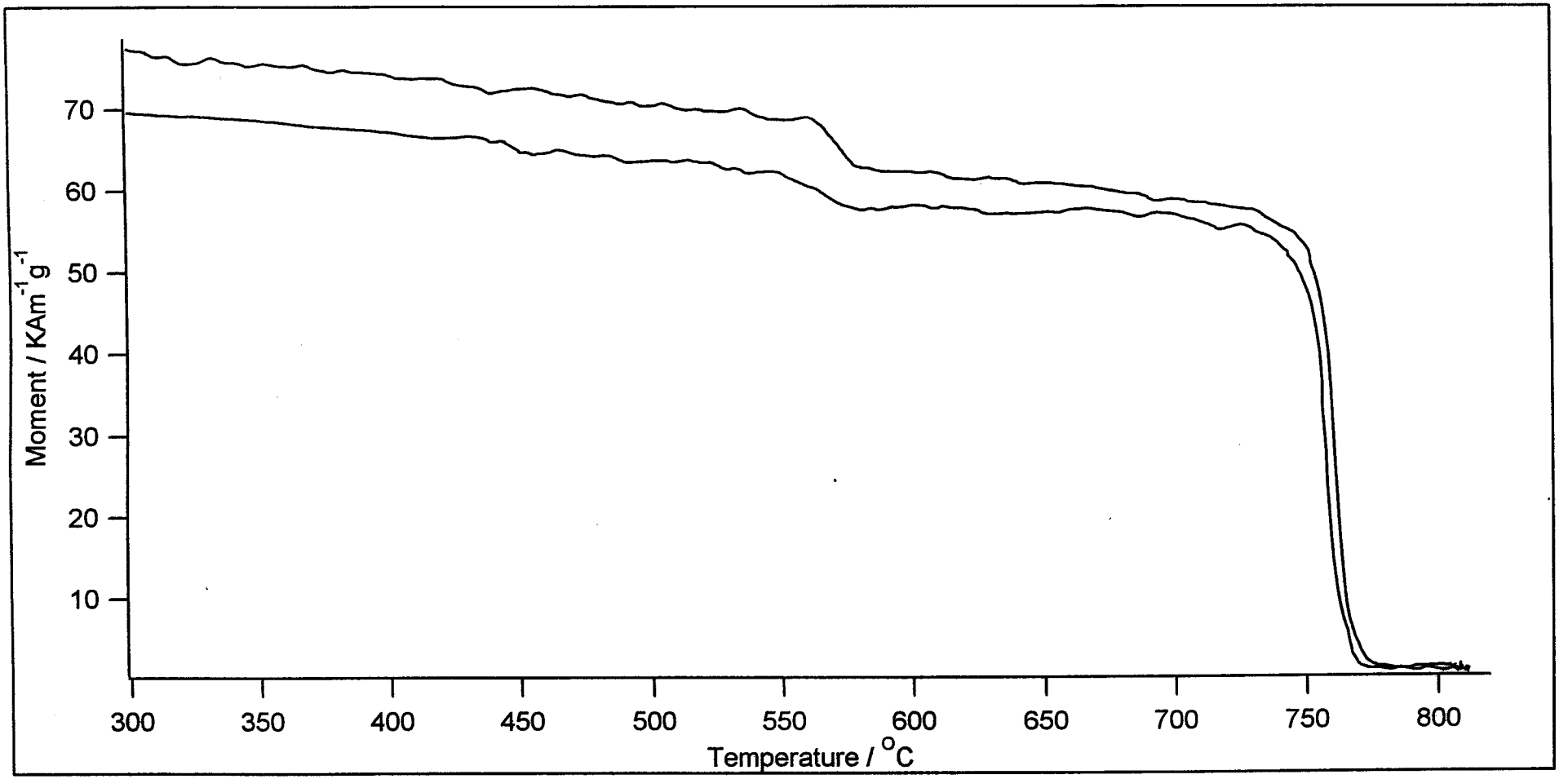

Figure 5.19: Temperature dependence of the remnant magnetic moment of mild steel

Chapter 6

Interferometric detection of EMAT generated ultrasound

6.1: Introduction

This chapter deals with an investigation into the ultrasound actually generated by the spiral coil EMAT. It begins with a justification for the method used and goes on to present the results of using this method on several different samples. The chapter ends with suggestions for further work that would hopefully answer some of the several questions still remaining.

6.2: Justification

A problem inherent in studying the ultrasound generated by any transducer is the response of the detector to that ultrasound. In the previous chapters we looked at the EMAT efficiency in terms of a send-receive system, ie: the generation/detection response as a whole was studied. This meant that the generation and detection mechanisms were assumed to be reciprocal, this is certainly the case for non-magnetic samples [1] but may not be for magnetic materials. Whilst this is fine in terms of EMAT applications, where a send-receive system is almost always used, it does not tell us purely about the ultrasound generated. To study only the generation mechanism it is necessary to use a different kind of transducer for detection, ie: a through transmission set up. This has usually been carried out in the past using

piezoelectric type detectors [2], as used prevalently in the NDE industry, but has never been done, as far as the author is aware, for the radial shear EMAT geometry of interest here. Piezoelectric transducers, however, have two drawbacks when considering this particular geometry. The first is common to all geometries and lies in the frequency response of the transducer, this is inherent in its design as these transducers are usually designed with some particular frequency range in mind. This means any components of the ultrasound with frequencies outside this range will not be effectively detected. The second lies in the fact that these EMATs are designed to generate in-plane shear waves. Piezoelectric transducers, whilst ideal for detecting longitudinal waves, are certainly less than ideal for studying shear waves. Shear piezo transducers require mechanical couplant which must be highly viscous to allow shear wave propagation and are also less efficient, generally, in detecting this wave mode. They are also designed to generate/detect only one polarisation of shear wave, this means they would have to be used off epicentre which would further complicate the experimental set up and analysis. The combination of "narrow" frequency response, low transduction efficiency and single polarisation means that some other form of detection is required to study the ultrasound generated by the spiral coil.

For the aforementioned reasons a modified Michelson interferometer was used as a detector to study the exact nature of the ultrasound generated and its dependence upon B_o. The details and specifications of this particular interferometer were given in [3] so are not reiterated here. The advantages of using this instrument are threefold. Firstly, it is possible to measure absolute surface displacements as the ultrasound wave impinges on the sample surface. Secondly, it has a much greater bandwidth than any other type of detector, the response not reducing significantly

from ~ 500 KHz up to around 80 MHz. Thirdly, it may be considered to be a genuine point detector (diameter of beam ~ 1mm), any other transducer output would be an integration of the displacement over the active area of the detector. This means we would not truly be looking at the epicentral displacement generated by the coil. The obvious disadvantage in its use is its sensitivity only to out of plane motion, to detect the in plane shear wave we obviously rely on detection of its associated out of plane motion. This said, however, any other transducer would suffer some other limitation by virtue of its design so it is unavoidable in any case. It was also known that at least one sample, ie: duplex, exhibited anomalous longitudinal mode generation, lending further weight to the argument in favour of this detector.

6.3: Waveform analysis

As will become clear when the results are presented, it was necessary to separate different frequency components from each other within the same ultrasonic echo. This required the FFT (Fast Fourier Transform) to be obtained for each echo of interest. This was done by first extracting the echo from the trace and then subtracting the background slope from it. The background was subtracted by applying a 45 point moving average to smooth out the high frequency components and then subtracting this from the original pulse. The waveform was then further processed by applying a Hanning [4] window function to it, this is basically a $\cos^2$ expression that ensures the waveform falls smoothly to zero on each side. As the FFT algorithm used required a 2^n (n = integer) number of points it was also then necessary to "pad" each side of the echo with zeroes, an example of the result of this is shown in figure 6.1, along with the original pulse (taken from British Gas duplex).

Finally this waveform was FFT'd and its magnitude plotted vs frequency to find the frequency spectrum of the pulse.

6.4: Aluminium

Figure 6.2 shows the interferometer traces recorded at increasing applied fields when the EMAT coil was placed against a 12.5mm thick aluminium sample and driven with a 4.5 MHz tone burst. The echoes detected by the coil are shown in figure 6.5. The results from each are discussed separately below and compared in the summary later. 4.5 MHz was chosen as the drive frequency, f, because this gave the most power transmission into the coil, obviously for different samples the optimum frequency changes due to the change in the coils inductance [5]. Maximum power transmission was used for all the samples studied by adjusting the frequency accordingly.

6.4.1: Interferometer results

The initial pulse at 1.4μs in figure 6.2 is due to electromagnetic pick up of the drive pulse in the wiring of the interferometer, the pick up was reduced using screened leads to connect the pulse generator to the coil. At B_o=0 there is evidence of a small L pulse with a pk-pk amplitude of 12pm at 3.8 μs, superimposed upon a shallow positive gradient in the baseline of the trace, it is also apparent that this pulse has a frequency, 2f, twice that of the drive, f. On application of B_o this 2f component is gradually dominated by one at f until the maximum attained field of 0.17T when the

pulse shape closely resembles that of the drive with a pk-pk amplitude of 60pm. As explained in chapter 2 the 2f component can only be due to the interaction between the self field of the coil and its induced eddy currents in the aluminium surface. The S wave does not appear to suffer any frequency doubling when B_o=0 although it must be remembered that the interferometer detects only out of plane motion so may just be not sensitive enough to detect the vertical displacement associated with the S wave. In order to analyse the field dependence of the f and 2f components the FFT of the 1st L and S arrivals was obtained using the method described earlier. The results of this are shown in figure 6.3, plots of the FFT amplitude vs B_o for the 4.5 and 9 MHz components. As one would expect, the S wave shows a linear relationship between B_o and the amplitude of the 4.5 MHz component. The linear relation between the 1L 4.5 MHz amplitude and B_o shows that this is also generated by the same source as that generating the 1S wave. The amplitude of the 1L 9MHz component, in contrast, is B_o independent, just as predicted by the self field model.

It was stated earlier that the displacement waveform is a convolution of the impulse response with the transient function of the drive pulse. The point normal force source was shown by Knopoff to generate a large longitudinal step with a much smaller shear step. Convolution of this response with the gaussian enveloped sinusoidal drive pulse therefore produces a noticeable L transient echo with a minimal S wave response (see figure 6.4a). This is just what is seen in zero field where it is predicted by the self-field model that the force is frequency doubled and acting normally to the surface. In sufficient B_o the source becomes more like the thermoelastic one predicted by Rose and exhibits a large S wave transient response with a longitudinal echo that should be ¼ of the size of this (see figure 6.4b).

Obviously, as the response of the interferometer is to the out of plane motion associated with the L and S modes, the relative amplitudes of both appears similar. Dixon [5] treated the spiral coil as a series of laser ring sources, the extended point thermoelastic source having been being dealt with by Bresse [6], and showed that this was consistent with the observed EMAT response, although measurements of the actual surface displacement were not made.

6.4.2: EMAT results

Figure 6.5 shows the waveforms received by the coil itself, ie: in send-receive mode, it is obvious that with B_o=0 no ultrasound is detected at all. Application of as little as 0.045T is sufficient to allow detection of the 1st and 2nd S echoes but no detection at all of the L mode. Higher applied fields lead to larger S mode amplitudes but still no reception of the L mode, even though the interferometer clearly shows that this mode is being generated. The conclusion from this is that the mechanism of detection on aluminium is sensitive purely to in-plane motion. This is reasonable given that we only have B_o normal to the surface and assume a purely Lorentzian generation and detection mechanism. Obviously during generation the self field of the coil interacts with the eddy currents and produces the 2f longitudinal mode, on reception this field is absent so we would not expect to detect it with the geometry we are using. This argument is further reinforced when we consider the longitudinal mode generation with an applied field of 0.143 T. The interferometer shows that a pulse is generated at the drive frequency but again is not detected by the coil, the in-plane motion associated with the L mode being too small to be detected in the B_o experimentally attainable.

6.4.3: Summary

The previous chapters have shown that the Lorentz interaction between the normal static field, B_o, and circular eddy currents, j, generates radial shear waves and that these are detected by a reciprocal mechanism. The interferometer has shown that a frequency doubled longitudinal mode is also generated, consistent with the model involving the coils radial dynamic field and these same eddy currents. The linear B_o dependence of the f component of the L wave shows that it is produced by the same mechanism as the S wave. This is expected given that the radial S waves produce mode conversions on reflection [7], ie: they are not strictly isovolumetric. The EMAT coil does not detect any L modes, either mode converted or direct, due to the relatively low B_o and smaller pulse currents than those used in the handheld EMATs discussed previously.

6.5: Nickel

The nickel sample used here was the same as that used in chapter 4, an 8.4 ± 0.05mm thick 99.99% pure polycrystalline block. The waveforms obtained by the interferometer and coil are shown in figures 6.6 and 6.7 respectively. In this case the coil was driven with a 5.7 MHz tone burst.

6.5.1: Interferometer results

As for aluminium there is evidence of e/m pick up of the drive pulse by the interferometer electronics. It was found that this was of some help in determining the exact trigger point at which the coil was energised so was left uncorrected. The L and S arrivals are apparent at 2.8 and 4μs respectively although due to the small sample thickness (8.4mm) they are not well separated. With B_o=0.02T there is evidence of a small frequency doubled L component together with some harmonic component in the S wave, although no frequency doubling. It is not until B_o=0.17T though that the shear harmonic component is seen to reduce almost to zero. This is consistent with chapter 4 although B_o at the S minimum in that case was 0.3T, a discrepancy of 0.13T. However, the f component of 1S when B_o=0.02T is reversed relative to that in 0.17T suggesting that the field measurement may be wrong and B_o is actually reversed until ~0.13T is applied. This is consistent with the experimental technique where B_o was measured after the interferometer traces were all recorded. Thus the sample was cycled through half a minor hysterisis loop before the B_o readings were taken. The figure of 0.13T also correlates with the VSM data that show a remnance of 0.12T after saturation. It was therefore concluded that this sample had been saturated with a reversed B_o prior to the experiment and that this had resulted in a 0.12T offset in the B_o measurements. With this taken into account the results give excellent agreement with those obtained earlier. Given this observation it was decided that each sample should be demagnetised both before using the interferometer and prior to the subsequent B_o measurements.

There is a striking positive "hump" associated with the S arrival in figure 6.6 and a smaller one with the L arrival. The presence of this large background displacement in the S arrival strongly suggests that it is due to a magnetoelastic source, being completely absent from the S mode in aluminium, in which only the self field mechanism can act when B_o=0. The background shear response can be accounted for by the action of a low frequency magnetostrictive source. It will be recalled that the tone burst consists of a sine wave convolved with a Gaussian envelope. This envelope has an effective frequency of ~ 400KHz and therefore extends ~ 3.5 times further into the surface than the sinusoidal component. Buchel'nikov [8] states that for a magnetostrictive source the highest ultrasonic amplitudes are produced when δ is large. Therefore, the large shear 'background' with little transient response when B_o=0 could be explained by the action of a 'strong', deep δ, 400KHz magnetostrictive source and a 'weaker', shallower δ, high frequency magnetostrictive source. It should also be mentioned that the coil being an extended source could account for the low frequency features observed. Bresse showed that the steps due to Rose's thermoelastic source become less sharp when the source is larger than a point. Convolution of this with the Gaussian enveloped pulse produces similar waveforms to those of figure 6.5 but with noticeable background trends just as seen with the interferometer. However, the actual source for this background must be magnetoelastic in origin as it is field independent and therefore cannot be due to the Lorentz mechanism.

It was stated previously that magnetostriction leads to frequency doubled ultrasonic generation [9] by virtue of its 180^{O} symmetry. The fact that it is anisotropic also allows the generation of strains normal to the surface to be produced by the action of

a purely radial field, such as that from a spiral coil. However, if this was the case, then the shear wave would also be expected to show such doubling and the impulse response would be more akin to the thermoelastic one. This is especially true for nickel where its low anisotropy means equation 2.25 always holds, unlike steels where λ_t could be quite different to $-\frac{1}{2}\lambda_l$ due to an orientated microstructure [10]. The question is raised therefore as to why no 2f element is seen in the S arrival. Even taking into account its small δ and the interferometer's sensitivity only to out of plane motion if the source was magnetostrictive and 'thermoelastic like' then some frequency doubled shear response should be visible. The lack of it suggests that the source of the 2f L mode is the normal self field Lorentz force. The lack of any doubling in the B_o=0 S mode can be explained by the lack of 180^O symmetry in the magnetostriction curve of nickel. An S mode is certainly generated when B_o=0, however, the turning point in λ for iron is not present at B=0 in nickel, due to the large hysterisis, and hence no frequency doubling is observed.

The FFT amplitudes of the 1L 5.7MHz and 11.4 MHz components are plotted in figure 6.8a together with the FFT amplitude of the 1S 5.7MHz component. The scatter in the 1L 11.4 MHz component makes any statement on its field dependence uncertain although it does appear similar to that in aluminium, confirming that it could be due to the same mechanism. The B_o dependence of the 1L 5.7 MHz FFT amplitude correlates with that of the same component in 1S and indicates that they are produced by the same source. Finally, the 1L waveform in aluminium shows a self field component that clips off the top of the harmonic component, in nickel the reverse is true. This suggests that whilst the 2f component is generated by the same self field mechanism, the f components in the two samples exhibit a 180^O phase

difference that can only be due to a 180^{O} difference in their sources. This is potentially consistent with generation purely by F_L in aluminium but predominantly by a 'negative' ε_m in nickel.

6.5.2: EMAT results

The signals detected by the EMAT coil are shown in figure 6.7. The traces are very similar to those recorded in chapter 4 with the S echoes dominating the trace and present when B_o=0. There is no evidence of detection of a 2L echo in any B_o even though the interferometer shows that an L wave is generated and SL mode conversions are clearly detected. The small ripple just after the initial drive noise at 0.33 T is almost certainly due to a poor earth connection between the sample and the coil. This feature has been seen many times before when using hand held EMATs and, given its sudden appearance, is certainly not due to a real ultrasonic echo. The 2S FFT amplitude is plotted vs B_o^2 in figure 6.8b and shows a non linear relationship consistent with that observed earlier.

6.5.3: Summary

The interferometer showed that, just as in aluminium, an L mode is generated by the spiral coil and that this exhibits frequency doubling in very low B_o. A marked difference between the two metals exists in the trace 'background' features which can only be due to the magnetoelastic nature of nickel. The fact that such a large, low frequency, shear response is observed in almost zero field is strongly suggestive

of a thermoelastic like magnetoelastic source. The frequency doubled component of 1S, however, is negligable suggesting that the Gaussian envelope to the pulse may be important in the production of the large S hump.

6.6: Invar

Traces recorded by the interferometer between 0 and 0.495T with the EMAT coil on the 13.3 ± 0.05mm thick invar sample are shown in figure 6.9. Figure 6.10 shows the signals detected by the same coil, a drive frequency of 4.5 MHz was used throughout the experiment.

6.6.1: Interferometer results

With B_o=0 there is clear evidence of a 2f L mode at ~ 9μs exhibiting a negative displacement (ie: inwards) background slope and a pk-pk amplitude of 75pm. The S arrival, as in nickel, exhibits no signs of frequency doubling and also has the large displacement hump seen previously. The small ripple just after the drive pulse (5μs) arrives too early to be due to any ultrasonic mode and must therefore be due to some e/m pickup, although the source of this could not be identified. The fact that the 1L arrival exhibits a negative trend sets it apart from the same mode in nickel and suggests that it is caused by a magnetoelastic source, the magnetostriction of invar being opposite to nickel. This would also correlate with the fact that the 9MHz L component clips the top of the pulse, whereas it clipped the bottom of it in nickel. However, just as in nickel, the magnetostriction in low fields is relatively small so

we would not expect to observe such a large L amplitude. Given this large amplitude it is also clear to see that the waveform is symmetric and sinusoidal.

Komarovs treatment of magnetostrictive frequency doubling assumed a 180^{O} symmetrical sinusoidal function for the magnetostriction with no hysterisis. Under these circumstances the resultant strain waveform would appear as a rectified sinewave as shown earlier. Obviously some degree of rectification must be lost due to inertial effects but we would still expect to see some evidence of asymmetry in the pulse. In contrast, the self field model predicts a perfectly sinusoidal and symmetric waveform just as that observed in invars 1L arrival. The apparent B_o independence of the 1L 9MHz component shown in figure 6.11a is also consistent with the model, the amplitude being dependent purely upon the pulse current. It should be mentioned, however, that a magnetostrictive source also shows only a slight reduction in the amplitude of the frequency doubled component with increasing field. Figure 6.12a shows the predicted waveforms produced by an oscillating field at various bias points on a quadratic approximation to a magnetostriction curve. The amplitudes of the f and 2f components are plotted in figure 6.12b and were found by taking the FFT of each waveform as described earlier. It is clear that whilst the amplitude of the f component experiences a significant increase there is a relatively small decrease in the 2f amplitude. Therefore, it cannot be assumed that just because the 2f component appears relatively field independent it is due to the self field. The self field force is normal to the surface and therefore should generate very little S response. This fits the results in terms of the large L transient amplitude but does not account for the large S feature seen in any B_o. The presence of this feature can, as for nickel, be explained by the action of a deeper low frequency magnetostrictive

source. It should be recalled, however, that the λ_l of invar exhibited unusually erratic behaviour below 0.8T so the assumption of a deeper magnetostrictive source is not safe.

6.6.2: EMAT results

The EMAT traces of figure 6.10 show immediately that the direct longitudinal wave is detected by the coil in fields as low as 0.15 T. With no field applied the coil also appears to detect a 2f mode at ~ 8.5 μs, although given its arrival time this cannot be a longitudinal echo. The source of this signal remains unidentified. The B_o dependence of the 2L amplitude appears to be linear suggesting that it is due to Lorentz detection of the in plane component. The mode conversion at ~ 9μs shows signs of frequency doubling in low fields suggesting that it is predominantly due to conversion from the 1L mode (ie: LS). Again, the amplitude of this echo increases linearly with increasing field, suggesting that its detection is also due to the Lorentz mechanism. The 2S FFT amplitude shows an almost linear dependence on B_o^2 (figure 6.11b), although signs of non linearity begin to show at the higher end of the range (> 0.4 T). These results differ markedly with those of chapter 4 and suggest that quite different mechanisms are dominant when using a broadband pulse or a Gaussian enveloped tone burst.

6.6.3: Summary

The interferometer showed a significant frequency doubled component to the L mode that was suppressed with application of B_o. The doubled component cut off the top of that of the drive indicating a distinct difference between the effect in invar and nickel. This is also consistent with the background to 1L that is negative here and positive in nickel. In contrast, the S mode exhibits the same trend in both samples even though λ is opposite in the two cases.

6.7: Duplex

Drive frequencies of 5.3 MHz and 4.7 MHz were used to drive the EMAT coil on BG (13.7 ± 0.05mm thick) and BS duplex (7.1 ± 0.05mm thick) samples respectively.

6.7.1: Interferometer results

The interferometer traces from the BG supplied sample and those from the BS sample are shown in figures 6.13 and 6.14 respectively. A marked difference between the two lies in the L wave generation, the BG sample showing a significant 2f component with very little indeed in the BS sample. In fact the BG results are almost identical to those from invar, strong evidence that the generation mechanisms are the same in each case. The two duplex samples also exhibit frequency doubling

of the S mode in low fields, to an extent not seen in invar, although it is bordering on being unresolvable. The fact that 1L in the BS sample shows such a small degree of frequency doubling is unexpected given the results from invar and BG duplex. It suggests that the doubling mechanism in this duplex is very much weaker than in the other. The argument that high attenuation could be responsible for the amplitude differences is effectively ruled out by the small BS sample thickness. We are left then with the conclusion that the doubling mechanism is genuinely much weaker in the BS sample than in the BG one. This is difficult to understand in the self field Lorentz model as F_L should be independent of both μ and σ for $d<<\lambda$. We are therefore lead to conclude that the 2f component of 1L in the BG sample is most likely generated via a magnetostrictive mechanism. Consequently the earlier proposition of invars 2f mode being due to the self field force is cast into doubt.

This said, as BG duplex possesses such a highly orientated microstructure we must also consider the effect this may have on the self field mechanism. Any regions under the coil with ferrite grains aligned radially will have a much lower N_d than those aligned orthogonally to it. As such the induced field in these grains will be higher than that in either the austenite grains or those ferrite grains aligned orthogonally. Consequently the self field Lorentz force will be higher and so will the resultant strains. In contrast, the BS sample, being far more isotropic, will exhibit a homogeneous B_o and therefore no regions of higher local strain. This could also produce the observed difference in the results from the two duplex samples. In fact, given the columnar microstructure of the BG sample it is possible that the grains could retain a higher remnant field, after the coil was pulsed, than any of the other

samples. This would then allow subsequent detection of a returning L mode with no B_o applied.

6.7.2: EMAT results

The traces detected by the coil on the BG and BS samples are shown in figures 6.15 and 6.16 respectively. Figure 6.15 shows evidence of detection of the 2L mode in the BG sample although this is minimal in extent, there is, as expected, no evidence of L detection at all in the BS sample. This contrasts quite starkly with the results of chapter 4 that showed clear longitudinal signals in the BG sample with a peak in efficiency when B_o=0. It was suggested above that the anomalous L mode detection could be due to a remnant field in the long, low N_d, ferrite grains of the BG sample. The fact that it appears to be very weak when using a tone burst correlates well with this argument. The gaussian enveloped pulse is, in effect, a demagnetising pulse, exhibiting a positive – negative swing with a gradually reducing amplitude. Therefore any net radial remnant field would be all but destroyed by this and the L detection would be correspondingly much weaker. In contrast, the broadband drive used in chapters 4 and 5 consists of a purely unipolar current pulse that would result in a radial field with no opposite swing and a high amplitude. Under these conditions the remnance could be much higher and L detection would be more efficient than with the tone burst. This may also account for the reduction in L amplitude on application of B_o. As the moment swings out of the plane of the surface, due to B_o, there is a lower net radial field and therefore the radial B_o required by the Lorentz mechanism is also lower.

6.8: Mild steel

The EMAT coil was driven by a 4.73 MHz tone burst on a 12.56 ± 0.05mm thick mild steel sample identical to that used in chapter 4.

6.8.1: Interferometer results

The interferometer results are shown in figure 6.17 for fields up to 0.4 T. The trace for B_o = 0.007 T shows very slight evidence of frequency doubling in both the L and S modes. This is consistent with the results of chapter 4 that showed low EMAT efficiency in this sample. The very low amplitude of the 2f L mode (pk-pk = 10pm), however, is difficult to account for using the self field Lorentz model. This predicts that, just as for Lorentzian S generation, ε should be independent of both μ and σ. Therefore, neglecting any 'focussing' of the radial field, ε should be higher, given its lower ρ, in mild steel than duplex. The results, however, are quite to the contrary and suggest that the self field ε is almost undetectably small in mild steel. This is surprising given the 2f amplitudes in nickel, invar and duplex and casts doubt on the earlier supposition that the self field force was responsible in these samples. Higher attenuation could of course be responsible for the much lower amplitudes although the previous chapters indicates that this is probably not the case. As the previous experiments strongly suggested that the signals in mild steel were almost entirely of Lorentzian origin it is difficult to see how a predominantly magnetostrictive source could be responsible for the weak 2f L mode. We are left then with the conclusion that the self field force is genuinely much weaker in mild steel than the other

ferromagnetic samples. The trace at B_o=0.352T shows very similar amplitudes for the 1L and 1S arrivals. This is consistent with the thermoelastic like radial source that exhibits an S feature Poissons ratio bigger than the L step. This factor is then cancelled by the interferometer's sensitivity only to out of plane motion to produce the waveform obtained with 1L and 1S amplitudes equal. It is confirmed then that the ultrasound generated in moderate B_o on mild steel is consistent with the thermoelastic source that was also found to correlate with the results from aluminium, a purely Lorentzian generator. The low frequency features of the traces are similar to those in both invar and duplex and can again be explained by a thicker Gaussian enveloped magnetostrictive source.

6.8.2: EMAT results

The coil detected traces are shown in figure 6.18 for B_o=0.007 up to 0.352T. It is noticeable that the 4S echo exhibits much lower amplitude than either 2S or 6S, this being due to the modulation caused by weak birefringence and consequent interference between the two polarisations. The 2S FFT amplitude vs B_o^2 plot of figure 6.19 shows signs of non linearity although given the low field range (B_o/B_s = 0 – 1/6) it is unclear whether this is an overall trend.

6.8.3: Summary

The small f and 2f amplitudes are consistent with the results of chapter 4 that showed low EMAT efficiency in this steel. The fact that the low frequency 'trends' are the

same as those seen in duplex and invar can again be accounted for by the action of a deeper magnetostrictive source. The lack of a significant frequency doubled 1L component is inconsistent with the self field model and raises doubts as to the previous assertion that this was responsible for generation of this mode on the other ferromagnetic samples.

6.9: Conclusions and further work

Using the interferometer has shown that in all the metals and alloys tested a frequency doubled L wave is generated by the spiral coil. In every case this component was seen to be swamped by one at the drive frequency on application of B_o. This B_o also lead to an increase in the transient amplitude of the S mode, similar behaviour being shown by the L. This contrasts with the background trends of both modes that appear relatively field independent and are likely due to a low frequency magnetostrictive excitation over the coils extended source. The fact that both S and L drive frequency components in all the samples exhibit similar field dependences suggests that they are due to the same source, this source being magnetostrictive in nickel, invar and duplex and leading to an L mode by virtue of the non isovolumetric nature of radial shear waves. The B_o=0 waveforms of all the ferromagnetic samples are consistent with a self field mechanism in that it acts normal to the surface and should therefore produce a very small transient S response compared to the L. This was modelled above for a point source and found to be consistent with the results from all of the samples.

An obvious extension of the present work would be to use higher applied fields to look for the re-emergence of frequency doubling in mild steel due to the turning point in its λ curve. This, however, would require considerable modification to the experimental arrangement employing, ideally, an electromagnet to produce a higher and more uniform field. A second potentially useful development would be to use a purely Gaussian unipolar pulse as the drive. This may help to elucidate whether the background trace features are indeed due to a low frequency magnetostrictive excitation and would also remove any doubt as to the phase of the ultrasound. Thirdly, measurements of the ultrasonic directivity may help in better determining the source distribution and therefore identifying the dominant mechanisms. For the moment it must suffice to say that the self field force does indeed act in a non magnetic conductor to produce a frequency doubled L mode and that this force must therefore also act in the conducting ferromagnetic samples tested here.

Chapter 6 references

1: E. R. Dobbs; *Physical Acoustics*; Academic Press, London; Ed: W. P. Mason and R. N. Thurston; **10**, pp 127 - 189.

2: M. Hanabusa, T Kushida and J. C. Murphy; *Journ. Appl. Phys.* **44**, pp 5106 - 5110 (1973)

3: A. C. Bushell, C. Edwards and S. B. Palmer; *Rev. Prog in QNDE* edited by D. O. Thompson and D. E. Chimenti, Plenum Press **11**, pp 1315 - 1322 (1992).

4: Igor Pro technical note.

5: S. Dixon; PhD thesis; Warwick University (1994).

6: L. F. Bresse and D. A. Hutchins; *Journ. Appl. Phys.* **65**, pp 1441 - 1446 (1988).

7: K. Kawashima; *Journ. Acoust. Soc. America* **60**, pp 1089 - 1099 (1976).

8: V. D. Buchel'nikov and A. N. Vasil'ev; *Usp. Fiz. Nauk*; **162**, pp 89 - 128 (1992).

9: V. A. Komarov; *Defektoskopiya*, **no 4**, pp 40 - 45 (1981).

10: M. E. Kuruzar and B. D. Cullity; *Internat. Journ. Magnetism* **1**, pp 323 - 325 (1971).

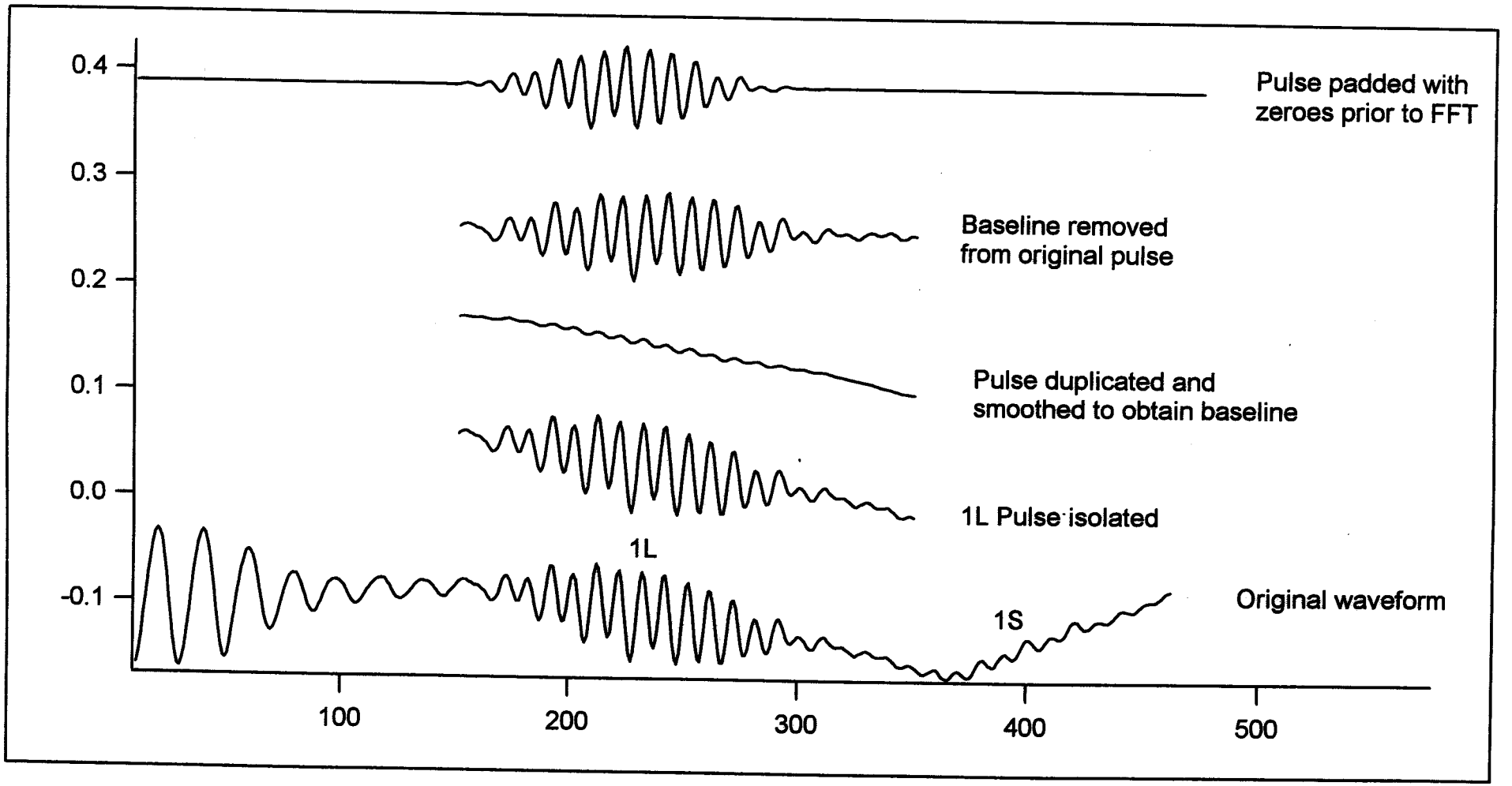

Figure 6.1: Example of the processing applied to the interferometer waveforms to obtain the FFT and thus amplitudes of its frequency components

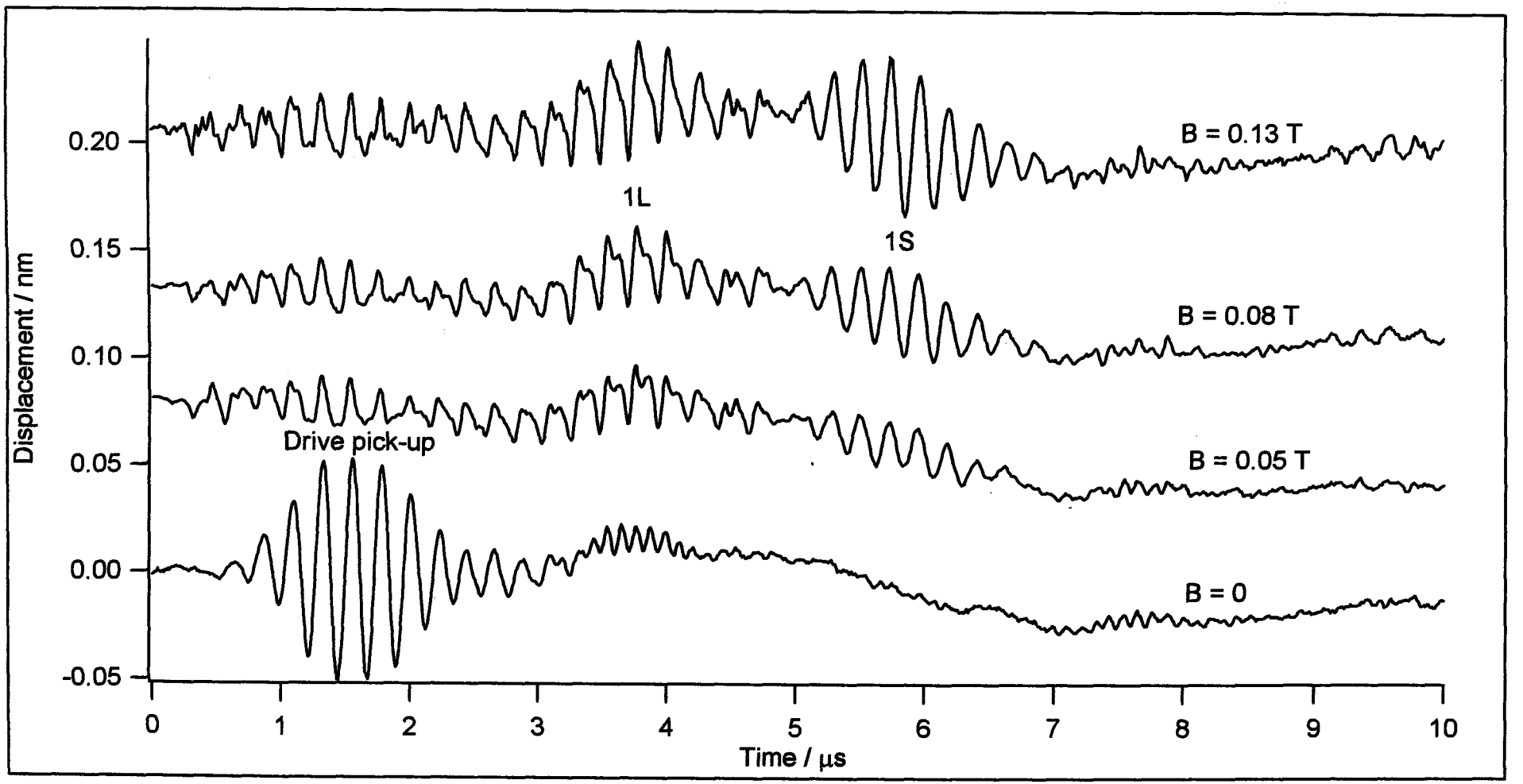

Figure 6.2: Out of plane displacement detected by Michelson interferometer from EMAT coil on aluminium

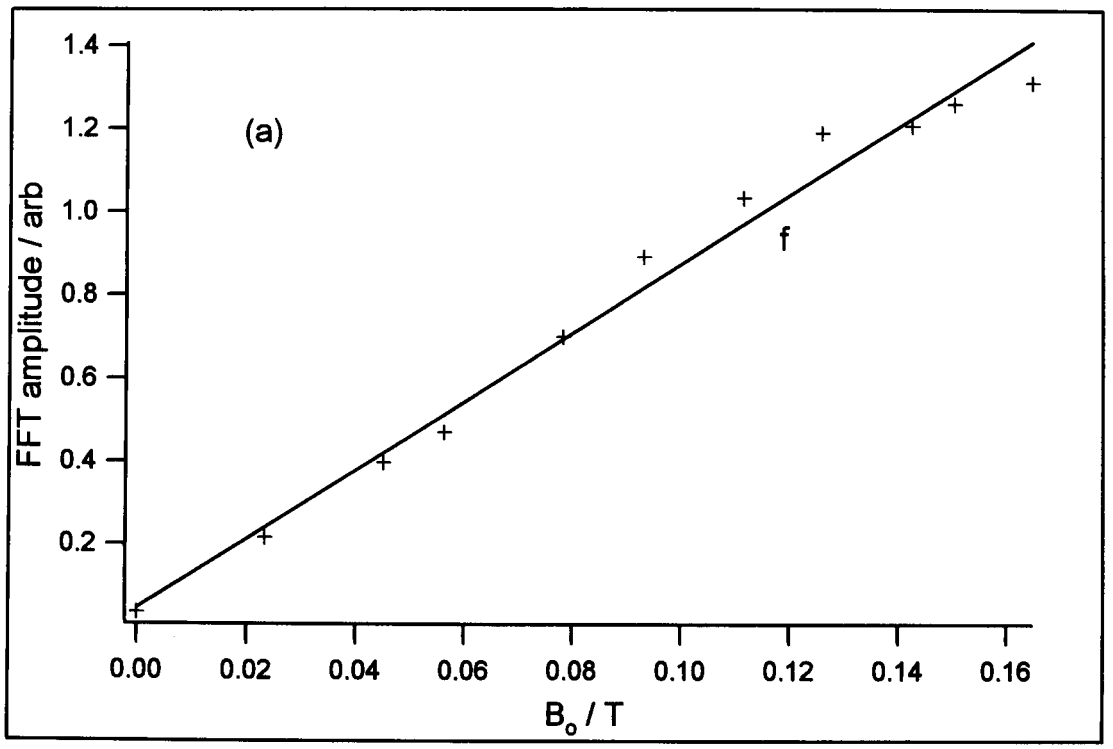

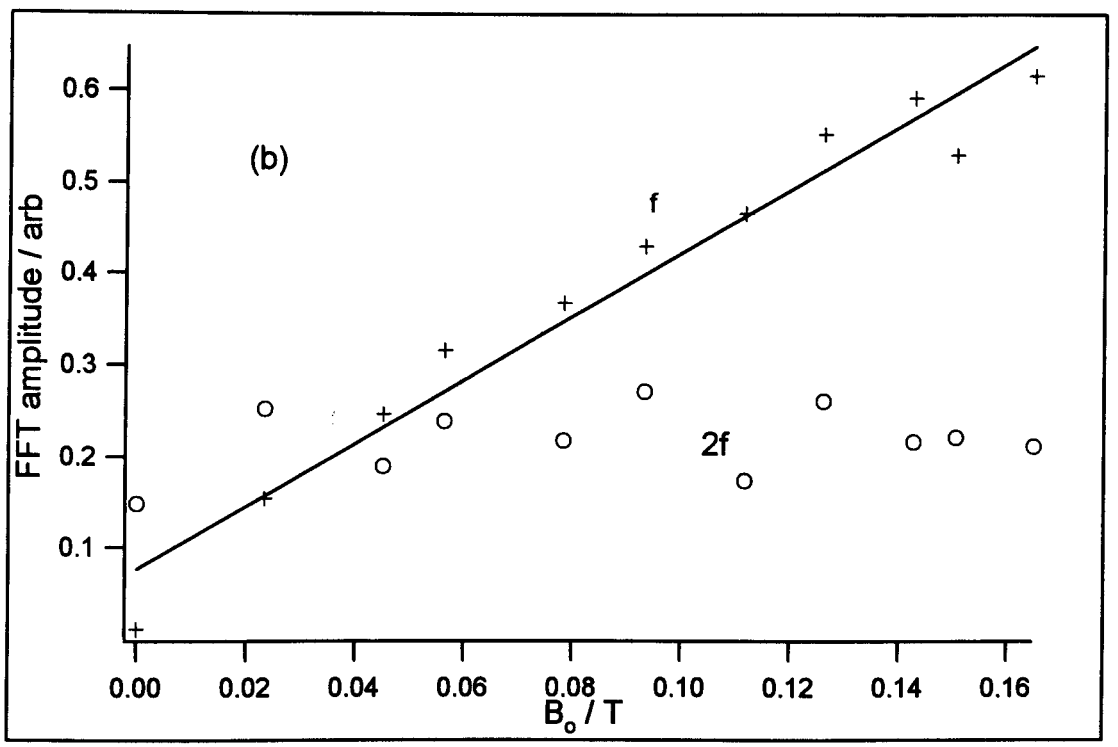

Figure 6.3: (a) FFT amplitude vs B_0 of 1S for EMAT coil on aluminium
(b) FFT amplitudes vs B_0 of 1L for EMAT coil on aluminium

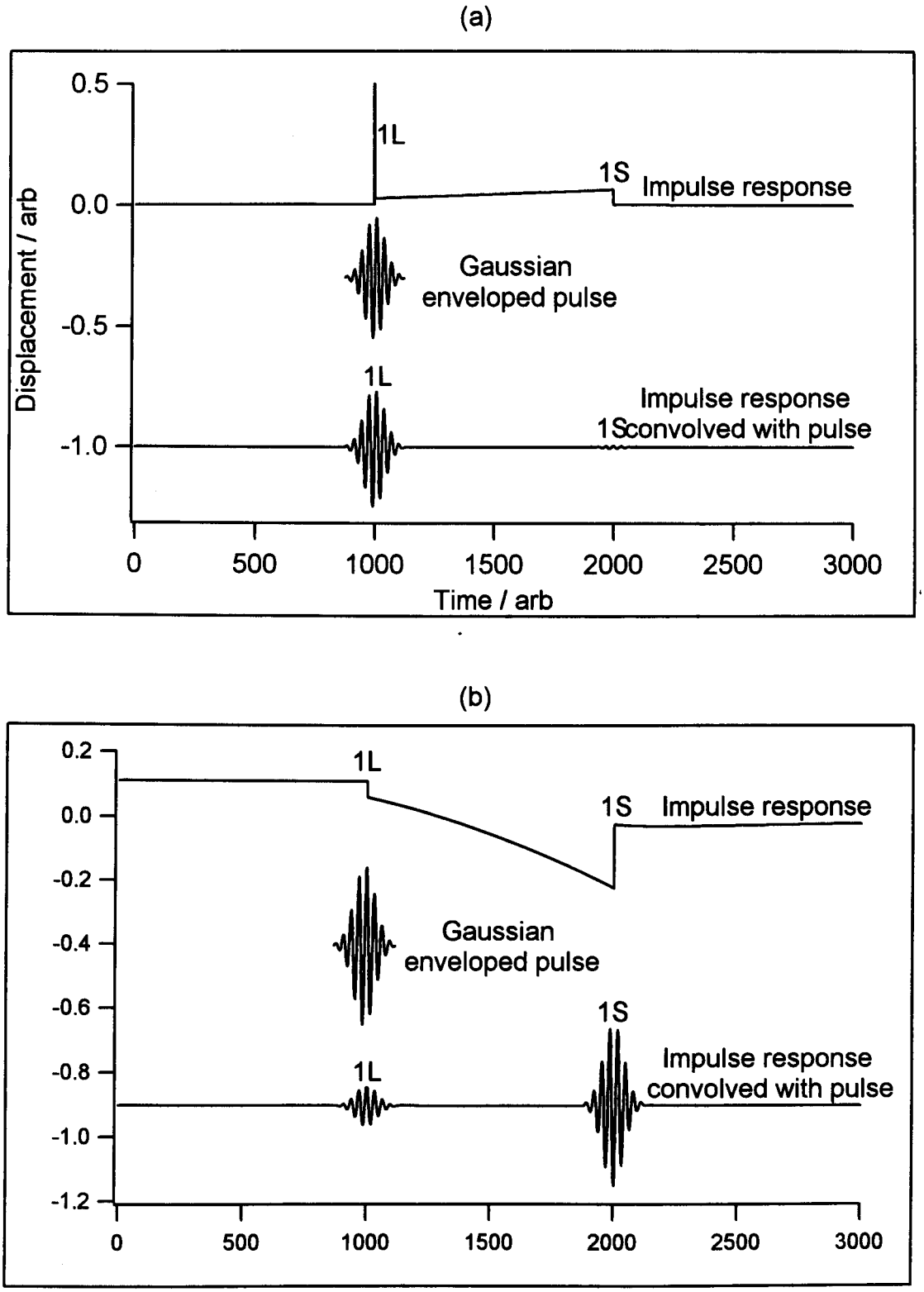

Figure 6.4: Convolutions of the Gaussian enveloped drive pulse with
(a) the point normal force impulse response (Knopoff) and
(b) the point thermoelastic impulse response (Rose)

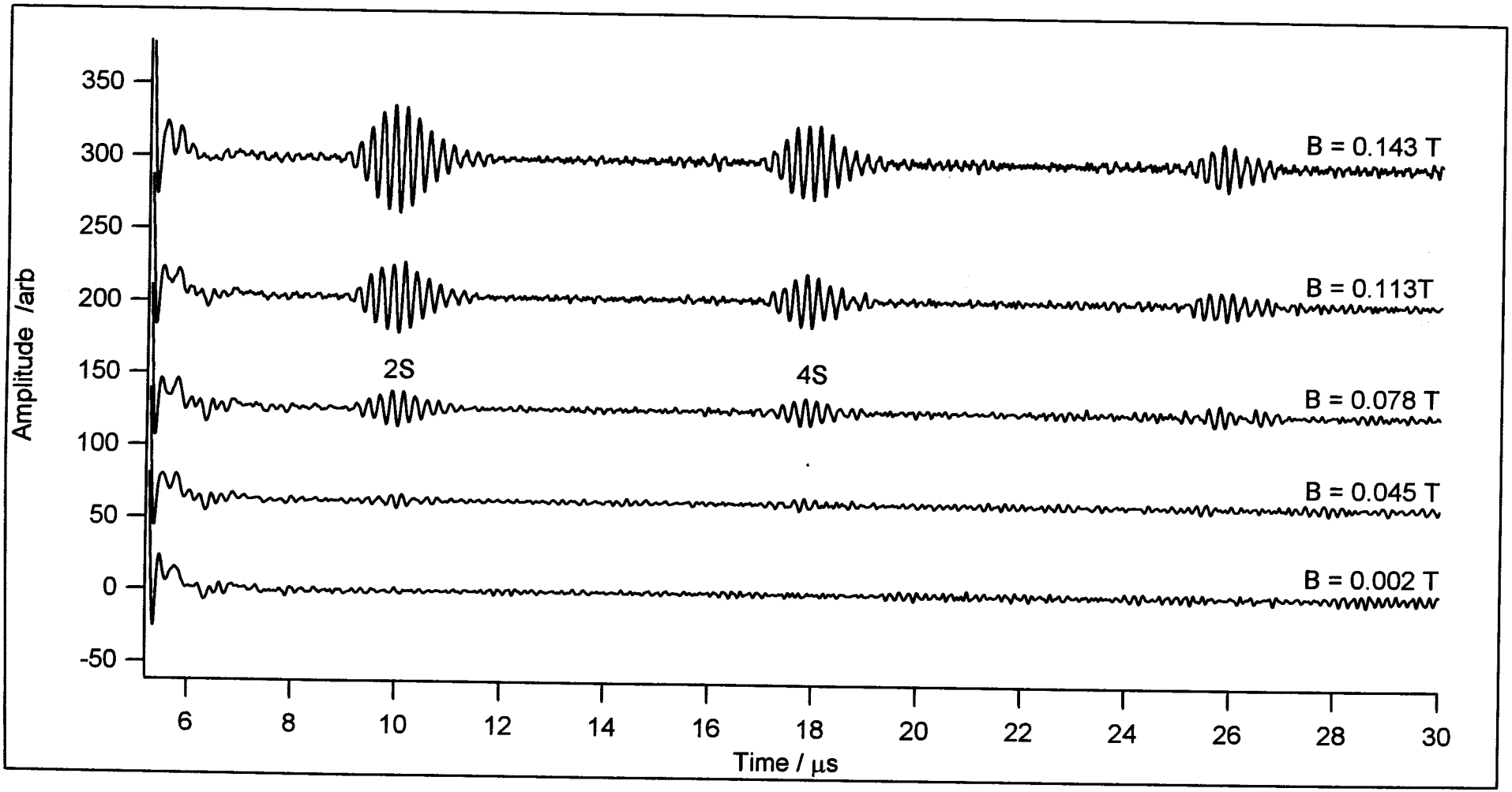

Figure 6.5: EMAT traces from aluminium

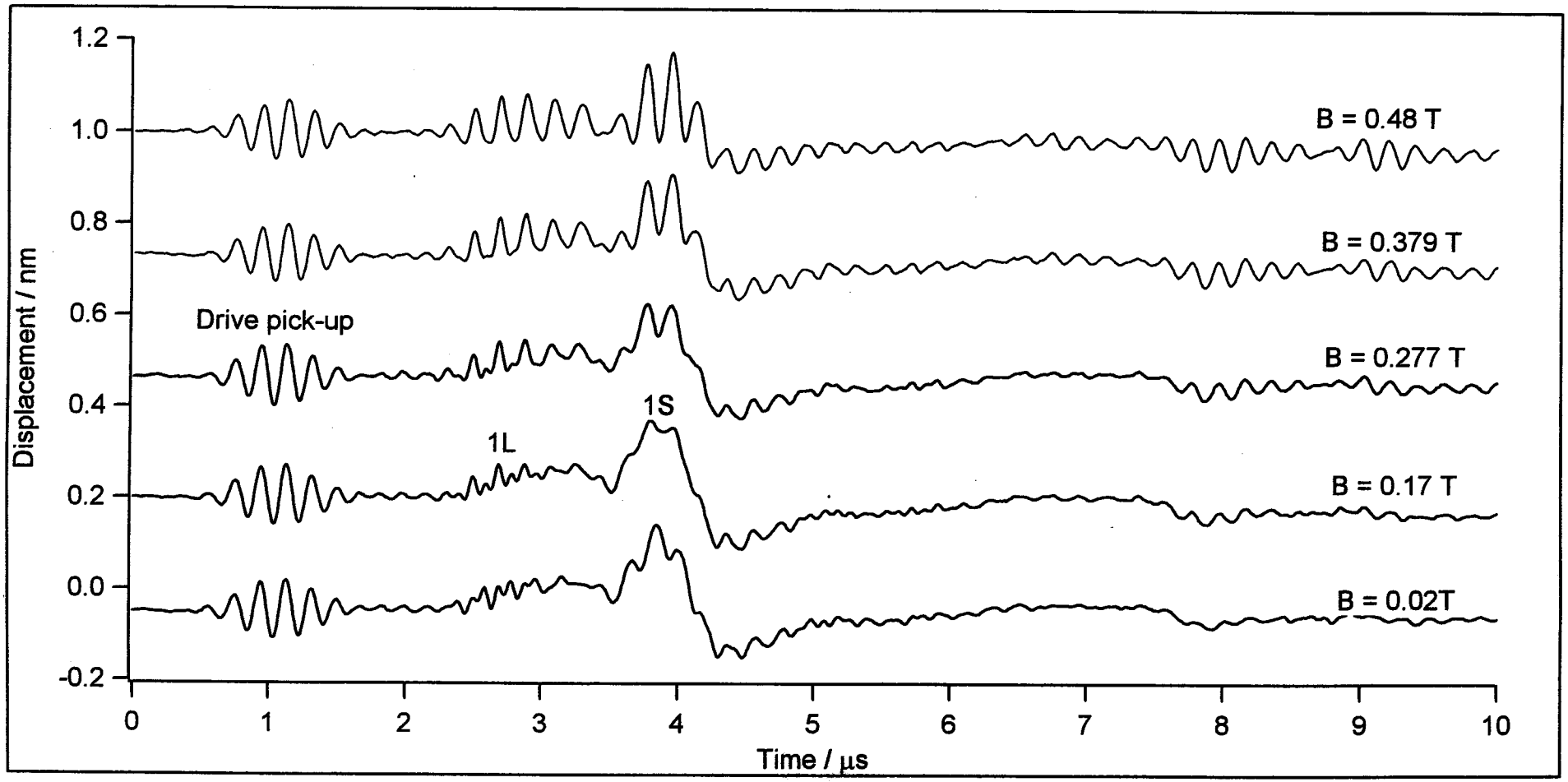

Figure 6.6: Out of plane displacement detected by Michelson interferometer from EMAT coil on nickel

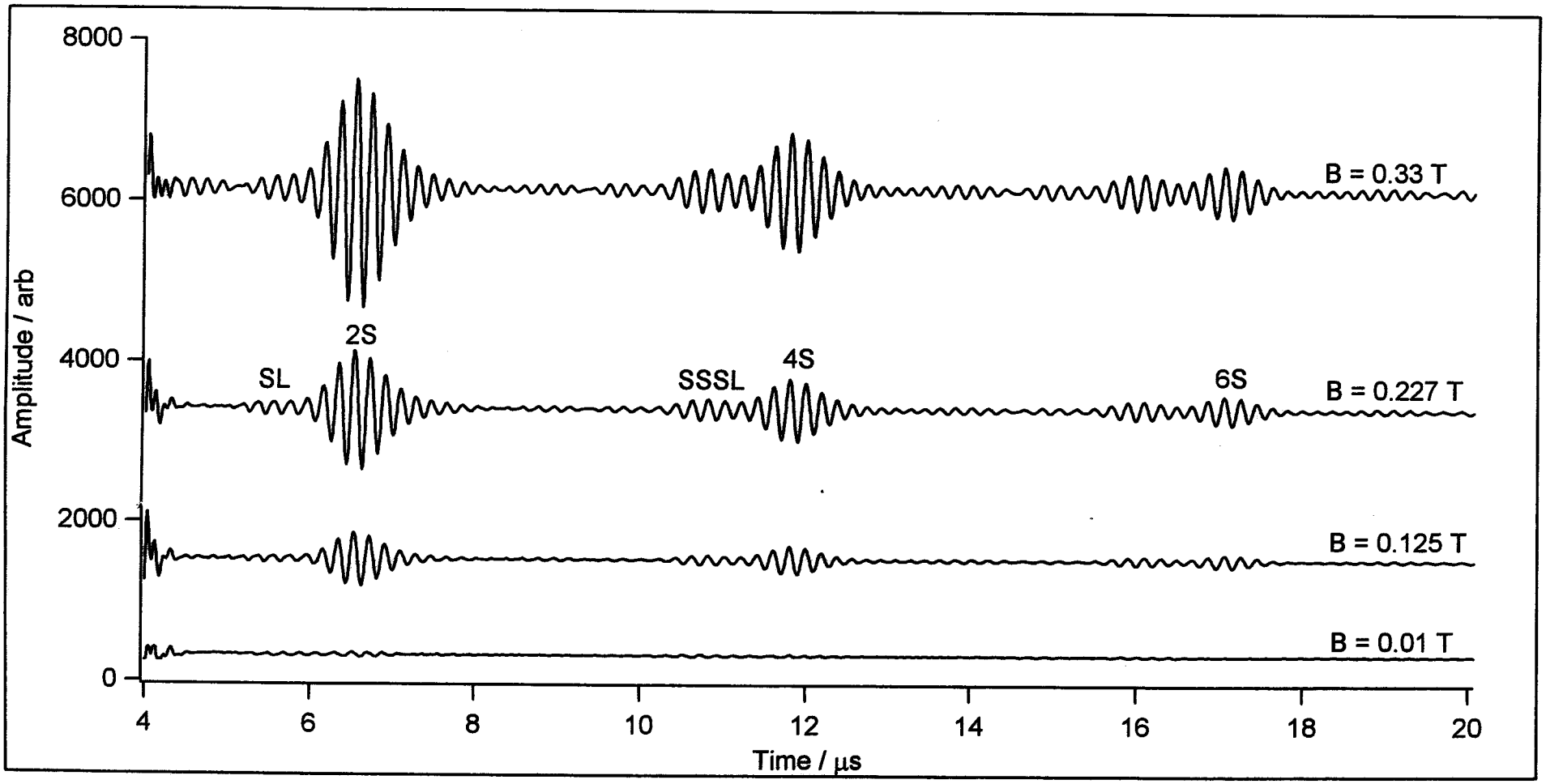

Figure 6.7: Traces detected by the EMAT coil on nickel

(a)

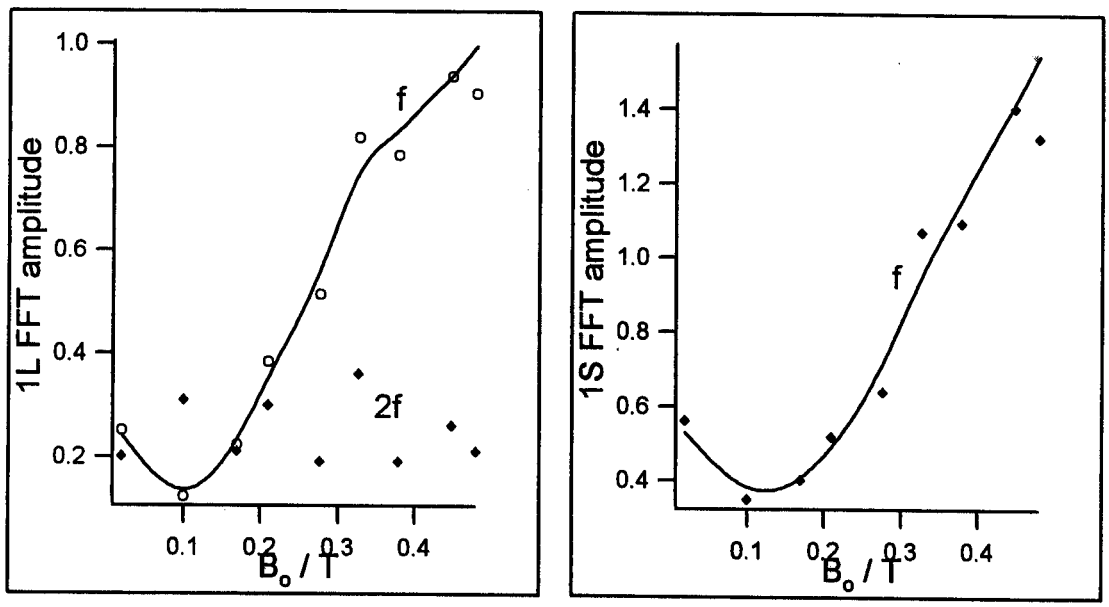

(b)

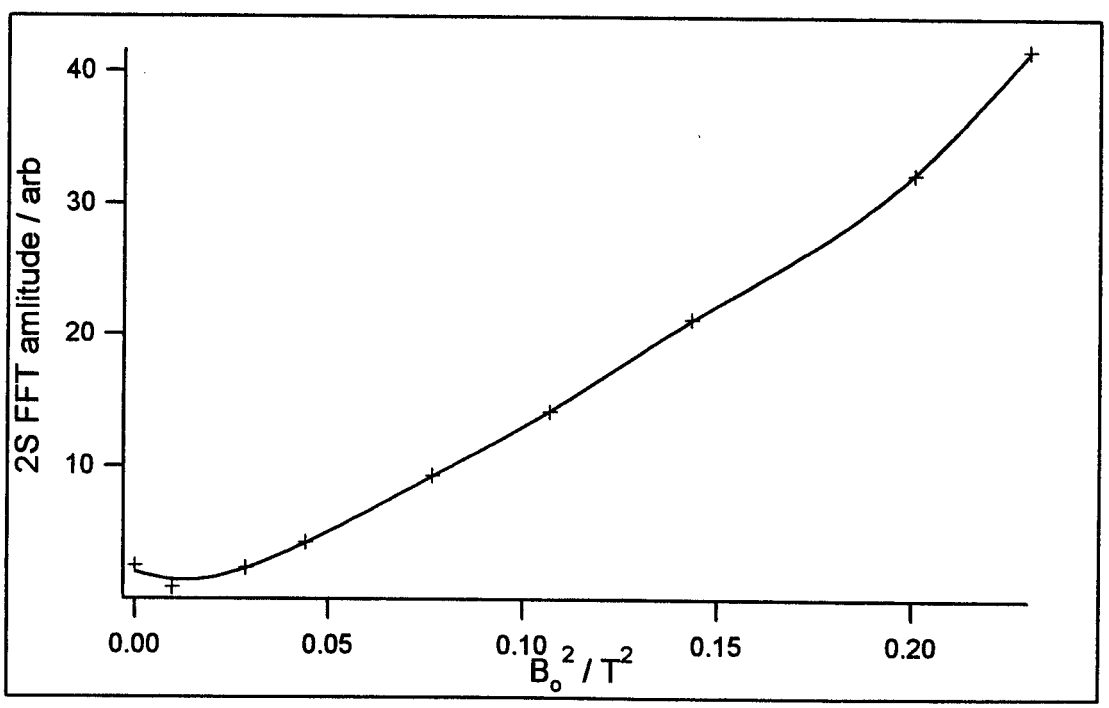

Figure 6.8 (a): FFT amplitudes of the f and 2f components vs B_o for the interferometrically detected waveforms from nickel
(b): FFT amplitude of the f component vs B_o^2 for the coil detected waveforms from nickel

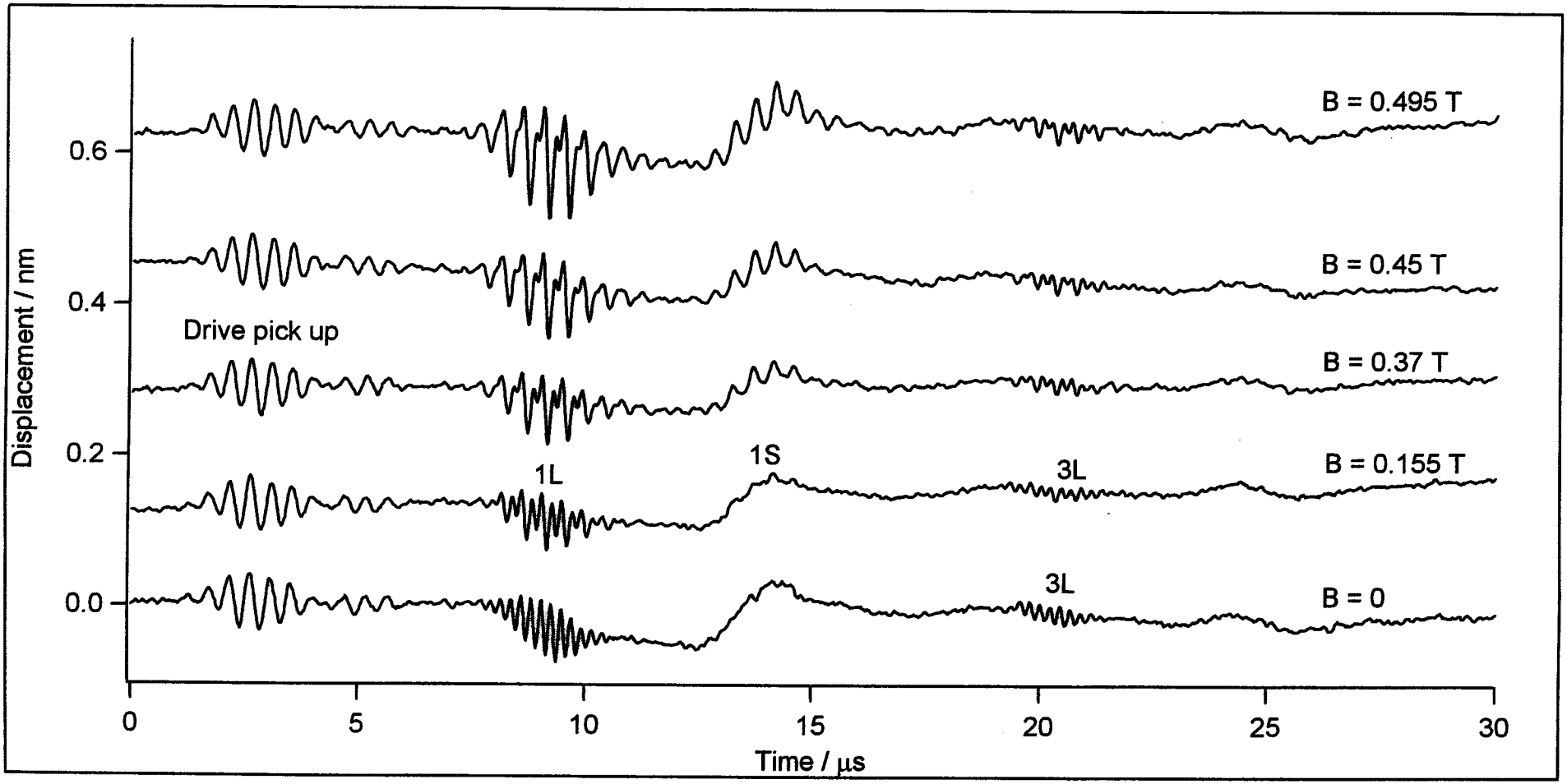

Figure 6.9: Out of plane displacement detected by Michelson interferometer from EMAT coil on Invar (64%Fe, 36%Ni)

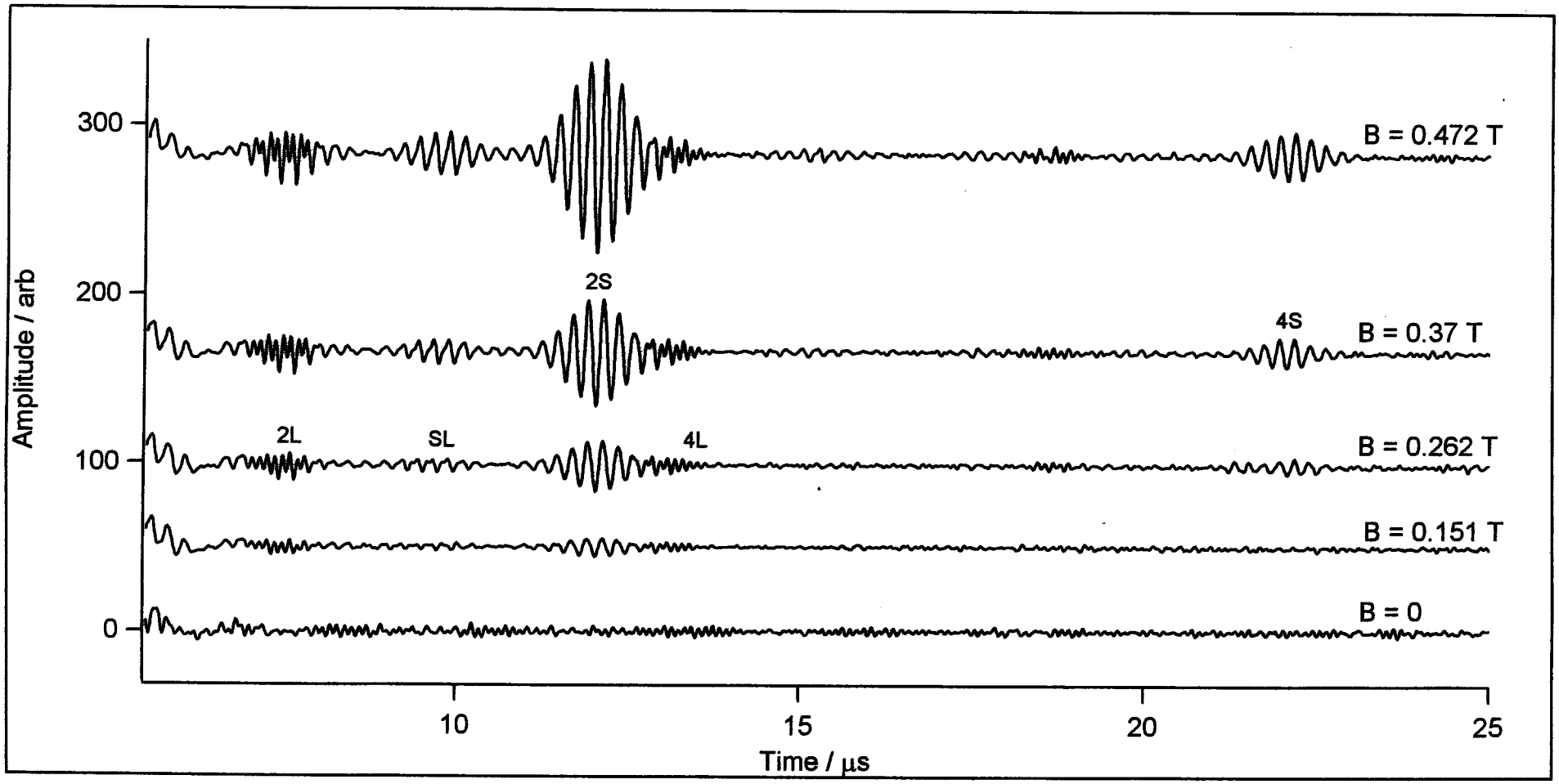

Figure 6.10: EMAT detected traces from Invar (64%Fe, 36% Ni)

(a)

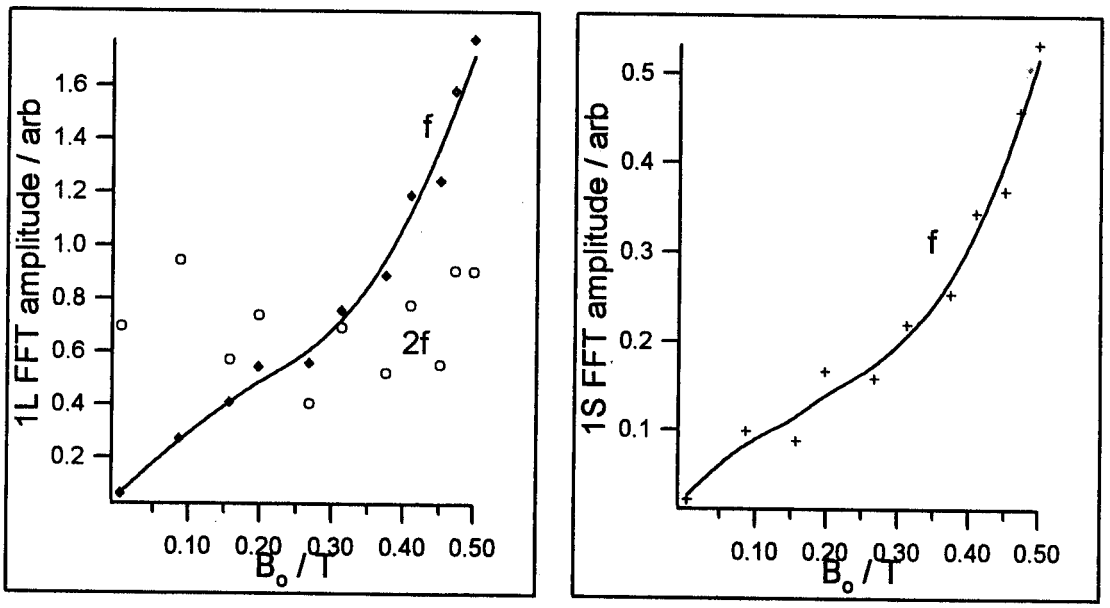

(b)

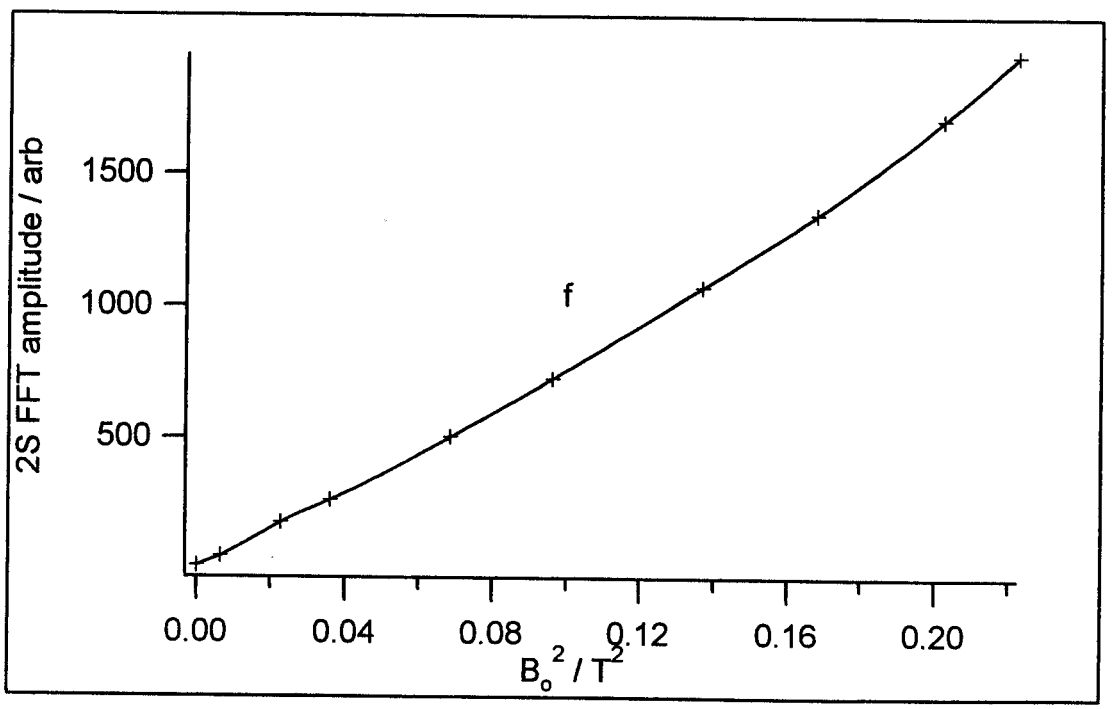

Figure 6.11 (a): FFT amplitudes of the f and 2f components vs B_o for interferometrically detected ultrasound on invar
(b): FFT amplitude of the f component of 2S vs B_o^2 detected by the EMAT coil on invar

(a)

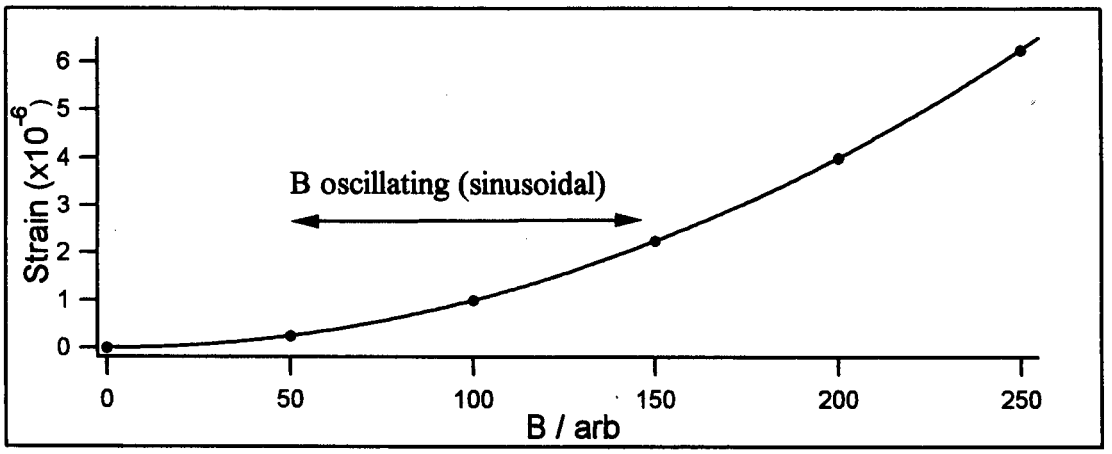

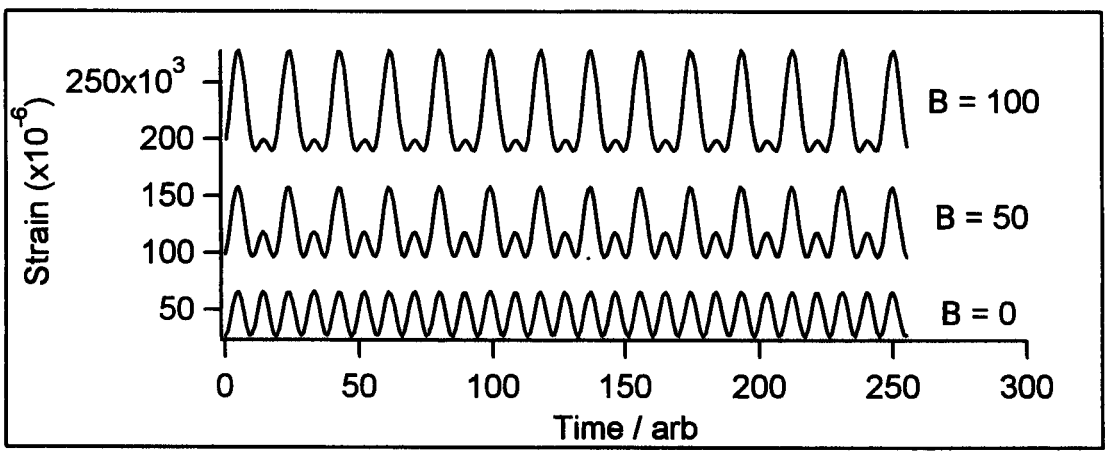

(b)

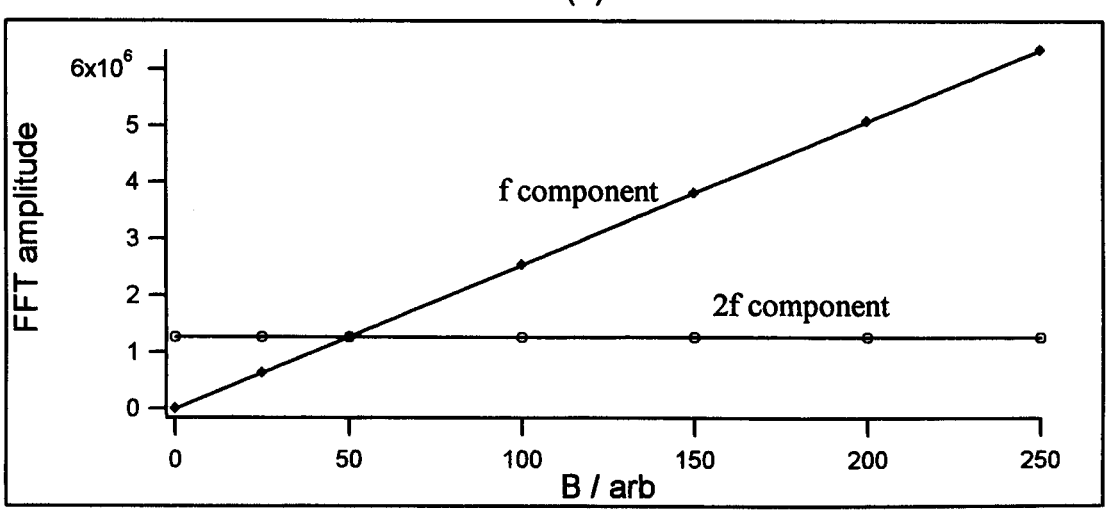

Figure 6.12 (a): Quadratic approximation to a magnetostriction curve and the corresponding predicted strain waveforms
(b): FFT amplitudes of the f and 2f components of the strain waveforms vs B_o showing relative independence of 2f

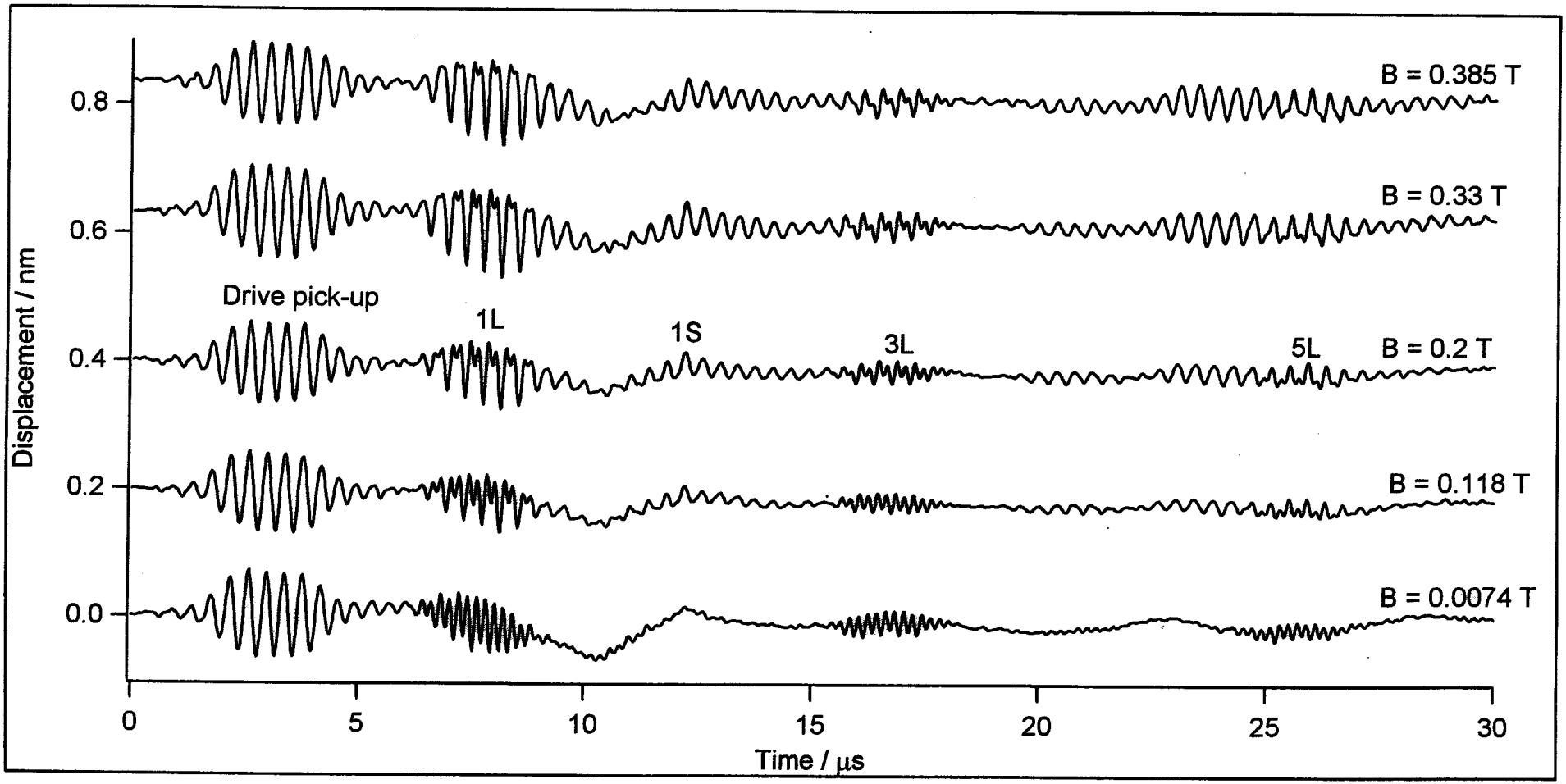

Figure 6.13: Out of plane epicentral displacement detected by Michelson interferometer due to EMAT coil on British Gas duplex

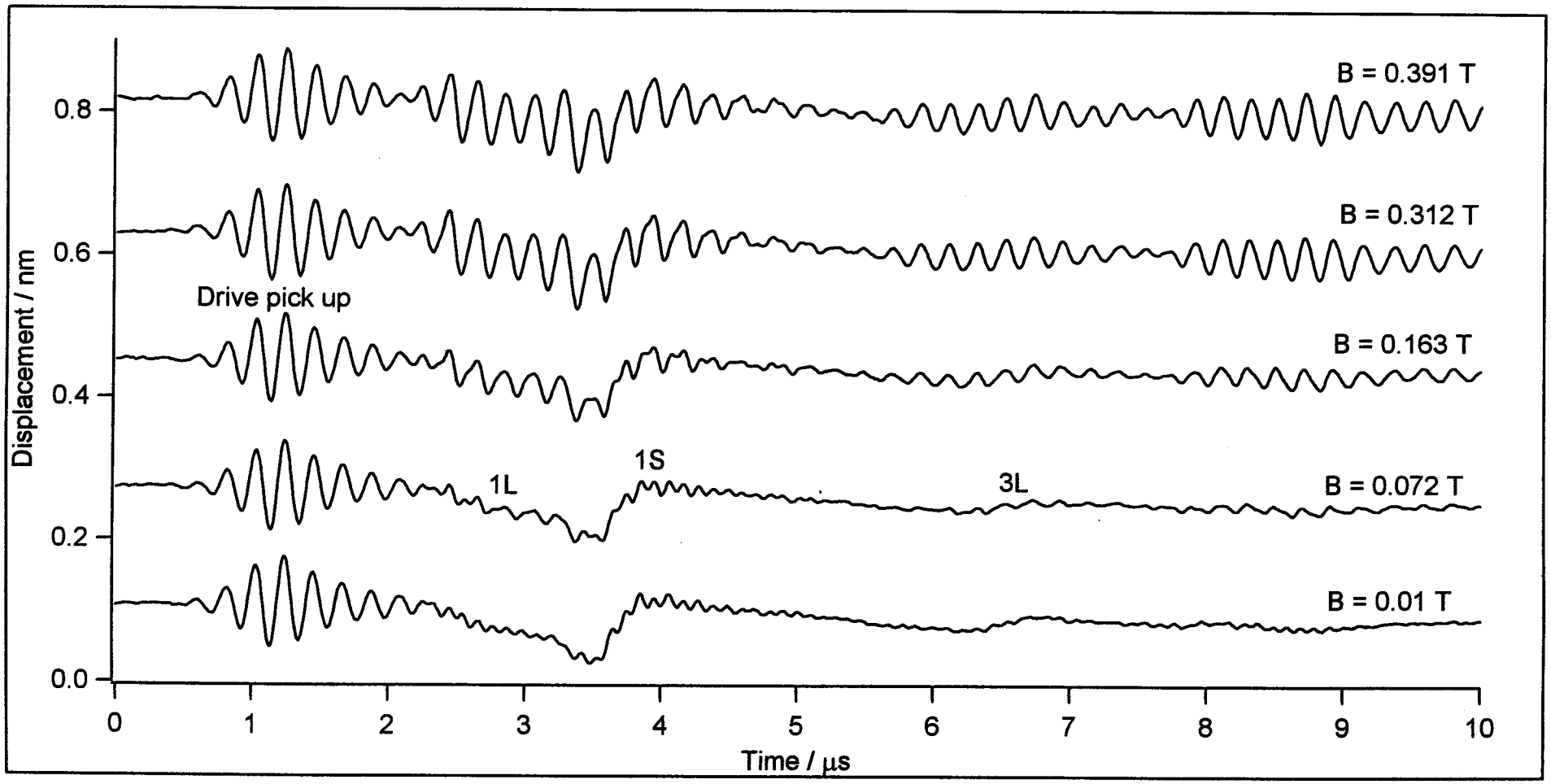

Figure 6.14: Out of plane displacement detected by the Michelson interferometer due to the EMAT coil on British Steel supplied duplex

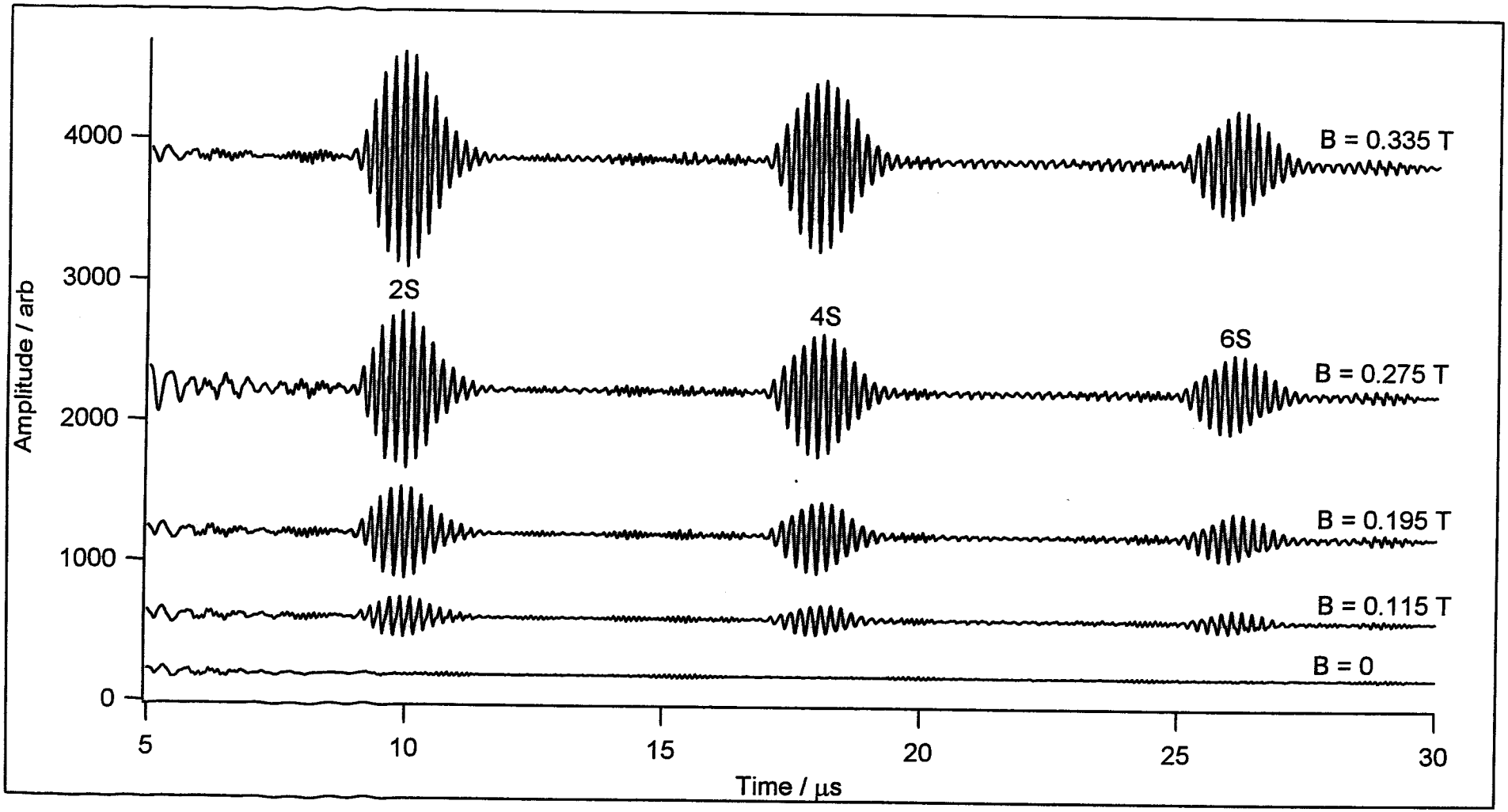

Figure 6.15: Waveforms detected by the coil on British Gas duplex

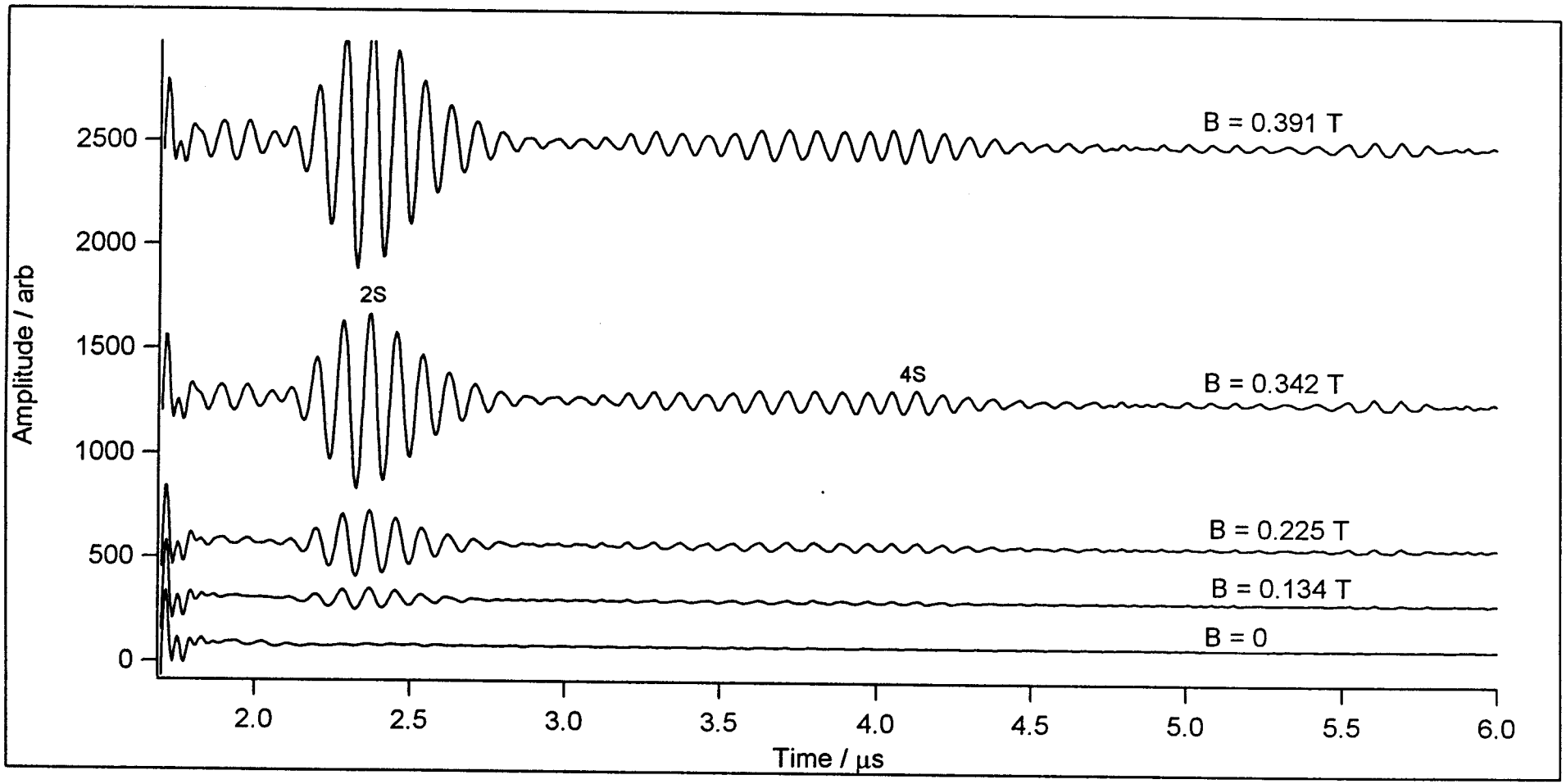

Figure 6.16: Waveforms detected by the coil on British Steel supplied duplex

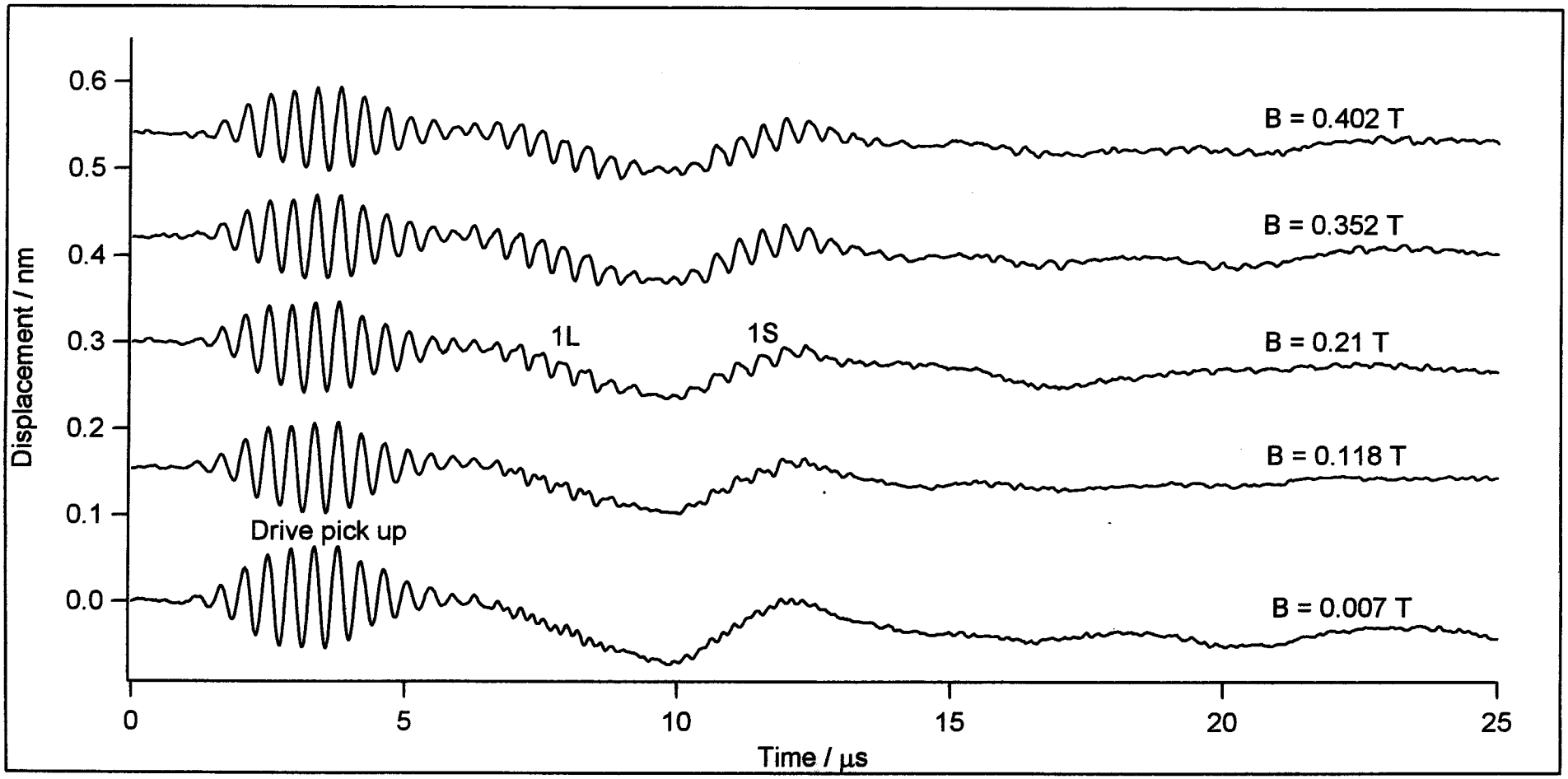

Figure 6.17: Out of plane displacement detected by the Michelson interferometer due to the EMAT coil on mild steel

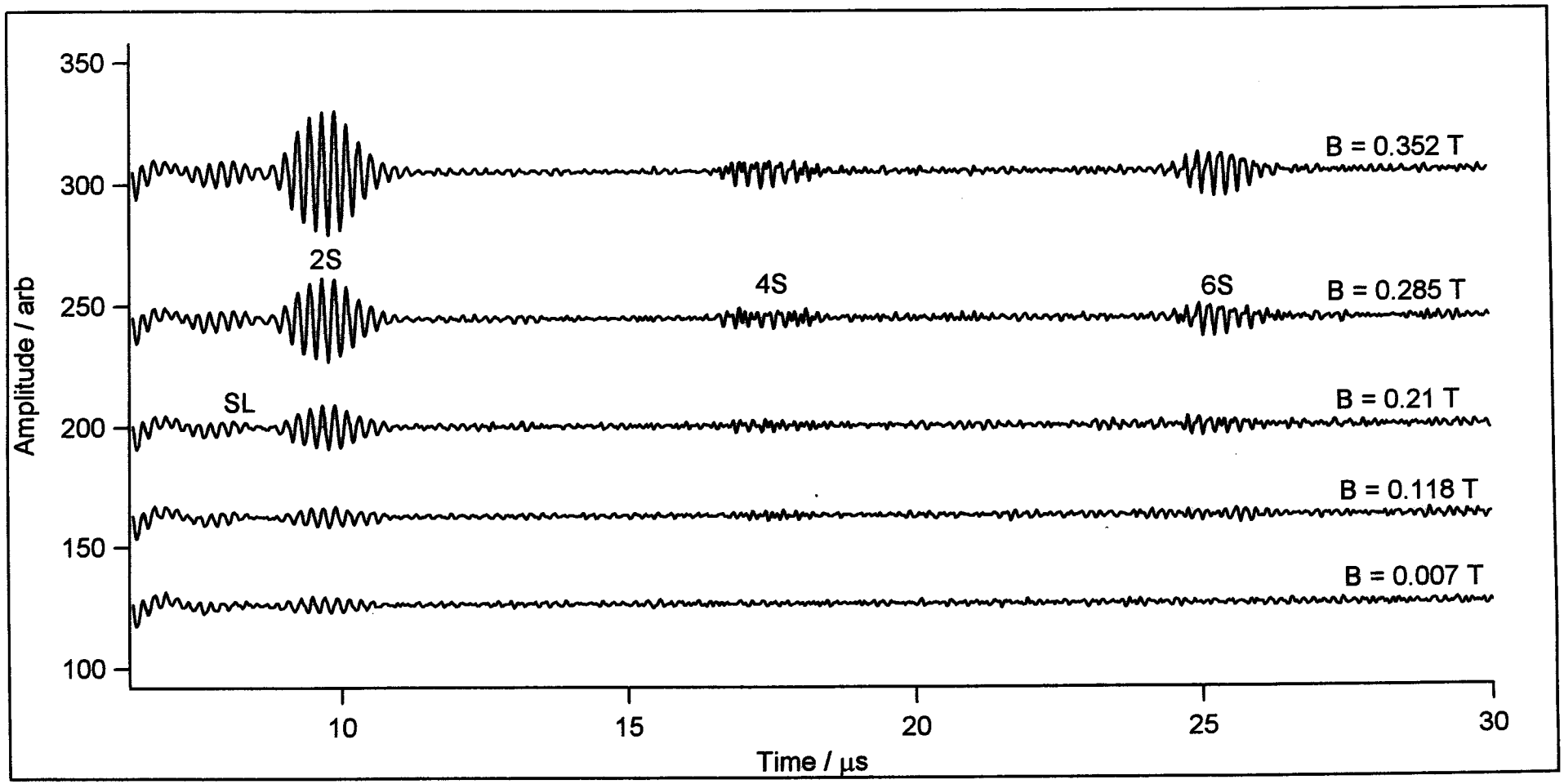

Figure 6.18: Waveforms detected by the EMAT coil on mild steel

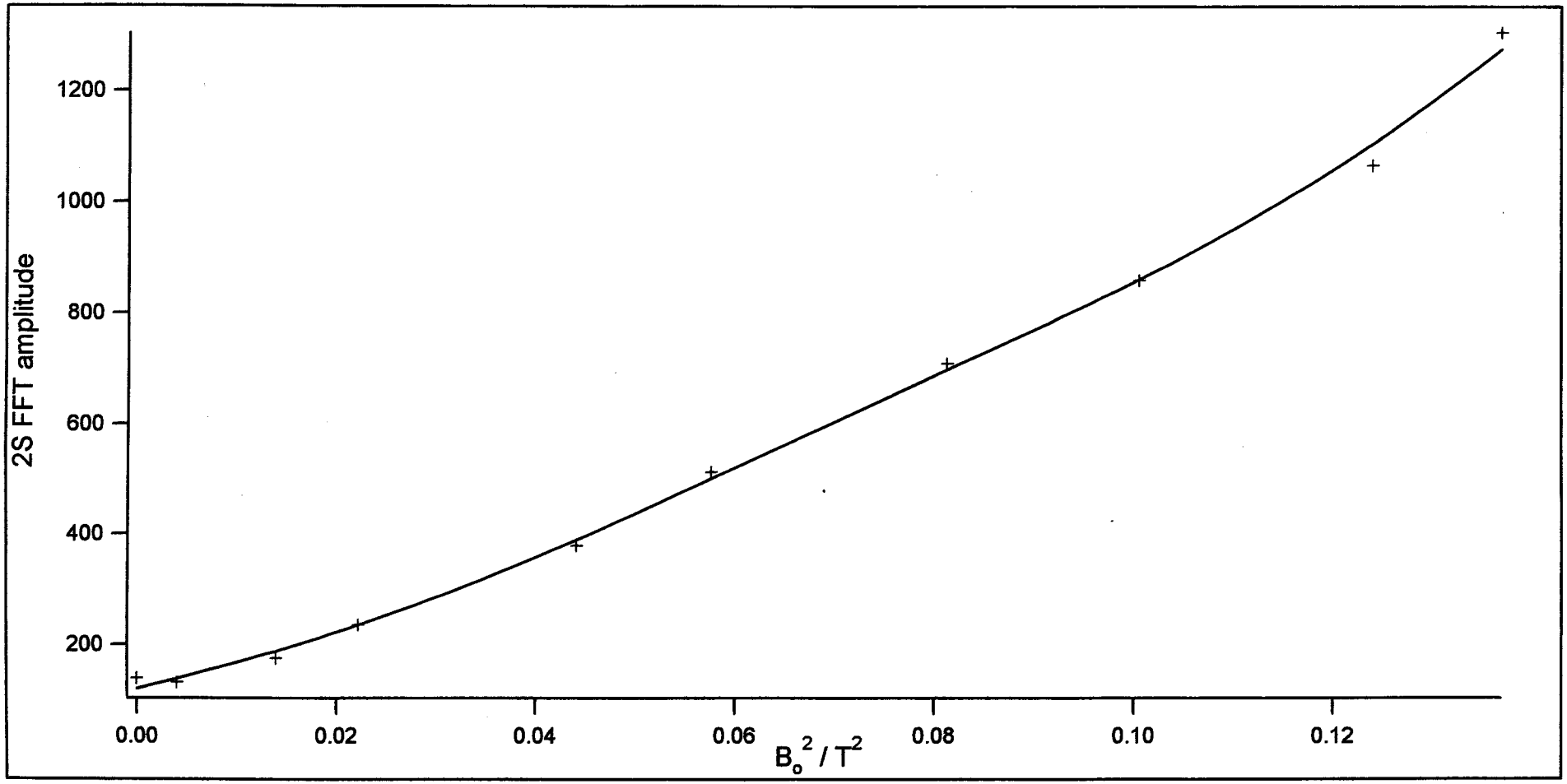

Figure 6.19: FFT amplitude of 2S vs B_o^2 for EMAT coil on mild steel

Chapter 7

Conclusions and further work

This chapter includes a copy of the conclusions from each results chapter so that the reader may review the major achievements and outcome of each. It finishes with a synopsis of the projects achievements as a whole and a discussion of the most useful directions for subsequent work to take.

7.1: Chapter 4 Conclusions

It has been shown that aluminium behaves as expected and obeys the predictions of the simple Lorentz theory. The results from the mild, low carbon tensile steels and cast irons have indicated that a predominantly Lorentzian mechanism is also responsible for S wave generation in these alloys. It has also been shown that the large changes in μ occuring throughout magnetisation from $B_o=0$ to B_s have no significant effect on the Lorentz generation process. This supports the assumption that, when $\delta<<\lambda$, ε is independent of both σ and μ for the Lorentz process. One of the original aims of this work was to assess which electrical and magnetic properties significantly affect EMAT generation on steels. It was seen that in the case of the 'ordinary' steels tested the spiral coil EMAT performance is more or less independent of μ and σ, the Lorentz mechanism being dominant, at the frequencies used here at least. In contrast, nickel and invar exhibited highly non linear B_o dependencies that are almost certainly due to an

essentially magnetostrictive mechanism. Given their high λ_s this is reasonable and fits the experimental results. The duplex, however, does not exhibit such large magnetostrictive strains, macroscopically at least, and is therefore somewhat enigmatic. Its two phase nature is certain to be linked to its high EMAT performance although this link, as outlined above, could be via a number of possible mechanisms. The fact, however, that the S efficiency has a maximum at B_s, in nickel, invar and duplex, suggests a common magnetostrictive generation mechanism that peaks at B_s due to the increase in δ and thus thicker ultrasonic source. Above B_s λ is much smaller and therefore, even though δ is much larger than when $B_o<B_s$, ε falls. Whilst this explanation is consistent with the results the detection mechanism itself must not be forgotten. Given the EMAT amplitudes obtained and the fact that the pulse current was a factor of 3-4 lower than on aluminium Lorentzian generation is ruled out on nickel and invar. It obviously cannot be ruled out for duplex due to the possibility of B_o focussing through the ferrite grains. Lorentzian detection of the reflected ultrasound, however, may still give a significant contribution to the EMAT signal as it is linearly dependent on B_o. It is therefore possible that on these samples the EMAT generates via magnetostriction but detects via the Lorentz mechanism. This may go some way to explaining the observed peak at B_s whereby the overall EMAT efficiency is a compromise between the increasing Lorentzian detection with the decreasing magnetostrictive strains as B_s is approached.

7.2: Chapter 5 Conclusions

7.2.1: Shear wave generation

The shear wave efficiency for all of the ferromagnetic samples showed very similar behaviour with a rapid drop to zero at, or very close to T_c. This is certainly consistent with earlier work on nickel and suggests that it is due to a similar cause, ie: an anisotropic magnetostrictive mechanism. We should not, however, discount the Lorentz mechanism simply because of the rapid drop in shear signal amplitude. As seen in aluminium, even the drop in σ with temperature causes a noticeable reduction in shear efficiency, although it does not fall to zero. This is, however, for a permanently paramagnetic metal and so takes no account of any change in μ and its corresponding effect on δ and B_o. We know already that B_o should fall by a factor of ~ 2 when the sample becomes paramagnetic, this being due to the loss of the effective 'image magnet' within the sample. Therefore the Lorentzian send-receive efficiency should drop by a factor of 4, as it is dependent upon B_o^2. The sudden drop in μ also has the obvious effect of drastically increasing δ, a drop from $\mu_r = 600$ say (eg: nickel) to $\mu_r = 1$ increasing δ by a factor of 25. Under these conditions we could expect the signal to fall very quickly until at T_c it was ~ 100 times less than when the sample was in the ferromagnetic state. This said, if the signals in duplex or nickel were of Lorentzian origin then we would still expect to observe them above T_c, given their large amplitude. This proves not to be the case and makes it very likely that magnetostriction is indeed responsible for the S mode generation. Again this agrees with the results of Gitis who found that the shear wave

signal in nickel disappeared completely at T_c even when $M > M_s$. Under these circumstances μ_r is always equal to 1 and therefore the only change in the variables in equation 2.17 is B_o which does not suffer the large swing experienced by δ. A notable exception to the general trend is invar which exhibits a sharp increase in S efficiency just below T_c. This said, however, none of the other samples exhibit the unusual thermal and magnetic properties of invar so it would be naive to expect it to behave as they do. This is borne out quite clearly by the increase in both V_S and V_L with increasing temperature.

7.2.2: Longitudinal wave generation

As expected, the results for aluminium showed no L mode detection at any temperature in the range 20°C to 420°C. It will be shown in the proceeding chapter that an L mode is in fact generated in aluminium but is not detected due to the lack of any static radial field. The lack of an L mode in nickel suggests that the power into the coil may simply not have been sufficient to excite this mode around Tc. Given the large L amplitudes observed in invar and mild steel this suggests that the spontaneous volume magnetostriction is much smaller in pure polycrystalline nickel than in either the 64%Fe:36%Ni alloy or mild steel. The fact that BG duplex displayed such a small peak in L efficiency at T_c suggests that the sample also exhibits a much smaller volume change on passing the ferro–paramagnetic transition. This is perhaps not unexpected given that half the alloy is paramagnetic in the first place. Thus, as T_c is passed, the ferrite grains undergo a volume change whilst the austenite grains do not. The lack of expansion in the austenite therefore 'absorbs', to some extent, the ferritic expansion and

the overall effect is reduced. This, of course, is only a simple intuitive argument but could explain the observed behaviour. In contrast, the inhomogeneity in invar is field dependent, therefore in the EMATs field far more of the alloy is ferromagnetic and the 'damping effect' due to its paramagnetic phase is reduced, hence the large L amplitudes.

7.3: Chapter 6 Conclusions

Using the interferometer showed that in all the metals and alloys tested a frequency doubled L wave was generated by the spiral coil. In every case this component was seen to be swamped by one at the drive frequency on application of B_o. This B_o also lead to an increase in the transient amplitude of the S mode, similar behaviour being shown by the L. This contrasts with the background trends of both modes that appear relatively field independent and likely due to a low frequency magnetostrictive excitation over the coils extended source. The fact that both S and L drive frequency components in all the samples exhibited similar field dependences suggests that they are due to the same source, this source being magnetostrictive in nickel, invar and duplex and leading to an L mode by virtue of the non isovolumetric nature of radial shear waves. The B_o=0 waveforms of all the ferromagnetic samples are consistent with a self field mechanism in that it acts normal to the surface and should therefore produce a very small transient S response compared to the L. This was modelled for a point source and found to be consistent with the results from all of the samples.

An obvious extension of the present work would be to use higher applied fields to look for the re-emergence of frequency doubling in mild steel due to the turning point in its λ curve. This, however, would require considerable modification to the experimental arrangement employing, ideally, an electromagnet to produce a higher and more uniform field. A second potentially useful development would be to use a purely Gaussian unipolar pulse as the drive. This may help to elucidate whether the background trace features are indeed due to a low frequency magnetostrictive excitation and would also remove any doubt as to the phase of the ultrasound. Thirdly, measurements of the ultrasonic directivity may help in better determining the source distribution and therefore identifying the dominant mechanisms. For the moment it must suffice to say that the self field force does indeed act in a non magnetic conductor to produce a frequency doubled L mode and that this force must therefore also act in the conducting ferromagnetic samples tested here.

7.4: Overall Conclusions and Further Work

The aim of this project was to determine the dominant mechanisms behind spiral coil EMAT ultrasound generation on ferromagnetic metals and alloys. The ultimate aim of this was to optimise EMAT parameters and allow their use on a wide range of alloys, particularly steels. Early work on the B_o dependence of EMAT efficiency showed that the Lorentz mechanism was probably dominant in all the steels and cast irons tested with the notable exception of duplex stainless steel. The results also strongly suggested that this mechanism is virtually independent of either the magnetic permeability, μ, or

electrical conductivity, σ, consistent with the predictions of several authors [1, 2, 3]. Magnetostriction curves in two orthogonal directions were also obtained for every sample studied, little correlation being found between EMAT efficiency and the gradient, $d\lambda/dB$, of these curves. The fact that the EMAT signals in low carbon steels are almost linearly dependent upon B_o is unpromising from an application viewpoint, no windows of opportunity really presenting themselves for exploitation. This said, however, the subsequent work at higher temperatures showed the presence of greatly enhanced L mode signals just above the Curie transition, T_c. This holds some promise in terms of process control where accurate thickness measurements of hot moving steel could be made in real time. However, more work is required to investigate whether this peak in L mode efficiency is due to the steel itself and not some associated oxide layer. This would require the use of a controlled atmosphere furnace that was not available at the time of writing. The high temperature experiments also served to confirm the proposition made in chapter 4 that magnetostriction was the dominant source of radial S waves in nickel, invar and probably duplex. In every case, however, the peak in L efficiency occurred above T_c, the difference being of the order of 10 degrees in all but invar. As the VSM results illustrated, T_c is field dependent, therefore the difference between it and the EMAT peak could be due to the field induced increase of T_c. It would therefore be useful to investigate the B_o dependence of the EMAT signals at various temperatures around T_c. To do this, however, would require control of both the applied magnetic field and the sample temperature up to and above T_c. The most likely route for achieving this would be to modify the current electromagnet to allow heating of the sample. This, however, would present several experimental challenges, how to

actually heat the sample in the first place and how to measure B_o next close to a sample at several hundred degrees being just two of the more obvious ones.

Use of the Michelson interferometer to detect EMAT generated ultrasound was very fruitful in proving the existence of a self field frequency doubling mechanism acting in aluminium. Ultrasound generation in aluminium by a pulsed coil alone is alluded to by Gitis although no reference is given by him. Apart from this mention of the effect no literature could be found detailing it, this work then constitutes the first time it has been observed and explained as far as the author is aware. The existence of a similar 2f L mode in several ferromagnetic samples is consistent both with the self field model and, to some extent, Komarovs treatment of magnetostrictive frequency doubling. However, Komarovs model was somewhat different to the case here in that B_o was aligned parallel with the ultrasonic propagation.

The duplex samples remain something of an enigma in that very little is known about their magnetostrictive properties. It is therefore impossible to try and state the source of their high EMAT efficiency although magnetostriction does seem a likely candidate given the BG samples highly orientated structure. Measurements of lattice parameters as a function of applied field, on a microscopic scale, would probably resolve this question although how this could be accomplished is unclear. Microscopically focussed X-rays seem a probable choice as this would not suffer the problems associated with the use of some form of electron microscopy, electrons being influenced by the static magnetic field. However, focussing a beam of X-rays onto a ferrite or austenite grain only 10's of microns across probably constitutes a significant challenge in itself before

being able to obtain any useful results. The possibilty of high remnance leading to enhanced detection of the L mode, whilst fitting the results empirically, was introduced in a purely ad hoc manner. This suggestion would also benefit from further study, some form of Kerr effect or magnetic force microscopy perhaps being the most likely methods. This would hopefully, even if only qualitatively, show up differences in the remnance of the ferrite grains of the BG and BS duplex samples due to their different shapes and therefore demagnetizing factors.

During this work it has become apparent that there is something of a gap in theoretical work concerning the spiral coil-normal B_o geometry on metal polycrystals. This has meant something of a lack of models with which to compare the experimental results and a somewhat empirical feel to the analysis. Whilst theoretical work has been done on the case of a plane electromagnetic wave incident on a ferromagnetic conductor [4, 5, 6], it is not really representative of the small spiral coil case. It is hoped that the results presented here will allow verification of any models developed subsequently, although such models would require far more than the humble mathematical skills possessed by this author. The EMAT generation process on ferromagnets is complex enough in an isotropic sample, let alone a two phase material such as duplex.

To conclude then, the original aim of the project has been fulfilled in showing that for the low carbon steels the overall EMAT efficiency is almost independent of both μ and σ. A good deal of further work is possible using the interferometric technique described here, high temperature experiments and the use of higher applied fields perhaps being

the most potentially valuable. Analysis of the results, however, would require more detailed theoretical treatments that are not yet available and would prove invaluable if further work was to continue.

Chapter 7 references

1: R. B. Thompson; *Journ. Appl. Phys.* **48**, pp 4942 - 4950 (1977).

2: I. V. Il'in and A. V. Kharitinov; *Defektoskopiya* **no 7**, pp 86 - 93 (1980).

3: A. Wilbrand; *New Proc. in Nondestr. Testing* edited by P. Holler p 71, published by Springer (Berlin) (1983).

4: D. J. Meredith et al; *Journ. Acoust. Soc. Am.* **45**, pp 1393 - 1401 (1968).

5: E. R. Dobbs; *Physical Acoustics*; Ed: W. P. Mason and R. N. Thurston; Academic Press (London) **10**, pp 127 - 189 (1973).

6: R. S. Il'yasov et al; *Defectoskopiya* **no 1**, pp 33 - 40 (1996).